Zeng, Zheng, Ph.D. Nanoscale Reactions In Opto-magneto-electric Systems. (2017)
Directed by Dr. Jianjun Wei. 270 pp.

My research is interdisciplinary in the areas of chemistry, physics and biology for better understanding of synergies between nanomaterials and opto-magneto-electric systems aimed at the practical applications in biosensor, energy (energy storage and electrocatalysis), and biomimetics, in particular, the associated electron transfer, light-matter interactions in nanoscale, such as surface plasmon resonance (SPR) (nanoplasmonics), and magnetic field effect on these phenomena with targeted nanomaterials. Specific research thrusts include: (1) investigation of surface plasmon generation from a novel nanoledge structure on thin metal film. The results are used for the nanostructure optimization for a nanofluidic-nanoplasmonic platform that may function as a multiplexed biosensor for protein biomarker detection; (2) examination of magnetic field effect on uniformly deposited metal oxide on electrospun carbon nanofiber (ECNF) scaffold for efficient energy storage (supercapacitor) and electrocatalytic energy conversion (oxygen reduction reduction). (3) magnetic response of cryptochrome 1 (CRY1) in photoinduced heterogeneous electron transfer (PHET).

# NANOSCALE REACTIONS IN OPTO-MAGNETO-ELECTRIC SYSTEMS

by

Zheng Zeng

A Dissertation Submitted to
the Faculty of The Graduate School at
The University of North Carolina at Grensboro
in Partial Fulfillment
of the Requirements for the Degree
Doctor of Philosophy

Greensboro
2017

Approved by

Jianjun Wei
Committee Chair

APPROVAL PAGE

This dissertation written by Zheng Zeng has been approved by the following committee of the Faculty of The Graduate School at The University of North Carolina at Greensboro.

Committee Chair Jianjun Wei

Committee Members Joseph M. Starobin

Dennis R. LaJeunesse

Shyam Aravamudhan

Tetyana Ignatova

10/11/2017
Date of Acceptance by Committee

10/11/2017
Date of Final Oral Examination

ACKNOWLEDGEMENTS

I have received a lot of help during the years and I feel truly grateful to many people. First and foremost, I would like to thank JSNN. JSNN means a lot to me. I tried my best to help it win the honor around the world. Although JSNN is a baby in research areas, I am very proud of studying and graduating from here. Wherever I will go in the near future, I will miss the time in JSNN.

Next I want to thank my academic advisor, Prof. Jianjun Wei. He has been a wonderful scientist and educator. He is not only my mentor but also my good friend. I used to be rush to do something, he always told me to calm down. He was always patient when I needed help and he has always provided me with useful guidance and invaluable advice in my study and life management.

I am also thankful to my other committee members and teachers, Prof. Starobin, Prof. LaJeunesse, Prof. Herr, Prof. Aravamudhan, Prof. Kelkar, and Prof. Ignatova, who have guided me over the years as well. Prof. Starobin is also the teacher of my math and physics and I have learnt a lot from him through our discussion about the protein diffusion calculations. Prof. LaJeunesse has become one of my favorite teachers and I feel so lucky that I could work some projects with him.

I am also thankful to my labmates, including Yiyang Liu, Wendi Zhang, Taylor Mabe, Zuowei Ji, Harish Chevva, Alex Sheardy, Durga M. Arvapalli, Kokougan Allado, Bhawna Bagra, and Ziyu Yin. I am very happy to discuss research with them. They are not only co-workers, but also my good friends. I am looking forward to hearing the success

from all of them. Especially Yiyang and Wendi help me a lot to go through the hard time of my life. Hope to keep this friendship and contact in the rest of my life.

I am also thankful to my other collaborators, Prof. David Waldeck, Dr. Madu Mendis and Dr. Brain Bloom in University of Pittsburgh, and Prof. Adam Smith and Dr. Xiaojun Shi in University of Akron. Especially Prof. David Waldeck, I have learnt a lot from him through our discussion about the papers of surface plasmon generation and carbon nonadots.

I am eternally indebted to my family. I want to give all of my love to my mother. She always told me not to worry about her and just go ahead to pursue my dream of science, but I can understand the feelings behind the words. I am especially thank my beloved wife. She is not only stay alone at home in China but also patiently take care my family things to support my study in USA. During the toughest time of my life, she has always been there for me. My father, the only idol in my life, He has great expectations on me. Although you have reached another world, I think you will be honor of your son. I miss you very much and I wish I could go ahead to lead our family!

TABLE OF CONTENTS

Page

LIST OF TABLES

Page

LIST OF FIGURES

Page

# CHAPTER I

# INTRODUCTION

Dramatic advances are on the horizon resulted from the rapid pace of technological developments and new interdisciplinary fields. Interdisciplinary research continually evolves beyond the boundaries of a single discipline or area of research practice, which integrates theories, methods, tools and/or concepts from multiple specialized knowledge bases.[1,2] My research is interdisciplinary in the areas of chemistry, physics and biology for better understanding of the complex behaviors of opto-magneto-electronic systems aimed at the practical applications in biosensor, energy (energy storage and electrocatalysis), and biomimetics, in particular, the associated electron transfer, light-matter interactions in nanoscale, such as surface plasmon resonance (SPR) (nanoplasmonics), and magnetic field effect on these phenomena with targeted nanomaterials.

Opto-electronic system: this part aims to develop an optimal nanoledge structure of a novel nanofluidic-nanoplasmonic platform to realize multiplexed monitoring of biological binding processes, specifically for detection of cardiovascular disease and cancer biomarkers in bio-fluids. In contrast to current large-sized, cumbersome surface plasmon resonance (SPR) sensing technology, the proposed device is comprised of a multilayer nanostructured array that combines the functions of nanofluidics for effective reagent transport and nanoplasmonics for sensing, concurrently. In order to achieve these goals, three key questions need to be addressed including high surface Plasmon (SP) for signal

transduction; signal/noise ratio and sensitivity, and possibility and efficacy of protein biomarker flowing into the nanoledge structure. For the first two questions, localized surface plasmon resonance (LSPR) of nanostructured thin metal films (so-called nanoplasmonics) has attracted intense attention due to its versatility for optical sensing and device integration. A semi-analytical model that enables decomposition and quantitative analysis of SP under plane-wave illumination is applied to a new complex nanoledge aperture structure, thus providing insight on how to design such plasmonic devices for optimal plasmonic generation efficiencies and RI sensitivity.[3-5] In concert with the analytical treatment, a finite-difference time-domain (FDTD) simulation and testing of the fabricated devices are used to validate the optical transmission spectra and RI sensitivity as a function of the nanoledge device's geometric parameters, and preliminary studies present good agreement with the analytical model. For the last question, we will try to address the challenge of efficient delivery of target bio-molecules to the plasmonic cavity by the experimental verification. Experimental measurements, including nano-confined dye solution flow-through the subwavelength channel and fluorescence correlation spectroscopy (FCS) of labeled proteins in nanoslits, will be carried out to visualize the trapping of molecules and migration in nanoscale. The present study seeks to develop (design, fabricate, and test) a prototype of the nano-fluidic-plasmonics array integrated in a microfluidic channel, to adapt protocols for nano-confined flow-through transport validation and to culminate with a clear demonstration of improved plasmonic sensing of biomarkers. The nanostructure arrays and device optimization as well as integration with

sample handling microfluidics for detecting multiple biomarkers in real biofluids will be planned for future research.

Magneto-electronic system: fundamental breakthroughs that are needed for discovery of new nanomaterials for efficient energy storage and conversion in various environments. For the electrochemical energy storage system, supercapacitors are used to provide high power in a short time by providing competitive energy density, high cycle lives and stable cell materials with low cost. Now supercapacitors are being used to increase the efficiency of hybrid electric vehicles, to protect the memory as an internal back-up power of personal electronics, and to eliminate the need for replacing batteries or running a power line in solar arrays for micro-energy harvesting applications. Fundamentally, Supercapacitors use the electric double layer capacitance (EDLC) or pseudocapacitance (specific ions are desolvated-adsorbed between the electrolyte and active materials (usually metal oxides)) or a combination of both to store charges and then provide rapid release of energy within short time duration. Regarding the research area, the key objective is (1) to further optimize the geometries and morphology of the 3D interconnection of nanomaterials, which can largely increase the specific surface area and facilitate the charge transfer; (2) to optimize the metal oxide nano architecture for better electrons exchange: nanoscale structure can bring higher capacitive value based on active materials only, but the overall performance is limited since the mass loading is small; microscale layers lead to better performance based on the whole electrode due to the high metal oxide-substrate ratio, but the internal resistance will increase as the metal oxide layers become thicker; (3) to enhance the interface charge density, facilitate electrolyte

transportation, and improve the efficiency of cation intercalation/de-intercalation of the energy storage system under an external condition. The focus is on developing a fundamental understanding of nanomaterials properties and their enhanced electrochemical energy storage abilities. For the electrochemical energy conversion system, a fuel cell has been one of the promising energy devices for generating clean and sustainable energy. The oxygen reduction reaction (ORR) is the most important reaction in energy converting systems such as proton exchange membrane (PEM) fuel cells. ORR in aqueous solutions undergoes mainly by two pathways: a 2-electron pathway from oxygen to hydrogen peroxide, and a 4-electron pathway from oxygen to water. In order to ensure that the fuel cell generates the maximum power output, a direct 4-electorn pathway is necessary because the 2-electron pathway involved in the cathodic process seriously compromises the energy yield of the fuel cell. Moreover, the cell membranes and other supporting materials will be impaired in the presence of an excess hydrogen peroxide due to the peroxide radical formation generated from a disproportionation reaction. In the search of catalysts for limiting the hydrogen peroxide generation or decomposing generated hydrogen peroxide, although the confinement of oxygen within the catalysts is effective, inhomogeneous surface coverage of the catalysts allows hydrogen peroxide to escape into the bulk solution, which decreases the decomposition efficiency of generated hydrogen peroxide. Hence, a study to achieve stable synthesis of catalysts may lead to better strategies for achieving a direct 4-electron pathway. Furthermore, considering that the electrochemically generated hydrogen peroxide can then be decomposed to water before it escapes into the bulk solution, the rate of hydrogen peroxide decomposition by catalysts should be faster than the

electrochemical generation process. In previous studies, it was found that an external magnetic field over a material with the magnetic susceptibility could facilitate the electron transfer rate due to the effects of Lorentz force acting on moving charge/ions, charge density gradient modulation, electron state excitation and oscillatory magnetization. Hence the focus is still on developing a fundamental understanding of nanomaterials properties and their enhanced electrochemical conversion abilities.[6-8]

Opto-magneto-electronic system: successful merging the capabilities of emerging nanomaterials with unique biomaterials will result in novel, low-power, ultra-scaled, bio-inspired electronics and photonics. The most important step is to find the unique biomaterials. Cryptochromes, a class of flavoproteins, can result in photo-induced electron transfer by absorbing blue light (300-500 nm), whose photochemistry is implicated to underpin crucial biological function associated with phototropism, circadian clocks and bird navigation. Many researchers have further reported that plants and animals (sea turtles, spotted newts, lobsters, honeybees, and European robins, etc.) have the ability to perceive magnetic fields from the earth to direct their circadian rhythms and orientation behaviors due to the magnetoreception role of cryptochromes. Furthermore, theoretical and spectroscopic studies suggest that electron transfer between light activated FAD and tryptophan (Trp) residues leads to the formation of a spin-correlated radical pair, whose subsequent relaxation is sensitive to external magnetic fields.[9-11] Towards this vision, the overall objective of this part is to realize functional nano-bioelectronic systems, e.g., field-effect electron transfer as biomimetic sensors that merges the unique physic-chemical properties of nanomaterials and cryptochromes that play a key role in the physiological

compass sensors of animals (insects and birds). To achieve this objective, a new investigation system should be developed to cover all of the electrical, photonic and magnetic functional properties.

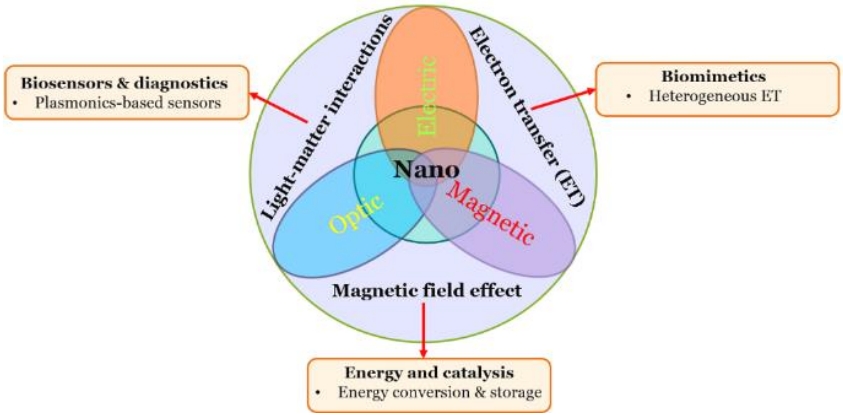


Figure 1.1. Research Overview. An overview of research interests, areas and goals.

Figure 1.1 illustrates an overview of my research interests, areas and goals. A primary goal of my research is to exploit synergies between Nanomaterials and opto-magneto-electronic systems and to address important fundamental and technological problems by employing methods of materials synthesis, advanced nanofabrication and analytical, electrochemical, spectroscopic means. The research will be beneficial to real-world applications in healthcare (disease prognosis/diagnosis, drug eligibility, and therapeutics), catalysis and energy (fuel cells and supercapacitor, etc.), and environment (e.g. biomimetic sensory and monitoring).

**References**


1. Noor, Ahmed. (2012) Open Engineering, 2.3, 315-324.
2. Huang, Y., Zhang, Y., Youtie, J., Porter, A. L., & Wang, X. (2016). PloS one, 11(5), e0154509.
3. Lal, S., Link, S., & Halas, N. J. (2007). Nature photonics, 1(11), 641-648.
4. Li, J., Chen, C., Lagae, L., & Van Dorpe, P. (2015). The Journal of Physical Chemistry C, 119(52), 29116-29122.
5. Quidant, R., & Kreuzer, M. (2010). Nature nanotechnology, 5(11), 762-763.
6. Choi, N. S., Chen, Z., Freunberger, S. A., Ji, X., Sun, Y. K., Amine, K., ... & Bruce, P. G. (2012). Angewandte Chemie International Edition, 51(40), 9994-10024.
7. Miller, J. R., Outlaw, R. A., & Holloway, B. C. (2010). Science, 329(5999), 1637-1639.
8. Shao, M., Chang, Q., Dodelet, J. P., & Chenitz, R. (2016). Chem. Rev., 116, 3594-3657.
9. Giovani, B., Byrdin, M., Ahmad, M., & Brettel, K. (2003). Nature Structural & Molecular Biology, 10(6), 489.
10. Sancar, A. (2003). Chemical reviews, 103(6), 2203-2238.
11. Maeda, K., Henbest, K. B., Cintolesi, F., Kuprov, I., Rodgers, C. T., Liddell, P. A., ... & Hore, P. J. (2008). Nature, 453(7193), 387-390.

# CHAPTER II

# SURFACE PLASMON GENERATION

This chapter has been published as: Zeng, Z., Mendis, M. N., Waldeck, D. H., & Wei, J. (2016). A semi-analytical analysis of surface plasmon generation and the optimal nanoledge plasmonic device. RSC advances, 6(21), 17196-17203.

## An Overview

Surface plasmon Resonance (SPR) of nanostructured thin metal films (so-called nanoplasmonics) has attracted intense attention due to its versatility for optical sensing and chip-based device integration. Understanding the underlying physics and developing applications of nanoplasmonic devices with desirable optical properties, e.g. intensity of light scattering and high refractive index (RI) sensitivity at the perforated metal film, is crucial for practical uses in physics, biomedical detection, and environmental monitoring. This work presents a semi-analytical model that enables decomposition and quantitative analysis of surface plasmon generation at a new complex nanoledge aperture structure under plane-wave illumination, thus providing insight on how to optimize plasmonic devices for optimal plasmonic generation efficiencies and RI sensitivity. A factor analysis of parameters (geometric, dielectric-RI, and incident wavelength) relevant to surface plasmon generation is quantitatively investigated to predict the surface plasmon polariton (SPP) generation efficiency. In concert with the analytical treatment, a finite-difference time-domain (FDTD) simulation is used to model the optical transmission spectra and RI

sensitivity as a function of the nanoledge device's geometric parameters, and it shows good agreement with the analytical model. Further validation of the analytical approach is provided by fabricating subwavelength nanoledge devices and testing their optical transmission and RI sensitivity.

**Introduction**

Surface plasmon Resonance (SPR), an optical phenomenon that are very sensitive to the near surface dielectric constant (refractive index, RI)[1], are well-suited to the detection of surface binding events of chemical and biological agents,[2,3] with single molecule sensitivity[4-6] and compatibility with point-of-care (POC) platforms.[7-9] Similarly, metal films that are perforated by subwavelength holes (or slits) display extraordinary optical transmission (EOT) in the nanostructure apertures,[10-15] which arises from strong surface plasmon excitation and displays high refractive index unit (RIU) sensitivity. Consequently, understanding the underlying physics and developing applications of nanoplasmonics with desirable optical properties,[16] e.g. intensity of light scattering and high RIU sensitivity at the perforated metal film,[17] are of particular interest for realizing their promise and integrating them into on-chip photonic sensing platforms.[18]

Real metals with a finite conductivity are capable of sustaining surface plasmon polariton (SPP) modes, which are bounded at the interface, and mediate the interaction between the nano-apertures at visible or near-infrared frequencies.[19-21] The SPP generation at the input and output aperture sides of an isolated

subwavelength slit, when illuminated by an incident plane-wave or a slit-mode, has been described in a quantitative manner.[22-24] The essential results can be generalized and applied to more complicated nano-aperture array structures, allowing for a quantitative analysis of SPP generation and its dependence on different device parameters. This analytical approach can be tested by numerical techniques: finite-element methods (FEM), finite-difference time-domain (FDTD), discrete dipole approximation (DDA), multiple multipole (MMP), and more recent a combination of surface integral equation (SIE) method of moments (MoM) formulation have all been applied for modeling the electromagnetic dynamics of nanoplasmonic systems.[25-27] Among them, the well-established FDTD technique solves Maxwell's equations and provides both qualitative insight and a quantitative link between the optical properties and the underlying SPP properties of the nanoaperture arrays.[28]

The present work considers a semi-analytical analysis and numerical simulations to investigate a complex nanoaperture–nanoledge device (Figure 2.1), which displays SPP phenomena and the extraordinary optical transmission of light, with the aim of elucidating the criteria for optimal optical performance and improving its refractive index sensitivity for sensing applications. First, we present an approximate model to examine the generation of surface plasmons on the nanoledge aperture and then combine it with plane wave and slit-mode illumination to quantify the interaction. Through a corresponding factor analysis we identify how the geometric features of the nanoledge structure affect the plasmon generation. This semi-analytical model is applied to predict the SPP generation in nanoledge

structures and investigate the origin of their high plasmonic generation efficiencies. In concert, the FDTD method is used to predict the optical transmission spectra and RI sensitivity as a function of the nanoledge structure's geometric parameters. Lastly, subwavelength nanoledge devices are fabricated and their optical response is measured in order to validate the results obtained from the semi-analytical analysis and FDTD modelling.

**Results and Discussion**

Analytical considerations: in order to study nanoledge geometries that are of interest in practice and consider the geometric diffraction with the bounded SPP modes launching on the flat interfaces surrounding the slits, a mechanistic description for SPP generation is needed, especially the SPP scattering coefficients and efficiencies at the slit apertures. Figure 2.1 illustrates schematic of a nanoledge structure in subwavelength thick gold film at quartz substrate (Figure 2.1a) and a straight nanoslit structure (Figure 2.1b) as a comparison. In this study, we focus on the SPP generation at the Au/medium interfaces upon light excitation without considering the height conditions (i.e. subwavelength thickness of the metallic film). Note that the thickness (height) predominately affects the SPP fundamental modes in the slit traveling upward and downward, not the SPP generation confined at the flat interfaces;[29] hence it is not considered in detail here.

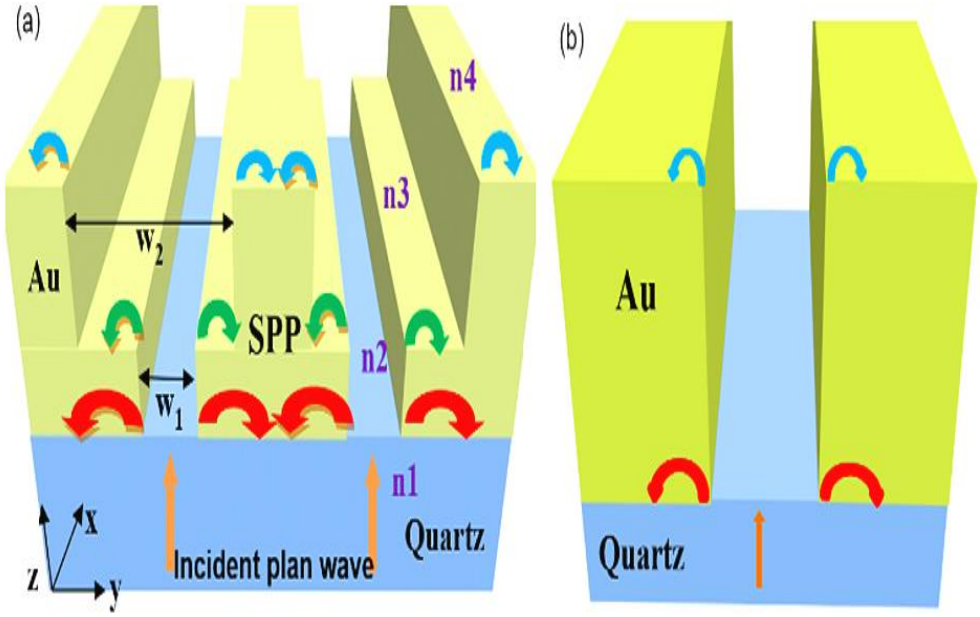


Figure 2.1. Schematic Illustration. (a) The schematic illustrates the parameters for the nanoledge structure and SPP generation by a plane wave at normal incidence. The $w_1$ and $w_2$ represent the slit widths at the Au-quartz and Au-air interfaces, and the $\alpha_1^+,\alpha_1^-,\alpha_2^+,\alpha_2^-,\alpha_3^+,\alpha_3^-$ represent the SPP generation coefficients at the three interfaces with inverse propagation directions. The refractive indexes inside the slits are represented by $n_2$ and $n_3$, and those at the outer slits are presented by $n_1$ and $n_4$, when exposed in air, $n_2=n_3=n_4=1$ (air), and $n_1=1.45$ (quartz). (b) The schematic of a straight single nanoslit structure is shown as a comparison.

With the semi-analytical model (see Method section), the SPP excitation efficiency *e* for one side of the aperture is readily calculated with analytical techniques.[30] Figure 2.2 shows the decomposed SPP excitation efficiency *e* on one side of the aperture for the interfaces of the nanoledge as a function of the scaled slit width w' and the incident light wavelength, from the visible to near-infrared (600-

1200 nm). The SPP excitation is efficient at visible frequencies while *e* rapidly decreases with the increase of wavelength. For the interfaces surrounding the ledge structure, all of the optimal scaled slit widths are similar with a value of w'=0.2.

If one selects $n_1$=1.45 for quartz and $n_2$=$n_3$=$n_4$=1 for air in the model,[31] then the optimal nanoledge widths (Figure 2.1a) are $w_1$=0.14λ for the bottom Au-quartz slit and $w_2$=0.2λ for the top Au-air slit. Moreover, at a visible wavelength of 600 nm, the SPP excitation efficiencies are fairly large. The maximum *e* is calculated as 0.496 for the Au-quartz interface and 0.224 for the Au-air interface of the nanoledge structure in Figure 2.1. It is expected that the total SPP excitation efficiency *e* will result from a "superposition" of the SPP arising from all the interfaces of the nanoledge structures.

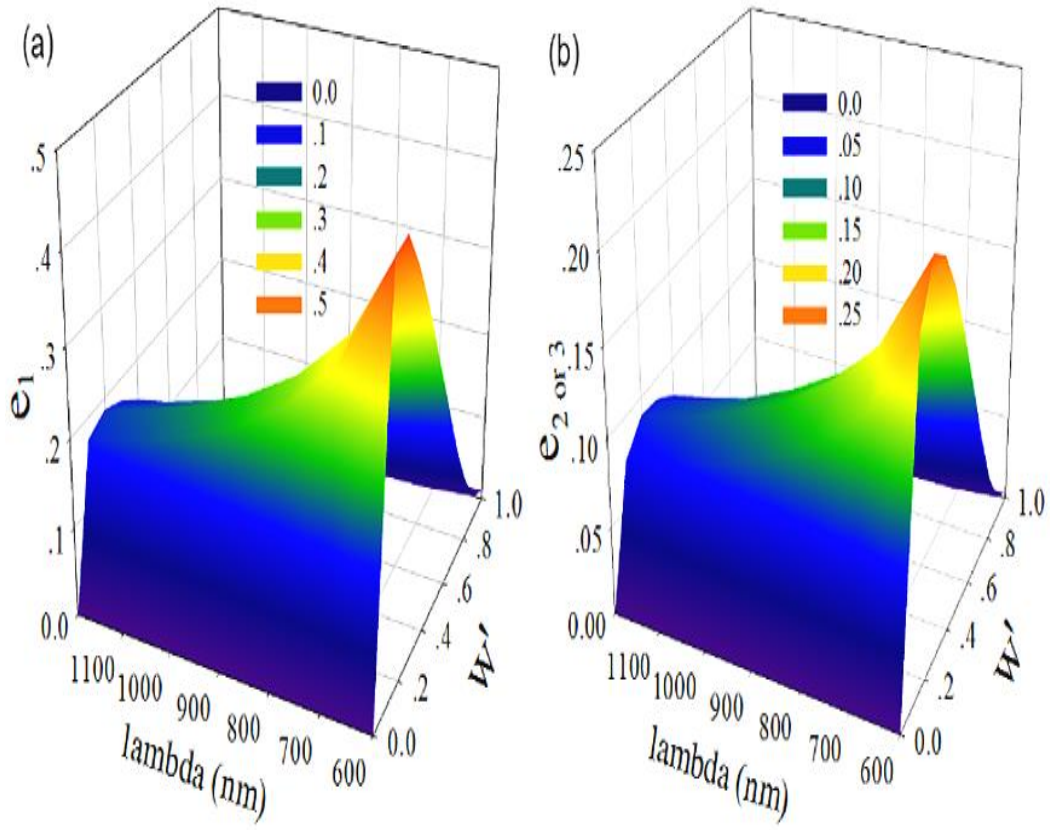


Figure 2.2. The SPP Generation Efficiencies. *e* at the Au-quartz and Au-air interfaces are plotted as a function of λ and w' obtained by the semi-analytical model. a). Au-quartz interface $e_1=|\alpha_1^+(w_1/2)|^2 = |\alpha_1^-(w_1/2)|^2$; b). Au-air interface, $e_2= |\alpha_2^+(w_1/2)|^2 = |\alpha_2^-(w_1/2)|^2$, the $e_3$ has the same performance as $e_2$. (see more in Fig. S2.1).

A factor analysis[32] of the semi-analytical equations was performed in order to assess the correlations of w, λ, $n_1$, $n_2/n_3/n_4$ ($n_2=n_3=n_4$ in this analysis), and u on the calculation variables of w', $I_0$, $I_1$, *e*, v, and ε in the SPP analysis (see details in SI, Fig. S2.2 and supporting data). Figure 2.3 shows some radar plots of the influence factor coefficient for different cases. For the Au/quartz interface (Figure 2.3a), the factor coefficient of the slit width w on the SPP generation efficiency, *e*, is 0.12, which is almost the same with that in

the Au-air interfaces as shown in Figure 2.3b. Moreover, the factor coefficient of the wavelength λ on *e* becomes larger from the Au-quartz interface to the Au-medium interfaces, in agreement with Eqns 2-6, 2-11, and 2-15 (see Method). Meanwhile, the factor coefficient of the refractive indices, $n_2/n_3/n_4$ on *e* becomes larger while that of substrate $n_1$ on *e* becomes smaller; evident from Eqns 2-4, 2-9 and 2-13. Beside this, the factor coefficient of wavelength λ on dielectric constant ε or numerical factor u on v is 1 because of their one-one correspondence. Using Figure 2.3a and 2.3b, we derived the total factor coefficient of each independent variable (w, λ, $n_1$, $n_2/n_3/n_4$, or u) on individual dependent variables (w', $I_0$, $I_1$, *e*, v, or ε) and this is shown in Figure 2.3c. In Figure 2.3c one can see that the numerical factor u plays the most important part in calculating *e*, as a factor coefficient of 0.29 according to the yellow area shown. Note that the area is formed by the connection between the six spots (like the six factor coefficients of u on w', $I_0$, $I_1$, *e*, v and ε). In order to more clearly understand the role of the slit width, w, in the analytical part (without u), the influence factor coefficient of w on *e* was obtained and found to be 0.17; see Figure 2.3d. From this analysis and the physical considerations described above, the nanoledge widths, $w_1$ and $w_2$, play an important role in SPP generation.

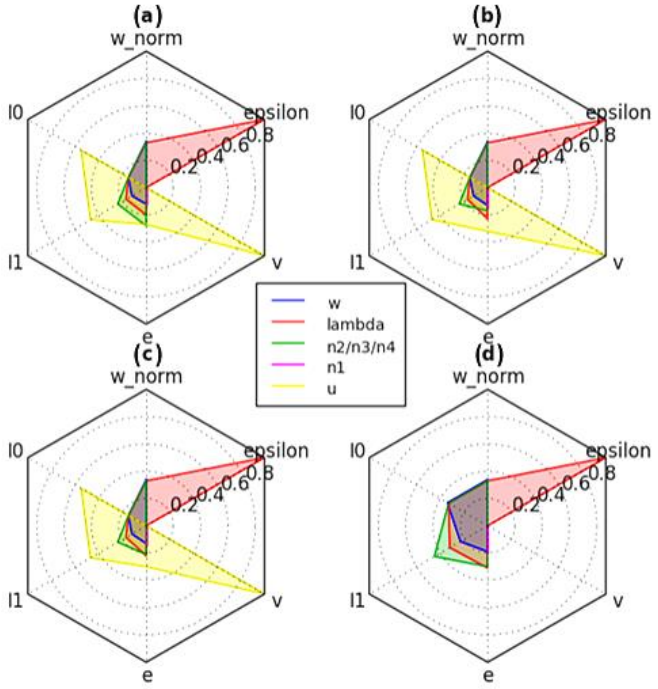


Figure 2.3. Radar Charts of The Factor Coefficients of Factors. (w, λ, $n_2/n_3/n_4$, $n_1$, u) on the calculation variables (w', $I_0$, $I_1$, *e*, v, ε) in the semi-analytical model are shown for four scenarios. (a) the algebraic operation for $e_1$ of SPP (red in Figure 2.1) at the Au/quartz interface; (b) the algebraic operation for $e_{2or3}$ of SPP (green and blue in Figure 2-1a) at the Au/Air interfaces; (c) the factor analysis combining a) with b); and (d) the analytical part (without u and v) of scenario c.

Numerical simulation: In order to study the optical transmission properties of the nanoledge structure with different $w_1$ and $w_2$, FDTD calculations were used to simulate the interaction between the metal and the incident light wave.

Figure 2.4 summarizes some results of these simulations. Panel a) in Figure 2.4 shows the calculated typical transmission spectra for one selected nanoledge of $w_2$-$w_1$ with 280-50 nm (geometries with $w_2$-$w_1$ of 280-40 nm, 300-40 nm, and 300-

50 nm also performed, see Fig. S2.8). The four nanoledges were predicted to have high optical transmission (see Figure 2.4b and Table S2.5) because of the transmission resonance corresponding to the Au/quartz mode. The four nanoledge devices have a predicted maximum transmittance of about 27%. The insert in Figure 2.4a shows the corresponding TE distribution (more details for the $w_2$-$w_1$ of 280-50 nm nanoledge device are shown in Fig. S2.3a). The SPP generation occurs at three different interfaces which are marked by the white arrows. This was further confirmed by the corresponding TM distributions, given in Fig. S2.3b. Along with the resulting TM profiles at the reflected surface and at the transmitted surface (see Fig. S2.4), it suggests that the transmission resonances may arise from localized surface plasmons along the x-direction and SPP propagating along the y-direction.[33]

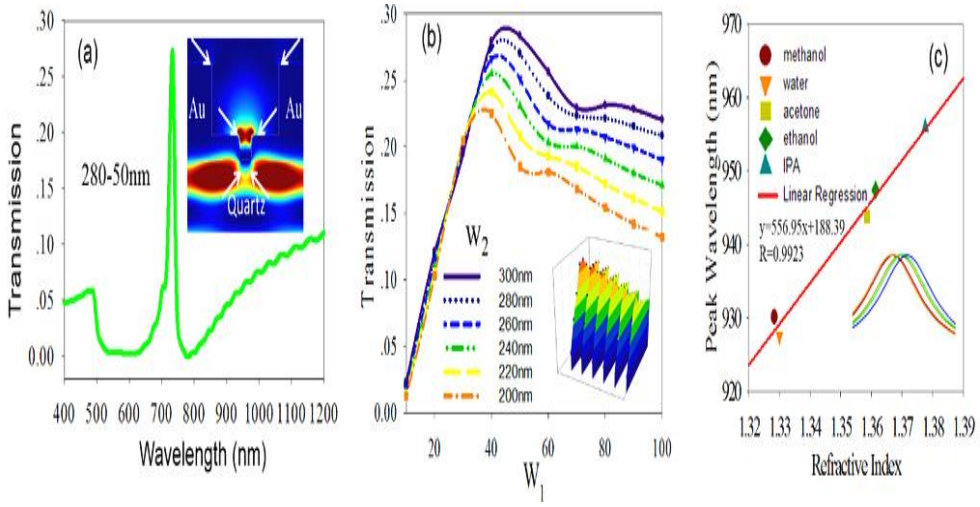


Figure 2.4. FDTD Simulation. Panel (a) shows the calculated typical transmission spectra of the $w_2$-$w_1$ of 280-50 nm nanoledge system with the inserted corresponding TE field dynamics at 3 seconds calculated for the systems. Panel (b) shows the maximum transmission regarding different $w_1$ and $w_2$ in the nanoledge systems with a 3D inset view. Panel (c) shows the peak wavelength of 280-50 nanoslit system vs refractive indices of bulk solutions, $n_{methanol}\approx1.32$, $n_{water}\approx1.33$, $n_{acetone}\approx1.35$, $n_{ethanol}\approx1.36$, and $n_{IPA}\approx1.37$ with a peak wavelength shift inset view.

The electromagnetic field distributions reveal that the plasmonic excitations arise from the Au/quartz interface and the gold/medium interfaces with the strength of Au/quartz>Au/air, which is consistent with the results of the semi-analytical model for SPP efficiencies of $e_1>e_2>e_3$ for the four nanoledge devices. According to the analytical considerations, the optimal slit widths are $w_1=0.14\lambda$ and $w_2=0.2\lambda$ for maximum SPP generation. From the FDTD simulations results for $w_1$ of 40/50 nm and $w_2$ of 280/300 nm over a broad spectrum ranging from the visible to near-

infrared, the $w_2$-$w_1$ of 280 nm-50 nm nanoledge system is optimal; i.e., close to optimal slit widths and with the highest optical transmission (Figure 2.4b). If we assume an incident light with wavelength of 600 nm, we obtain the scaled widths $w_1$'=0.121, $w_2$'=0.083 and $w_3$'=0.467, corresponding to the three Au/medium interfaces from bottom to top, and the SPP generation efficiencies of $e_1$=0.48, $e_2$=0.18, and $e_3$=0.16, which is consistent with the order of the TE field intensities of the three Au-medium interfaces; see the white arrows shown in Figure 2.4a insert. These results indicate that the semi-analytical approach provides insight into the SPP generation efficiencies by enabling a decomposition analysis of the SP in such a complex perforated metal film nanostructure.

Figure 2.4c shows an analysis in which the FDTD simulations are used to calculate the refractive index sensitivity of the optimal $w_2$-$w_1$ of 280-50 nm nanoledge device. In these simulations the peak wavelength shift was monitored for different refractive indices of the external medium and chosen to mimic the index of refraction of common solvents; namely, methanol, deionized water, acetone, ethanol, and isopropyl alcohol (IPA).[34] The calculated wavelength red shifted as the RI of the solvent increased, and the sensitivity was found to be 556 nm/RIU.

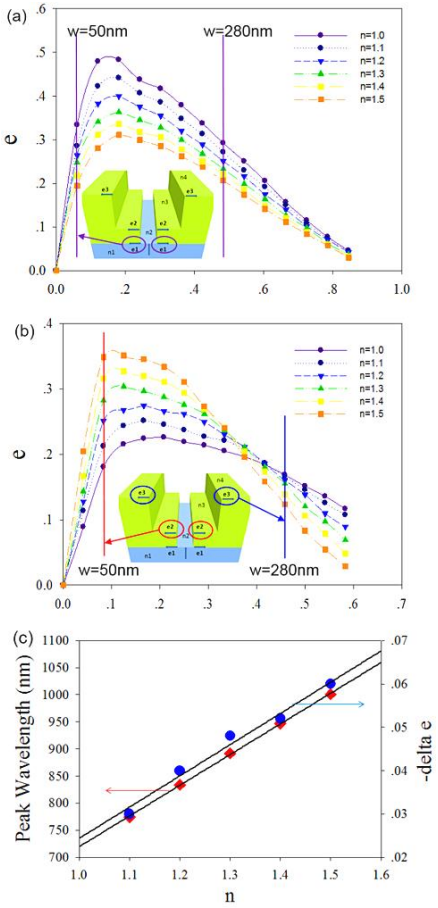


Figure 2.5. Decomposition of The SPP Generation Efficiency. *e* is shown as a function of the nanoledge geometries at different refractive index of $n_2=n_3=n_4$ (=n). Panel (a) shows the SPP generation efficiency *e* at the Au/quartz interfaces; the two vertical lines indicate the efficiency *e* at 50 nm and 280 nm slit width. Panel (b) shows the SPP generation efficiency *e* at the Au/RI-media interfaces, the red and blue lines illustrating the efficiency *e* of the slit width at 50 nm and 280 nm. Panel (c) compares the EOT peak shift and the total SPP generation efficiency changes as a function of bulk media RIs. (see table S2.6 and Fig. S2.5 for individual *e* values).

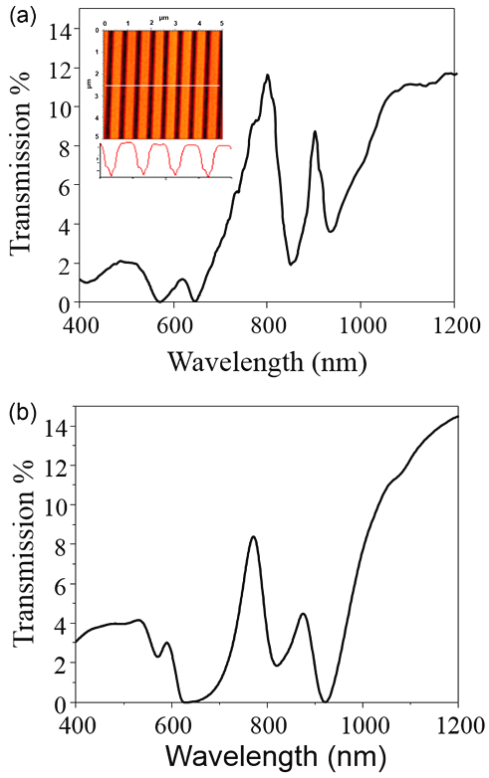


Figure 2.6. Experimentally Obtained Transmission Spectrum. A 600 nm periodicity nanoledge structure in air is illustrated in panel (a). The insert in (a) is the AFM image of the nanoledge structure with a cross along the white line is depicted; the scale bar is 1 micron. In panel (b) a FDTD calculated transmission spectrum is shown, in which the slit dimensions/geometry obtained from AFM.

A comparison of semi-analytical approach and numerical simulation: as a comparison between the FDTD and the semi-analytical decomposition analysis of SPP generation, Figure 2.5 presents the main results of the predicted SPP-generation efficiencies *e* as a function of the nanoledge widths ($w_1$, $w_2$) and RIs ($n_2$=$n_3$=$n_4$=n) at the incident wavelength λ=600 nm. For the bottom Au/Quartz interface, the SPP generation efficiencies *e* (obtained from Eq. 4 with $\mathbf{w_1' = n_1 w_1/\lambda}$) decrease as the surrounding

medium's RI increases (up to 1.5) for the slit width $w_1$ smaller than λ (Figure 2.5a). In contrast, the SPP-generation efficiency *e* ($e_2/e_3$) of the Au/medium interfaces increase as the medium's RI increases for slit width below 0.33λ (~200 nm at 600 nm incident light), and thereafter transitions to the same dependence as for the Au/Quartz interfaces (Figure 2.5b). With a specific nanoledge geometry of $w_1$=50 nm and $w_2$=280 nm, it is interesting to note that the total SPP generation efficiency change, $-\Delta(e_1+e_2+e_3)$, has the same dependence on the bulk media RI as the EOT peak shift (Figure 2.5c). Given that a weakened SPP generation efficiency correlates with a red shift of the optical transmission peak from a coupling of RI and geometry parameters (w'), the SP decomposition analysis suggests that, for the specific nanoledge $w_2$-$w_1$ of 280-50 nm, the SPP generation efficiency ($e_2$) of Au/medium interface in the center of the nanoledge would result in a blue shift as the RI increases, while a decrease of SPP generation efficiencies ($e_1$, $e_3$) at the bottom and top Au/medium interfaces would result in a red shift for the optical transmission. Indeed, the blue shift of optical transmission in a nanoslit cavity has been reported in a previous study.[35]

Experimental studies: to further validate our analysis, electron beam lithography (EBL) and focused ion beam (FIB) milling were used to fabricate Au nanoledge structures in arrays (30×30 $\mu m^2$), and the optical transmission spectra were measured as function of the change of refractive index in the nanoledge area. Figures 2.6a inserted and 2.7a present AFM and SEM images of geometrically different nanoledge structures that were fabricated.

The experimental transmission spectrum for a FIB fabricated nanoledge array collected in air with a periodicity of 600 nm in air is shown in Figure 2.6a. It

can be noted that FDTD calculations predict a sharper main transmission feature (Figure 2.4a) in the transmission spectrum as compared to what is experimentally achieved. Broadening of the peaks in the experimental transmission spectrum may arise from fabrication imperfections. It should also be noted that the spectrophotometer, which has a wavelength resolution of 0.782 nm, will not be able to capture these sharp features into the experimental transmission spectrum. To account for fabrication defects, FDTD simulations were performed with realistic slit dimensions taken from AFM imaging of the focused ion beam fabricated nanoledge (Figure 2.6a insert). The calculated transmission spectra of the 600 nm periodicity nanoledge structure is illustrated in Figure 2.6b. With these dimensions, the main transmission peak appears less sharp and have much reduced intensity compared the idealized structure. This observation could account for differences in coupling of the cavity modes with SPP modes in the two geometries.

Figure 2.7b-c shows the representative transmission spectra of the FIB fabricated nanoledge device (gold thin film on quartz) and the primary transmission peak (D) as a function of the medium RI in the nanoledge. As for the geometry $w_2$-$w_1$ of 245 nm-54 nm, the RI sensitivity ($S_{bulk}$) is 522 nm/RIU, while for the geometry 256 nm/90 nm, the RI sensitivity is 311 nm/RIU (see SI Fig. S2.9), which demonstrates a good quantitative agreement with the FDTD simulation. The RI sensitivity is somewhat less than the optimal SPP generation efficiency geometry with $w_2$-$w_1$ of 280 nm-50 nm obtained from the perfectly-conducting metal approximation.

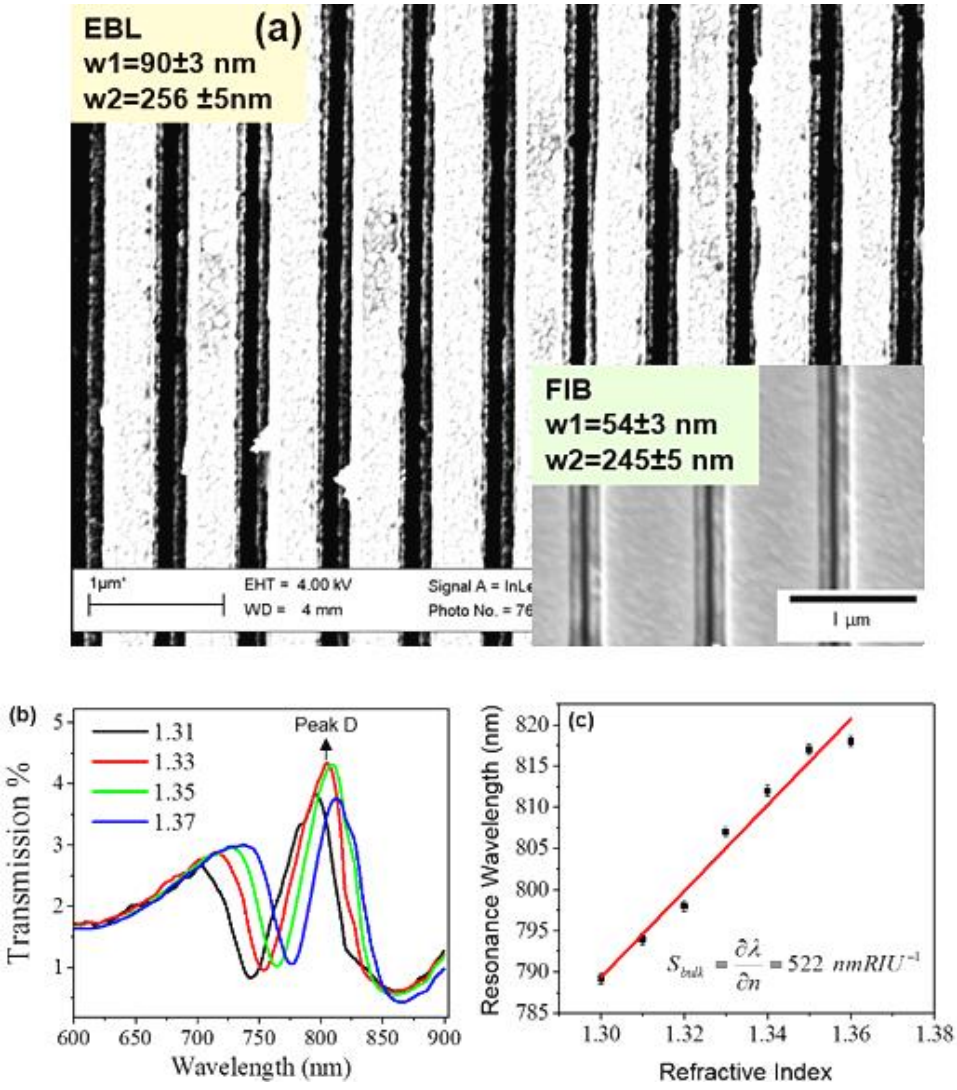


Figure 2.7. Nanoledge Structure. (a) SEM images of two nanoledge fabricated by EBL and FIB, respectively; (b) The transmission spectra of the FIB fabricated nanoledge arrays ($w_2$-$w_1$=245 nm-54 nm) with changes of bulk refractive index; and (c) the primary peak position (peak D) as a function of refractive index obtained from (b).

**Methods**

Semi-analytical approach: based on the mode orthogonality condition,[23,36] the SPP generation efficiency is governed by the following equations:

$$\int_{-\infty}^{\infty} dz H_y\left(\frac{w}{2}, z\right) E_{SP}(z) = 2\left(\alpha^{+}\left(\frac{w}{2}\right) + \alpha^{-}\left(\frac{w}{2}\right)\right) \quad (2\text{-}1)$$

and

$$\int_{-\infty}^{\infty} dz E_z\left(\frac{w}{2}, z\right) H_{SP}(z) = 2\left(\alpha^{+}\left(\frac{w}{2}\right) - \alpha^{-}\left(\frac{w}{2}\right)\right) \quad (2\text{-}2)$$

where H and E represent the magnetic and electric field amplitudes, respectively, w is the width of the slit, and $\alpha^{+}(w/2)$ and $\alpha^{-}(w/2)$ represent SPP excitation coefficients at the exit sides of the slit,[23] The strength of the SPP generation is provided by $|\alpha|^2$. Using this approach one can derive the following equation for the surface plasmon generation by a single straight slit mode:[36,37]

$$|\alpha|^2 = f\left(\frac{w}{\lambda}\right)\frac{n_1}{n_2}|\varepsilon|^{-1/2} \quad (2\text{-}3)$$

with the assumption that the metal is a perfect conductor. This assumption simplifies the dependence of the geometric diffraction on the dielectric properties of the metal, and the dependence of the bounded SPP mode on the dielectric properties of the metal-dielectric interface.[38] In Eqn 2-3, λ is the wavelength of the incident light, ε is

the dielectric constant, and $n_1$ and $n_2$ represent two refractive indexes of the two media on either side of the interface (see Figure 2.1a).

Combining the SPP fundamental mode with transmission mode in the plane wave basis, we can obtain the SPP generation efficiencies on both sides of the aperture, under the assumption of $\alpha^{+}(-w/2) = \alpha^{-}(w/2) = 0$, regarding the electromagnetic field below and inside the slit. By generalizing the procedure used by Lalanne for a single straight slit (Figure 2.1b),[37,39,40] one can obtain the SPP generation efficiencies *e* at both sides of the apertures on the three Au interfaces; see Figure 2.1a. For the Au/quartz interface *e* (red) is given by:

$$e_1 = \left|\alpha_1^{+}\left(w_1/2\right)\right|^2 = \left|\alpha_1^{-}\left(w_1/2\right)\right|^2 = \frac{4w_1' n_1^3}{\pi n_2^2}\left|\frac{\varepsilon^{1/2}}{\varepsilon + n_1^2}\right|\left|\frac{I_1}{1+\left(n_1/n_2\right)w_1' I_0}\right|^2 \tag{2-4}$$

in which

$$I_0 = \int_{-\infty}^{\infty} du\left[\sin\left(\pi w_1' u\right)/\left(\pi w_1' u\right)\right]^2 / v \tag{2-5}$$

$$I_1 = \int_{-\infty}^{\infty} du \frac{\exp\left(-i\pi w_1' u\right)\sin\left(\pi w_1' u\right)/\left(\pi w_1' u\right)}{v\left\{v + \left[n_1^2/\left(\varepsilon + n_1^2\right)\right]^{1/2}\right\}} \tag{2-6}$$

$$w_1' = n_1 w_1/\lambda \tag{2-7}$$

where w' represents the scaled width and u and v are applied for numerical integration with $u^2+v^2=1$.

For the slit mode case, the corresponding SPP efficiencies can be obtained by the following equation:[37]

$$\left|\alpha\left(w/2\right)\right|^2_{slit-\mathrm{mod}e} = \frac{N_p}{N_0}\left|\alpha\left(w/2\right)\right|^2_{plane-wave} \tag{2-8}$$

with the assumption that the forward and backward fundamental modes compose the field in the slit and the normalization constants $N_0$ and $N_p$ are given by $N_0=w/(2\varepsilon n_2)$ and $N_p= w/(2\varepsilon n_1)$. For the inside Au/medium interface of the ledge (green), *e* is expressed as:

$$e_2 = \left|\alpha_2^+\left(w_1/2\right)\right|^2 = \left|\alpha_2^-\left(w_1/2\right)\right|^2 = \frac{4w_2^{'}n_3^2}{\pi n_2}\left|\frac{\varepsilon^{1/2}}{\varepsilon+n_3^2}\right|\left|\frac{I_1^{'}}{1+\left(n_3/n_2\right)w_2^{'}I_0^{'}}\right|^2 \tag{2-9}$$

with

$$I_0^{'} = \int_{-\infty}^{\infty} du\left[\sin\left(\pi w_2^{'}u\right)/\left(\pi w_2^{'}u\right)\right]^2/v \tag{2-10}$$

$$I_1^{'} = \int_{-\infty}^{\infty} du\,\frac{\exp\left(-i\pi w_2^{'}u\right)\sin\left(\pi w_2^{'}u\right)/\left(\pi w_2^{'}u\right)}{v\left\{v+\left[n_3^2/\left(\varepsilon+n_3^2\right)\right]^{1/2}\right\}} \tag{2-11}$$

$$w_2^{'} = n_2 w_1/\lambda \tag{2-12}$$

Similarly, for the Au/medium interface at the top of the nanoledge aperture (blue), *e* is given by

$$e_3 = \left|\alpha_3^+\left(w_2/2\right)\right|^2 = \left|\alpha_3^-\left(w_2/2\right)\right|^2 = \frac{4w_3^{'}n_4^2}{\pi n_3}\left|\frac{\varepsilon^{1/2}}{\varepsilon+n_4^2}\right|\left|\frac{I_1^{"}}{1+\left(n_4/n_3\right)w_3^{'}I_0^{"}}\right|^2 \tag{2-13}$$

with

$$I_0^{"} = \int_{-\infty}^{\infty} du\left[\sin\left(\pi w_3^{'}u\right)/\left(\pi w_3^{'}u\right)\right]^2/v \tag{2-14}$$

$$I_1^{"} = \int_{-\infty}^{\infty} du\,\frac{\exp\left(-i\pi w_3^{'}u\right)\sin\left(\pi w_3^{'}u\right)/\left(\pi w_3^{'}u\right)}{v\left\{v+\left[n_4^2/\left(\varepsilon+n_4^2\right)\right]^{1/2}\right\}} \tag{2-15}$$

$$w_3^{'} = n_3 w_2/\lambda \tag{2-16}$$

Details of the derivation of these results are provided in the SI. Because the full integrand, weighted by v, is singular over the interval of -1 and +1 and complex for |u|> 1, the integrals $I_0$ ($I_0'$, $I_0''$), and $I_1$ ($I_1'$, $I_1''$), were calculated numerically.[37,41] Tables S2.1-S2.4 provide numerical results for different values of the normalized slit width w' and wavelength λ with the corresponding dielectric constant values of quartz.

Numerical simulation: the metal's dielectric response was modeled by a Drude-Lorentz model,[42]

$$\varepsilon_r = \varepsilon_\infty + \sum_{n=1}^{N}\frac{x_0 G_n \omega_{0n}^2}{\omega_{0n}^2 + i\Gamma_n\omega - \omega^2} with \sum_{n=1}^{N} G_n = 1 \tag{2-17}$$

where $\varepsilon$ is the permittivity, $\omega_{0n}$ is the resonant frequency, $\Gamma_n$ is the damping coefficient, and $x_0$ is the permittivity at $\omega_0$. By using a single resonance and the Fourier transform of the polarization in the algorithm, the FDTD formalism was used to calculate the transverse electric (TE) and transverse magnetic (TM) fields.[28]

The geometry of the nanoledge structure was modeled in three-dimensional (3D) environments. The dielectric function of Au used in the simulations was from Johnson and Christy[43] and the substrate was simulated as an infinite block with a dielectric constant of silicon dioxide taken from Palik.[31] The simulations were performed using a single aperture as the unit cell with periodic boundary conditions in the y-direction to describe an infinite rectangular array and perfectly matched layers in the boundary along the x and z-direction. The period of the nanoslit array is 600 nm and the heights of the two slits are 50 nm and 150 nm, respectively. Note that the period and height are chosen to correspond to our previous work with nanoplasmonic nanofluidics.[44] As with the experiments, the calculations consider a linearly polarized broadband plane wave source, which propagates through the quartz substrate and is incident on the back surface of the gold layer at normal incidence.

Device fabrication and testing: subwavelength nanoledge structures were fabricated using electron beam lithography (EBL) and focused ion beam (FIB) techniques. Sample imaging was done using an SEM in the nanofabrication systems. Spectral characterization of the nanoledge arrays was carried out using a microspectrophotometer (Craic QDI

2010).[45] The details of the experimental procedures and supporting data are included in the SI.

## Conclusion

In conclusion, we extended a semi-analytical model to perform a decomposition analysis of the SPP wave generation at metallic interfaces perforated by a subwavelength nanoledge structure. The factor analysis of parameters (geometric, dielectric-RI, and incident wavelength) relevant to surface plasmon (SP) generation has been quantitatively investigated for the prediction of surface plasmon polariton (SPP) generation efficiency. The rigorous formalism for the model has been validated by comparisons with the FDTD modelling of the EOT and its sensitivity of RI changes and by experimental testing of fabricated nanoledge devices through measurement of their optical transmission and RI sensitivity. The analysis shows that SPP-generation is very efficient for a gold film. The reported semi-analytical approach provides a new tool for a quantitative decomposition analysis of SPP generation in other related slit structures and should prove useful for plasmonic device development.

## References


1. Lal, S., Link, S., & Halas, N. J. (2007). Nature photonics, 1(11), 641-648.
2. Li, J., Chen, C., Lagae, L., & Van Dorpe, P. (2015). The Journal of Physical Chemistry C, 119(52), 29116-29122.
3. Quidant, R., & Kreuzer, M. (2010). Nature nanotechnology, 5(11), 762-763.
4. Stockman, M. I. (2011). Optics express, 19(22), 22029-22106.
5. Beuwer, M. A., Prins, M. W., & Zijlstra, P. (2015). Nano letters, 15(5), 3507-3511.
6. Al Balushi, A. A., & Gordon, R. (2014). ACS Photonics, 1(5), 389-393.
7. Brolo, A. G. (2012). Nature Photonics, 6(11), 709-713.
8. Stewart, M. E., Anderton, C. R., Thompson, L. B., Maria, J., Gray, S. K., Rogers, J. A., & Nuzzo, R. G. (2008). Chemical reviews, 108(2), 494-521.
9. Tokel, O., Inci, F., & Demirci, U. (2014). Chemical reviews, 114(11), 5728-5752.
10. Couture, M., Live, L. S., Dhawan, A., & Masson, J. F. (2012). Analyst, 137(18), 4162-4170.
11. Hendry, E., Mikhaylovskiy, R. V., Barron, L. D., Kadodwala, M., & Davis, T. J. (2012). Nano letters, 12(7), 3640-3644.
12. Lee, K. L., Chen, P. W., Wu, S. H., Huang, J. B., Yang, S. Y., & Wei, P. K. (2012). ACS Nano, 6(4), 2931-2939.

13. Ebbesen, T. W., Lezec, H. J., Ghaemi, H. F., Thio, T., & Wolff, P. A. (1998). Nature, 391(6668), 667.
14. Yanik, A. A., Huang, M., Kamohara, O., Artar, A., Geisbert, T. W., Connor, J. H., & Altug, H. (2010). Nano letters, 10(12), 4962-4969.
15. Mayerhöfer, T. G., Knipper, R., Hübner, U., Cialla-May, D., Weber, K., Meyer, H. G., & Popp, J. (2015). ACS Photonics, 2(11), 1567-1575.
16. Hess, O., Pendry, J. B., Maier, S. A., Oulton, R. F., Hamm, J. M., & Tsakmakidis, K. L. (2012). Nature materials, 11(7), 573.
17. Feuz, L., Jönsson, P., Jonsson, M. P., & Höök, F. (2010). Acs Nano, 4(4), 2167-2177.
18. Acimovic, S. S., Ortega, M. A., Sanz, V., Berthelot, J., Garcia-Cordero, J. L., Renger, J., ... & Quidant, R. (2014). Nano letters, 14(5), 2636-2641.
19. Chang, S. H., Gray, S. K., & Schatz, G. C. (2005). Optics Express, 13(8), 3150-3165.
20. Lalanne, P., & Hugonin, J. P. (2006). Nature Physics, 2(8), 551.
21. Schlather, A. E., Large, N., Urban, A. S., Nordlander, P., & Halas, N. J. (2013). Nano letters, 13(7), 3281-3286.
22. Garcia-Vidal, F. J., Martin-Moreno, L., Ebbesen, T. W., & Kuipers, L. (2010). Reviews of Modern Physics, 82(1), 729.
23. Lalanne, P., Hugonin, J. P., Liu, H. T., & Wang, B. (2009). Surface Science Reports, 64(10), 453-469.
24. Liu, H., & Lalanne, P. (2008). Nature, 452(7188), 728.

25. Litz, J. P., Camden, J. P., & Masiello, D. J. (2011). The Journal of Physical Chemistry Letters, 2(14), 1695-1700.
26. Tanemura, T., Balram, K. C., Ly-Gagnon, D. S., Wahl, P., White, J. S., Brongersma, M. L., & Miller, D. A. (2011). Nano letters, 11(7), 2693-2698.
27. Solis, D. M., Taboada, J. M., Obelleiro, F., Liz-Marzan, L. M., & García de Abajo, F. J. (2014). ACS nano, 8(8), 7559-7570.
28. Zeng, Z., Liu, Y., & Wei, J. (2016). TrAC Trends in Analytical Chemistry, 75, 162-173.
29. Aigouy, L., Lalanne, P., Hugonin, J. P., Julié, G., Mathet, V., & Mortier, M. (2007). Physical review letters, 98(15), 153902.
30. Skudrzyk, E. (2012). The foundations of acoustics: basic mathematics and basic acoustics. Springer Science & Business Media.
31. Palik, E. D. (Ed.). (1998). Handbook of optical constants of solids (Vol. 3). Academic press.
32. Kline, P. (2014). An easy guide to factor analysis. Routledge.
33. Cetin, A. E., Etezadi, D., Galarreta, B. C., Busson, M. P., Eksioglu, Y., & Altug, H. (2015). ACS Photonics, 2(8), 1167-1174.
34. Sanders, M., Lin, Y., Wei, J., Bono, T., & Lindquist, R. G. (2014). Biosensors and Bioelectronics, 61, 95-101.
35. Jung, Y. S., Wuenschell, J., Kim, H. K., Kaur, P., & Waldeck, D. H. (2009). Optics Express, 17(18), 16081-16091.

36. Lalanne, P., Hugonin, J. P., & Rodier, J. C. (2005). Physical review letters, 95(26), 263902.
37. Lalanne, P., Hugonin, J. P., & Rodier, J. C. (2006). JOSA A, 23(7), 1608-1615.
38. Yao, W., Liu, S., Liao, H., Li, Z., Sun, C., Chen, J., & Gong, Q. (2015). Nano letters, 15(5), 3115-3121.
39. Wei, P. K., Chou, H. L., Cheng, Y. R., Wei, C. H., Fann, W., & Tegenfeldt, J. O. (2005). Optics communications, 253(1), 198-204.
40. Xie, Y., Zakharian, A. R., Moloney, J. V., & Mansuripur, M. (2004). Optics express, 12(25), 6106-6121.
41. Chimento, P. (2013). Two-dimensional optics: diffraction and dispersion of surface plasmons. Quantumoptica Group, Leiden Institute of Physics (LION), Faculty of Science, Leiden University.
42. Vial, A., Grimault, A. S., Macías, D., Barchiesi, D., & de La Chapelle, M. L. (2005). Physical Review B, 71(8), 085416.
43. Johnson, P. B., & Christy, R. W. (1972). Physical review B, 6(12), 4370.
44. Wei, J., Kofke, M., Rexius, M., Singhal, S., Wang, Y., & Waldeck, D. H. (2011). Nanotechnology, 3, 79-82.
45. Mendis, M. N., Mandal, H. S., & Waldeck, D. H. (2013). The Journal of Physical Chemistry C, 117(48), 25693-25703.

# CHAPTER III

# PROTEIN SENSING IN PLASMONIC NANOSLIT

This chapter has been published as: Zeng, Z., Shi, X., Mabe, T., Gilmore, G., Smith, A. W., & Wei, J. (2017). Protein Trapping in Plasmonic Nanoslit and Nanoledge Cavities: The Behavior and Sensing. Analytical Chemistry, 89(10), 5221-5229.

## An Overview

A novel plasmonic nanoledge device was presented to explore the geometry-induced trapping of nanoscale biomolecules and meanwhile examine a generation of surface plasmon resonance (SPR) for plasmonic sensing. To design an optimal plasmonic device, a semi-analytical model was implemented for a quantitative analysis of SPR under plane-wave illumination and a finite-difference time-domain (FDTD) simulation was used to study the optical transmission and refractive index (RI) sensitivity. In addition, total internal reflection fluorescence (TIRF) imaging was used to visualize the migration of fluorescently labeled bovine serum albumin (BSA) into the nanoslits; And fluorescence correlation spectroscopy (FCS) was further used to investigate the diffusion of BSA in the nanoslits. Transmission SPR measurement of similarly sized free prostate specific antigen (f-PSA) was used to validate the trapping of the molecules via specific binding reactions in the nanoledge cavities. The present study may facilitate further development of single nanomolecule detection and new nano-microfluidic arrays for effective detection of multiple biomarkers in clinical biofluids.

## Introduction

The latest advances in manipulation, trapping, alignment, and separation of molecules embrace fields as diverse as quantum optics, soft condensed-matter physics, biophysics and clinical medicine.[1,2] Many technologies, whether active techniques (external fields) or passive ones (hydrodynamic interactions or inertial effects),[3-7] have been developed to counter and trap the Brownian motion of small molecules in solution. However, confinement of nanomolecules in the absence of external fields and visualizing the dynamics of nanomolecules in the nanometric-sized objects remain challenging. Total internal reflection fluorescence (TIRF) imaging could be a potential solution to these challenges, since the incident light creats a thin surface electromagnetic field (around 100 nm) enabling the detection of only the labeled fluorophores that are within the nanometric depth. In addition, fluorescence correlation spectroscopy (FCS), a type of time-resolved fluorescence method, could be used to analyse the temporal fluctuations due to diffusion of the labeled fluorophores in and out of a nanostructure, by utilising a confocal laser beam with ~0.2 fL of volume to detect the diffusion of particles crossing the laser focus.[8-11] The recorded fluorescence fluctuations are then correlated for analysis, directly yielding information about the mobility of the diffusing particles.[12] Recently, FCS has been applied to measure tracer diffusion in nanofluids[13] and to investigate membrane dynamics through nanoapertures.[14]

For practical purpose, stable nanomolecule trapping and detection have received intense attention because of the focus on in vitro detection of target molecules. This approach makes use of the versatility for optical sensing and also the convenience of

nanoplasmonics-chip-based device integration with different nanostructures including pores, channels and slits.[15-18] The useful phenomenon which underlies the ability of such nanoapertures to light with high efficiency is the transmission surface plasmon resonance (T-SPR), which has sparked a special interest in deep understanding of fundamentals of the T-SPR physics,[19-21] and encouraged researchers to explore new ways for the nanoscale molecules trapping and creating novel robust nanoscale sensors.[22-25] It has been recently understood that nanoplasmonic devices with strong plasmon excitation and stable convective trapping of nanomolecules can be especially suitable for applications if they incorporate real metals with a finite conductivity,[26] sufficiently high intensity of light scattering,[27] extraordinary optical transmission (EOT),[28,29] high refractive index (RI) sensitivity at the perforated metal films,[30] and a single nanometer-scale pore for single molecule thermodynamics and kinetics.[31]

Here, we present and investigate novel nanoledge aperture structures for the convective molecular trapping and implement a quantitative analysis of surface plasmon (SP) generation using an earlier developed semi-analytical model.[32] In addition, we perform numerical simulations using a finite-difference time-domain (FDTD) method to model optical transmission spectra and RI sensitivity as a function of the nanoledge device geometrical parameters.[33] Experimentally, we use the techniques of TIRF to visualize the migration of Texas Red-labeled bovine serum albumin (TxR-BSA) molecules into the nanoslits and FCS to detect its dynamics in nanoslits with different widths. Later, the molecular trapping and sensing in the nanoledge structure are validated using a specially fabricated sub-wavelength gold-film nanoledge device which is integrated with a

microfluidic channel allowing us to measure the SPR induced optical transmission and RI sensitivity, and detect the specific binding events of free prostate specific antigen (f-PSA) biomarkers to the gold surfaces functionalized with antibody of f-PSA in the nanoslit cavities.

**Methods and Materials**

Semi-analytical analysis of SP generation and FDTD simulations: the SP scattering coefficients and efficiencies at the slit apertures can be determined from the analysis of diffraction of bounded SP modes originated on the flat interfaces surrounding the slits in order to study nanoledge geometries that are of interest in practice and consider the geometric diffraction with the bounded SP modes launching on the flat interfaces surrounding the slits. Moreover, FDTD simulations reiterated the previous study by adding additional 10 nm $SiO_2$ film at the top of Au layer.[32] RI of the $SiO_2$ film used in calculations was equal to 1.41. More details of the semi-analytical model analysis applied to the $SiO_2$ film topped nanoledge devices and results are provided in supporting information (SI).

Fabrication of ledged flow-through nanoplasmonic device: standard photolithography was used to pattern soda lime glass slides (75x25 mm, Globe Scientific). Slides were fully covered with a 600 nm layer of aluminum by DC sputtering (PVD 75, Kurt Lesker). A dark field mask was designed in AutoCAD and printed on a transparency film using a 25400 dpi printer. The mask design, shown in Fig. S3.5, consisted of a flow channel with two dam structures, each of which was 30 μm wide. Shipley 1827 positive

photoresist was applied to hexamethyldisilazane (HMDS) treated glass slides by spin coating. The slides were then exposed with deep UV using an OAI 8800 mask aligner and developed with a Microposit MF-321 developer. The aluminum layer was wet etched using the Aluminum Etchant Type A (Transene Company) and the glass was then wet or dry etched to yield an isotropic or anisotropic dam structure, respectively. This process is fully outlined in Fig. S3.6. The patterned glass slides were covered with 2 nm Ti, 150 nm Au, and 10 nm of $SiO_2$ by electron beam evaporation (PVD75, Kurt Lesker). Focused ion beam milling (Zeiss, Auriga) was used to introduce the nanoledge structures atop the 30 μm dams. A slit, 50 nm wide, was milled completely through the $SiO_2$ and gold layers, followed by a 280 nm wide ledge that was milled through the $SiO_2$ and partially though the gold layer. The nanoledge channel was completely aligned with the direction of microchannels. The device was then enclosed using a poly(dimethylsiloxane) (PDMS) flow channel, which was also fabricated using standard lithographic techniques.[34]

Total internal reflection fluorescence (TIRF) imaging: nanoslits were fabricated by FIB on the glass coverslip. The coverslip was soaked in detergent solution and IPA/water (50:50) accordingly. The coverslip was rinsed with excess amount of Type I water and dried under nitrogen stream. Ozone plasma was used to further clean the surface of coverslip. The coverslip was assembled in AttoFluor sample chamber. TIRF imaging was recorded on a Nikon Eclipse Ti inverted microscope equipped with a 2 mW 488 nm diode laser (85-BCD-020-115, Melles Griot) and 100X TIRF objective (NA 1.47 oil, Nikon Corp., Tokyo, Japan). Fluorescence signal was collected by an EM-CCD camera (Evolve 512, Photometrics) with frame rate of 12 frames per second. The raw images were

processed by ImageJ and the Mosaic Particle Tracker plugin for ImageJ was used to perform background subtraction and deconvolution of the raw images.

Fluorescence correlation spectroscopy (FCS): FCS measurements were performed on a customized Nikon Eclipse Ti inverted microscope. Briefly, a 561 nm laser beam was picked out by 561 nm ± 20 nm dichroic mirror from a pulsed continuum white light laser (9.7 MHz, SuperK NKT Photonics). And the beam was focused on the sample through a 100X TIRF objective (oil, NA 1.49, Nikon). The laser beam was carefully placed at the nanoslit position. The emitted photons were collected through the same objective and directed a single photon avalanche diode (SPAD) detector (Micro Photon Devices). Photons collected by the detector were recorded with the time-correlated single photon counting (TCSPC) card (Picoharp 300) which was synchronized with the white light laser source. Five times of 30 s measurement were performed at the same spot of each nanoslit and were averaged in the correlation analysis. Correlation analysis was then performed on a computer with the home-written Matlab script.

Preparation of immobilized mAb detector at nanoplasmonic gold surfaces: the approach combining self-assembled monolayer (SAM) and crosslink reaction has been used for monoclone antibody (mAb) immobilization.[35] The gold coated chips were first cleaned with $O_2$ plasma (South Bay Technologies PC2000 Plasma Cleaner) for 15 minutes. Then, overnight the chips were processed by a SAM using incubation in a mixture of 1 mM HSC10COOH (Aldrich) and HSC8OH (Aldrich) in absolute ethanol solution with 1:2 mole ratio. After that SAM was activated by incubation in a 10 mM phosphate buffer solution (PBS, pH 7.0) with 0.5 mM of EDC/NHS (Aldrich) for 2 hours. The activated

SAM was rinsed with 10 mM PBS and immediately moved to a freshly prepared 10 mM PBS containing 10 μg/mL of the detector mAb for subsequent 4 hours incubation. Then, the chip was rinsed with the PBS again and was dipped into a 0.2 M PBS for 10 minutes in order to deactivate the remaining active sites at the SAM. The immobilized mAb was ready for f-PSA binding detection.

Experimental setup for flow control: a New Era pump system (NE-300) was used to control the flow rate to inject the sample solution to the microfluidic channel where the nanoledge array located in the center of the channel. Figure 3.1 shows the device sketch and an image of actual device topped with a PDMS microfluidic channel connected with the syringe pump for flow sample injection and flow rate control.

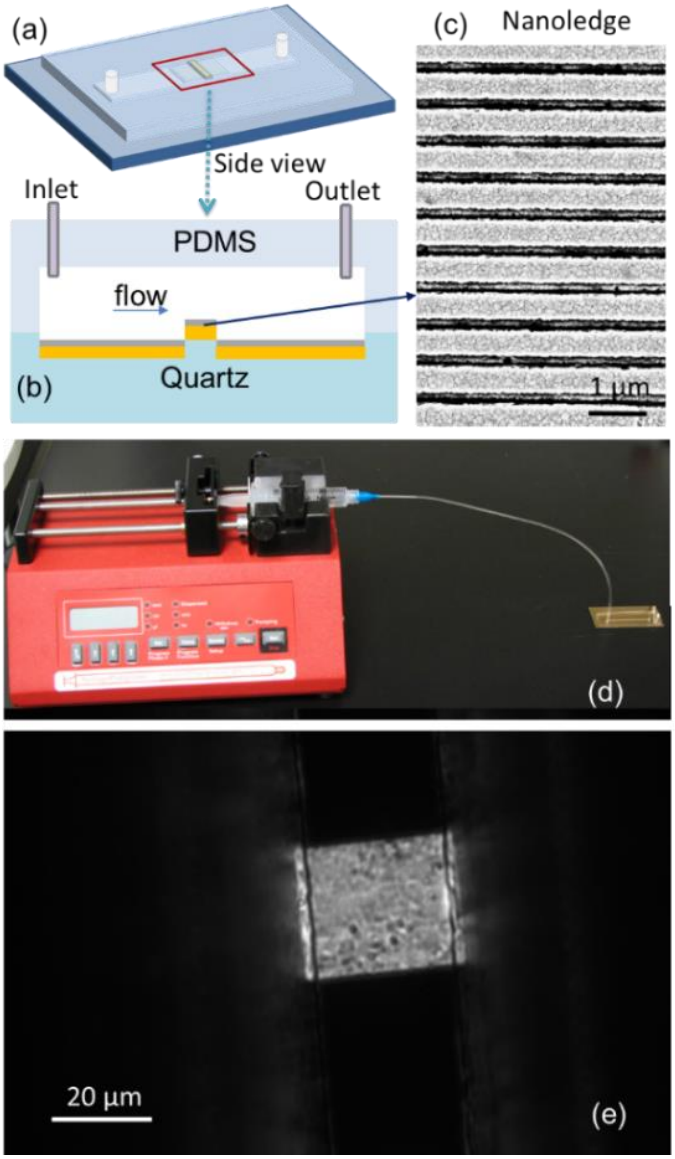


Figure 3.1. Setup. (a) Schematic illustration of the interface between the nanoledge array at the quartz chip and PDMS microfluidic channel, (b) side view of the micro-channel and, (c) a SEM image of the nanoledge array. (d) Microfluidic syringe pump connected to the PDMS microfluidic channel to control the flow rates for sample delivery. (e) Bright field image cross the "dam" with a 60x objective.

**Results and Discussion**

Two types of nanoledge structures, as shown in Figure 3.2a, b, were investigated. One nanoledge structure has open gold surfaces and the other has $SiO_2$ film (~10 nm thickness) coated at top surfaces. The nanoledge cavity array will allow for the geometry induced nanoscale particles (e.g. proteins) trapping study and plasmonic sensing using the embedded metal film via T-SPR measurement. It is expected that the $SiO_2$ film topped nanoledge structure will allow in-cavity detection with enhanced sensitivity.[36,37] Especially, the in-plane nanoledged slit array platform, different from the well-recognized EOT nanohole flow-through pattern[38,39] in which the sample flow direction is parallel to the incident light and normal to the chip plane, offers a solution-flow pattern parallel to the chip plane and perpendicular to the incident light for plasmonic transmission in sensing application. Hence, when used for real clinical protein detection in whole blood or tissue lysates, it potentially provides a simple way to integrate with the microfluidic channels for nanometric-sized protein delivery to the nanoledge cavities, while larger particles (e.g. cells, or bio-fragments) to flow-over the top space of $SiO_2$-filmed nanoledge array, thus minimizing or avoiding the interference from the non-specific biological bindings of cells or bio-fragments.

Semi-analytical analysis of SP generation and FDTD simuation: based on our recent fundamental work[32] and the SP generation results of the open nanoledge structure, the optimal geometry of the plasmonic nanoledge slit has 280-300 nm open width and ~50 nm bottom slit width. To develop the nanoledge structure for investigating the trapping of molecules by the T-SPR measurement, we performed a proof-of-principle calculation of

the SP generation at the flat interface of the nanoledge structures with and without $SiO_2$ layers at the top of Au using a semi-analytical approach.[32,40] A comparison of the semi-analytical decomposition analysis of the SP generation efficiency, which is defined as the rate of surface plasmon polaritons (SPPs) launching, propagation and scattering by matching the continuous electromagnetic fields quantities at the interface,[26,32] between the two different nanoledge structures shown in Figure 3.2a, b. Predicted SP generation efficiencies *e* were calculated as functions of the nanoledge widths (top 280 nm and bottom 50 nm) and RIs ($n_1$=1.41, $n_2$=$n_3$= bulk media RI, $n_4$= stochastic RI) caused by a plane light wave ($\lambda$=600 nm) scattering at normal incidence to the nanoledge structure (details in SI). We found that when the RI of bulk media changed from 1.0 to 1.2, the absolute value of the total SP generation efficiency, $\Delta$(e1+e2+e3), decreased from 0.08 for the nanoledge structure with $SiO_2$ to the value of 0.06 for the nanoledge structure without $SiO_2$.

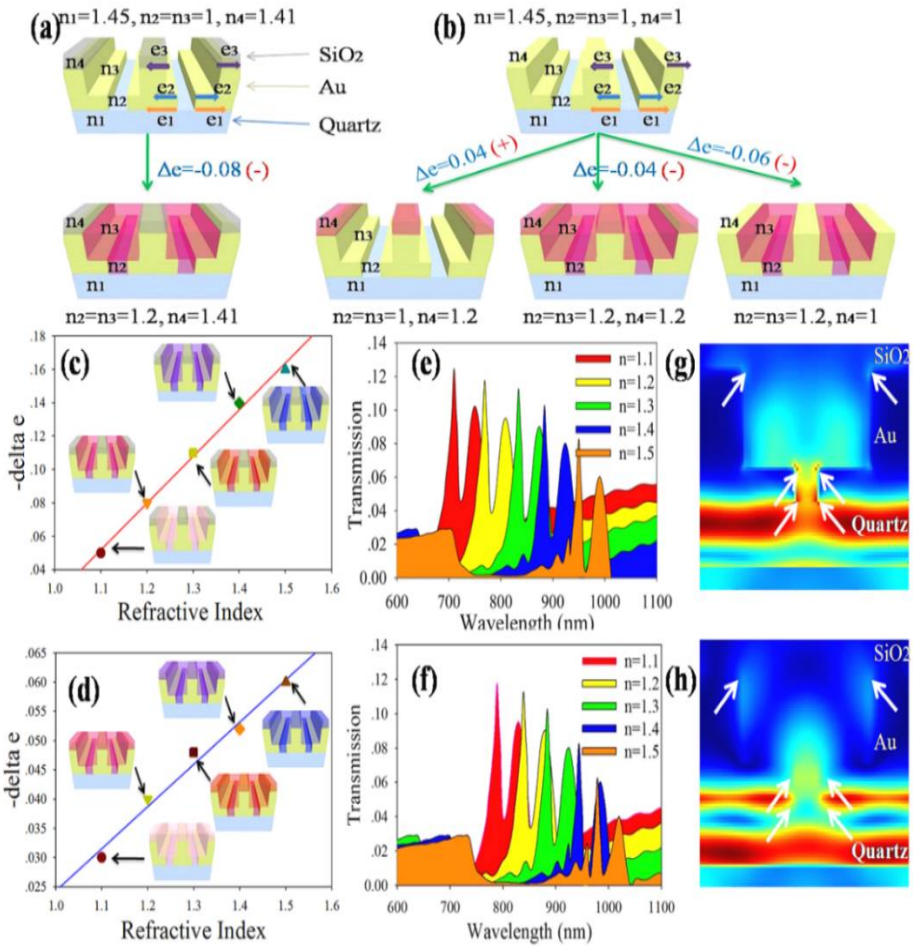


Figure 3.2. The SP Generation Efficiency Change. Δ(e1+e2+e3) for the nanoledge geometry of 280-50 nm with on-top $SiO_2$ layer (a) and without on-top $SiO_2$ layer (b) for the bulk media RI ranging from 1.0 to 1.2. The SP generation efficiency for the nanoledge with on-top $SiO_2$ layer (c) and without on-top $SiO_2$ layer (d) as the surrounding medium RI increases from 1.1 to 1.5. The calculated transmission spectra with on-top $SiO_2$ layer (e) and without on-top $SiO_2$ layer (f) as the surrounding medium RI increases from 1.1 to 1.5. The TE field distribution (g) and TM field distribution (h) of the 280-50 nm nanoledge with on-top $SiO_2$ layer.

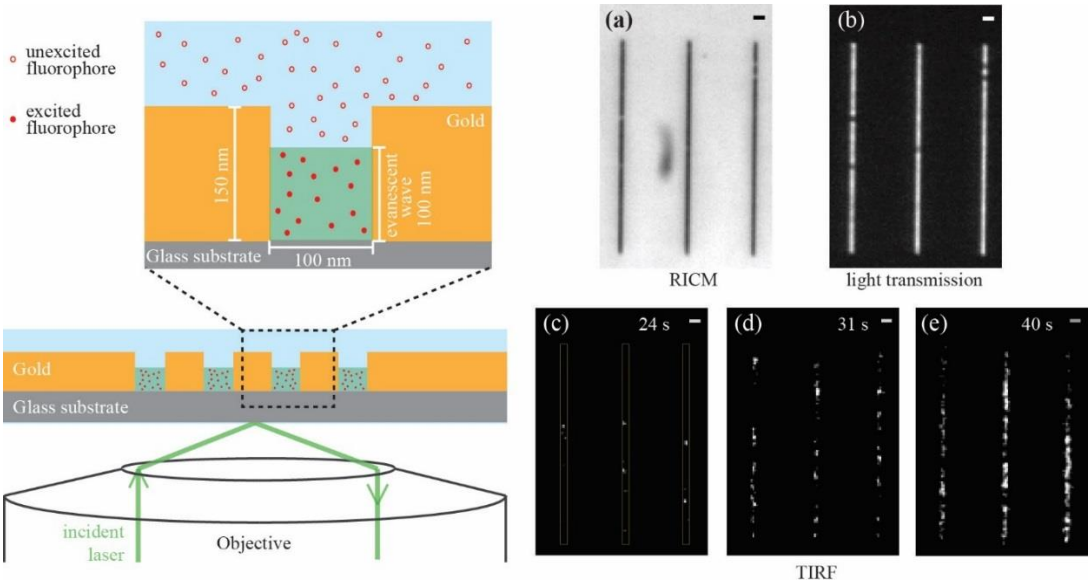


Figure 3.3. TIRF Imaging. TIRF incident laser creates an evanescent wave that only excites fluorophores within 100 nm range from the glass substrate. With the depth of 150 nm, only those fluorophores that enter the nanoslit will be excited and observed. Right: (a) RICM and (b) TLM image of 100 nm nanoslits. (c-e) TIRF images of TxR-BSA diffusion into the nanoslits at time points of 24 s, 31 s, and 40 s, respectively, after the sample injection. The density and intensity of fluorescence increase along with time, indicating that TxR-BSA molecule can diffuse into the nanoslits. A video clip of the process is available in the SI. The positions of nanoslits were indicated by white boxes. All scale bars are 1 μm.

It was found that the EOT peak shift due to a weakened SP generation efficiency correlates with a red shift of the optical transmission peak resulted from a coupling of dielectric changes with nanoledge geometry parameters.[32] The in-gap surfaces of the nanoledge structure have a larger RI sensitivity than the top-of-gap surface mode; therefore the nanoledge structure with $SiO_2$ demonstrates higher sensitivity to the binding events

when the molecule is trapped into the nanoledge gap. As the surrounding medium RI increased up to 1.5, this effect was further elucidated by almost three-fold decrease of the total SP generation efficiency from 0.16 to 0.06 for nanoledge structures with and without $SiO_2$ topping, respectively (Figure 3.2c, d).

In concert with the semi-analytical analysis, Figure 3.2e, f summarize transmission spectra computed by a numerical 3D FDTD method for two selected nanoledges for RIs of a variety of surrounding medium from 1.1 to 1.5. Note that the setup of the FDTD method was similar to that of a previous study[32,33] except the topped 10 nm $SiO_2$ surface layer. The peak wavelength shift of the nanoledge structure with $SiO_2$ (ca. 595 nm/RIU, Fig. S3.1) was larger than that of the nanoledge structure without $SiO_2$ (ca. 556 nm/RIU[32]).

We calculated the transverse electric (TE) and transverse magnetic (TM) modes for the nanoledge structure topped with $SiO_2$ (Figure 3.2g, h). Using a Drude dielectric function for bulk Au,[33,41] we analyzed Au interfaces with quartz, air and $SiO_2$. It was found that the enhanced electromagnetic fields were located near in-gap surfaces for all three interfaces and those fields were higher in magnitude than that in the nanoledge structure without $SiO_2$. This finding was further confirmed by the computing TE wave propagation through the simulation volume of 280-50 nm nanoledge system with $SiO_2$ as shown in Fig. S3.2. The simulation results prove the higher SP generation, and enhanced sensitivity of the nanoledge structure topped with $SiO_2$ for detection of RI changes in the nanoledge gap area.

TIRF and FCS studies of protein behavior: to study the diffusion of nanomolecules in the nanoledge structure, two kinds of nanoslits array chips (period of 5.4 μm as Fig. S3.3

shown) with slit width of 100 nm and 300 nm were fabricated. The 100 nm nanoslits array can be located and observed with the reflection interference contrast microscopy (RICM) and transmitted light microscopy (TLM) (Figure 3.3a, b). Since the size of the nanoslits is below the wavelength of visible light, diffracted features of the nanoslits were obtained. Once the nanoslits were located, a 561 nm laser was sent through the objective to allow TIRF imaging of the TxR-BSA molecules in the nanoslits. Note that TIRF incident laser generates an evanescent excitation field which decays exponentially from the substrate interface and penetrates to a depth of only around 100 nm into the sample medium. Because the height of the nanoslits was set to 150 nm, the fluorescent signals picked up by TIRF imaging would be the emission of fluorophores within the nanoslits only (Figure 3.3 left panel). The nanoslits firstly appear to be totally non-fluorescent under TIRF imaging. Upon adding TxR-BSA to the medium above nanoslits, weak fluorescent signal was detected at the location of the nanoslits after 24 s (Figure 3.3c), indicating that TxR-BSA molecules entered the nanoslits. The fluorescent signal increased with longer observation time (Figure 3.3d, e) and finally reached a steady state. The TIRF imaging observation clearly demonstrates that TxR-BSA can diffuse into the 100 nm nanoslits. The gradual increase of the fluorescent signal suggests that the diffusion is driven by a concentration gradient and short-range energetic interactions at higher confinement grades.

The diffusion of TxR-BSA molecules was further studied by FCS (Figure 3.4a), which collects time-resolved fluorescence fluctuation caused by diffusion of fluorophores in and out of a confocal laser beam.[42] The detection volume of the laser beam is diffraction limited, about 1.2 femtoliter, which makes FCS a single molecule sensitive method. The

information of the diffusion of the molecules which is concealed in the fluorescence fluctuation can be extracted by correlation:[43,44]

$$G(\tau) = \frac{\langle \delta F(t+\tau)\delta F(t) \rangle}{\langle F(t) \rangle^2} \quad (3\text{-}1)$$

where $\langle\ \rangle$ stands for a time average, F(t) is fluorescence intensity at time t, and $\delta F(t) = F(t) - \langle F(t) \rangle$. The infliction point of the resulted auto-correlation function (ACF) curve represents the average dwell time ($\tau_D$) of the diffusive molecule (Figure 3.4b). The $\tau_D$ of three-dimensional diffusion can be obtained by fitting the ACF curve with the three-dimensional diffusion model:

$$G(\tau) = G(0)\frac{1}{\left(1+\frac{\tau}{\tau_D}\right)}\frac{1}{\sqrt{1+\left(\frac{\omega_0}{z_0}\right)^2\frac{\tau}{\tau_D}}} \quad (3\text{-}2)$$

where $\omega_0/z_0$ is the ration of lateral and axial waist of the detection volume. The term $\omega_0/z_0$ is used to allow to float in the fitting process and only affects the fitting at the end of the decay. Uncertainty in $\omega_0/z_0$ does not bias $\tau_D$ by more than a couple of percent. Once $\tau_D$ and $\omega_0$ are calibrated, the diffusion coefficient (D, typically reported in $\mu m^2/s$) of the molecule can be calculated using

$$\tau_D = \frac{\omega_0^2}{4D} \quad (3\text{-}3)$$

As illustrated in Figure 3.4a, the confocal laser beam was sent through the nanoslits to excite and detect fluorophores in the nanoslits. Since the size of the nanoslits is smaller than the diffraction limited laser beam, the actual detection volume is limited by the geometry of the nanoslits. A three-dimensional model is not perfectly fit for a slit structure to obtain the exact shape and size of the detection volume where the molecule is laterally confined, however, a standard method using a molecule with known diffusion coefficient can be used to estimate the so-called effective detection volume. In order to quantify the lateral detection area, a standard dye molecule, fluorescein, with known D (430 $\mu m^2/s$) was used.[45] By measuring the $\tau_D$ of fluorescein in the nanoslits, the effective detection area ($A_{eff}$) can be estimated using

$$\tau_D = \frac{A_{eff}}{D} \qquad (3\text{-}4)$$

The calibrated $A_{eff}$ was then used for D calculation for BSA diffusion with the $\tau_D$ extracted from the ACF curve. Figure 3.4b, c show examples of ACF curves of fluorescein motion in 300 nm and 100 nm nanoslits. The $\tau_D$ of fluorescein in the 300 nm and 100 nm nanoslits is 0.052 ms and 0.028 ms, respectively. Based on the $\tau_D$, the calculated $A_{eff}$ for 300 nm and 100 nm nanoslits is 0.0224 $\mu m^2$ and 0.0120 $\mu m^2$. The data were summarized in Table 3.1.

Table 3.1. Results Obtained From FCS Measurements

| | fluorescien $\tau_D$ (ms) | $A_{eff}$ ($\mu m^2$) | TxR-BSA $\tau_D$ (ms) | TxR-BSA D ($\mu m^2/s$) |
|---|---|---|---|---|
| 300 nm nanoslits | 0.052±0.002 | 0.0224±0.001 | 0.320±0.006 | 69.88±1.31 |
| 100 nm nanoslits | 0.028±0.006 | 0.0120±0.003 | 0.180±0.001 | 66.89±0.38 |

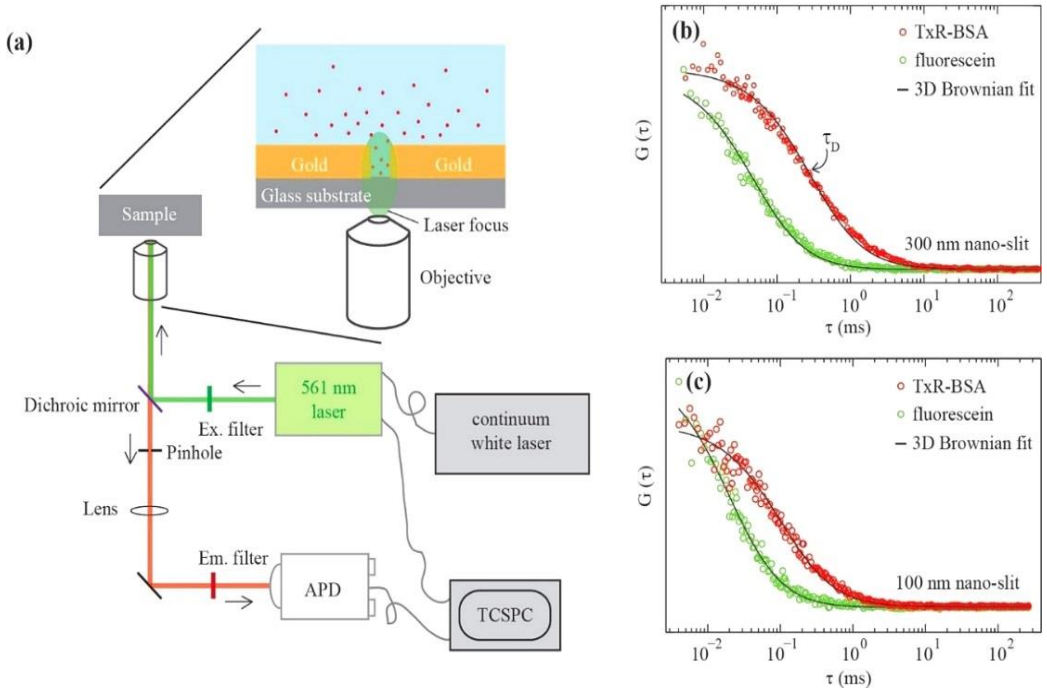


Figure 3.4. Protein Diffusion. (a) Diagram of FCS setup for measuring protein diffusion in the nanoslits. The effective detection area, which is defined by the size of the nanoslits, is smaller than the diffraction limited confocal detection area (laser focus). Sample ACF curves of fluorescein and TxR-BSA diffusion in the 300 nm nanoslits (b) and in the 100 nm nanoslits (c). The inflection point of the ACF curve indicates the average dwell time ($\tau_D$) of fluorescent molecules within the detection volume.

The diffusion of TxR-BSA was measured by FCS as well, as expected, the larger molecule, BSA, has a slower motion than fluorescein molecule does. As shown in Figure 3.4b, c, the ACF curves of TxR-BSA motion shift towards the longer time domain. The $\tau_D$ extracted from ACF curve is 0.320 ms and 0.180 ms for 300 nm and 100 nm nanoslits respectively, and the $\tau_D$ of TxR-BSA is one magnitude larger than that of fluorescein.

Obviously, the D of TxR-BSA in 300 nm and 100 nm nano-slit are both around 70 $\mu m^2/s$ (Table 3.1). Based on Stokes-Einstein equation:[46]

$$D = \frac{kT}{6\pi r_h \eta} \tag{3-5}$$

where k is Boltzmann's constant, T is the temperature, $r_h$ is the hydrodynamic radius, and $\eta$ is the viscosity of the solvent. TxR-BSA molecules have a hydrodynamic radius of ~3 nm, which agrees with the reported size of BSA protein.[47] This result indicates that the diffusion of TxR-BSA within the two different sized nanoslits is Brownian motion with the same mobility. Combined with TIRF imaging results, the FCS measurements clearly demonstrate that TxR-BSA molecules can diffuse into the nanoslits via concentration gradient and short-range energetic interactions.

Protein f-PSA in nanoledge cavities and sensing: next, we performed a preliminary study to use the nanoledge structure for plasmonic sensing. We choose f-PSA biomarker for this performance due to its similar protein size with BSA. To detect such nanomolecule trapping experimentally, we employed a technique based on T-SPR spectrum measurements. A setup for flow-through nanoledge array shown in Figure 3.1 was established to test the sample at the flow rate of 10 µL/min. Note that the detection of T-SPR is under the condition of steady state of full-flow in the nanoledge slits. In this way, the nanoledge array was functioning as the nano-micro-fluidics that can direct sample delivery of analytes to the plasmonic sensing area via nanomolecule migration. We firstly measured the transmission spectra of the nanoledge array chip in air and confirmed the SAM formation and mAb of f-PSA attachment to the nanoplasmonic sensing area in the

gap.[35] Fig. S3.4 displays the transmission spectra of the blank, alkanethiol SAM with carboxylic groups, and after mAb immobilization. The later peaks of the transmission were normalized to the maximum transmission of the primary peak as shown in Figure 3.5b. The primary peaks of the three spectra were located at 725.4 nm, 731.1 nm, and 746.5 nm for blank, SAM only, and SAM plus mAb, respectively. The red shifts of the primary peak were 5.7 nm for SAM and 15.4 nm for mAb immobilization. Based on SPR sensing principle, it has been established to determine the relationship between the peak wavelength and the thickness of added layer using the following equation:[48,49]

$$\Delta\lambda = m(n_A - n_B)[1 - \exp(-2d_E / l_d)] \quad (3\text{-}6)$$

where $\Delta\lambda$ is defined as the peak wavelength shift after the addition of molecule layer to the precedent step modification, $m$ is the RIU sensitivity, $d_E$ is the effective thickness of the existing layer, $l_d$ is the decay length of surface plasmon mode into the dielectric with 110 nm for the nanoledge dimension, and refractive indices of organic layer is taken to be 1.5 and that of air is 1.0.[50]

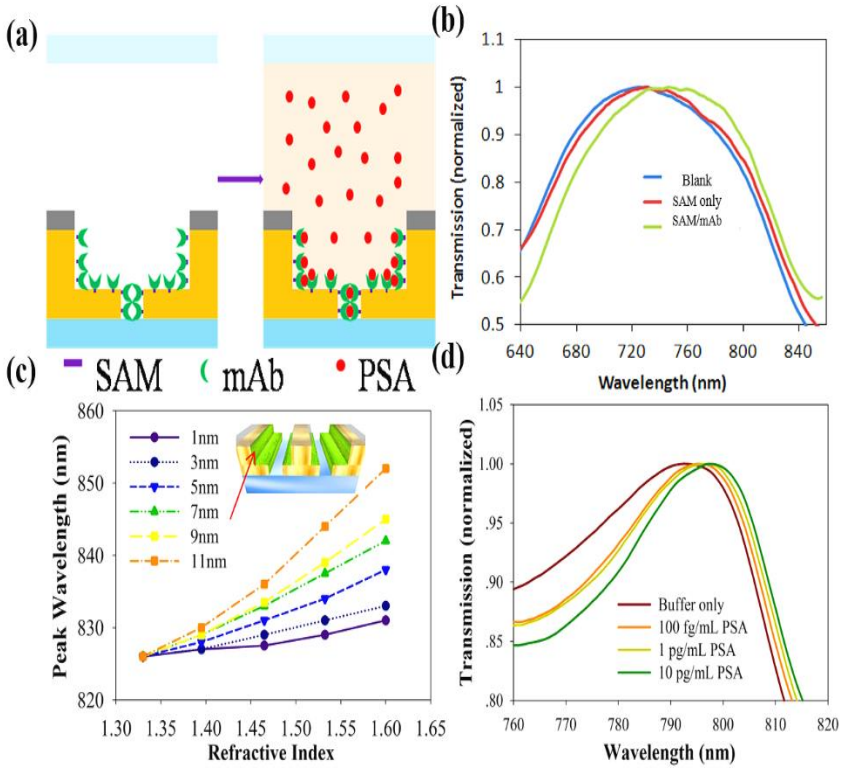


Figure 3.5. The Binding Experiment. (a) An illustration of detector mAb at SAM for binding. (b) Normalized transimission spectra of the nanoledge device at the primary peak. (c) FDTD calculated peak wavelength for a nanoledge device in which the SAM was located on the walls within the nanochannel for varying thickness values of the SAM as the RI index varied from 1.33 (water) to 1.6 (protein SAM). (d) The normalized spectra with different concentration of f-PSA in buffer solution.

Assuming the SAM is packed well at the surface with thickness of 1.1 nm, one is able to estimate the equivalent molecular thickness of mAb according to the following equation:

$$\frac{\Delta\lambda_{SAM}}{\Delta\lambda_{SAM+mAb}} = \frac{1-\exp\left(-2d_{SAM}/l_d\right)}{1-\exp\left(-2d_{SAM+mAb}/l_d\right)} \tag{3-7}$$

According to our measured average $\Delta\lambda$, the calculated equivalent thickness of mAb was found to be 1.9 nm. Moreover, the sensitivity was calculated as 576 nm/RIU, which agrees with the FDTD result above. To obtain a more realistic understanding of the device sensitivity to biological interactions through adsorption onto a SAM, a series of FDTD simulations were conducted in which the sidewall RI was changed while the background RI in the channel remained at 1.33. As we have seen from Figure 3.5c with the nanoledge device, changing the thickness of organic layer on the sidewalls of the device resulted in marked red-shifts of peak wavelengths, since overall thickness of the organic layer increased, the magnitude of the RI increased as well.

In the end, we moved it to the validation of the f-PSA, with the same hydrodynamic radius of ~3 nm as BSA,[51] trapping in nanoledge gap and binding to the surface in the nanoledge cavities by measuring the peak wavelength shift using the T-SPR sensing scheme. It is addressed by the transmission spectra of a series of f-PSA solutions of different concentrations, which were prepared for the f-PSA binding events at the SAM-mAb immobilized at the cavity gold surfaces, starting with incubation of buffer solution and increasing f-PSA concentration from 0.1 pg/mL to 10 pg/mL. Figure 3.5d shows the primary peak also has a red shift consistently within the concentration range of 0.1-10 pg/mL, which proves the trapping of f-PSA into the nanoledge structure array and plasmonic detection.

In this study, the nanoledge structure topped with $SiO_2$ thin film using transmission SPR light signal transduction provides a few advantages over traditional thin film SPR sensors based on total internal reflection light signal with a prism. Specifically, the $SiO_2$-topped nanoledge offers a highly sensitive in-cavity detection mode,[37] meanwhile avoid the nonspecific binding at the top surfaces. Even though the apparent bulky RI sensitivity (576 nm/RIU for the nanoledge) is smaller than that of traditional thin film SPR (usually thousands nm/RIU), the actual measurable sensitivity for affinity sensing is comparable or higher, because the evanescent field in the nanoledge has much shorter decay and stronger near field enhancement than that of the propagating SPR along the thin film, greatly enhancing the sensitivity in detecting RI changes at the sensing vicinity of the metal/dielectric interface.[52-54] In order to obtain strong SPR induced optical transmission for sensing, narrowed nanoslit (<100 nm) is necessary;[37] however it limits charged analytes (e.g. proteins) diffusion into the nanoslit due to the overlap of electric double layer effect in the nanochannel.[55,56] The nanoledge structure, by combining narrow slit at the bottom and the wide open top, not only generates strongly coupled SPR induced optical transmission, but also overcomes the limit of small (<100 nm) nanochannel for migration of protein analytes into the channel, as shown in the results presented above. Moreover, the $SiO_2$ topped nanoledge structure would not allow large biological species, e.g. cells, transporting into the ledge sensing area when it is used for protein detection from whole blood or serum samples. This research is underway and some preliminary results have been obtained and will be submitted for publication later.

## Conclusion

In summary, we presented a new $SiO_2$ topped nanoledge aperture structure for nanometric-sized protein trapping and sensing. For the nanoledge structure, we applied the decomposition and quantitative analysis of SP generation by a semi-analytical model, and numerical simulation of optical transmission spectra and RI sensitivity by a FDTD method, which certificated that nanoledge structure with on-top $SiO_2$ layer had the potential to be effectively applied in T-SPR for protein detection. Experimentally, TIRF imaging showed that proteins can diffuse into the nanoledge structure (with 280 nm open gap) by using similar size straight nanoslits (100 nm and 300 nm) to investigate the protein migration behavior. The diffusion of the labeled BSA into the nano-structure was measured by FCS with the results indicating that BSA molecules in the nanostructure undergo Brownian motion and have a diffusion coefficient of around 70 $\mu m^2/s$, which helped to estimate its hydrodynamic radius of 3 nm. Further studies of the protein trapping and potential sensing applications were provided by fabricating the subwavelength nanoledge device and testing the SPR optical transmission shift and RI sensitivity for determining the binding events between the mAb and a cancer biomarker f-PSA in the nanoledge cavity.

## References


1. Krishnan, M., Mojarad, N., Kukura, P., & Sandoghdar, V. (2010). Nature, 467(7316), 692.
2. Zheng, B. Y., Wang, Y., Nordlander, P., & Halas, N. J. (2014). Advanced Materials, 26(36), 6318-6323.
3. Cohen, A. E. (2005). Physical review letters, 94(11), 118102.
4. Huang, L. R., Cox, E. C., Austin, R. H., & Sturm, J. C. (2004). Science, 304(5673), 987-990.
5. Singh, P. S., Kätelhön, E., Mathwig, K., Wolfrum, B., & Lemay, S. G. (2012). ACS nano, 6(11), 9662-9671.
6. Cohen, A. E., & Moerner, W. E. (2006). Proceedings of the National Academy of Sciences of the United States of America, 103(12), 4362-4365.
7. Krishnan, M., Mönch, I., & Schwille, P. (2007). Nano letters, 7(5), 1270-1275.
8. Wenger, J., & Rigneault, H. (2010). International journal of molecular sciences, 11(1), 206-221.
9. Geissbuehler, M., Bonacina, L., Shcheslavskiy, V., Bocchio, N. L., Geissbuehler, S., Leutenegger, M., ... & Lasser, T. (2012). Nano letters, 12(3), 1668-1672.
10. Foquet, M., Korlach, J., Zipfel, W. R., Webb, W. W., & Craighead, H. G. (2004). Analytical chemistry, 76(6), 1618-1626.

11. Gérard, D., Wenger, J., Bonod, N., Popov, E., Rigneault, H., Mahdavi, F., ... & Ebbesen, T. W. (2008). Physical Review B, 77(4), 045413.
12. Mütze, J., Ohrt, T., & Schwille, P. (2011). Laser & photonics reviews, 5(1), 52-67.
13. Subba-Rao, V., Hoffmann, P. M., & Mukhopadhyay, A. (2011). Journal of Nanoparticle Research, 13(12), 6313-6319.
14. Kelly, C. V., Wakefield, D. L., Holowka, D. A., Craighead, H. G., & Baird, B. A. (2014). ACS nano, 8(7), 7392-7404.
15. Nicoli, F., Verschueren, D., Klein, M., Dekker, C., & Jonsson, M. P. (2014). Nano letters, 14(12), 6917-6925.
16. Chen, P., Chung, M. T., McHugh, W., Nidetz, R., Li, Y., Fu, J., ... & Kurabayashi, K. (2015). ACS nano, 9(4), 4173-4181.
17. Lee, K. L., You, M. L., Tsai, C. H., Lin, E. H., Hsieh, S. Y., Ho, M. H., ... & Wei, P. K. (2016). Biosensors and Bioelectronics, 75, 88-95.
18. Lee, K. L., Chen, P. W., Wu, S. H., Huang, J. B., Yang, S. Y., & Wei, P. K. (2012). Acs Nano, 6(4), 2931-2939.
19. Emam, A. N., Mohamed, M. B., Girgis, E., & Rao, K. V. (2015). RSC Advances, 5(44), 34696-34703.
20. Cheng, Z. Q., Nan, F., Yang, D. J., Zhong, Y. T., Ma, L., Hao, Z. H., ... & Wang, Q. Q. (2015). Nanoscale, 7(4), 1463-1470.
21. Baba, A., Tada, K., Janmanee, R., Sriwichai, S., Shinbo, K., Kato, K., ... & Phanichphant, S. (2012). Advanced Functional Materials, 22(20), 4383-4388.

22. Malic, L., Morton, K., Clime, L., & Veres, T. (2013). Lab on a Chip, 13(5), 798-810.
23. Wang, P., Zhang, L., Xia, Y., Tong, L., Xu, X., & Ying, Y. (2012). Nano letters, 12(6), 3145-3150.
24. Hill, R. T., Kozek, K. M., Hucknall, A., Smith, D. R., & Chilkoti, A. (2014). ACS photonics, 1(10), 974-984.
25. Knoll, W. (1998). Annual Review of Physical Chemistry, 49(1), 569-638.
26. Lalanne, P., Hugonin, J. P., & Rodier, J. C. (2005). Physical review letters, 95(26), 263902.
27. Kress, S. J., Richner, P., Jayanti, S. V., Galliker, P., Kim, D. K., Poulikakos, D., & Norris, D. J. (2014). Nano letters, 14(10), 5827-5833.
28. Cetin, A. E., Etezadi, D., Galarreta, B. C., Busson, M. P., Eksioglu, Y., & Altug, H. (2015). ACS Photonics, 2(8), 1167-1174.
29. Gordon, R., Sinton, D., Kavanagh, K. L., & Brolo, A. G. (2008). Accounts of chemical research, 41(8), 1049-1057.
30. Melikyan, A., Alloatti, L., Muslija, A., Hillerkuss, D., Schindler, P. C., Li, J., ... & Chen, B. (2014). Nature Photonics, 8(3), 229-233.
31. Reiner, J. E., Robertson, J. W., Burden, D. L., Burden, L. K., Balijepalli, A., & Kasianowicz, J. J. (2013). Journal of the American Chemical Society, 135(8), 3087-3094.
32. Zeng, Z., Mendis, M. N., Waldeck, D. H., & Wei, J. (2016). RSC advances, 6(21), 17196-17203.

33. Zeng, Z., Liu, Y., & Wei, J. (2016). TrAC Trends in Analytical Chemistry, 75, 162-173.

34. Wei, J., Kofke, M., Rexius, M., Singhal, S., Wang, Y., & Waldeck, D. H. (2011). Nanotechnology, 3, 79-82.

35. Sanders, M., Lin, Y., Wei, J., Bono, T., & Lindquist, R. G. (2014). Biosensors and Bioelectronics, 61, 95-101.

36. Eftekhari, F., Escobedo, C., Ferreira, J., Duan, X., Girotto, E. M., Brolo, A. G., ... & Sinton, D. (2009). Analytical chemistry, 81(11), 4308-4311.

37. Lee, K. L., Wang, W. S., & Wei, P. K. (2008). Biosensors and Bioelectronics, 24(2), 210-215.

38. Gordon, R., Brolo, A. G., McKinnon, A., Rajora, A., Leathem, B., & Kavanagh, K. L. (2004). Physical review letters, 92(3), 037401.

39. Escobedo, C., Brolo, A. G., Gordon, R., & Sinton, D. (2010). Analytical chemistry, 82(24), 10015-10020.

40. Lalanne, P., Hugonin, J. P., & Rodier, J. C. (2006). JOSA A, 23(7), 1608-1615.

41. Vial, A., & Laroche, T. (2008). Applied Physics B: Lasers and Optics, 93(1), 139-143.

42. Aouani, H., Wenger, J., Gérard, D., Rigneault, H., Devaux, E., Ebbesen, T. W., ... & Blair, S. (2009). ACS nano, 3(7), 2043-2048.

43. Shi, X., Li, X., Kaliszewski, M. J., Zhuang, X., & Smith, A. W. (2015). Langmuir, 31(5), 1784-1791.

44. Shi, X., Li, X., Kaliszewski, M. J., Zhuang, X., & Smith, A. W. (2015). Langmuir, 31(5), 1784-1791.

45. Petrášek, Z., & Schwille, P. (2008). Biophysical journal, 94(4), 1437-1448.

46. De Santo, I., Causa, F., & Netti, P. A. (2010). Analytical chemistry, 82(3), 997-1005.

47. González Flecha, F. L., & Levi, V. (2003). Biochemistry and Molecular Biology Education, 31(5), 319-322.

48. Jung, L. S., Campbell, C. T., Chinowsky, T. M., Mar, M. N., & Yee, S. S. (1998). Langmuir, 14(19), 5636-5648.

49. Haemers, S., Koper, G. J., van der Leeden, M. C., & Frens, G. (2002). Langmuir, 18(6), 2069-2074.

50. Chen, S., Svedendahl, M., Käll, M., Gunnarsson, L., & Dmitriev, A. (2009). Nanotechnology, 20(43), 434015.

51. Mulder, S. D., Heijst, J. A., Mulder, C., Martens, F., Hack, C. E., Scheltens, P., ... & Veerhuis, R. (2009). Annals of clinical biochemistry, 46(6), 477-483.

52. Yonzon, C. R., Jeoung, E., Zou, S., Schatz, G. C., Mrksich, M., & Van Duyne, R. P. (2004). Journal of the American Chemical Society, 126(39), 12669-12676.

53. Haes, A. J., & Van Duyne, R. P. (2004). Analytical and bioanalytical chemistry, 379(7-8), 920-930.

54. Lee, K. L., Chang, C. C., You, M. L., Pan, M. Y., & Wei, P. K. (2016). Scientific reports, 6, 33126.

55. Pennathur, S., & Santiago, J. G. (2005). Analytical chemistry, 77(21), 6772-6781.

56. Karnik, R., Fan, R., Yue, M., Li, D., Yang, P., & Majumdar, A. (2005). Nano letters, 5(5), 943-948.

# CHAPTER IV

# IMPROVED SUPERCAPACITOR PERFORMANCE

This chapter has been published as: Zeng, Z., Liu, Y., Zhang, W., Chevva, H., & Wei, J. (2017). Improved supercapacitor performance of $MnO_2$-electrospun carbon nanofibers electrodes by mT magnetic field. Journal of Power Sources, 358, 22-28.

## An Overview

This work reports on a finding of mT magnetic field induced energy storage enhancement of $MnO_2$-based supercapacitance electrodes (magneto-supercapacitor). Electrodes with $MnO_2$ electrochemically deposited at electrospun carbon nanofibers (ECNFs) film are studied by cyclic voltammetry (CV), galvanostatic charge/discharge, electrochemical impedance spectroscopy (EIS), and life cycle stability tests in the presence/absence of milli-Tesla (mT) magnetic fields derived by Helmholtz coils. In the presence of 1.34 mT, $MnO_2$/ECNFs shows a magneto-enhanced capacitance of 141.7 F $g^{-1}$ vs. 119.2 F $g^{-1}$ (~19% increase) with absence of magnetic field at the voltage sweeping rates of 5 mV/s. The mechanism of the magneto-supercapacitance is discussed and found that the magnetic susceptibility of the $MnO_2$ significantly improves the electron transfer reaction of pseudo-reaction of Mn(IV)/Mn(III) at the electrode, along with the magnetic field induced impedance effect, which may greatly enhance the interface charge density, facilitate electrolyte transportation, and improve the efficiency of cation intercalation/de-intercalation of the pseudocapacitor under mT-magnetic field exposure, resulting

enhancement of energy storage capacitance and longer charge/discharge time of the $MnO_2$/ECNFs electrode without sacrificing its life cycle stability.

## Introduction

Electrochemical double layer supercapacitors have drawn a lot of attention due to fast charging/discharging rate, increased energy density and power density, and large life cycle stability.[1-4] However, regarding the energy storage capability, there is an emerging need to develop supercapacitors with high relative dielectric constant or redox reactions in the double layer and surface area of the electrode for higher energy density and larger life cycle stability.[5-7] Some of the electroactive metal oxide, e.g. ruthenium oxide ($RuO_2$),[8] manganese oxide ($MnO_x$),[9] nickel oxide ($NiO_x$),[10] cobalt oxide ($Co_3O_4$),[11] tin oxide ($SnO_2$),[12] zinc oxide (ZnO),[13] and vanadium (V) oxide ($V_2O_5$)[14] etc. were used in supercapacitor (so-called pseudocapacitor) electrodes to offer fast and reversible redox reactions, contributing to higher energy density capacity[15]. To increase surface area, carbon nanomaterials, such as carbon nanotubes (CNTs)[16], carbon nanofibers (CNFs)[17], graphene nanofoam (GF)[18], and reduced graphene oxide (rGO)[19] were used in supercapacitors, which not only provide unique size and surface dependent properties but also excellent intrinsic physical (e.g. electrical, thermal, chemical and mechanical) properties. Among these, electrospun carbon nanofibers (ECNFs) is known for its large porosity, high conductivity, low cost in production with freestanding nature, and good scaffolds to uniformly support nanostructured metal oxide[20]. Electrospinning is an efficient fiber production method which uses electric force to draw charged threads of polymer solutions or polymer melts

up to form polymer nanofibers[21] which can be converted to porous ECNFs with subsequent carbonization[22]. Electrospinning has become a powerful and easy method to form carbon nanofibers in large scale for broad applications. It has been used for electrode material production or separator materials for supercapacitors[23-25], Li (or Na)-ion batteries[26-29], as well as preparation of electrical double-layer capacitor half-cells[30].

Recently, the influence of an external magnetic field over the capacitance of electrodes has won some attention due to effects of Lorentz force acting on moving charges/ions, charge density gradient modulation, electron state excitation and oscillatory magnetization,[31-33] thus energy storage improvement. Two magnetic strategies for enhancing the electrochemical process in capacitors have been demonstrated. One is to introduce magnetic nanoparticles into the electrode in the presence of an external magnetic field. For instance, $Fe_2O_3$/graphene nanocomposites[33], $Fe_3O_4$/active carbon nanocomposites[34], and $Fe_3O_4$/active carbon nanocomposites[35] demonstrated enhancement of the capacitance and energy density with an external magnetic field. The other one is to reconstruct the charge density and electric polarization in the magnetic material system. For example, ionic liquid was used in charge carrier engineering to achieve tunable dielectric permittivity.[31]

During the past years, $MnO_2$ has been one of the most commonly used transition-metal oxides that have been used as pseudocapacitive electrode materials due to its unique characteristics, such as easy-for-deposition, stability and significantly enhanced energy storage performance;[36,37] however, little is known about the magnetic field effect on its energy storage. Herein, for the first time, we present a magnetization-induced capacitance

enhancement in $MnO_2$/ECNFs nanocomposite electrodes fabricated by electrochemical deposition of $MnO_2$ on ECNFs. The $MnO_2$/ECNFs electrode was characterized by scanning electron microscopy (SEM), x-ray powder diffraction (XRD), energy-dispersive x-ray spectroscopy (EDX), Raman spectroscopy, Fourier transform infrared spectroscopy (FTIR), thermogravimetric analysis (TGA), and superconducting quantum interference device vibrating sample magnetometer (SQUID VSM). The electrochemical performance of the $MnO_2$/ECNFs electrodes for capacitive energy storage was studied by cyclic voltammetry (CV), galvanostatic charge/discharge, electrochemical impedance spectroscopy (EIS), and life cycle stability tests in the presence/absence of milli-Tesla (mT) to sub-mT magnetic fields derived by Helmholtz coils.

**Results and Discussion**

The morphologies of ECNFs and $MnO_2$/ECNFs were characterized by SEM (Figure 4.1b,d). The ECNFs with nanofiber diameter of about 521 nm (Figure 4.1c) are decorated by $MnO_2$ coating with thickness of ~2.1 μm making a total diameter of the fiber as about 2.63 μm (Figure 4.1e). The charge current of 40 μA, the charge time of 3 hours in an aqueous precursor solution with 10 mM $MnSO_4$ and 100 mM $Na_2SO_4$ were applied to achieve the electrochemical deposition of the $MnO_2$ at the 1 $cm^2$ ECNFs film. The success of $MnO_2$ deposition was confirmed with Raman spectra (Fig. S4.1 Mn-O at the Raman shift of 627 $cm^{-1}$), XRD pattern (in Fig. S4.2, the well resolved peak at 37.1° is attributed to $MnO_2$), and FTIR spectra (in Fig. S4.3, Mn-O stretch is presented at the wavenumber of 648 $cm^{-1}$ and 731 $cm^{-1}$).[38,39] TGA shows the weight fraction of $MnO_2$ of the $MnO_2$/ECNFs

electrode is about 53% (Fig. S4.4), which was further verified using EDX analysis by averaging different spectrum zones (Fig. S4.5).

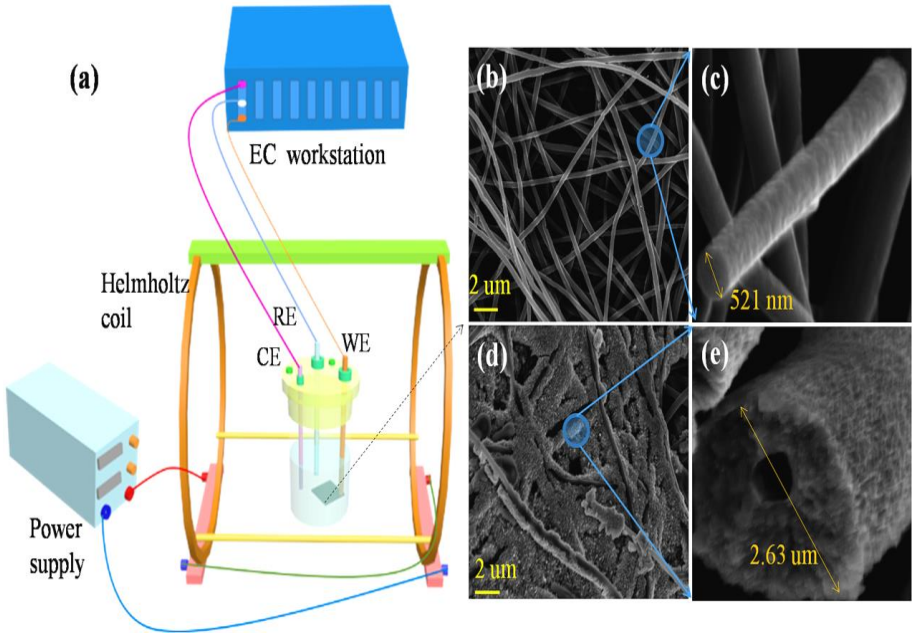


Figure 4.1. Setup and SEM Images. (a) The schematic of the electrochemical cell in the presence of an external magnetic field. (b)-(e) SEM images of the electrode materials (b) ECNFs, (c) enlarged ECNFs, (d) $MnO_2$/ECNFs, and (e) enlarged $MnO_2$.

As a pseudocapacitive electrode, the $MnO_2$/ECNFs electrode possesses combined contribution of spacers and redox reaction, i.e., the electrochemical double layer capacitance and the pseudocapacitance from $MnO_2$ for energy storage. The former stores charge electrostatically due to the adsorption of ions at electrode surfaces and is mainly determined by the electrode surface area. While, for the latter, the energy is stored in virtue of highly reversible redox reactions (e.g. electron transfer reactions) between Mn(IV)/Mn(III) species and cation intercalation/de-intercalation at the $MnO_2$/electrolyte interfaces.[36,40,41] The charge storage mechanism can be expressed as:[36,42]

$$Mn(IV)O_2 + mH^+ + nK^+ \leftrightarrow Mn(III)Mn(IV)OOH_mK_n \quad (4\text{-}1)$$

Equation 4-1 represents the successive multiple surface redox reactions between the Mn(IV)/Mn(III) complexes leading to the pseudo-capacitive charge storage mechanism.[42]

To measure the specific capacitance of the $MnO_2$/ECNFs electrode and magnetic field effect, CV was performed using the classical three-electrode method[43] in 6.0 M KOH electrolyte solution. Figure 4.2 shows the representative, stable cyclic voltammetry (CV) loops with or without an external magnetic field, which present a combination of both double layer and pseudocapacitive behaviors within the scan voltage from 0.0 V to 0.8 V. There are a pair of peaks at the voltage between 0.4-0.5 V vs. Ag/AgCl which might be attributed to the redox reaction of the Mn(IV)/Mn(III) species in the form of $K^+$ intercalation.[41] The overall specific capacitance is calculated from the integrated area of the CV loops (see details in supporting information). In the absence of an external magnetic field, the specific capacitance of a $MnO_2$/ECNFs electrode was calculated to be 119.2, 105.8, 92.8, 71.0, 53.4 F $g^{-1}$ at the voltage sweeping rates of 5, 10, 20, 50, and 100 mV $s^{-1}$, respectively. Compared to that of the ECNFs-only electrode (Fig. S4.6a), $MnO_2$/ECNFs shows higher capacitance because of the higher relative dielectric constant of $MnO_2$ and its pseudo-activity. In the presence of 1.34 mT magnetic field, the capacitance of the $MnO_2$/ECNFs magneto-supercapacitor electrode increased by about avg. 19% for all sweeping rates (Figure 4.2b-d, Fig. S4.7). Since there is no measurable enhancement of capacitance of the ECNFs-only electrodes at the same range of voltage sweeping rates (Fig. S4.6) under the magnetic field, the magnetocapacitance enhancement of the $MnO_2$/ECNFs electrode is resulted from the magnetic field effect on the $MnO_2$ at the ECNFs substrate.

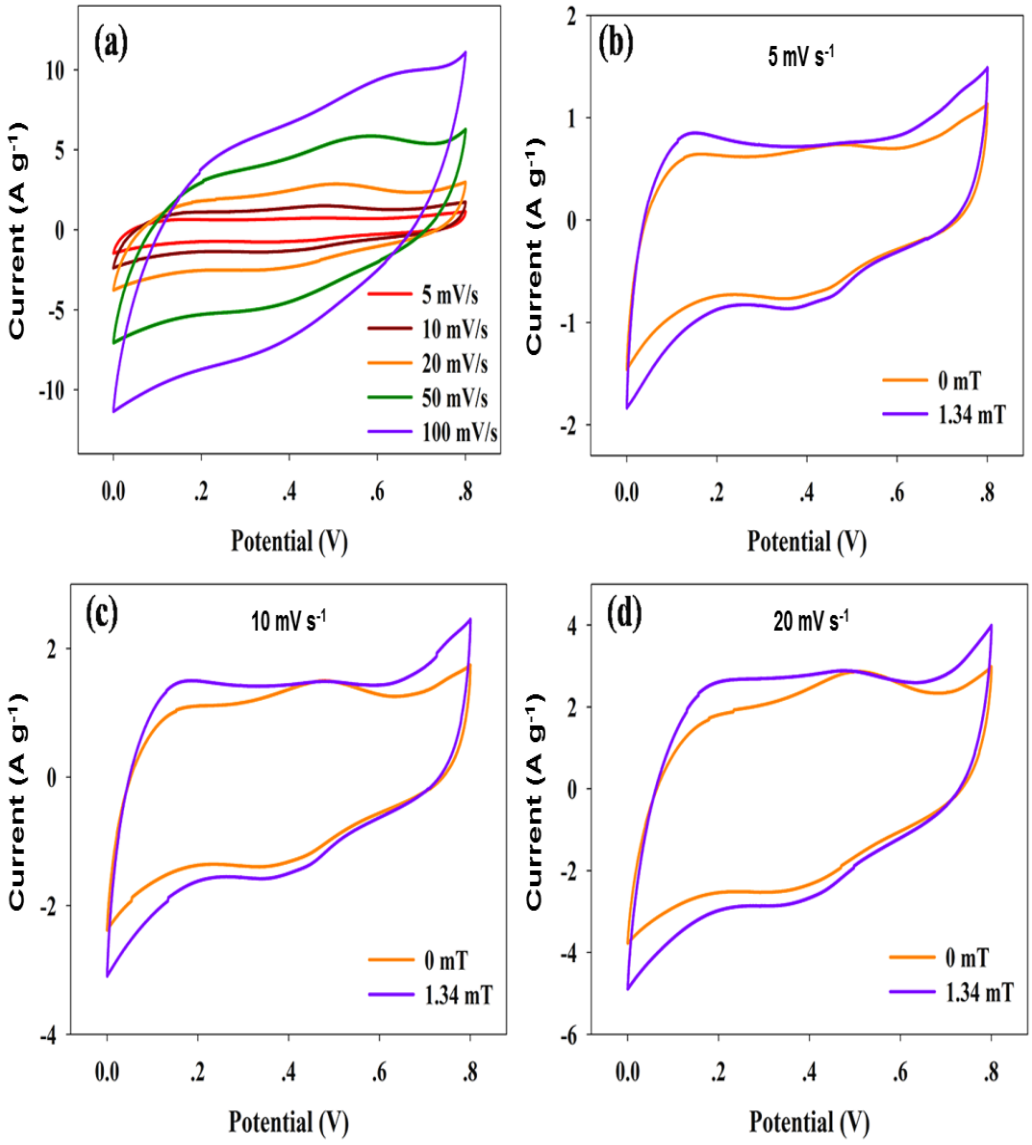


Figure 4.2. CV Experiment. (a) Cyclic voltammetry loops of the $MnO_2$/ECNFs electrodes tested in the absence of magnetic field (0 mT) at different voltage sweeping rates. Cyclic voltammetry loops of the $MnO_2$/ECNFs electrodes tested in the presence (1.34 mT)/ absence (0 mT) of magnetic field at different scan rates of 5 mV $s^{-1}$ (b), 10 mV $s^{-1}$ (c), 20 mV $s^{-1}$ (d).

The effect of magnetization on the galvanostatic charge/discharge performance of $MnO_2$/ECNFs was studied under different current densities (0.5-20 A $g^{-1}$, Figure 4.3abc & Fig. S4.8). The curvature of the charge step between the voltage of 0.0-0.4 V and larger growth of the discharge curve between the same range voltages suggest a combined contribution from pseudocapacitance and double layer capacitance,[44] which is consistent with the observation from CV studies. With the applied magnetic field from 0.45 mT to 1.34 mT and the same current density, the charge/discharge time increases (Figure 4.3b-c, Fig. S4.8) comparing to that of the absence of magnetic field. The charge/discharge time under smaller current density increases more significantly than that of the larger current density (e.g. 58.1% increase at 0.5 A $g^{-1}$ vs. 13.6% at 1 A $g^{-1}$ with 1.34 mT magnetic field), suggesting the magnetic field effects on both the pseudocapacitive electrolyte-electrode interface and double layer region, resulting in the magneto-capacitance enhancement.

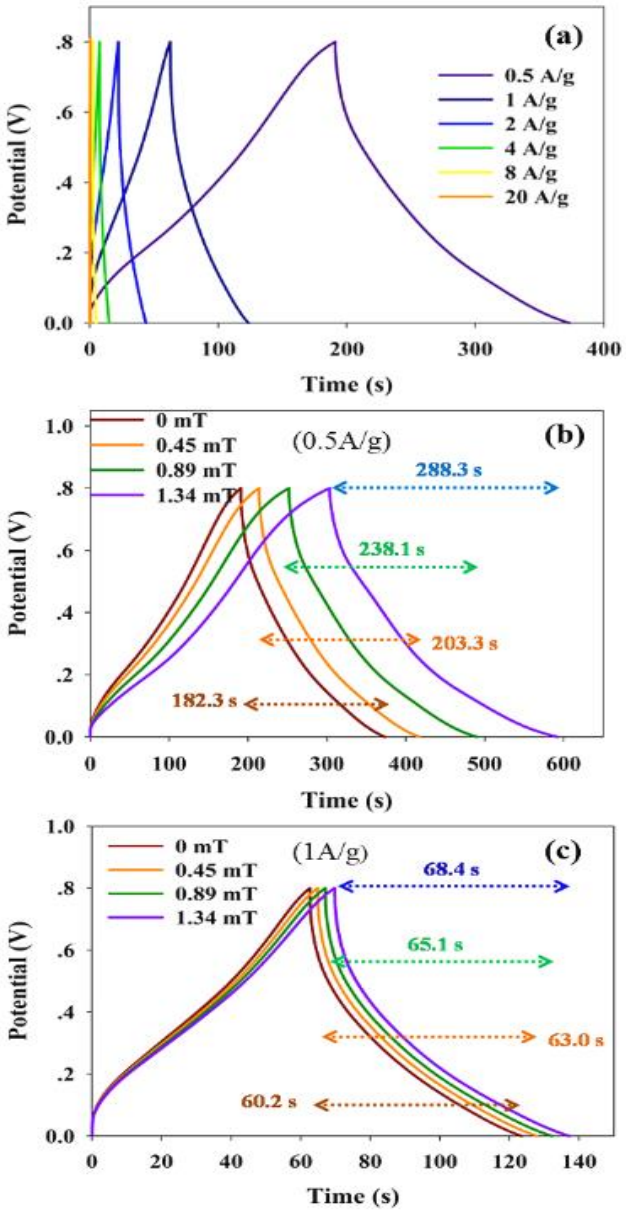


Figure 4.3. Charge/discharge. (a) charge/discharge curves of the $MnO_2$/ECNFs electrodes tested in the absence of magnetic field. Galvanostatic charge/discharge curves of the $MnO_2$/ECNFs tested in the presence of different magnetic fields under different current densities of 0.5 A $g^{-1}$ (b), and 1 A $g^{-1}$ (c).

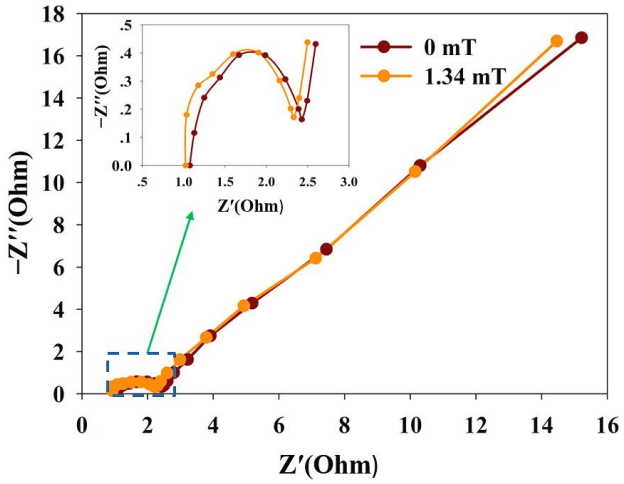


Figure 4.4. Nyquist Plots. $MnO_2$/ECNFs electrodes tested in the presence (1.34 mT)/ absence (0 mT) of magnetic field.

From the charge/discharge curves, specific capacitance is calculated from the discharge curves,[45] i.e., $C = I \cdot t/(m \cdot \Delta E)$, in which $I$ is the discharge current, $t$ is the discharge time, and $\Delta E$ is the potential drop during discharge in V (see more in SI). It was found that, under the magnetic field of 1.34 mT, the electrode of $MnO_2$/ECNFs enhanced the capacitance by 58.1% (Figure 4.3b) at the current density of 0.5 A $g^{-1}$, by 13.6% under the current 1 A $g^{-1}$ (Figure 4.3c) and 6% under 2 A $g^{-1}$ (Fig. S4.8), respectively. Moreover, to quantitatively analyze the pseudocapacitance contribution to the overall capacitance performance, the non-faradaic contribution from double layer capacitance and the faradaic contribution from pseudocapacitance were separated in galvanostatic charge-discharge curves.[44,46] By considering the area corresponding to faradaic contribution in $MnO_2$/ECNFs electrode, at current density of 0.5 A $g^{-1}$, the pseudocapacitance contribution from $MnO_2$ in overall performance was approximately 56.5%, 61.0%, 62.4%, and 67.8% with the applied magnetic field of 0 mT, 0.45 mT, 0.89 mT, and 1.34 mT, respectively. The

fraction of the pseudocapacitive contribution in energy storage increases along with the magnetic field strength, suggesting the more significant effect on pseudo-redox reaction at the $MnO_2$/ECNFs electrode than that on the non-faradaic contribution.

Next, the effect of magnetic field on the impedance of the $MnO_2$/ECNFs within the electrochemical cell (6 M KOH electrolyte) was investigated using EIS, which may provide understanding of the different electrochemical behaviors in the absence/presence of magnetic field. Figure 4-4 shows the performance of EIS for the $MnO_2$/ECNFs electrodes over the frequency range of 10 kHz to 0.01 Hz with the potential amplitude of 10 mV. Both the Nyquist plots of EIS spectra in the absence/presence of an external magnetic field show a semicircle arc in the high frequency region and a linear line in the low frequency region, indicating a low internal resistance of the $MnO_2$/ECNFs electrodes[47]. In the presence of 1.34 mT magnetic field, the capacitor system superficially seems to be a more ideal double layer supercapacitor, since the semicircle arc is more obvious and straight line seems to be little more vertical. Zhu, et al[33,47] reported that additional Lorentz force acts on the moving ions in a perpendicular magnetic field flux density (magnetohydrodynamic phenomenon), which may promote the electrolyte convection in the bulk electrolyte. Hence, it is not surprising that the changes of the solution resistance ($R_s$ ~1 Ohms) in bulky electrolyte, the charge transfer resistance ($R_{ct}$) at the electrode-electrolyte interface, and the leakage resistance ($R_{leak}$) of the double layer region at low frequency are observed for $MnO_2$/ECNFs electrodes under magnetic field. Specifically, the solution resistance (Rs) with 1.34 mT magnetic field decreases about 0.1 Ohms from 1 Ohms. The resistance of charge transfer ($R_{ct}$) of the electrode reaction obtained from the diameter of the semicircle

in the high frequency region (1.26 Ohms) decreased from 1.35 Ohms of the non-magnetized $MnO_2$/ECNFs electrode, indicating a faster contact and charge transfer which may result in an improved rate performance.[48] The low frequency leakage resistance ($R_{leak}$)[34] in the double layer region increased for the $MnO_2$/ECNFs electrode with the presence of magnetic field, suggesting that leakage current flowing across the double layer at the electrode-electrolyte interface was better restricted, which may also improve the $MnO_2$/ECNFs electrode capacitance.

The EIS analysis of this work agrees with the previous studies by Zhu, et al[33,47] on different metal oxide (Fe, Ni, Co)-carbon supercapacitors. The magnetohydrodynamic phenomenon is the major factor for the electrode internal resistance decrease and the magnetic induced electrolyte convection to reach extra electrode surfaces, which may help to generate larger specific capacitance of the electrodes, and build up a complete double layer that restricts the leakage of free electrons, thus improving the capacitance performance. However, in this study, much smaller magnetic field strength, i.e. 1.34 mT on $MnO_2$/ECNFs electrode and much smaller resistance change, achieved comparable capacitance enhancement of 72 mT magnetic field on metal-oxide (Fe, Ni, Co) nanocomposite electrodes.[33,47] It is known that $MnO_2$ has the paramagnetic property due to multiple unpaired electrons involving in the pseudo-active electron transfer reaction. Hence it may help to better understand the capacitance enhancement by measuring the magnetization of the $MnO_2$/ECNFs electrodes.

The magnetic susceptibility of the $MnO_2$/ECNFs was performed using the SQUID VSM at room temperature and Figure 4.5 shows the moment response of the $MnO_2$/ECNFs

electrode under different magnetic field strength. The magnetization, measured as the magnetic moment associated with electron's spin state, $\mu_{e,}$ at 1.34 mT magnetic field is found to be $4.23\times10^{-4}$ emu $g^{-1}$ of the $MnO_2$/ECNFs electrode and ~$7.98\times10^{-4}$ emu $g^{-1}$ of the pure $MnO_2$ mass fraction (ca. 53%) in the electrode. The spin-dependent torque the $MnO_2$ experienced, representing the improved energy state of the electron, is $1.07\times10^{-9}$ J $g^{-1}$ (~$93.0\times10^{-9}$ J $mol^{-1}$) obtained by multiplying the magnetic field by the magnetic moment. The magnetic field induced spin-dependent torque on an electron with spin quantum number $m_s$=+1/2 and -1/2 causes the degeneracy, namely different energy levels of the "+" and "-" spin states.[49] which is expressed as, $h\nu=g\beta H$ where $h\nu$ is the quantum of energy corresponding to a characteristic frequency $\nu$, $g$ is dimensionless constant called the "electron g-factor", $\beta$ is the electronic Bohr magneton ($9.2740154\times10^{-24}$ J $T^{-1}$), and $H$ is the magnetic field strength. The enhanced energy state of the electrons will increase the electron transfer kinetics between the species of Mn(IV)/Mn(III), as well as the electron transportation efficiency at the electrolyte-$MnO_2$/ECNTs interfaces, hence contributes to the capacitance enhancement.

The magnetic field effect on the redox electron transfer kinetics of Mn(IV)/Mn(III) is further analyzed according to transition state theory by considering the contribution of the enhanced electron energy states to the activation energy due to magnetic field induced degeneracy. The rise of Zeeman energy, $g\beta HS$ ($S$ is spin), relative to the reactant energy when there is no applied field, of the unpaired electrons in $MnO_2$ with magnetic field contributes to the activation energy by reducing the net enthalpy of activation barrier and thus the reaction rate is facilitated. The redox electron transfer rate of Mn(IV)/Mn(III) at

the electrode can be expressed according to an Arrhenius form as follows, and more details in SI):

$$k_m = A\exp\left[\frac{\Delta S_0^{*}}{k_b}\right]\exp\left[\frac{\Delta S_m^{*}}{k_b}\right]\exp\left[-\frac{\Delta H_0^{*}}{k_b T}\right]\exp\left[-\frac{\Delta H_m^{*}}{k_b T}\right] \quad (4\text{-}2)$$

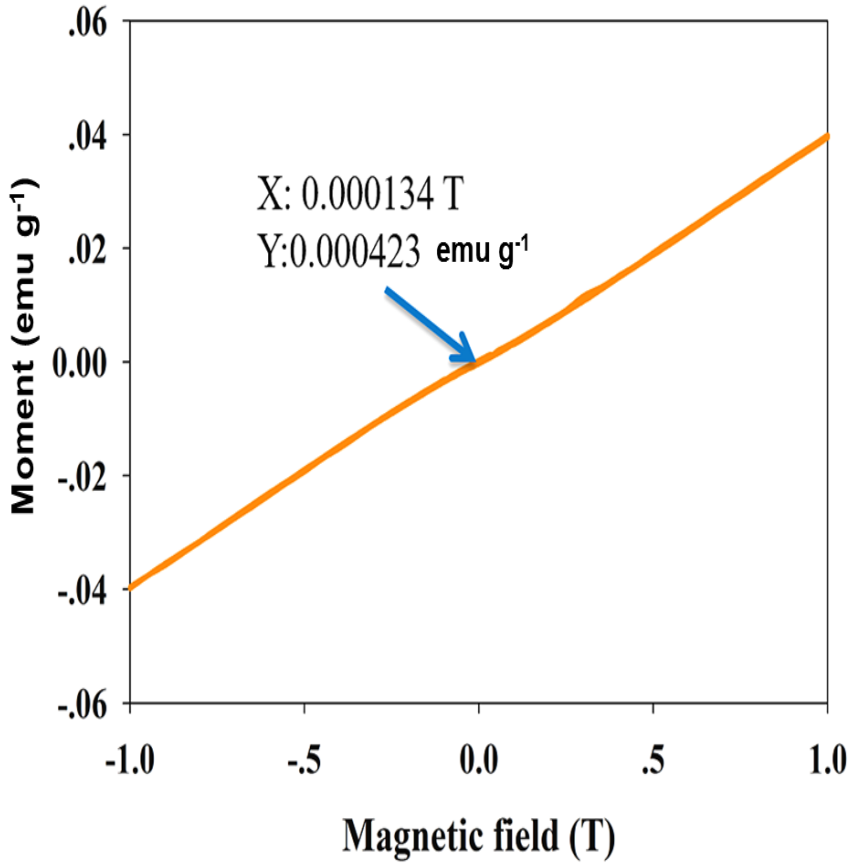


Figure 4.5. SQUID VSM Result. $MnO_2$/ECNFs at room temperature. The closely straight line shows the magnetization of $MnO_2$/ECNFs is $4.23\times10^{-4}$ emu $g^{-1}$ at 1.34 mT magnetic field. Since the weight ratio of $MnO_2$ in $MnO_2$/ECNFs is about 53%, the magnetization on pure $MnO_2$ is calculated to be $7.98\times10^{-4}$ emu $g^{-1}$.

With $\Delta H_m^* = -gHS\beta$, A is the pre-factor depending on the convolution of a suitable weighted frequency ($v_n$) for crossing the activation barrier and the transmission coefficient or averaged transition probability for electron transfer per passage of the system through the intersection region from reactant to product, and in classical transition theory, A is taken as $k_bT/h$ where $k_b$ is Boltzmann's constant, T is absolute temperature, and $h$ is

Planck constant. With sufficient magnetic field for the energy degeneracy of single unpaired electron spin, the electron transfer rate can be doubled (see SI). The measured magnetic susceptibility response to the external magnetic field suggests that the $MnO_2$/ECNTs electrode is sensitive to magnetic field due to the multiple unpaired electron spins of $MnO_2$. While it is difficult to quantitatively analyze how the field impact the electron transfer in the electrode, these analyses suggest that the facilitated electron transfer kinetics of the pseudo-redox reaction in the $MnO_2$/ECNFs electrode contribute significantly in the energy storage performance with respect to the small magnetic field applied to the electrode. Building upon the results and analysis, one can find that the mT magnetic field significantly enhances energy storage capacitance of the $MnO_2$/ECNFs electrodes with a comprehensive mechanism due to the combined contribution of both the double layer and pseudo-active capacitance.

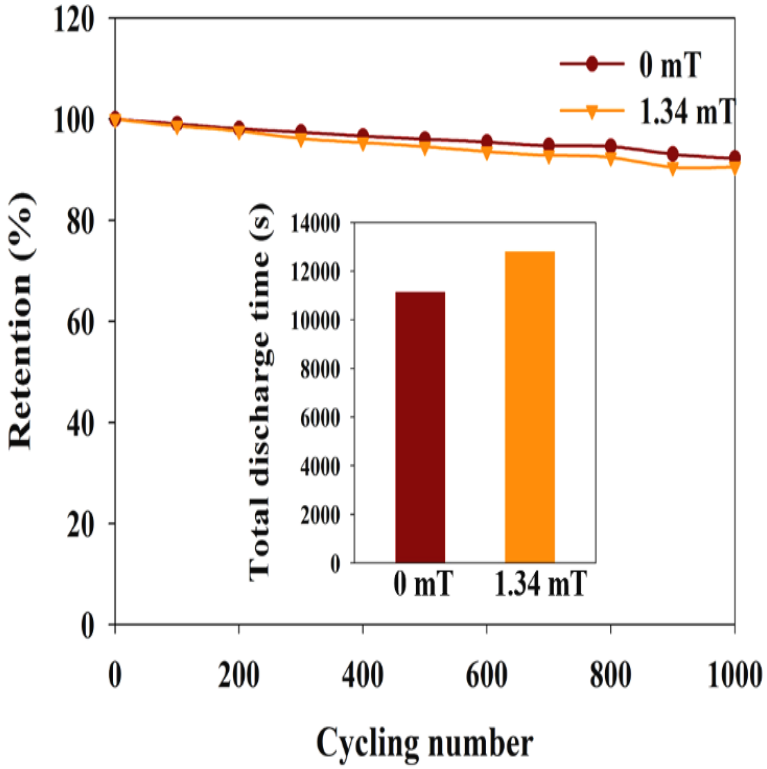


Figure 4.6. Cycling Performance. $MnO_2$/ECNFs electrodes tested in the presence (1.34 mT)/ absence (0 mT) of magnetic field under the current density of 4 A $g^{-1}$.

Firstly, the change of the electrode resistance in electrochemical cell, though small, indicate that the changes of dipole moment in the transition and vibrational states of electrolyte at the double layer area can enhance the conductivity and reduce the resistance (impedance effect), thus enhancing the electrochemical adsorption/desorption of cations and anions at the electrode/electrolyte interfaces; Secondly, and more significantly in this case, the paramagnetic nature of the $MnO_2$ with multiple unpaired electrons and magnetic susceptibility may largely facilitate the Mn(IV)/Mn(III) pseudo-redox reaction and electron transfer to the electrolyte-electrode interfaces, which may result in higher charge density at the electrode interfaces, more efficiency of cation intercalation/de-intercalation, and

thicker double layer, therefore the enhanced capacitance. Since both the impedance effect and the electron spin energy degeneracy depend on the strength of the magnetic field, the dissimilarity of the magneto-capacitance enhancement at different magnetic field during charge and discharge process is expected.

Finally, for practical purpose, the life cycle performance of the $MnO_2$/ECNFs electrodes was performed by galvanostatic charge/discharge cycling in term of two important parts, i.e., cycling capability or capacitance retention, and total discharge time. As shown in Figure 4.6, in the absence of 1.34 mT magnetic field, 92.3% of the initial capacitance was maintained after 1000 cycles. With presence of 1.34 mT magnetic field, 90.6% of the initial capacitance was maintained after 1000 cycles. Note that with the same cycling, the total discharge time increased by 15.1% with presence of magnetic field (Figure 4.6 inserted) due to magnetic field induced discharge time extension. Experimental performance and data analysis indicate that the magnetic susceptibility largely increases the charge transfer rate thus improves the pseudo-reactions of $MnO_2$ at the electrode and interfaces. A supercapacitor nanocomposite electrode composed of $MnO_2$ deposition on ECNFs exhibits significantly enhanced galvanostatic charge/discharge cycling at a 1.34 mT of magnetic field even under a high current density of 4 A $g^{-1}$, suggesting that the enhanced magneto-supercapacitive performance is mainly attributed to magnetic susceptibility of the $MnO_2$ in the electrode because of the improvement of the pseudocapacitive behavior at the electrode and the electrode/electrolyte interfaces.

## Conclusion

In summary, after applying 1.34 mT magnetic field, $MnO_2$/ECNFs showed enhanced magneto-capacitance of 141.7 F $g^{-1}$ at the cyclic voltage sweeping rates of 5 mV $s^{-1}$. The capacitance of $MnO_2$/ECNFs was increased by 58.1% at the current density of 0.5 A $g^{-1}$ during the galvanostatic charge/discharge test. Meanwhile, in the presence of 1.34 mT magnetic field, the magneto-supercapacitor presented "low resistance shift" for bulk electrolyte and the $MnO_2$/ECNFs electrode. Longer charge/discharge time of the electrode is observed under magnetic field than that without magnetic field, while did not sacrifice its life cycle stability. The insightful discussion of the potential mechanism suggests that the magneto-supercapacitance enhancement can be primarily attributed to the magnetic susceptibility of $MnO_2$ induced electron spin energy degeneracy for facilitated electron transfer reaction, the magnetohydrodynamic impact on electrolyte transportation and improved cation intercalation/de-intercalation under the mT magnetic field, thus resulting in higher charge density at the electrode/electrolyte interfaces, thicker double layer, and lower internal resistance. This study may pave a way to the development of sustainable metal oxide-based supercapacitors with magneto-capacitance enhancement by applying a low magnetic field.

## References


1. Choi, N. S., Chen, Z., Freunberger, S. A., Ji, X., Sun, Y. K., Amine, K., ... & Bruce, P. G. (2012). Angewandte Chemie International Edition, 51(40), 9994-10024.
2. Miller, J. R., Outlaw, R. A., & Holloway, B. C. (2010). Science, 329(5999), 1637-1639.
3. Itoi, H., Nishihara, H., Kogure, T., & Kyotani, T. (2011). Journal of the American Chemical Society, 133(5), 1165-1167.
4. Yu, G., Hu, L., Vosgueritchian, M., Wang, H., Xie, X., McDonough, J. R., ... & Bao, Z. (2011). Nano letters, 11(7), 2905-2911.
5. Chun, S. E., Evanko, B., Wang, X., Vonlanthen, D., Ji, X., Stucky, G. D., & Boettcher, S. W. (2015). Nature communications, 6.
6. Choi, H. J., Jung, S. M., Seo, J. M., Chang, D. W., Dai, L., & Baek, J. B. (2012). Nano Energy, 1(4), 534-551.
7. Lian, C., Liu, K., Van Aken, K. L., Gogotsi, Y., Wesolowski, D. J., Liu, H. L., ... & Wu, J. Z. (2016). ACS Energy Letters, 1(1), 21-26.
8. Wang, W., Guo, S., Lee, I., Ahmed, K., Zhong, J., Favors, Z., ... & Ozkan, C. S. (2014). Scientific reports, 4.
9. Jiang, Y., Ling, X., Jiao, Z., Li, L., Ma, Q., Wu, M., ... & Zhao, B. (2015). Electrochimica Acta, 153, 246-253.

10. Jiang, Y., Wang, P., Zang, X., Yang, Y., Kozinda, A., & Lin, L. (2013). Nano letters, 13(8), 3524-3530.
11. Kumar, R., Kim, H. J., Park, S., Srivastava, A., & Oh, I. K. (2014). Carbon, 79, 192-202.
12. An, G. H., & Ahn, H. J. (2013). Carbon, 65, 87-96.
13. Kim, C. H., & Kim, B. H. (2015). Journal of Power Sources, 274, 512-520.
14. Kim, B. H., Yang, K. S., & Yang, D. J. (2013). Electrochimica Acta, 109, 859-865.
15. Zhi, M., Xiang, C., Li, J., Li, M., & Wu, N. (2013). Nanoscale, 5(1), 72-88.
16. Yang, P., Chen, Y., Yu, X., Qiang, P., Wang, K., Cai, X., ... & Mai, W. (2014). Nano Energy, 10, 108-116.
17. Zhang, G., & Lou, X. W. D. (2013). Scientific reports, 3.
18. Yu, X., Lu, B., & Xu, Z. (2014). Advanced materials, 26(7), 1044-1051.
19. Peng, L., Peng, X., Liu, B., Wu, C., Xie, Y., & Yu, G. (2013). Nano letters, 13(5), 2151-2157.
20. Liu, Y., Zeng, Z., Wei, J. (2016). Front. Nanosci. Nanotech., 2, 78-85.
21. Huang, Z. M., Zhang, Y. Z., Kotaki, M., & Ramakrishna, S. (2003). Composites science and technology, 63(15), 2223-2253.
22. Zhang, L., Aboagye, A., Kelkar, A., Lai, C., & Fong, H. (2014). Journal of Materials Science, 49(2), 463-480.
23. Tõnurist, K., Jänes, A., Thomberg, T., Kurig, H., & Lust, E. (2009). Journal of The Electrochemical Society, 156(4), A334-A342.

24. Tõnurist, K., Thomberg, T., Jänes, A., Kink, I., & Lust, E. (2012). Electrochemistry Communications, 22, 77-80.
25. Tõnurist, K., Thomberg, T., Jänes, A., Romann, T., Sammelselg, V., & Lust, E. (2013). Journal of Electroanalytical Chemistry, 689, 8-20.
26. Yang, C., Jia, Z., Guan, Z., & Wang, L. (2009). Journal of Power Sources, 189(1), 716-720.
27. Janakiraman, S., Surendran, A., Ghosh, S., Anandhan, S., & Venimadhav, A. (2016). Solid State Ionics, 292, 130-135.
28. Hao, J., Lei, G., Li, Z., Wu, L., Xiao, Q., & Wang, L. (2013). Journal of membrane science, 428, 11-16.
29. Yanilmaz, M., Lu, Y., Zhu, J., & Zhang, X. (2016). Journal of Power Sources, 313, 205-212.
30. Tõnurist, K., Vaas, I., Thomberg, T., Jänes, A., Kurig, H., Romann, T., & Lust, E. (2014). Electrochimica Acta, 119, 72-77.
31. Wu, Y., Bhalla, A., & Guo, R. (2016). Materials Research Express, 3(3), 036102.
32. Bund, A., Koehler, S., Kuehnlein, H. H., & Plieth, W. (2003). Electrochimica Acta, 49(1), 147-152.
33. Zhu, J., Chen, M., Qu, H., Luo, Z., Wu, S., Colorado, H. A., ... & Guo, Z. (2013). Energy & Environmental Science, 6(1), 194-204.
34. Wang, G., Xu, H., Lu, L., & Zhao, H. (2014). Journal of Energy Chemistry, 23(6), 809-815.

35. Wu, Q., Chen, M., Chen, K., Wang, S., Wang, C., & Diao, G. (2016). Journal of Materials Science, 51(3), 1572-1580.
36. Toupin, M., Brousse, T., & Bélanger, D. (2004). Chemistry of Materials, 16(16), 3184-3190.
37. Wang, Y., Song, Y., & Xia, Y. (2016). Chemical Society Reviews, 45(21), 5925-5950.
38. Wang, T., Song, D., Zhao, H., Chen, J., Zhao, C., Chen, L., ... & Xie, E. (2015). Journal of Power Sources, 274, 709-717.
39. Dubal, D. P., Dhawale, D. S., Salunkhe, R. R., & Lokhande, C. D. (2010). Journal of the Electrochemical Society, 157(7), A812-A817.
40. Pang, X. F., & Deng, B. (2008). Physica B: Condensed Matter, 403(19), 3571-3577.
41. Mai, L., Li, H., Zhao, Y., Xu, L., Xu, X., Luo, Y., ... & Zhang, Q. (2013). Scientific reports, 3.
42. Simon, P., & Gogotsi, Y. (2008). Nature materials, 7(11), 845-854.
43. Liu, Y., Dolidze, T. D., Singhal, S., Khoshtariya, D. E., & Wei, J. (2015). The Journal of Physical Chemistry C, 119(27), 14900-14910.
44. Chen, S., Zhu, J., Wu, X., Han, Q., & Wang, X. (2010). ACS nano, 4(5), 2822-2830.
45. Zang, J., & Li, X. (2011). Journal of materials Chemistry, 21(29), 10965-10969.
46. Tian, W., Gao, Q., & Qian, W. (2016). ACS Sustainable Chemistry & Engineering, 5(2), 1297-1305.
47. Zhu, J., Chen, M., Wei, H., Yerra, N., Haldolaarachchige, N., Luo, Z., ... & Guo, Z. (2014). Nano Energy, 6, 180-192.

48. Choi, N. S., Chen, Z., Freunberger, S. A., Ji, X., Sun, Y. K., Amine, K., ... & Bruce, P. G. (2012). Angewandte Chemie International Edition, 51(40), 9994-10024.

49. Eremin, I., & Chubukov, A. V. (2010). Physical Review B, 81(2), 024511.

# CHAPTER V

# OXYGEN REDUCTION REACTION

This chapter has been published as: Zeng, Z., Zhang, W., Liu, Y., Lu, P., & Wei, J. (2017). Uniformly electrodeposited α-$MnO_2$ film on super-aligned electrospun carbon nanofibers for a bifunctional catalyst design in oxygen reduction reaction. Electrochimica Acta, 256, 232-240.

## An Overview

Metal oxide/carbonaceous nanomaterials are promising candidates for the oxygen reduction in energy converting systems. However, inhomogeneous surface coverage allows hydrogen peroxide to escape into the bulk solution due to unstable metal or metal oxide/carbonaceous nanomaterial synthesis, which limits their performance in fuel cells. Here, we show that the above problems can be mitigated through a stable low-current electrodeposition of $MnO_2$ on super-aligned electrospun carbon nanofibers (ECNFs). The key to our approach is coupling a self-designed four steel poles collector for aligned ECNFs and a constant low-current (45 μA) electrodeposition technique for 4 h to form a uniform $Na^+$ induced α-$MnO_2$ film. By using the cyclic voltammetry to proceed the electrocatalytic oxygen reduction reaction (ORR), the bifunctional catalysts show a 3.84-electron pathway due to the rapid decomposition of hydrogen peroxide by the uniform α-$MnO_2$ film and ending with formation of water. This research may enable a practical catalyst with a large number of cycling of oxygen reduction/regeneration to reduce the risk of the fuel cell

degradation and an effective confinement of oxygen and hydrogen peroxide in the catalyst matrix to maximize the energy output of the fuel cell.

## Introduction

A fuel cell has been one of the promising energy devices for generating clean and sustainable energy. Since the oxygen reduction reaction (ORR) is the most important reaction in energy converting systems such as proton exchange membrane (PEM) fuel cells, techniques used in electrocatalytic ORR studies have been widely developed,[1-3] such as steady-state polarization,[4] rotating disk electrode (RDE),[5] rotating ring-disk electrode (RRDE),[6] and cyclic voltammetry.[7] ORR in aqueous solutions undergoes mainly by two pathways: a 2-electron pathway from oxygen to hydrogen peroxide, and a 4-electron pathway from oxygen to water.[3] In order to ensure that the fuel cell generates the maximum power output, a direct 4-electorn pathway is necessary because the 2-electron pathway involved in the cathodic process seriously compromises the energy yield of the fuel cell.[8,9] Moreover, the cell membranes and other supporting materials will be impaired in the presence of an excess hydrogen peroxide due to the peroxide radical formation generated from a disproportionation reaction.[10,11]

In the search of catalysts for limiting the hydrogen peroxide generation or decomposing generated hydrogen peroxide, carbon-based materials (glassy carbon (GC),[11] graphite,[12] active carbon,[13] and carbon nanotubes[14]), Pt catalysts (Pt electrode[15] and Pt alloys[16]), various porous materials,[17-20] and transition metal-based catalyst (cobalt[21] and iron[22]) have been greatly reported. The ORR performance of these metal-carbon catalysts

varies with synthesis conditions, nitrogen type, metal type, and pyrolysis temperature.[23] In terms of number-electron pathway of ORR, 3.45 and 3.70 have been obtained by using the catalysts of hematite nanoparticles supported on carbon nanotubes[24] or GC[8]. Although the confinement of oxygen within the catalysts is effective, inhomogeneous surface coverage allows hydrogen peroxide to escape into the bulk solution, which decreases the decomposition efficiency of generated hydrogen peroxide. Hence, a study to achieve stable synthesis of catalysts may lead to better strategies for achieving a direct 4-electron pathway.

Manganese dioxide ($MnO_2$) has been demonstrated to be one of the most promising catalyst materials for ORR, with a high electrocatalytic activity, ecofriendly properties, and abundant earth reserves.[25,26] $MnO_2$ can exhibit diverse structures and polymorphs with the order of $\delta$-$MnO_2$ < $\beta$-$MnO_2$ < amorphous $MnO_2$ < $\alpha$-$MnO_2$ in ORR catalytic activity.[27,28] Their ORR activity enhancement has been reported by introducing nitrogen-doping, oxygen vacancies, hydrogenation, metal-ion doping.[29-32] More importantly, the catalytic decomposition of hydrogen peroxide by $MnO_2$ with high catalytic efficiency has been examined.[33,34] However, a uniform $MnO_2$ film focusing on stable confinement of hydrogen peroxide for decomposing has not been achieved.

Carbon nanofibers (CNFs) are well known for their inexpensive production, freestanding nature, large porosity, and high conductivity as substrate materials.[35,36] Electrospinning, which uses electric force to draw charged threads of polymer solutions or polymer melts into nanofibers, has become an efficient fiber production method for creating porous electrospun CNFs (ECNFs) with a subsequent carbonization.[37] The nitrogen-doped ECNFs by carbonizing electrospun polyacrylonitrile (PAN) could be an

electrocatalyst for ORR.[38,39] In addition, aligned ECNF structures can be used as scaffolds to uniformly support metal oxide nano-architectures because their alignment can significantly enhance the deposition rate by shortening the distance of electron transport.

We hypothesize that the combination of these two materials ($MnO_2$ and super-aligned ECNFs) in a nanoscale structure will exhibit superior electrocatalytic, electrochemical, and mechanical properties for ORR catalytic activity. In this study, we describe the rational design and fabrication of $MnO_2$/ECNFs by wrapping $MnO_2$ onto super-aligned ECNFs. The nanocomposite of $MnO_2$/ECNFs is well-characterized. The as-prepared $MnO_2$/ECNFs-GC electrocatalytic system (electrodeposition of 4 h) exhibits a 3.84-electron pathway near the theoretical limit with a desirable confinement ability for both oxygen and hydrogen peroxide.

**Experimental**

Super-aligned ECNFs fabrication: the fabrication technique for the super-aligned ECNFs is schematically illustrated in Fig. 5.1a. A facile electrospinning method was used with a self-designed sample collector. Different from a normal cylinder design, four steel poles were welded on a plate in order to collect the ECNFs without any substrates. A 10 wt.% polyacrylonitrile (PAN, Mw = 150,000, ACROS Organics) solution in dimethylformamide (ACROS Organics) was electrospun onto the collector. The applied positive voltage was 18 kV and the distance between the needle tip and the collector was 15 cm. The collector was maintaining at a rate of 2000 revolutions per minute (rpm) during the electrospun to form the super-aligned precursors. The obtained sheets were then put

into a furnace (Oxidation and Annealing Furnace) for stabilization to ensure that the fibers did not melt during pyrolysis. The heating rate was 1 °C/min from room temperature to 280 °C and kept for 6 h. The as-stabilized nanofibers were finally carbonized at 1200 °C for 1 h at a heating rate of 5 °C/min under $N_2$ atmosphere to yield high mechanical strength ECNFs.

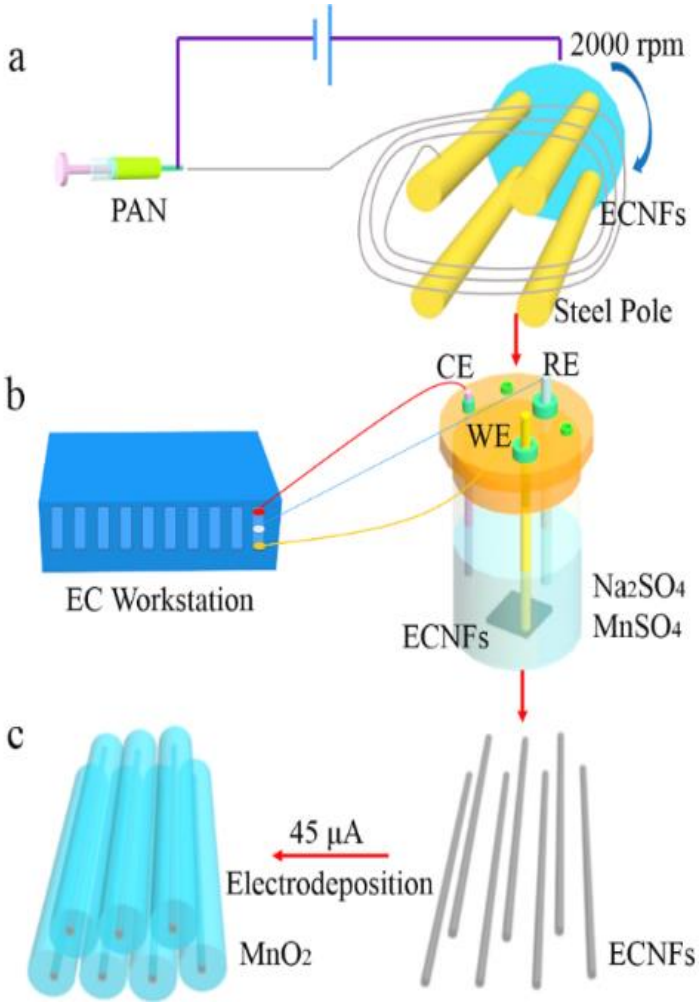


Figure 5.1. Electrodeposition. (a) Illustrations of the electrospinning technique for the super-aligned ECNFs fabrication, (b) uniform electrodeposition of $MnO_2$ on the super-aligned ECNFs using a three-electrode setup with a ECNF mat working electrode, an Ag/AgCl reference electrode, and a platinum counter electrode, and (c) stable $MnO_2$ film formation after a uniform electrodeposition of 4 h.

$MnO_2$ electrodeposition on ECNFs: after the super-aligned ECNFs were prepared, $MnO_2$ was electrodeposited onto 1 $cm^2$ ECNFs with a three-electrode setup using a charging current of 45 μA performed on a bio-logic VMP3 electrochemical workstation

(Fig. 5.1b). Here, a gold electrode taped with ECNFs, a platinum wire, and an Ag/AgCl were used as the working electrode, the counter electrode, and the reference electrode (Fisher Scientific), respectively. To assure that the deposition of $MnO_2$ took place uniformly and firmly at the ECNFs' surfaces (Fig. 5.1c), the ECNFs electrode was prior-treated with 4 M $HNO_3$ (J.T. Baker) solution at 70 °C for 2 h to introduce –OH and –COOH groups to facilitate the deposition. An aqueous precursor solution containing 10 mM $MnSO_4$ (ACROS Organics) and 100 mM $Na_2SO_4$ (ACROS Organics) was used as the supporting electrolyte. After the deposition, the working electrodes were washed with deionized water and then dried at 80 °C for 3 h.

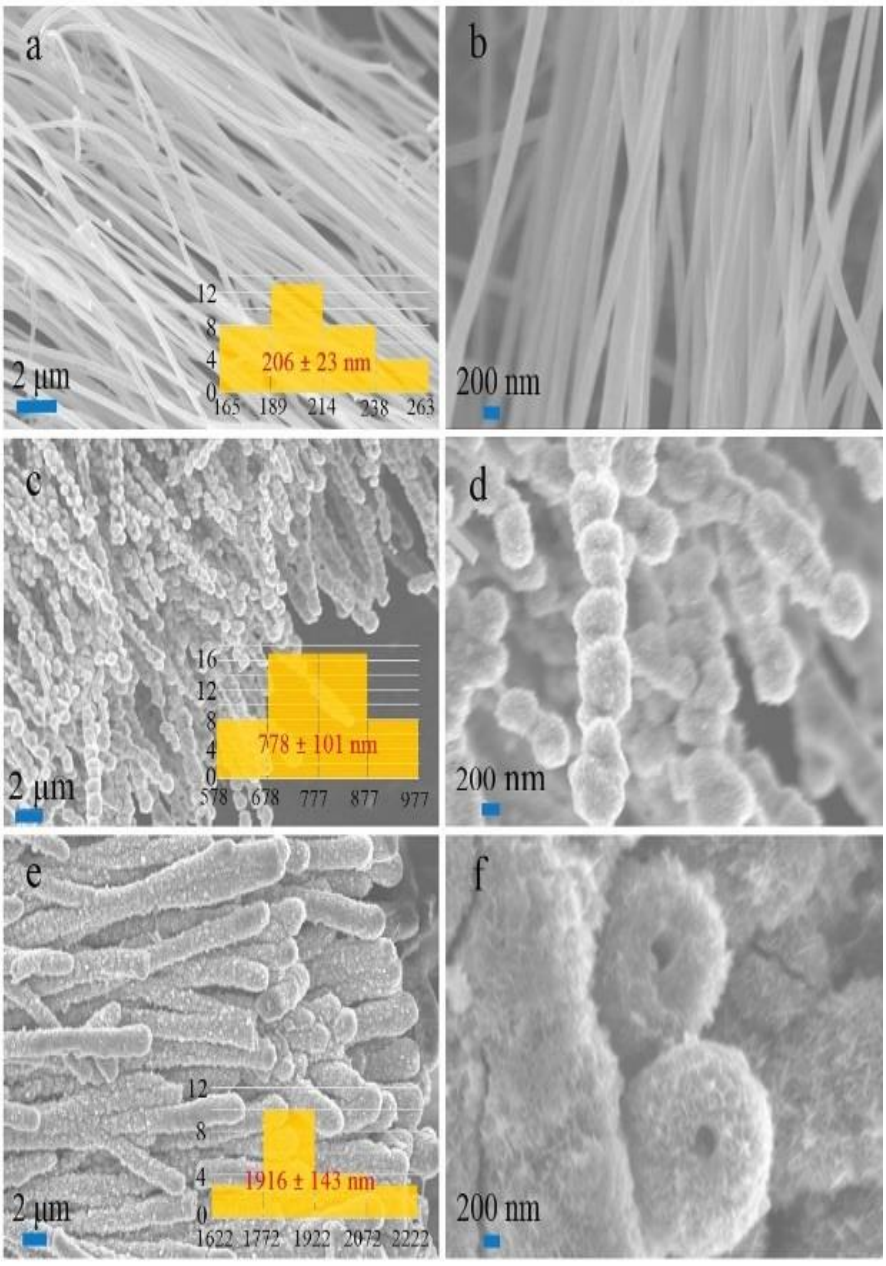


Figure 5.2. SEM Images. Super-aligned ECNFs and $MnO_2$/ECNFs (electrodeposition for 2 h and 4 h) with the histograms of size distribution analysis. Note that b, d and f are enlarged images.

Characterization: field emission scanning electron microscope (FESEM) (Carl Zeiss Auriga-BU FIB FESEM Microscope) was performed to study the morphological properties of super-aligned ECNFs and $MnO_2$/ECNFs. Energy-dispersive X-ray spectroscopy (EDX) (Hitachi S-4800-I FESEM w/Backscattered Detector & EDX) and thermogravimetric analysis (TGA) (SDT Q600) were performed to study the atomic ratio of Mn : O and weight ratio of $MnO_2$ on $MnO_2$/ECNFs. Raman spectroscopy (Horiba XploRA One Raman Confocal Microscope System), Fourier transform infrared spectroscopy (FTIR) (Varian 670), and X-ray photoelectron spectroscopy (XPS, Thermo Fisher ESCALAB 250 Xi), were employed to study the elements components of $MnO_2$/ECNFs. X-ray powder diffraction (XRD) (Agilent Technologies Oxford Germini X-Ray Diffractometer) was employed to study the crystal structures of $MnO_2$/ECNFs.

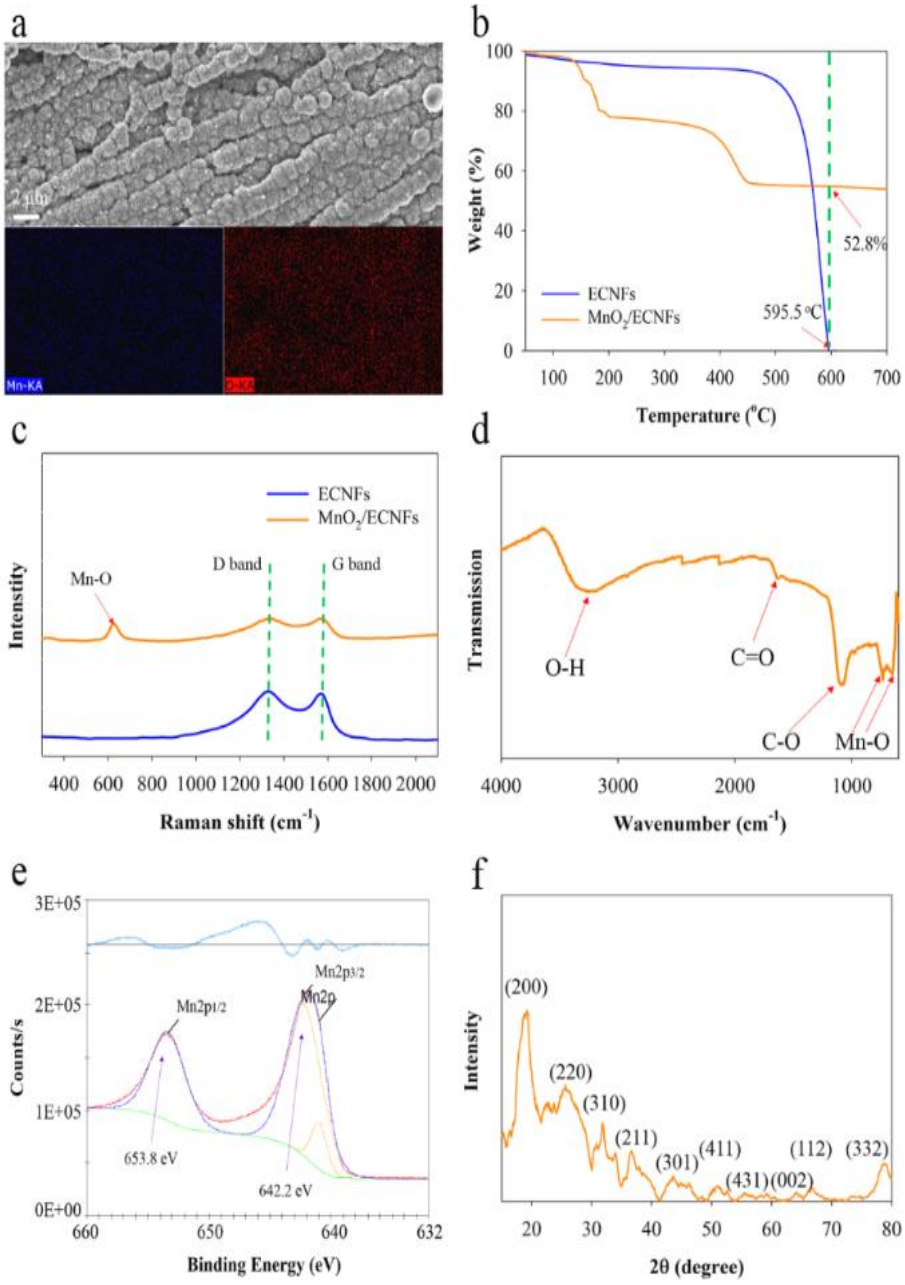


Figure 5.3. Properties. The super-aligned ECNFs and $MnO_2$/ECNFs are characterized using different techniques: a) SEM associated with EDX mapping analysis, b) TGA analysis, c) Raman spectrum, d) FTIR spectrum, e) XPS spectrum, f) XRD analysis.

Electrochemical study: electrochemical performance was performed on a bio-logic VMP3 electrochemical workstation using a three-electrode testing system with a 3 mm diameter GC as the working electrode, a platinum wire as the counter electrode and an Ag/AgCl as the reference electrode (Fisher Scientific) in 20 mM KCl (Sigma-Aldrich) electrolyte solution that was thoroughly degassed with $O_2$ gas. Usually acidic electrolytes are used in platinum or its alloys catalytic systems and give high measured catalytic activity and help to conduct 4-electron ORR process.[40] However, acidic electrolytes are corrosive to fuel cell electrode materials. In addition, biological full cells are operated at physiological pH and $Cl^-$ is one of the most common anions presented in surface water.[8] Hence, in this work the benign neutral chloride solution is chosen on purpose to conduct the catalytic activity of $MnO_2$/ECNFs in ORR process. The super-aligned ECNFs and $MnO_2$/ECNFs were cut as 3 mm diameter wafers and then tapped onto the GC as modified electrodes for the electrochemical analysis of electro-reduction of oxygen. Cyclic voltammetry was then carried out after the modified GC electrode being immersed in a $N_2$ saturated 20 mM KCl solution for 15 min. Cyclic voltammetry was carried out at different scan rates (20, 40, 60, 80, 100, 150, and 200 mV/s) with a potential window between -1.0 V and 0.9 V.

**Results and Discussion**

Characterization: the as-prepared pure ECNFs exhibit super-aligned structure (Fig. 5.2a and 5.2b). It is hypothesized that the alignment of ECNFs can reduce the disordered electron flow, leading to a more uniform electrodeposition process by introducing reaction

sites for nucleation of $MnO_2$ crystallites. $MnO_2$ was electrodeposited onto the ECNFs with a three-electrode setup (Fig. 5.1b). After electrodeposition for 2 h, small balls around the ECNFs present as the "kebab"-like structures. Although the SEM images clearly show surface structures corresponding to these firmly merged balls (Figure 5.2c and 5.2d), the fibers are not fully covered. After electrodeposition for 4 h, the ECNFs with nanofiber diameter of about 206 nm are decorated by a $MnO_2$ film with a thickness of about 1710 nm, making a total diameter of ~1916 nm (Fig. 5.2e and 5.2f). These data corroborate the inference that the ECNFs' alignment promotes the homogenous electron flow and facilitates the uniform $MnO_2$ growth.

The composites by 4 h electrodeposition were further analyzed by different kinds of techniques. EDX spectrum (Fig. 5.3a, Fig. S5.1) shows the surface composition is composed of the elements O and Mn. The atomic ratio of O and Mn is close to 2:1, which implies the formation of $MnO_2$. TGA of ECNFs and $MnO_2$/ECNFs to 700 $^{\circ}$C in air was shown in Fig. 5.3b. Due to the residue solvent evaporation, the ECNFs sample shows a weight loss before 425.0 $^{\circ}$C. And then the ECNFs sample decomposes until 595.5 $^{\circ}$C. Unlike ECNFs, the $MnO_2$/ECNFs still achieve about 52.8% after 595.5 $^{\circ}$C, indicating the weight fraction of $MnO_2$ on the $MnO_2$/ECNFs sample is about 52.8%. The success of $MnO_2$ deposition was further confirmed with Raman spectra and FTIR spectra. At Raman shift of 1325 $cm^{-1}$ and 1569 $cm^{-1}$, the ECNFs sample shows D-band and G-band, respectively. While, for the $MnO_2$/ECNFs sample, Mn-O presents at the Raman shift of 624 $cm^{-1}$ (Fig. 5.3c).[41] Correspondingly, ν(Mn-O) presents at the wavenumber of 643 $cm^{-1}$ and 727 $cm^{-1}$ according to the FTIR spectra (Fig. 5.3d). And IR transitions at 1176, 1647, and 3263 $cm^{-}$

[1] are assigned to ν(C-O), ν(C=O), and ν(O-H), respectively.[42,43] The chemical composition of the $MnO_2$/ECNFs sample was also investigated by the XPS. The high resolution Mn 2p spectra for $MnO_2$/ECNFs is presented in Fig. 5.3e. Two strong peaks at 642.2 and 653.8 eV can be clearly seen,[44] corresponding to the Mn $2p^{3/2}$ and Mn $2p^{1/2}$ spin–orbit peaks of $MnO_2$, respectively.[45] Furthermore, the crystal structures of the as-prepared $MnO_2$/ECNFs were also recorded by XRD (Fig. 5.3f), the patterns of which can be fully indexed to α-$MnO_2$ (JCPDS No. 44-0141).[46]

Herein, the excellent electrodeposition of $MnO_2$ originates from the stable structure of ECNFs, which contributes to a uniform $Mn^{2+}$ flux. The electrochemical reaction occurs according to:[47]

$$Mn^{2+} + 2H_2O \rightarrow MnO_2 + 4H^+ + 2e^- \quad (5\text{-}1)$$

It is known that $MnO_2$ has different main structural motifs due to edge- or corner-sharing $MnO_6$ octahedra in different connectivity schemes, resulting in different tunnels extending in a direction parallel to the unit cell.[28,48] In this study, the cations ($Na^+$) were introduced during the synthesis process, but the 1×1 tunnels (with a size of 0.189 nm) are generally too small for $Na^+$ to stabilize the structure, consequently resulting in the formation of α-$MnO_2$ due to structurally constructed from the double chains of edge-sharing $MnO_6$ octahedra which are linked at the corners to form 2×2 (with a size of 0.460 nm) and 1×1 tunnel structures.[28,48] The crystal structure is confirmed by the XRD analysis of $MnO_2$/ECNFs by electrodeposition for 2 h (Fig. S5-2) and 4 h (Fig. 5.3f). Meanwhile,

these cations inside 2×2 tunnels of α-$MnO_2$ increase the electronic conductivity of the $MnO_2$/ECNFs system, which indirectly enhance the electrodeposition of α-$MnO_2$.[49]

Catalytic properties: the ORR activity was firstly conducted by studying the cyclic voltammetric responses of a bare GC electrode as Fig. 5.4 shows. The cathodic peak resulted from the electrochemical reduction of oxygen and the magnitude of the cathodic peaks increases (Fig. 5.4a) with increasing of the voltage scan rates. In addition, the peak current, $i_p$ (A), is measured as a function of the square root of the voltage scan rate ($v$ (V/s)), which is found to exhibit a liner dependence (Fig. 5.4b). According to the electrochemical models, the dependence of the peak current position on the square root of the voltage scan rate for the bare GC electrode without modification can be firstly used to characterize the concentration of oxygen in the bulk solution ($C$, mol/mL) through Randles-Sevcik equation:[50]

$$|slope| = \left(2.99\times10^5\right) n^{3/2}\alpha^{1/2} A C D_0^{1/2} \qquad (5\text{-}2)$$

where $n$ is the number of electrons exchanged during the electrochemical process, $\alpha$ is the transfer coefficient (reported value of 0.26),[51] $A$ is the active surface area of the bare GC electrode (0.071 $cm^2$), $D_0$ is the diffusion coefficient (reported value of $1.95\times10^{-5}$ $cm^2/s$).[52] Since the reduction of oxygen to hydrogen peroxide is known at the bare GC electrode, the number of electrons exchanged is 2.[53] When the above constants are applied for absolute value of the slope obtained from Fig. 5.4b, the oxygen concentration of $3.11\times10^{-7}$ mol/mL is extracted.

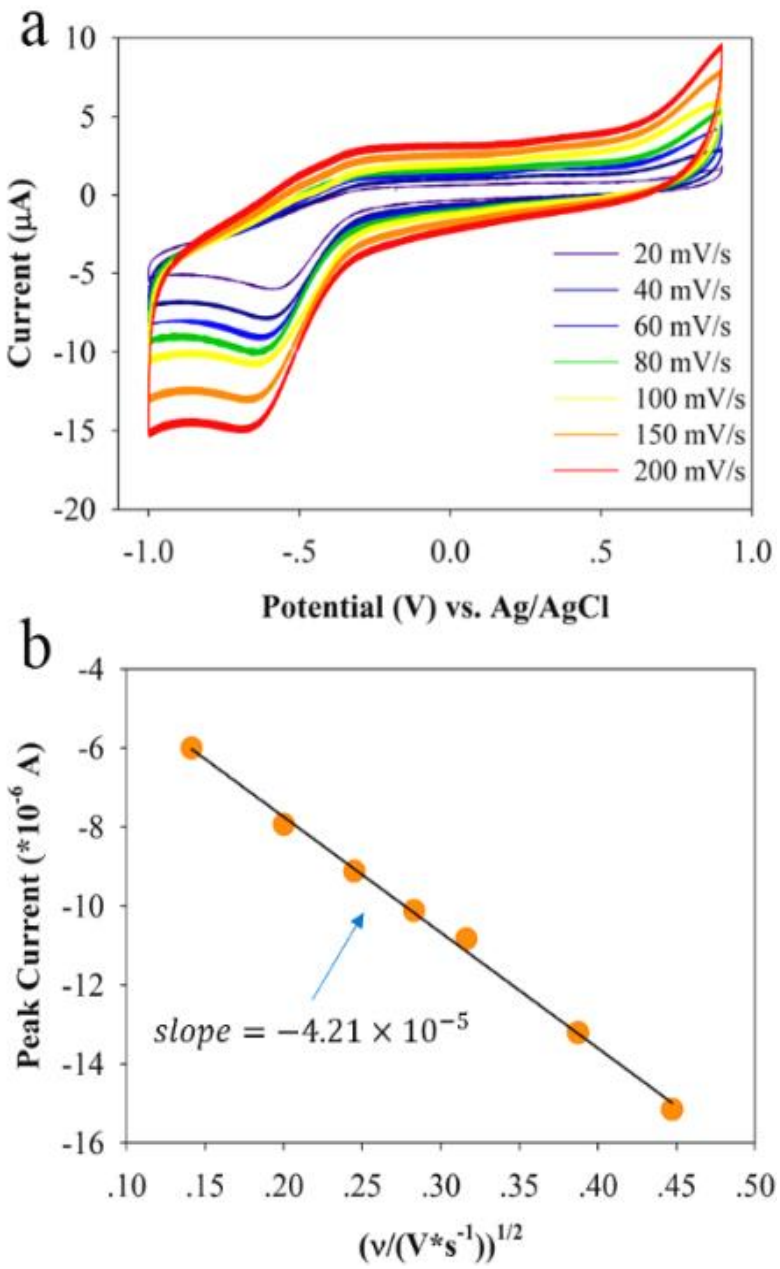


Figure 5.4. Cyclic Voltammograms of A Bare Glassy Carbon Electrode. (a) in $O_2$ saturated 20 mM KCl electrolyte solution at different scan rates. (b) The linear dependence of the peak current on the square root of the voltage scan rate for the $O_2$ concentration calculation.

Next the cyclic voltammetric responses of the ECNFs modified electrode and $MnO_2$/ECNFs (2 h and 4 h) modified electrode were examined by varying the scan rates from 20 mV/s to 200 mV/s, which also show an increase in the cathodic peak current with respect to the scan rate as Fig. 5.5a and 5.5b show. In comparison, there is a marked enhancement in the ORR of the electrode modified with $MnO_2$/ECNFs (4 h). Note that the anodic peak presented at 0.32 V is attributed to the oxidation reactions between the Mn(IV)/Mn(III) complexes.[54] As mentioned above, eq. (5-2) is also used to calculate the number of electrons in the overall electrochemical processes for electrodes modified with super-aligned ECNFs and $MnO_2$/ECNFs. The peak currents are directly proportional to the square roots of scan rates for both modified electrodes with a slope of $-8.01\times10^{-5}$ (ECNFs modified electrode) and $-1.59\times10^{-4}$ ($MnO_2$/ECNFs (4 h) modified electrode), respectively (Fig. 5.5c). Moreover, the slope of a plot of $\log(i_p)$ versus potential (Fig. 5.5d) and the following equation is used to determine the transfer coefficient:[55]

$$Slope = \frac{-\alpha F}{2.3RT} \tag{5-3}$$

where $R$ is the gas constant, $F$ is the Faraday's constant, and $T$ is the temperature. The transfer coefficient is obtained to be 0.65 (ECNFs modified electrode) and 0.52 ($MnO_2$/ECNFs (4 h) modified electrode), respectively. By using eq. (5-2), this value can then be coupled with the active surface area, the diffusion coefficient of oxygen, and the concentration of oxygen to extract the number of electrons exchanged as 2.26 (ECNFs modified electrode) and 3.84 ($MnO_2$/ECNFs (4 h) modified electrode), respectively. Meanwhile, in comparison, with a transfer coefficient of 0.58 (Fig. 5.5d) and a slope of -

$1.39\times10^{-4}$ (Fig. 5.5c), the number of electrons exchanged is obtained to be 3.37 for the $MnO_2$/ECNFs (2 h) modified electrode, since the oxygen and hydrogen peroxide are not effectively confined within the imperfectly fiber-covered $MnO_2$/ECNFs-GC system. As expected, the voltammetric curve of an ECNFs modified electrode exceeds a 2-electron transfer ORR through an energetically favored association to assist the adsorption and reduction of oxygen molecules, which is characteristics of the activity of ECNFs.[38,39] However, for the $MnO_2$/ECNFs modified electrode, considering that the hydrogen peroxide molecule generated from the electrochemical reduction of oxygen to be decomposed repeatedly at the surface of a uniform $MnO_2$ film, a 4-electron pathway presents contributed with a cycle of oxygen decomposition/regeneration.

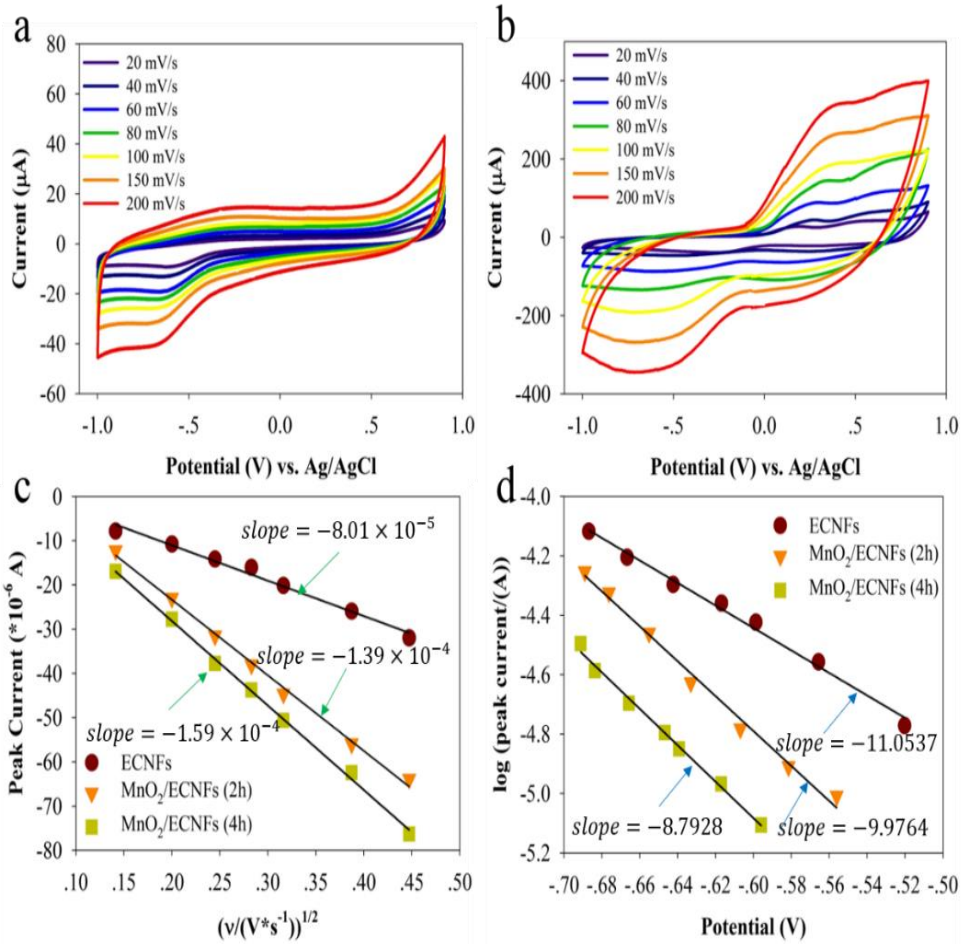


Figure 5.5. Cyclic Voltammograms of The Electrode Modified. With super-aligned ECNFs (a) and $MnO_2$/ECNFs (4 h) (b) in $O_2$ saturated 20 mM KCl electrolyte solution at different scan rates. (c) The linear dependence of the peak current on the square root of the scan rate for the number of electrons exchanged calculation. (d) The linear dependence of the log of the peak current on the potential for the transfer coefficient calculation.

Since the catalytic decomposition of hydrogen peroxide typically follows the first order kinetics,[56] to support our hypothesis of hydrogen peroxide decomposition at the surface of a uniform $MnO_2$ film (4 h), the cyclic voltammogram of a $MnO_2$/ECNFs modified electrode was studied in an $N_2$ saturated 20 mM KCl electrolyte solution with 1

mM hydrogen peroxide at different scan rates (Fig. 5.6a). Since no measureable reduction peak shows for an ECNFs modified electrode in an $N_2$ saturated 20 mM KCl electrolyte solution with 1 mM hydrogen peroxide (Fig. S5.3), a marked increase in the voltammetric performance of the $MnO_2$/ECNFs modified electrode is resulted from the electrochemical decomposition of hydrogen peroxide successfully taking place at the electrode surface, which is reasonable agreement with the results reported for the catalytic decomposition of hydrogen peroxide by using hematite,[57] cobalt,[58] and iron.[59] Furthermore, in the same way, slope of the plot of $\log(i_p)$ versus potential (Fig. 5.6b inserted) and eq. (5-3) were used to determine the transfer coefficient of 0.09. When the constants of active surface area (0.071 $cm^2$), diffusion coefficient of hydrogen peroxide (reported value of $1.0\times10^{-5}$ $cm^2/s$)[60] and concentration of hydrogen peroxide ($1.0\times10^{-6}$ mol/mL) are applied for the slope obtained from the $MnO_2$/ECNFs modified electrode (Fig. 5.6b), a n value of 1.91 is extracted, which highly supports that the hydrogen peroxide molecules generated from the electrochemical reduction of oxygen are decomposed by the uniform $MnO_2$ film. The hydrogen peroxide decomposition by the uniform α-$MnO_2$ film can be ascribed to two reasons: one is the open crystal structure of α-$MnO_2$ with 2×2 tunnels providing favorable surface coordination,[61] such as the higher Miller index (211) and (112) surfaces are expressed in the XRD results; and the other is the low oxygen vacancy formation energy providing a favorable thermodynamic pathway, such as 1.09 eV for (211) and 0.07 eV for (112).[62]

To compare the rate of the hydrogen peroxide generation by ECNFs modified electrodes ($O_2$-ECNFs) with the hydrogen peroxide decomposition by $MnO_2$/ECNFs modified electrode ($H_2O_2$-$MnO_2$), the electron transfer kinetics should be taken into

account. The Gileadi method based upon the determination of critical scan rate ($v_c$) was further used to evaluate the heterogeneous electron transfer rate constant ($k^0$). When the experimental results from $O_2$-ECNFs and $H_2O_2$-$MnO_2$ are applied for this analysis, the critical scan rate can be found from the intersection of two lines as Fig. 5.7 shows. Then the following equation was used to calculate the $k^0$ (cm/s).[63]

$$\log\left(k^0\right) = -0.48\alpha + 0.52 + \log\left[\frac{nF\alpha v_c D_0}{2.303RT}\right]^{1/2} \quad (5\text{-}4)$$

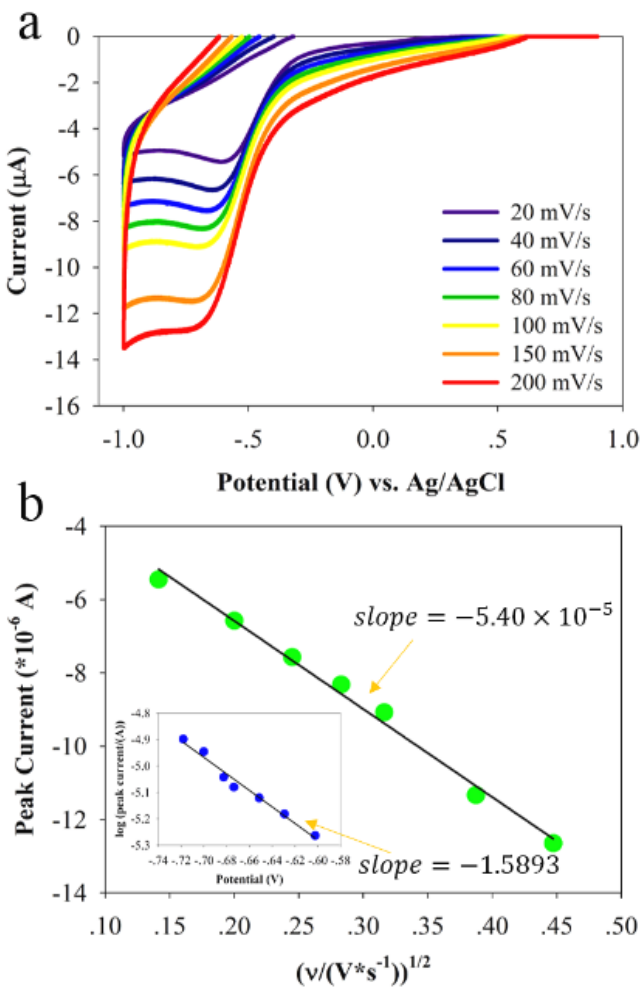


Figure 5.6. Cyclic Voltammograms of The $H_2O_2$ Reduction Reaction. At the electrode modified with $MnO_2$/ECNFs (4 h) in $N_2$ saturated 20 mM KCl electrolyte solution with 1 mM $H_2O_2$ at different scan rates (a). (b) The linear dependence of the peak current on the square root of the scan rate for the number of electrons exchanged calculation, inserted with the linear dependence of the log of the peak current on the potential for the transfer coefficient calculation.

By using this method, associated with the transfer coefficient, number of electron transfer, and diffusion coefficient obtained above, the value of heterogeneous electron

transfer rate constant for $O_2$-ECNFs and $H_2O_2$-$MnO_2$ is calculated to be $1.30\times10^{-2}$ cm/s and $1.37\times10^{-2}$ cm/s, respectively, indicating the rate of hydrogen peroxide decomposition by $MnO_2$/ECNFs modified electrode is faster than the electrochemical generation process by ECNFs modified electrodes, which maybe partly ascribed to the presence of $K^+$ inside the 2×2 tunnels of the α-$MnO_2$ enhancing the electrocatalytical performance of the catalyst.[49]

4-electron pathway mechanism: from the catalytic properties, a 4-electron pathway mechanism was further proposed as Fig. 5.8 shows. When the oxygen molecule has been adsorbed onto the $MnO_2$/ECNF-GC electrode surfaces, the redox between $MnO_2$ species assists the charge transfer involved in oxygen reduction, and the first step undergoes a 2-electron pathway forming hydrogen peroxide (eq. (5-5)).[64]

$$O_{2ads} + 2H^+ + 2e^- \rightarrow H_2O_2 \qquad (5\text{-}5)$$

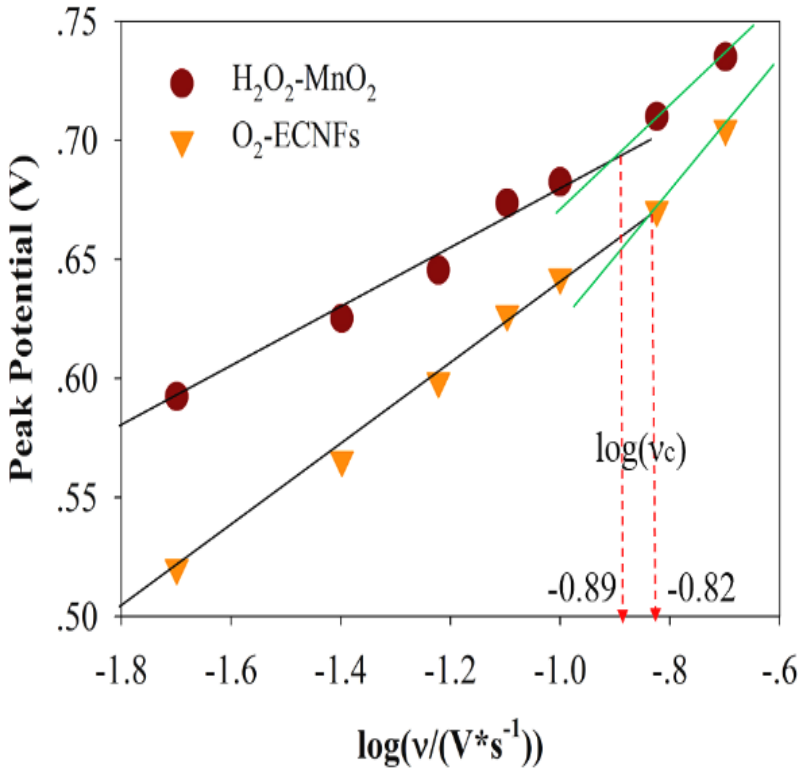


Figure 5.7. Critical Scan Rate Determination. Plots of peak potential versus log of scan rate under the conditions of $H_2O_2$-$MnO_2$ and $O_2$-ECNFs.

The electrochemically generated hydrogen peroxide can then be decomposed to water via a disproportionation reaction before it escapes into the bulk solution by a uniform α-$MnO_2$ film (eq. (5-6)),[65] though an electrochemical decomposition to $OH^-$ may occur.[64]

$$2H_2O_2 \xrightarrow{\alpha\text{-}MnO_2} O_2 + 2H_2O \qquad (5\text{-}6)$$

The rate of hydrogen peroxide decomposition by α-$MnO_2$/ECNFs modified electrode is faster than the electrochemical generation process by ECNFs modified electrode, and the presence of $K^+$ inside the 2×2 channels of the α-$MnO_2$ has a strong beneficial effect on the electrochemical performance of the catalyst,[64] which improves the

efficiency of the ORR process proved by our results shown above. A half of the oxygen concentration shown in eq. (5-6) is electrochemically regenerated after each cycle, which reduces the risk of the fuel cell degradation for practical uses.[8]

As a result, Eq. (5-5) and eq. (5-6) occurring in series give the α-$MnO_2$/ECNF-GC catalytic system as much efficiency as a 4-electron pathway:

$$O_2 + 4H^+ + 4e^- \rightarrow 2H_2O \tag{5-7}$$

Considering that a cycle of decomposition/regeneration of a half of the oxygen concentration at the $MnO_2$/ECNF-GC electrode, the contribution for the electron pathway from the bifunctional catalyst can be divided into two parts, i.e. the first 2-electron transfer oxygen reduction to hydrogen peroxide at the GC-$MnO_2$ interfaces, and following hydrogen peroxide decomposition at the α-$MnO_2$ surfaces. Fig. 5.8 shows the proposed reactions where *i* is the number of cycles regarding the reduction of oxygen and regeneration of oxygen with respect to the oxygen and hydrogen peroxide confinement ability. The total number electron pathway can be expressed:

$$N = 2\sum_{i=0}^{\infty}\left(\frac{1}{2}\right)_{GC-MnO_2} + 2\sum_{i=0}^{\infty}\left(\frac{1}{2}\right)_{MnO_2} \tag{5-8}$$

where *N* is the number-electron pathway, sigma notation is the contribution from different parts, and *i* is the number of cycles regarding the reduction of oxygen and regeneration of oxygen with respect to the oxygen and hydrogen peroxide confinement ability in the aligned $MnO_2$/ECNFs structures. As the result analysis provided above, the number of

electrons exchanged is obtained to be 3.37 (*i* is estimated to be 3) for the 2-hour electrodeposited $MnO_2$/ECNF electrode ($MnO_2$ ununiformly covered at ECNFs), because the oxygen and hydrogen peroxide are not completely reduced within the $MnO_2$/ECNFs-GC system due to the insufficient catalytic activity and confinement (number of cycling). Whereas at 4-hour deposited $MnO_2$/ECNFs, the number of electrons exchanged is achieved to be 3.84, suggesting a large cycle number (namely good confinement, *i* is estimated to be 5) and excellent catalytic activity are obtained from the uniform electrodeposition of α-$MnO_2$ on ECNFs.

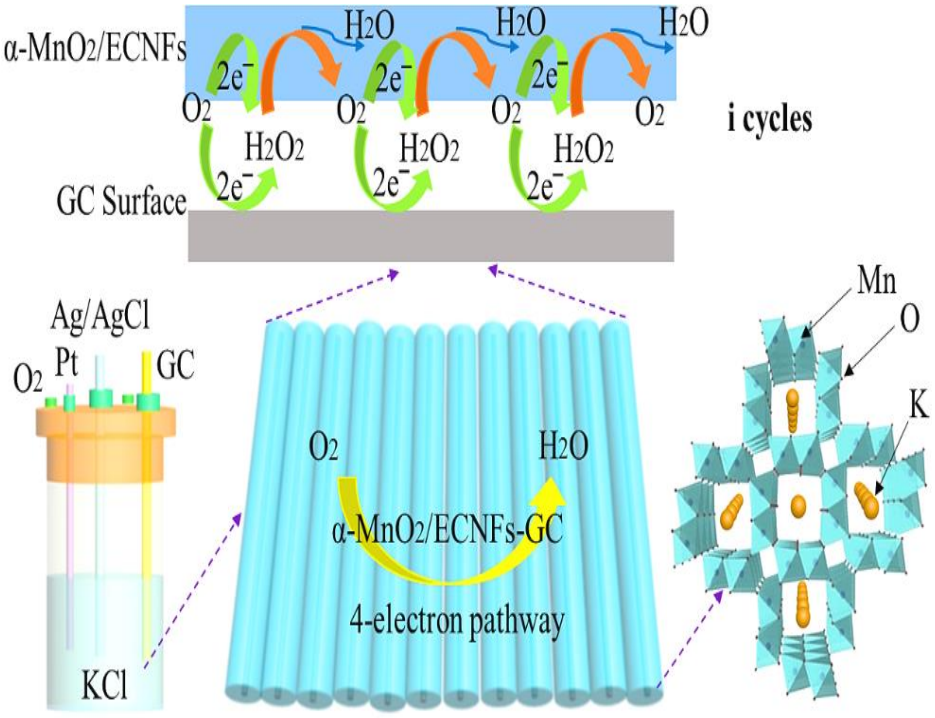


Figure 5.8. Illustration of The 4-electron Pathway Mechanism. The bifunctional catalyst α-$MnO_2$/ECNFs-GC electrode.

**Conclusion**

This work demonstrates a new strategy for uniformly electrodepositing α-$MnO_2$ film on aligned ECNFs and the α-$MnO_2$ film was well characterized. In contrast to earlier studies with an inhomogeneous surface coverage, the reported α-$MnO_2$ film with a 4 h-45 μA electrodeposition was homogenous with a thickness of 1710 nm. From the electrocatalytic performance studies, the bifunctional catalyst system of α-$MnO_2$/ECNFs-GC displayed a 3.84-electron pathway through the rapid decomposition of hydrogen peroxide at the α-$MnO_2$ surfaces. The analysis of electron transfer kinetics suggested a faster hydrogen peroxide decomposition than its generation from reduction of oxygen, and a two-step four-electron pathway cycling mechanism was proposed to give an insightful

understanding of the electrocatalytic ORR at the bifunctional catalyst system. These findings represent significant improvement in stable metal oxide/carbonaceous nanomaterial-based oxygen reduction catalysts.

## References


1. Gasteiger, H. A., Kocha, S. S., Sompalli, B., & Wagner, F. T. (2005). Activity benchmarks and requirements for Pt, Pt-alloy, and non-Pt oxygen reduction catalysts for PEMFCs. Applied Catalysis B: Environmental, 56(1), 9-35.
2. Wang, B. (2005). Recent development of non-platinum catalysts for oxygen reduction reaction. Journal of Power Sources, 152, 1-15.
3. Sahin, N. E., Napporn, T. W., Dubau, L., Kadirgan, F., Léger, J. M., & Kokoh, K. B. (2017). Temperature-dependence of oxygen reduction activity on Pt/C and PtCr/C electrocatalysts synthesized from microwave-heated diethylene glycol method. Applied Catalysis B: Environmental, 203, 72-84.
4. Song, C., Tang, Y., Zhang, J. L., Zhang, J., Wang, H., Shen, J., ... & Kozak, P. (2007). PEM fuel cell reaction kinetics in the temperature range of 23–120 C. Electrochimica Acta, 52(7), 2552-2561.
5. Lüsi, M., Erikson, H., Sarapuu, A., Tammeveski, K., Solla-Gullón, J., & Feliu, J. M. (2016). Oxygen reduction reaction on carbon-supported palladium nanocubes in alkaline media. Electrochemistry Communications, 64, 9-13.
6. Bocchetta, P., Sánchez, C. R., Taurino, A., & Bozzini, B. (2016). Accurate Assessment of the Oxygen Reduction Electrocatalytic Activity of Mn/Polypyrrole Nanocomposites Based on Rotating Disk Electrode Measurements, Complemented with Multitechnique Structural Characterizations. Journal of analytical methods in chemistry, 2016.

7. Baker, R., Wilkinson, D. P., & Zhang, J. (2008). Electrocatalytic activity and stability of substituted iron phthalocyanines towards oxygen reduction evaluated at different temperatures. Electrochimica Acta, 53(23), 6906-6919.
8. Shimizu, K., Sepunaru, L., & Compton, R. G. (2016). Innovative catalyst design for the oxygen reduction reaction for fuel cells. Chemical Science, 7(5), 3364-3369.
9. Sun, H., Zhang, G., Guo, L. J., & Liu, H. (2006). A novel technique for measuring current distributions in PEM fuel cells. Journal of Power Sources, 158(1), 326-332.
10. Ghassemzadeh, L., Kreuer, K. D., Maier, J., & Müller, K. (2010). Chemical degradation of Nafion membranes under mimic fuel cell conditions as investigated by solid-state NMR spectroscopy. The Journal of Physical Chemistry C, 114(34), 14635-14645.
11. Zhang, S., Yuan, X. Z., Hin, J. N. C., Wang, H., Friedrich, K. A., & Schulze, M. (2009). A review of platinum-based catalyst layer degradation in proton exchange membrane fuel cells. Journal of Power Sources, 194(2), 588-600.
12. Freguia, S., Rabaey, K., Yuan, Z., & Keller, J. (2007). Non-catalyzed cathodic oxygen reduction at graphite granules in microbial fuel cells. Electrochimica Acta, 53(2), 598-603.
13. Guo, D., Shibuya, R., Akiba, C., Saji, S., Kondo, T., & Nakamura, J. (2016). Active sites of nitrogen-doped carbon materials for oxygen reduction reaction clarified using model catalysts. Science, 351(6271), 361-365.

14. Gong, K., Du, F., Xia, Z., Durstock, M., & Dai, L. (2009). Nitrogen-doped carbon nanotube arrays with high electrocatalytic activity for oxygen reduction. science, 323(5915), 760-764.
15. Marković, N. M., & Ross, P. N. (2002). Surface science studies of model fuel cell electrocatalysts. Surface Science Reports, 45(4), 117-229.
16. Stassi, A., D'urso, C., Baglio, V., Di Blasi, A., Antonucci, V., Arico, A. S., ... & Triaca, W. E. (2006). Electrocatalytic behaviour for oxygen reduction reaction of small nanostructured crystalline bimetallic Pt–M supported catalysts. Journal of applied electrochemistry, 36(10), 1143-1149.
17. Jiang, B., Li, C., Malgras, V., Imura, M., Tominaka, S., & Yamauchi, Y. (2016). Mesoporous Pt nanospheres with designed pore surface as highly active electrocatalyst. Chemical Science, 7(2), 1575-1581.
18. Li, C., Sato, T., & Yamauchi, Y. (2013). Electrochemical Synthesis of One‐Dimensional Mesoporous Pt Nanorods Using the Assembly of Surfactant Micelles in Confined Space. Angewandte Chemie International Edition, 52(31), 8050-8053.
19. Chaikittisilp, W., Torad, N. L., Li, C., Imura, M., Suzuki, N., Ishihara, S., ... & Yamauchi, Y. (2014). Synthesis of Nanoporous Carbon–Cobalt‐Oxide Hybrid Electrocatalysts by Thermal Conversion of Metal–Organic Frameworks. Chemistry-A European Journal, 20(15), 4217-4221.
20. Tang, J., Liu, J., Li, C., Li, Y., Tade, M. O., Dai, S., & Yamauchi, Y. (2015). Synthesis of nitrogen‐doped mesoporous carbon spheres with extra‐large pores through

assembly of diblock copolymer micelles. Angewandte Chemie International Edition, 54(2), 588-593.

21. Mao, S., Wen, Z., Huang, T., Hou, Y., & Chen, J. (2014). High-performance bi-functional electrocatalysts of 3D crumpled graphene–cobalt oxide nanohybrids for oxygen reduction and evolution reactions. Energy & Environmental Science, 7(2), 609-616.
22. Deng, D., Yu, L., Chen, X., Wang, G., Jin, L., Pan, X., ... & Bao, X. (2013). Iron encapsulated within pod‐like carbon nanotubes for oxygen reduction reaction. Angewandte Chemie International Edition, 52(1), 371-375.
23. Chen, G., Sunarso, J., Zhu, Y., Yu, J., Zhong, Y., Zhou, W., & Shao, Z. (2016). Highly Active Carbon/α‐MnO2 Hybrid Oxygen Reduction Reaction Electrocatalysts. ChemElectroChem, 3(11), 1760-1767.
24. Sun, M., Dong, Y., Zhang, G., Qu, J., & Li, J. (2014). α-Fe 2 O 3 spherical nanocrystals supported on CNTs as efficient non-noble electrocatalysts for the oxygen reduction reaction. Journal of Materials Chemistry A, 2(33), 13635-13640.
25. Gorlin, Y., & Jaramillo, T. F. (2010). A bifunctional nonprecious metal catalyst for oxygen reduction and water oxidation. Journal of the American Chemical Society, 132(39), 13612-13614.

26. Meng, Y., Song, W., Huang, H., Ren, Z., Chen, S. Y., & Suib, S. L. (2014). Structure–property relationship of bifunctional MnO2 nanostructures: highly efficient, ultra-stable electrochemical water oxidation and oxygen reduction reaction catalysts identified in alkaline media. Journal of the American Chemical Society, 136(32), 11452-11464.
27. Lee, J. S., Park, G. S., Lee, H. I., Kim, S. T., Cao, R., Liu, M., & Cho, J. (2011). Ketjenblack carbon supported amorphous manganese oxides nanowires as highly efficient electrocatalyst for oxygen reduction reaction in alkaline solutions. Nano letters, 11(12), 5362-5366.
28. Xiao, W., Wang, D., & Lou, X. W. (2009). Shape-controlled synthesis of MnO2 nanostructures with enhanced electrocatalytic activity for oxygen reduction. The Journal of Physical Chemistry C, 114(3), 1694-1700.
29. Lambert, T. N., Davis, D. J., Lu, W., Limmer, S. J., Kotula, P. G., Thuli, A., ... & Tour, J. M. (2012). Graphene–Ni–α-MnO 2 and–Cu–α-MnO 2 nanowire blends as highly active non-precious metal catalysts for the oxygen reduction reaction. Chemical Communications, 48(64), 7931-7933.
30. Cheng, F., Zhang, T., Zhang, Y., Du, J., Han, X., & Chen, J. (2013). Enhancing electrocatalytic oxygen reduction on MnO2 with vacancies. Angewandte Chemie International Edition, 52(9), 2474-2477.
31. Zhang, T., Cheng, F., Du, J., Hu, Y., & Chen, J. (2015). Efficiently enhancing oxygen reduction electrocatalytic activity of MnO2 using facile hydrogenation. Advanced Energy Materials, 5(1).

32. Duan, J., Zheng, Y., Chen, S., Tang, Y., Jaroniec, M., & Qiao, S. (2013). Mesoporous hybrid material composed of Mn 3 O 4 nanoparticles on nitrogen-doped graphene for highly efficient oxygen reduction reaction. Chemical Communications, 49(70), 7705-7707.
33. Choe, J. E., You, J. M., Yun, M., Lee, K., Ahmed, M. S., Üstundağ, Z., & Jeon, S. (2015). Manganese dioxide/reduced graphene oxide with poly (3, 4-ethylenedioxythiophene) for improved electrocatalytic oxygen reduction reaction. Journal of nanoscience and nanotechnology, 15(8), 5684-5690.
34. Roche, I., & Scott, K. (2009). Carbon-supported manganese oxide nanoparticles as electrocatalysts for oxygen reduction reaction (orr) in neutral solution. Journal of Applied Electrochemistry, 39(2), 197-204.
35. Liu, D., Zhang, X., Sun, Z., & You, T. (2013). Free-standing nitrogen-doped carbon nanofiber films as highly efficient electrocatalysts for oxygen reduction. Nanoscale, 5(20), 9528-9531.
36. Zeng, Z., Lu, P., Li, C., Mai, L., Li, Z., & Zhang, Y. (2012). Removal of NO by carbonaceous materials at room temperature: A review. Catalysis Science & Technology, 2(11), 2188-2199.
37. Zeng, Z., Liu, Y., Zhang, W., Chevva, H., & Wei, J. (2017). Improved supercapacitor performance of MnO 2-electrospun carbon nanofibers electrodes by mT magnetic field. Journal of Power Sources, 358, 22-28.

38. Shin, D., Jeong, B., Mun, B. S., Jeon, H., Shin, H. J., Baik, J., & Lee, J. (2013). On the origin of electrocatalytic oxygen reduction reaction on electrospun nitrogen–carbon species. The Journal of Physical Chemistry C, 117(22), 11619-11624.
39. Qiu, Y., Yu, J., Shi, T., Zhou, X., Bai, X., & Huang, J. Y. (2011). Nitrogen-doped ultrathin carbon nanofibers derived from electrospinning: Large-scale production, unique structure, and application as electrocatalysts for oxygen reduction. Journal of Power Sources, 196(23), 9862-9867.
40. Banham, D., Ye, S., Pei, K., Ozaki, J. I., Kishimoto, T., & Imashiro, Y. (2015). A review of the stability and durability of non-precious metal catalysts for the oxygen reduction reaction in proton exchange membrane fuel cells. Journal of Power Sources, 285, 334-348.
41. Li, X., Liu, J., Zhao, Y., Zhang, H., Du, F., Lin, C., ... & Sun, Y. (2015). Significance of surface trivalent manganese in the electrocatalytic activity of water oxidation in undoped and doped MnO2 nanowires. ChemCatChem, 7(12), 1848-1856.
42. Dubal, D. P., Dhawale, D. S., Salunkhe, R. R., & Lokhande, C. D. (2010). Conversion of chemically prepared interlocked cubelike Mn3O4 to birnessite MnO2 using electrochemical cycling. Journal of the Electrochemical Society, 157(7), A812-A817.
43. Zeng, Z., Zhang, W., Arvapalli, D. M., Bloom, B., Sheardy, A., Mabe, T., ... & Wei, J. (2017). A fluorescence-electrochemical study of carbon nanodots (CNDs) in bio-and photoelectronic applications and energy gap investigation. Physical Chemistry Chemical Physics, 19(30), 20101-20109.

44. Lee, S. W., Kim, J., Chen, S., Hammond, P. T., & Shao-Horn, Y. (2010). Carbon nanotube/manganese oxide ultrathin film electrodes for electrochemical capacitors. ACS nano, 4(7), 3889-3896.
45. Yuan, L., Lu, X. H., Xiao, X., Zhai, T., Dai, J., Zhang, F., ... & Hu, C. (2011). Flexible solid-state supercapacitors based on carbon nanoparticles/MnO2 nanorods hybrid structure. ACS nano, 6(1), 656-661.
46. Yu, P., Zhang, X., Wang, D., Wang, L., & Ma, Y. (2008). Shape-controlled synthesis of 3D hierarchical MnO2 nanostructures for electrochemical supercapacitors. Crystal Growth and Design, 9(1), 528-533.
47. Devaraj, S., & Munichandraiah, N. (2005). High capacitance of electrodeposited MnO2 by the effect of a surface-active agent. Electrochemical and Solid-State Letters, 8(7), A373-A377.
48. Gao, T., Fjellvåg, H., & Norby, P. (2009). A comparison study on Raman scattering properties of α-and β-MnO 2. Analytica chimica acta, 648(2), 235-239.
49. Yuan, Y., Zhan, C., He, K., Chen, H., Yao, W., Sharifi-Asl, S., ... & Wang, H. (2016). The influence of large cations on the electrochemical properties of tunnel-structured metal oxides. Nature communications, 7, 13374.
50. Muhammad, H., Tahiri, I. A., Muhammad, M., Masood, Z., Versiani, M. A., Khaliq, O., ... & Hanif, M. (2016). A comprehensive heterogeneous electron transfer rate constant evaluation of dissolved oxygen in DMSO at glassy carbon electrode measured by different electrochemical methods. Journal of Electroanalytical Chemistry, 775, 157-162.

51. Nissim, R., & Compton, R. G. (2014). Nonenzymatic Electrochemical Superoxide Sensor. ChemElectroChem, 1(4), 763-771.
52. Ju, L. K., & Ho, C. S. (1985). Measuring oxygen diffusion coefficients with polarographic oxygen electrodes: I. electrolyte solutions. Biotechnology and bioengineering, 27(10), 1495-1499.
53. Sundberg, K. M., Smyrl, W. H., Atanasoska, L., & Atanasoski, R. (1989). Surface modification and oxygen reduction on glassy carbon in chloride media. Journal of The Electrochemical Society, 136(2), 434-439.
54. Toupin, M., Brousse, T., & Bélanger, D. (2004). Charge storage mechanism of MnO2 electrode used in aqueous electrochemical capacitor. Chemistry of Materials, 16(16), 3184-3190.
55. Wang, J. (2006). Analytical electrochemistry. John Wiley & Sons.
56. Huang, H. H., Lu, M. C., & Chen, J. N. (2001). Catalytic decomposition of hydrogen peroxide and 2-chlorophenol with iron oxides. Water Research, 35(9), 2291-2299.
57. Sun, M., Zhang, G., Liu, H., Liu, Y., & Li, J. (2015). α-and γ-Fe2O3 nanoparticle/nitrogen doped carbon nanotube catalysts for high-performance oxygen reduction reaction. Science China Materials, 58(9), 683-692.
58. Su, Y., Zhu, Y., Yang, X., Shen, J., Lu, J., Zhang, X., ... & Li, C. (2013). A highly efficient catalyst toward oxygen reduction reaction in neutral media for microbial fuel cells. Industrial & Engineering Chemistry Research, 52(18), 6076-6082.

59. Chen, P., Zhou, T., Xing, L., Xu, K., Tong, Y., Xie, H., ... & Xie, Y. (2017). Atomically Dispersed Iron–Nitrogen Species as Electrocatalysts for Bifunctional Oxygen Evolution and Reduction Reactions. Angewandte Chemie International Edition, 56(2), 610-614.

60. Katsounaros, I., Schneider, W. B., Meier, J. C., Benedikt, U., Biedermann, P. U., Auer, A. A., & Mayrhofer, K. J. (2012). Hydrogen peroxide electrochemistry on platinum: towards understanding the oxygen reduction reaction mechanism. Physical Chemistry Chemical Physics, 14(20), 7384-7391.

61. Giordani, V., Freunberger, S. A., Bruce, P. G., Tarascon, J. M., & Larcher, D. (2010). H2O2 decomposition reaction as selecting tool for catalysts in Li–O2 cells. Electrochemical and solid-state letters, 13(12), A180-A183.

62. Tompsett, D. A., Parker, S. C., & Islam, M. S. (2014). Surface properties of α-MnO 2: relevance to catalytic and supercapacitor behaviour. Journal of Materials Chemistry A, 2(37), 15509-15518.

63. U. Eisner, E. Gileadi, Anodic oxidation of hydrazine and its derivatives: Part I. The oxidation of hydrazine on gold electrodes in acid solutions, Journal of Electroanalytical Chemistry and Interfacial Electrochemistry, 28 (1970) 81-92.

64. Cheng, F., Su, Y., Liang, J., Tao, Z., & Chen, J. (2009). MnO2-based nanostructures as catalysts for electrochemical oxygen reduction in alkaline media. Chemistry of Materials, 22(3), 898-905.

65. Mao, L., Zhang, D., Sotomura, T., Nakatsu, K., Koshiba, N., & Ohsaka, T. (2003). Mechanistic study of the reduction of oxygen in air electrode with manganese oxides as electrocatalysts. Electrochimica Acta, 48(8), 1015-1021.

# CHAPTER VI

# MAGNETIC FIELD ENHANCED 4-ELECTRON PATHWAY

This chapter has been submitted as: Zeng, Z., Zhang, T., Liu, Y., Zhang, W., Yin, Z., & Wei, J. Magnetic Field Enhanced 4-electron Pathway by the Well-aligned $Co_3O_4$/ECNFs Design in the Oxygen Reduction Reaction. ChemSusChem.

## An Overview

The uniform catalytic center and 4-electron pathway are the most challenging issues in the oxygen reduction reaction (ORR) of energy converting systems. Here, we report a constant low-current (50 μA) electrodeposition technique to develop a uniform $Co_3O_4$ film formation at the well-aligned electrospun carbon nanofibers (ECNFs) with a time-dependent growth mechanism. Furthermore, this work also reports a new finding of milli-Tesla (mT) magnetic field induced enhancement of electron exchange number of the ORR at the electrode modified with $Co_3O_4$/ECNFs, the magnetic susceptibility of the unpaired electrons in $Co_3O_4$ improving the electron transfer rate, which shows a 3.92-electron pathway in the presence of a 1.32 mT magnetic field. This research presents a potential revolution of traditional electrocatalysts by simply applying an external magnetic field on metal oxides as replacement of noble metals to reduce the risk of the fuel cell degradation and maximize its energy output.

## Introduction

Since a fuel cell has been one of the promising energy devices for generating clean and sustainable energy, the desirable electrocatalytic oxygen reduction reaction (ORR) research has been widely studied by steady-state polarization, rotating disk electrode (RDE), rotating ring-disk electrode (RRDE), and cyclic voltammetry.[1-3] The electrocatalysts including carbon-based materials (glassy carbon (GC), graphite, active carbon, and carbon nanotubes),[4-7] Pt catalysts (Pt nanoparticles and Pt alloys),[8-10] and transition metal-based catalyst (cobalt and iron) have been reported for conducting the ORR,[11-14] The ORR performance of which varies with synthesis conditions, nitrogen doping, metal type, and pyrolysis temperature.[15-18] In order to ensure that the fuel cell generates the maximum power output, a 4-electorn pathway (from oxygen to water) is necessary because the 2-electron pathway (from oxygen to hydrogen peroxide) involved in the cathodic process seriously compromises the energy yield of the fuel cell. Moreover, the cell membranes and other supporting materials will be impaired in the presence of an excess hydrogen peroxide due to the peroxide radical formation generated from a disproportionation reaction.[19-20]

In the search of 4-electron pathway by effectively decomposing generated hydrogen peroxide, the catalysts of hematite nanoparticles supported on carbon nanotubes[21] or GC[22] were reported. Although the confinement of oxygen within the catalysts is effective, inhomogeneous surface coverage allows hydrogen peroxide to escape into the bulk solution, which decreases the decomposition efficiency of generated hydrogen peroxide. Furthermore, considering that the electrochemically generated hydrogen

peroxide can then be decomposed to water before it escapes into the bulk solution, the rate of hydrogen peroxide decomposition by catalysts should be faster than the electrochemical generation process. In previous studies, it was found that an external magnetic field over a material with the magnetic susceptibility could facilitate the electron transfer rate due to the effects of Lorentz force acting on moving charge/ions, charge density gradient modulation, electron state excitation and oscillatory magnetization.[23-24] Herein, we propose a new strategy to combine stable synthesis of a paramagnetic electrocatalyst and its electron transfer rate enhancement for maximizing a 4-electron pathway in the ORR.

A metal oxide, $Co_3O_4$, which is of mixed valences $Co^{2+}$ and $Co^{3+}$, has been demonstrated to be one of the most promising electrocatalytic materials for ORR with high electrocatalytic activities and ecofriendly properties.[25-26] Its ORR activity enhancement has been reported by introducing nitrogen-doping, oxygen vacancies, hydrogenation, and metal-ion doping,[27-28] which requires additional material replacement or structural modification. $Co_3O_4$ owns magnetic susceptibility due to spins/spin-orbit coupling-induced magnetic moment.[29-30] However, little is known about how the external magnetic field affects the electrochemical performance of the electrocatalyst. In addition, the nitrogen-doped electrospun carbon nanofibers (ECNFs) by carbonizing electrospun polyacrylonitrile (PAN) could be an electrocatalyst for ORR.[31-32] Aligned ECNF structures may be used as scaffolds to uniformly support metal oxide nano-architectures because their alignment could potentially enhance the deposition rate by shortening the distance of electron transport. We hypothesize that the combination of these two materials ($Co_3O_4$ and well-aligned ECNFs) in a nanoscale structure may exhibit superior electrocatalytic,

electrochemical, and mechanical properties for the ORR catalytic activity. In this study, we describe the rational design and fabrication of $Co_3O_4$/ECNFs by wrapping $Co_3O_4$ onto the well-aligned ECNFs. Furthermore, we explore the magnetic effect on the number-electron pathway of ORR at the electrodes modified with $Co_3O_4$/ECNFs (5 h electrodeposition) in a comparison of presence/absence of milli-Tesla (mT) to sub-mT magnetic fields derived by Helmholtz coils.

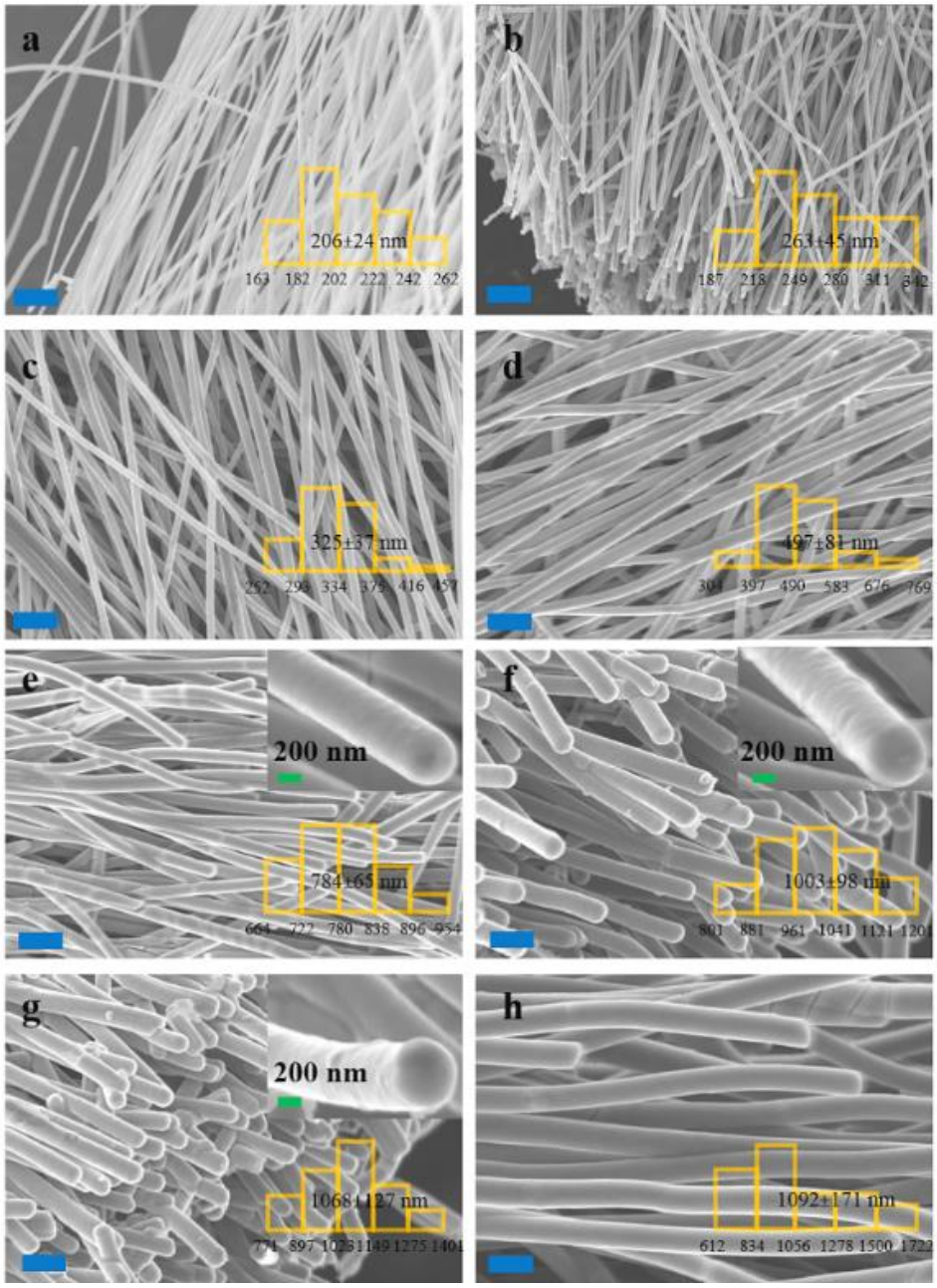


Figure 6.1. SEM Images. Well-aligned ECNFs (a) and $Co_3O_4$/ECNFs for different electrodeposition times from 1 h to 8 h (b-h) with the histograms (y-axis is the frequency) of size distribution analysis. All of the blue scale bars are 2 μm.

**Results and Discussion**

$Co_3O_4$ growth characterization and mechanism: the fabrication technique for the well-aligned ECNFs is based on a facile electrospinning method with a self-designed sample collector (Fig. S6.1). Different from a normal cylinder design, four steel poles were welded on a plate in order to collect the ECNFs without any substrates. After carbonization, the as-prepared pure ECNFs exhibit well-aligned structure (Figure 6.1a). A nitric acid pre-treatment, which introduces hydroxyl and carboxyl groups, was used to make the ECNFs surface more hydrophilic and to introduce reaction sites for nucleation of $Co_3O_4$ crystallites. A constant low current (50 μA) was applied for the electrodeposition by an electrochemical workstation for various times ranging from 1 h to 8 h under an $N_2$ atmosphere with an aqueous precursor solution containing 20 mM $CoSO_4$ and 100 mM $Na_2SO_4$. The composites' structure and morphology were characterized by scanning electron microscopy (SEM) (Figure 6.1b-h). When the electrodeposition starts, thin films form on the functionalized sites distributed on the fibers (Figure 6.1b,c). As the electrodeposition continues, the films begin to grow denser/thicker and the fibers are fully covered (Figure 6.1d,e). After electrodeposition for 5 h, the ECNFs with nanofiber diameter of about 206 nm are decorated by a $Co_3O_4$ film with a thickness of about 797 nm, making a total diameter of ~1003 nm (Figure 6.1f). $Co_3O_4$ electrodeposition beyond a 5 h time does not show obvious thickness increase with the applied constant current (Figure 6.1g,h). We can assume a feature of self-cessation that probably arises from the increased resistance of the $Co_3O_4$ layers.

The chemical composition of the composites under different electrodeposition times from 1 h to 8 h was analyzed by energy dispersive X-ray (EDX) spectroscopy, Raman spectroscopy, and Fourier transform infrared spectroscopy (FTIR). The EDX spectrum (Figure 6.2a) show that the surface composition of the electrochemically deposited electrodes is composed of the elements C, O and Co. The peaks observed at 567 and 668 $cm^{-1}$ in the FTIR spectrum correspond to the stretching vibrations of metal oxide for tetrahedrally coordinated $Co^{2+}$ and octahedrally coordinated $Co^{3+}$ (Figure 6.2b),[33] which is further verified at the Raman shift of 510 and 682 $cm^{-1}$ (Figure 6.2c).[34] To investigate the $Co_3O_4$ crystal structure, the as-prepared $Co_3O_4$/ECNFs materials were examined by X-ray diffraction (XRD) as Figure 6.2d shows (JCPDS No. 009-0418).[35]

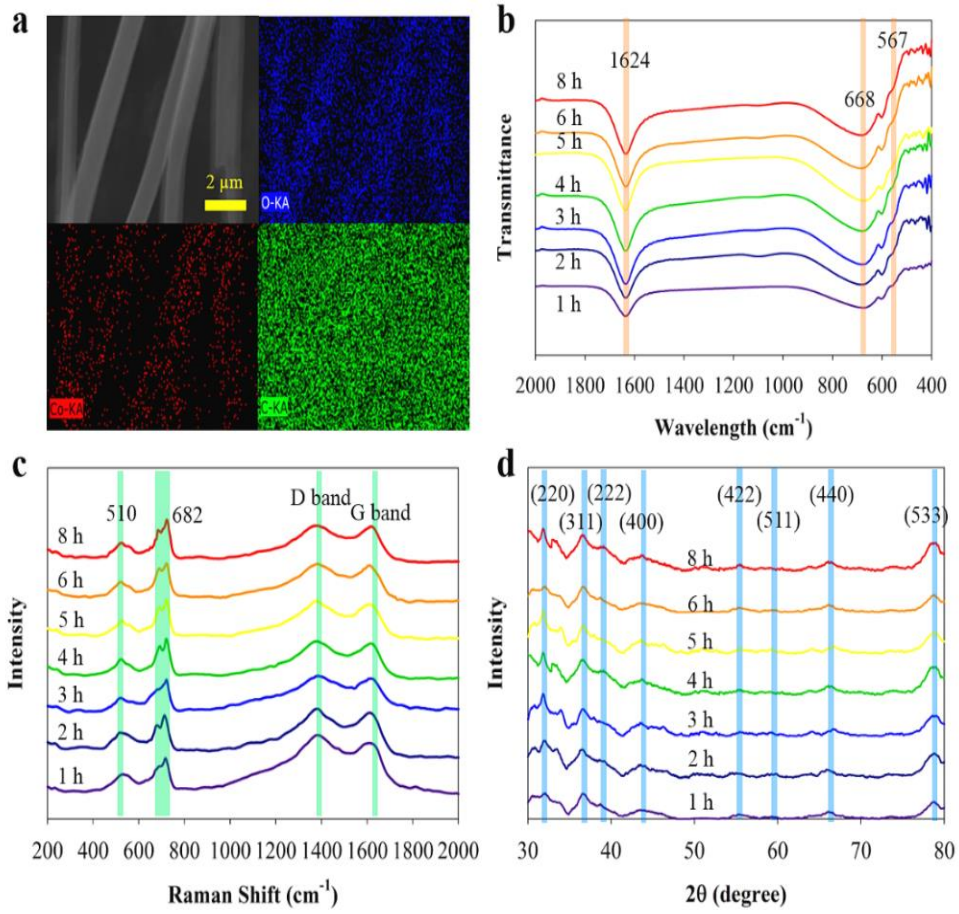


Figure 6.2. Properties. (a) SEM associated with EDX mapping analysis of the $Co_3O_4$/ECNFs under electrodeposition of 5 h. FTIR spectrum (b), Raman spectrum (c), and XRD analysis (d) of the $Co_3O_4$/ECNFs under different electrodeposition times.

The comprehensive electrodeposition of $Co_3O_4$ originates from the stable structure of ECNFs, which contributes to a uniform $Co^{2+}$ flux (Figure 6.3a). The electrochemical reaction occurs according to:

$$3Co^{2+} + 4H_2O \rightarrow Co_3O_4 + 8H^+ + 2e^- \quad (6\text{-}1)$$

In this growth process, the thickness of the $Co_3O_4$ film can be controlled by the electrodeposition time (Figure 6.3b). We can write a kinetic equation to describe the $Co_3O_4$ growth for the electrodeposition as:[36]

$$dh/dt = c\left(j - j_d\right) \tag{6-2}$$

where $dh/dt$ is the rate of $Co_3O_4$ film formation and growth, $c$ is the coulombic efficiency ($cm^3\ C^{-1}$), $j$ is the measured current density, and $j_d$ is the required current density to prevent dissolution. Here, the measured current density has a nonlinear exponential relationship with the applied voltage ($V$):[36]

$$j = A\ \exp(BV/h) \tag{6-3}$$

where $A$ and $B$ are characteristic constants of the system. According to the nonlinear relationship between current density and field strength, the saturation of film growth is thus given by the equation:

$$h_{\max} = BV/\left(\ln\left(j_d/A\right)\right) \tag{6-4}$$

According to the measured results, the $Co_3O_4$ thickness ($h$) versus deposition time ($t$) could be best fit as (Figure 6.3b):

$$h = h_{\max}/(1+10^{(\tau_{0.5}-t)})\left(t>0\right) \tag{6-5}$$

with a $h_{max}$ of about 851 nm and a half-life time constant ($\tau_{0.5}$) of about 3.59 h. The time-dependent growth analysis suggests a three-step kinetics mechanism for the

electrodeposition (Figure 6.3c). The first step involves thin film formation on a boundary layer distributed along the fibers (0-2 h). The second step involves dense film formation and the ECNFs are fully covered (2-5 h). The last step involves the cessation of $Co_3O_4$ growth and establishment of a uniform, dense film with a self-limiting thickness (>5 h).

$Co_3O_4$ thickness dependent electron-pathway: the ORR activity was firstly conducted by studying the cyclic voltammetric responses of a bare GC electrode as Fig. S6.2 shows. The cathodic peak resulted from the electrochemical reduction of oxygen and the magnitude of the cathodic peaks increases with increasing of the voltage scan rates. The slope of a plot of log (peak current) versus peak potential ($E_p$ (V)) (Fig. S6.3) and the following equation are used to determine the transfer coefficient ($\alpha$):[37]

$$Slope1 = \frac{-\alpha F}{2.3RT} \tag{6-6}$$

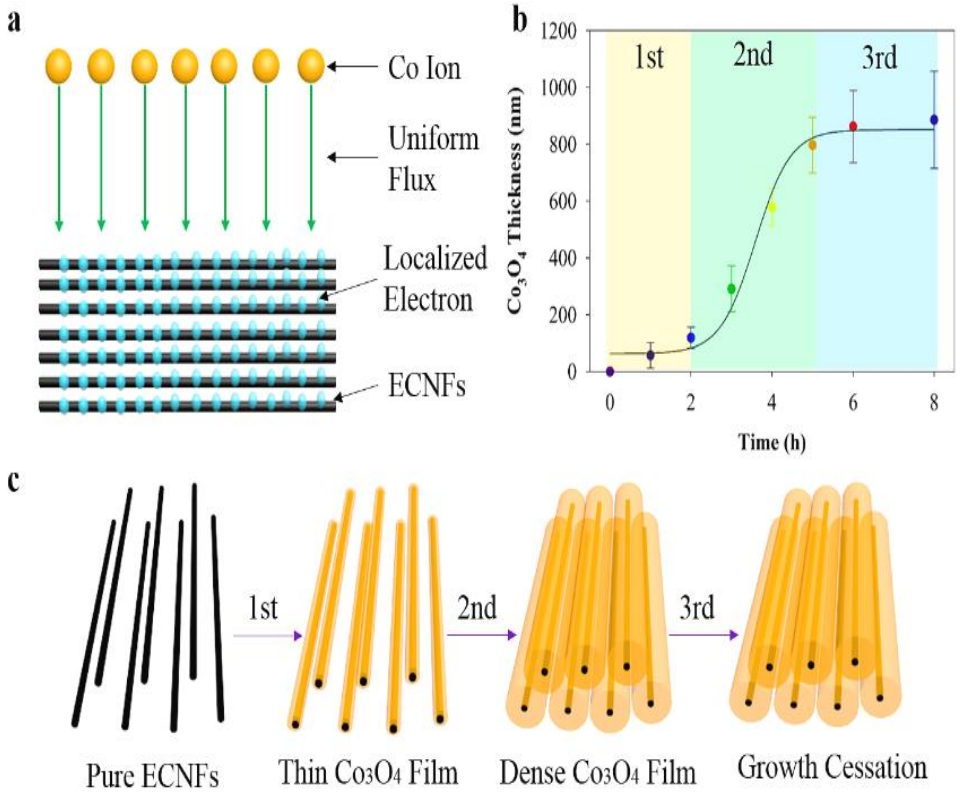


Figure 6-3. Growth Mechanism. (a) The schematic description of $Co^{2+}$ uniform flux. (b) Time-dependent $Co_3O_4$ growth with data analysis. (c) Mechanistic view.

Where $R$ is the gas constant, $F$ is the Faraday's constant, and $T$ is the temperature. In addition, the peak current, $i_p$ (A), is measured as a function of the square root of the voltage scan rate ($v$ (V $s^{-1}$)) (Fig. S6.4), which can be firstly used to characterize the concentration of oxygen in the bulk solution ($C$, mol $mL^{-1}$) through Randles-Sevcik equation:[38,39]

$$|Slope2| = \left(2.99\times10^{5}\right) n^{3/2} \alpha^{1/2} A C D_0^{1/2} \qquad (6\text{-}7)$$

where $n$ is the exchanged electron number during the electrochemical process ($n$=2 at a bare GC electrode), $A$ is the active surface area of the bare GC electrode (0.071 $cm^2$), $D_0$ is the diffusion coefficient ($1.95\times10^{-5}$ $cm^2$ $s^{-1}$).[11] When the above constants are applied for absolute value of the slope 2 obtained from Fig. S6.4, the oxygen concentration of $2.50\times10^{-7}$ mol $mL^{-1}$ is extracted. Note that change the range of potential scan rate does not affect the results of slope 1 and slope 2 (Fig. S6.5).

Next the cyclic voltammetric responses of the ORR at the $Co_3O_4$/ECNFs (1-8 h electrodeposition) modified electrode were examined to get the number of exchanged electrons. The cyclic voltammograms show an increase in the cathodic peak current (at about -0.50 V) with respect to the scan rate (Fig. S6.6). The cathodic peak presented at about 0.60 V is attributed to the reduction reactions between the Co(III)/Co(II) complexes.[40] As mentioned above, equ. (6-6) and (6-7) (Fig. S6.7,8 as an example) are also used to calculate the number of exchanged electrons in the overall electrochemical processes for electrodes modified with $Co_3O_4$/ECNFs (1-8 h electrodeposition). The number of exchanged electrons is obtained to be 3.09, 3.27, 3.36, 3.43, 3.48, 3.46, 3.42 for the $Co_3O_4$/ECNFs modified electrodes under the electrodeposition time of 1 h, 2 h, 3 h, 4 h, 5 h, 6 h, 8 h, respectively (Table S6.1). The cyclic voltammogram of a $Co_3O_4$/ECNFs modified electrode was also studied in an $N_2$ saturated 20 mM KCl electrolyte solution with 1 mM hydrogen peroxide at different scan rates (Fig. S6.9). Since no measurable reduction peak shows for both a bare GC electrode and an ECNFs modified GC electrode in an $N_2$ saturated 20 mM KCl electrolyte solution with 1 mM hydrogen peroxide (Fig. S6.10), a marked increase in the voltammetric performance of the $Co_3O_4$/ECNFs modified

electrode is resulted from the electrochemical decomposition of hydrogen peroxide successfully taking place at the electrode surface. Since the hydrogen peroxide molecule generated from the electrochemical reduction of oxygen is decomposed repeatedly at the surface of a uniform $Co_3O_4$ film, a 4-electron pathway presents contributed with a cycle of oxygen decomposition and regeneration, which is agreement with the results reported for the ORR by the hematite nanoparticles modified electrodes.[22]

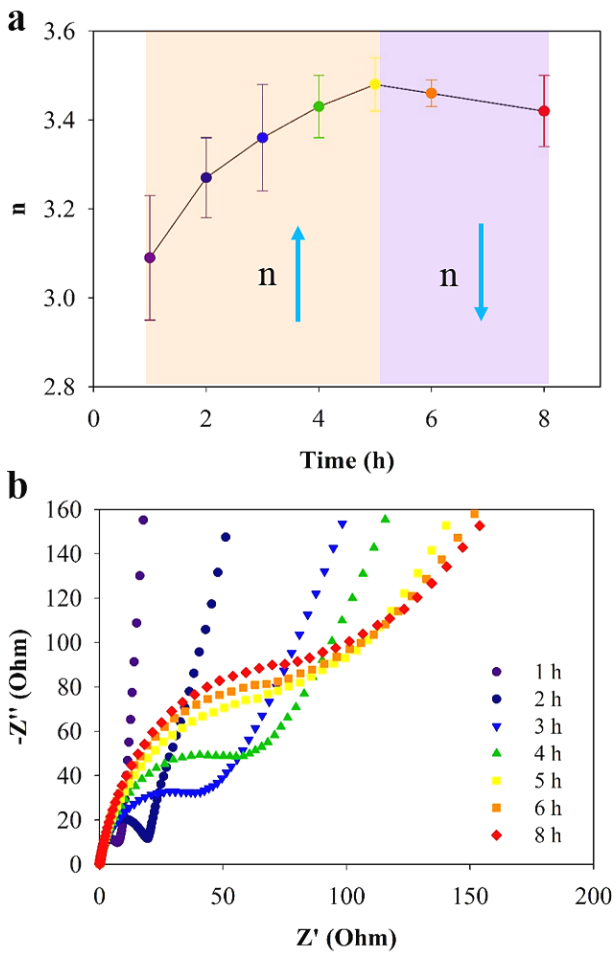


Figure 6.4. Time-dependent Exchanged Electron Number. (a) *n* of the ORR at the electrode modified with $Co_3O_4$/ECNFs in $O_2$ saturated 20 mM KCl electrolyte solution. (b) Electrochemical impedance spectroscopy at frequencies from 100 kHz to 0.1 kHz.

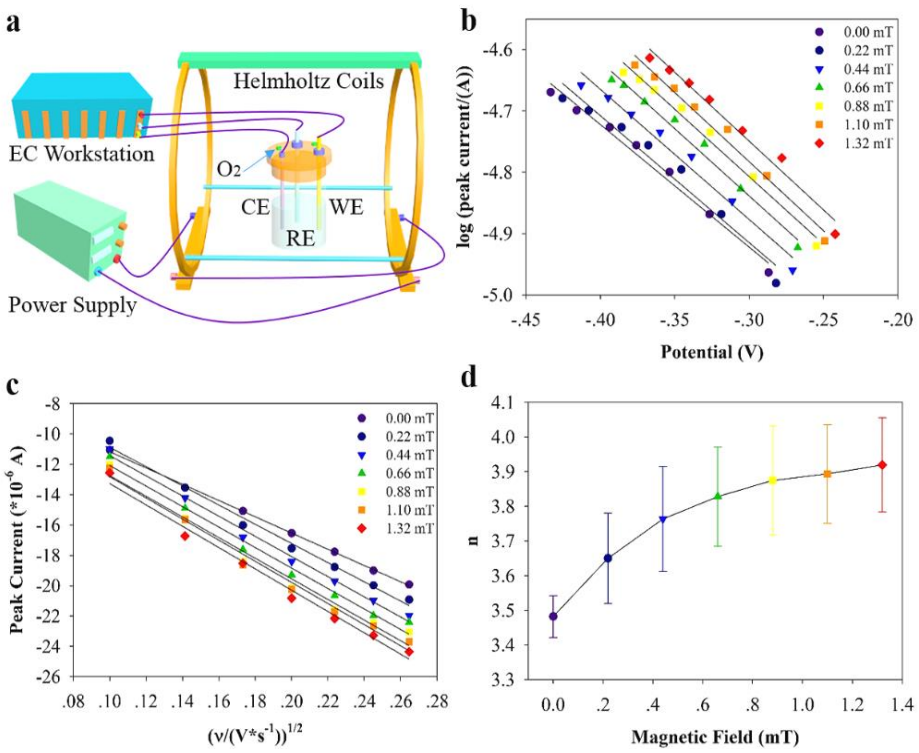


Figure 6.5. Magnetic-dependent Exchanged Electron Number. (a) Schematic description of the magnetic field setup. (b) The linear dependence of the log of the peak current on the potential for the transfer coefficient calculation. (c) The linear dependence of the peak current on the square root of the scan rate for the exchanged electron number calculation. (d) The dependence of *n* on the magnetic field applied to the ORR at the GC electrode modified with $Co_3O_4$/ECNFs (5 h electrodeposition).

Therefore, with the increase of $Co_3O_4$ thickness (1-5 h electrodeposition), the number of exchanged electrons (*n*) increases due to the oxygen and hydrogen peroxide are effectively confined within the aligned $Co_3O_4$/ECNFs system (Figure 6.4a). Even though there is no obvious thickness difference, $Co_3O_4$ electrodeposition beyond a 5 h time shows a decreased *n* due to the factor of resistance, since $Co_3O_4$/ECNFs electrodes with 6 h

(charge transfer resistance of about 137 Ohms) and 8 h (charge transfer resistance of about 149 Ohms) electrodeposition have higher resistance, which is deduced from the electrochemical impedance spectroscopy (EIS) Nyquist plots (Figure 6.4b) and a Randles circuit model.

Magnetic enhanced electron transfer (MEET): the cyclic voltammetric responses of the $Co_3O_4$/ECNFs (5 h electrodeposition) modified electrode were examined under different magnetic fields (Figure 6.5a and Fig. S6.11). According to the slope 1 of a plot of log (peak current) versus potential (Figure 6.5b), the slope 2 of the peak current position on the square root of the voltage scan rate (Figure 6.5c), and equ. (6-6) and (6-7), the increased number of exchanged electrons is obtained for the $Co_3O_4$/ECNFs modified electrodes under the magnetic fields of 0.22 mT, 0.44 mT, 0.66 mT, 0.88 mT, 1.10 mT, 1.32 mT, respectively (Figure 6.5d, Table 6.1). Since there is no measurable difference between the bare GC electrode without an external magnetic field (Fig. S6.2) and that with 1.32 mT (Fig. S6.12), which is different from other reports that a much larger magnetic field improves oxygen diffusion/transfer,[41,42] one can conclude that the external mT magnetic field does not have obvious effect on the oxygen diffusion/transfer, indicating that the obvious difference for $Co_3O_4$/ECNFs modified electrode under different magnetic fields is resulted from the magnetic effect on $Co_3O_4$/ECNFs. On the other hand, the magnitude of slope 1 increases with the increase of magnetic fields (Table 6.1), suggesting the magnetic enhanced electron transfer rate presents.[43,44]

Table 6.1. Magnetic Effect

| Magnetic field | Slope 1 | Slope 2 | n |
|---|---|---|---|
| **0.00 mT** | -2.10±0.08 | $(-5.36\pm0.04)\times10^{-5}$ | 3.48±0.06 |
| **0.22 mT** | -2.12±0.14 | $(-5.78\pm0.13)\times10^{-5}$ | 3.65±0.13 |
| **0.44 mT** | -2.14±0.17 | $(-6.08\pm0.14)\times10^{-5}$ | 3.76±0.15 |
| **0.66 mT** | -2.19±0.12 | $(-6.31\pm0.19)\times10^{-5}$ | 3.82±0.14 |
| **0.88 mT** | -2.20±0.11 | $(-6.44\pm0.24)\times10^{-5}$ | 3.87±0.16 |
| **1.10 mT** | -2.25±0.13 | $(-6.56\pm0.18)\times10^{-5}$ | 3.89±0.14 |
| **1.32 mT** | -2.28±0.12 | $(-6.67\pm0.17)\times10^{-5}$ | 3.92±0.13 |

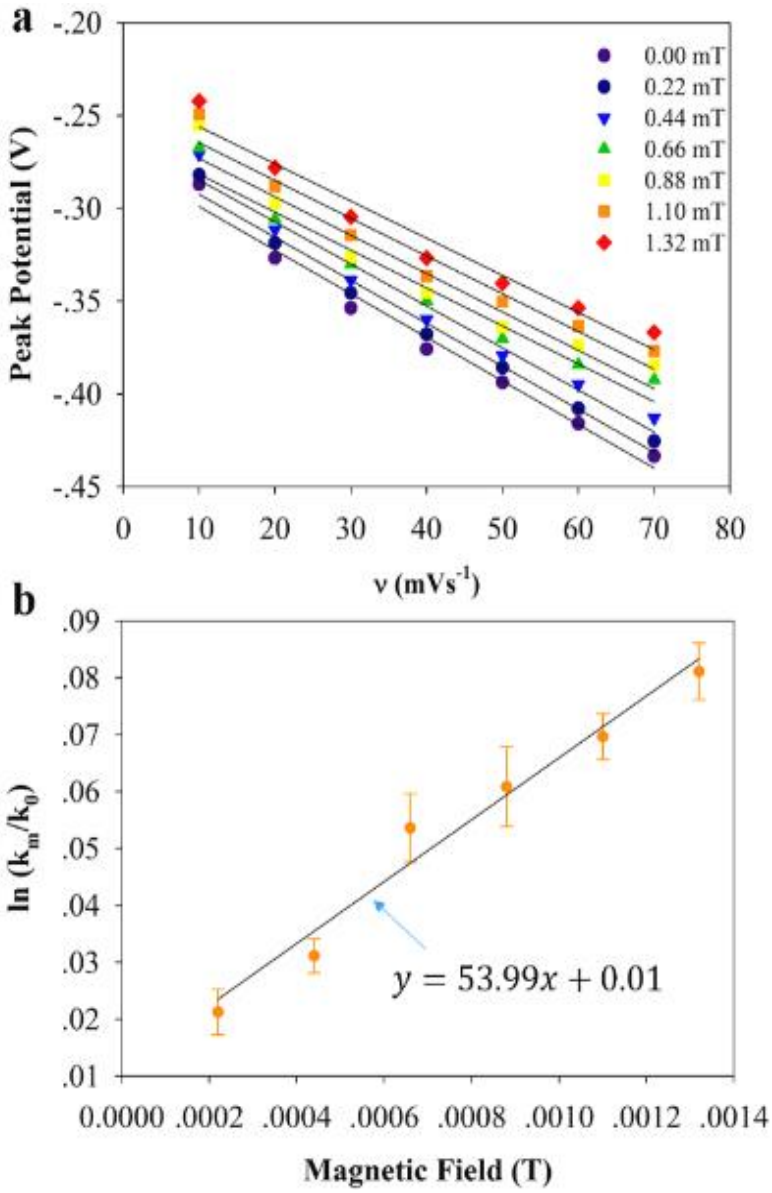


Figure 6.6. ORR Part. (a) The dependence of the peak potential on the scan rate under different magnetic fields of the ORR at the electrode modified with $Co_3O_4$/ECNFs (5 h electrodeposition). (b) Plot of $ln(k_m/k_0)$ versus magnetic field for the electrode modified with $Co_3O_4$/ECNFs with the linear fit.

The following model was further used to estimate the heterogeneous electron transfer rate constant during the oxygen reduction reaction process ( $k_{ORR}^{0}$ (cm $s^{-1}$)):[45]

$$k_{ORR}^{0} = 2.18\left(\frac{\alpha D_0 nF\nu}{RT}\right)\exp\left(\frac{-2\alpha^2 nF\left(E_0 - E_p\right)}{RT}\right) \quad (6\text{-}8)$$

where $E_0$ is the y-intercept at the scan rate of 0 mV $s^{-1}$ in Figure 6.6a. By using the experimental results at different scan rates (20 mV $s^{-1}$ in Table S6.2 as an example), associated with the transfer coefficient, number of electrons exchanged, and diffusion coefficient obtained above, the values of heterogeneous electron transfer rate constant could be calculated. A best fit to the experimentally obtained $ln(k_m/k_0)$ versus magnetic field ($H$) gives the following equation (Figure 6.6b):

$$\left(\frac{k_m}{k_0}\right)_{ORR} = \exp\left(53.99 \cdot H + 0.01\right) \quad (6\text{-}9)$$

where $k_m$, $k_0$ is the electron transfer rate constant of oxygen reduction with or without magnetic fields.

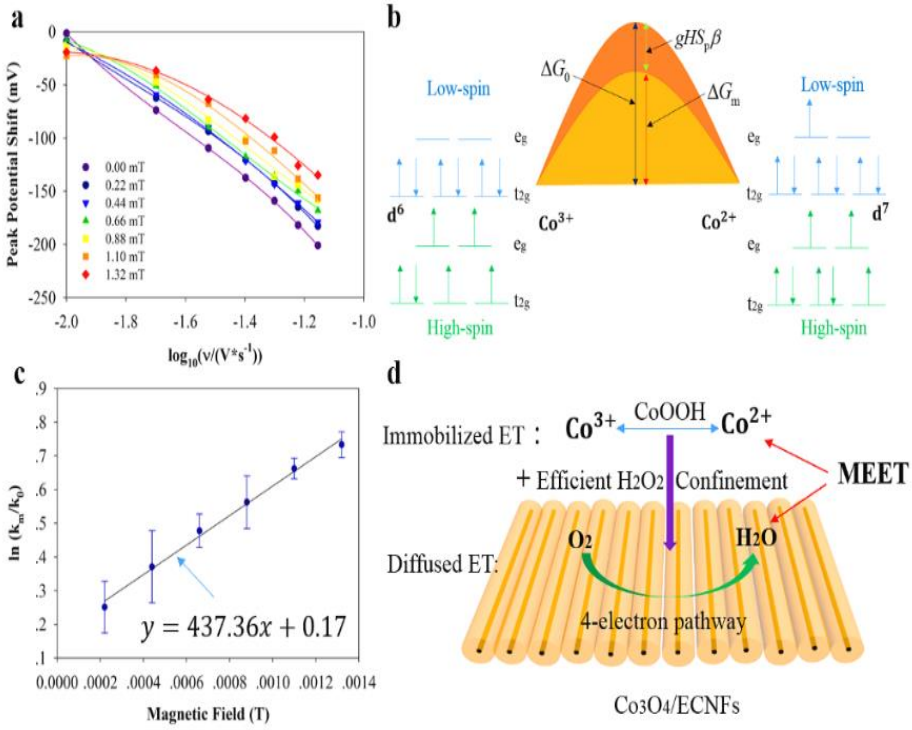


Figure 6.7. $Co_3O_4$ Part. (a) The dependence of the peak potential shift on the scan rate under different magnetic fields regarding the electron transfer kinetics of the $Co_3O_4$-electrode system. (b) Schematic illustration of a case at magnetic field effects on the electron transfer/exchange. (c) Plot of $ln(k_m/k_0)$ versus magnetic field with the linear fit regarding the electron transfer kinetics of the $Co_3O_4$-electrode system. (d) Mechanistic view of the magnetic enhanced 4-electron pathway.

Liang, et al found that the oxygen reduction strongly coupled with cobalt oxide catalyst.[28] A similar redox reaction of Co(III)/Co(II) was observed at the $Co_3O_4$/ECNFs electrode with presence of oxygen (no redox peaks in the absence of oxygen), suggesting the coupling of the Co(III)/Co(II) redox reaction and the ORR process presents. The magnetic effect on the electron transfer kinetics of the $Co_3O_4$-electrode system focusing on

Co(III)/Co(II) redox couple (reduction peak at around 0.5 V vs. Ag/AgCl) at ECNFs was further analyzed by using Laviron Method for a diffusionless electrochemical system.[46] The standard rate constants of Co(III)/Co(II) were obtained via the fitting of cyclic voltammetry data (Figure 6.7a, Fig. S6.13) with the function of overpotential vs. (1/m) value expressed as:[46]

$$\psi_c = m\eta^{-\gamma}\left\{1-m(1+\eta)\exp\left[f(\eta)\right]\int_{\infty}^{\eta} x^{-(1+\gamma)}\exp\left[-f(x)\right]dx\right\} \qquad (6\text{-}10)$$

where $\psi_c$ is the function for the cathodic curve and γ is the fitting coefficient. In the absence of an external magnetic field, the standard heterogeneous rate constant for the $Co_3O_4$/ECNFselectrode system is calculated to be about 0.049 $s^{-1}$. In the presence of an external magnetic field, the standard rate constant is obtained to be about 0.063, 0.071, 0.079, 0.086, 0.095, 0.102 $s^{-1}$ at the magnetic fields of 0.22, 0.44, 0.66, 0.88, 1.10, 1.32 mT (Table S6.3), respectively.

According to the transition state theory by considering the contribution of the enhanced electron energy states to the activation energy due to magnetic field induced degeneracy (Figure 6.7b), and the electron transfer resulting in $Co^{3+}$ ($e_g^0t_{2g}^6$ or $e_g^2t_{2g}^4$) to $Co^{2+}$ ($e_g^1t_{2g}^6$ or $e_g^2t_{2g}^5$),[47] the rise of Zeeman energy, $g\beta HS_p$,[48] with magnetic field contributes to the activation energy by reducing the net enthalpy of activation barrier and thus the reaction rate is facilitated. The electron transfer rate constant ratio at the electrode surface can be expressed in an Arrhenius form as (see details in SI):

$$\frac{k_m}{k_0} = \exp\left(\frac{gS_p\beta}{k_BT}\cdot H + \frac{\Delta S_m}{k_B}\right) \quad (6\text{-}11)$$

where $g$ is the magnetic response to an applied magnetic field, $S_p$ is electron spin, $\beta$ is the Bohr magneton, $k_B$ is Boltzmann's constant, and $\Delta S_m$ is the magnetically dependent entropy term. Qualitatively, according to equ. (6-11), the initial energy is shifted by the Zeeman energy under sufficient magnetic field with minimal entropy ($\Delta S_m/kB \rightarrow 0$). Quantitatively, a best fit to the experimentally obtained $ln(k_m/k_0)$ versus $H$ gives the following equation (Figure 6.7c):

$$\left(\frac{k_m}{k_0}\right)_{Co} = \exp\left(437.36\cdot H + 0.17\right) \quad (6\text{-}12)$$

According to equ. (6-9) and (6-12), the pre-factor (437.36) of MEET for the Co(III)/Co(II) redox reaction in the $Co_3O_4$-electrode system is much larger than that (53.99) for the ORR at the electrode surfaces. As a summary of the data analysis and discussion: (1) the magnetic field polarization on unpaired electron spin of $Co_3O_4$ and the energy degeneracy can enhance the kinetics of Co(III)/Co(II) redox reaction (probably between $Co^{2+}$ and $Co^{3+}$ by a CoOOH surface layer[28]) in the $Co_3O_4$/ECNFs catalytic centers (Figure 6.7d); (2) the coupling of Co(III)/Co(II) redox reaction and the ORR process facilitate a faster rate of oxygen reduction by the $Co_3O_4$/ECNFs to fulfill a 4-electron pathway during the oxygen reduction reaction process.

$$O_2 \xrightarrow{Co_3O_3 \overset{MEET}{\longleftrightarrow} CoOOH} H_2O \quad (6\text{-}13)$$

## Conclusion

This work demonstrates a new strategy for uniformly electrodepositing $Co_3O_4$ on well-aligned ECNFs with a constant low-current of 50 μA and the change in the mechanism of $Co_3O_4$ growth with the electrodeposition time was explored, which provides the three-stage kinetics of the $Co_3O_4$ growth process with a halfway growth at about 3.59 h. From the $Co_3O_4$ thickness dependent ORR performance, the GC electrode modified with $Co_3O_4$ /ECNFs (5 h electrodeposition) shows a high exchanged electron number of 3.48, which is ascribed to an effective confinement of hydrogen peroxide. Furthermore, a significant improvement in exchanged electron number can be achieved by applying an external magnetic field at a mT level due to the magnetic field polarization on unpaired electron spin of $Co_3O_4$ and the electron energy degeneracy which facilitates a faster rate of oxygen reduction by the $Co_3O_4$/ECNFs to fulfill a 4-electron pathway during the oxygen reduction reaction process.

## Experimental

Super-aligned ECNFs fabrication: a 10 wt.% polyacrylonitrile (PAN, Mw = 150,000, ACROS Organics) solution in dimethylformamide (ACROS Organics) was electrospun onto the collector. The applied positive voltage was 18 kV and the distance between the needle tip and the collector was 15 cm. The collector was maintaining at a rate of 2000 revolutions per minute (rpm) during the electrospun to form the well-aligned precursors. The obtained sheets were then put into a furnace (Oxidation and Annealing Furnace) for stabilization to ensure that the fibers did not melt during pyrolysis. The heating

rate was 1 °C/min from room temperature to 280 °C and kept for 6 h. The as-stabilized nanofibers were finally carbonized at 1200 °C for 1 h at a heating rate of 5 °C/min under $N_2$ atmosphere to yield high mechanical strength ECNFs.

$Co_3O_4$ electrodeposition on ECNFs: after the well-aligned ECNFs were prepared, $Co_3O_4$ was electrodeposited onto 1 $cm^2$ ECNFs with a three-electrode setup using a charging current of 50 μA performed on a bio-logic VMP3 electrochemical workstation. Here, a gold electrode taped with ECNFs, a platinum wire, and an Ag/AgCl were used as the working electrode, the counter electrode, and the reference electrode (Fisher Scientific), respectively. To assure that the deposition of $Co_3O_4$ took place uniformly and firmly at the ECNFs' surfaces, the ECNFs electrode was prior-treated with 2% $HNO_3$ (J.T. Baker) solution at 60 °C for 2 h to introduce –OH and –COOH groups to facilitate the deposition. An aqueous precursor solution containing 20 mM $CoSO_4$ (ACROS Organics) and 100 mM $Na_2SO_4$ (ACROS Organics) was used as the supporting electrolyte. After the deposition, the working electrodes were washed with deionized water and the samples were dried for further experiments.

Characterization: field emission scanning electron microscope (FESEM) (Carl Zeiss Auriga-BU FIB FESEM Microscope) was performed to study the morphological properties of well-aligned ECNFs and $Co_3O_4$/ECNFs. Energy-dispersive X-ray spectroscopy (EDX) (Hitachi S-4800-I FESEM w/Backscattered Detector & EDX), Raman spectroscopy (Horiba XploRA Raman Confocal Microscope System), and Fourier transform infrared spectroscopy (FTIR) (Varian 670) were employed to study the elements components of $Co_3O_4$/ECNFs. Furthermore, X-ray powder diffraction (XRD) (Agilent

Oxford Germini X-Ray Diffractometer) was also employed to study the crystal structures of $Co_3O_4$.

Electrochemical study: electrochemical performance was performed on a bio-logic VMP3 electrochemical workstation using a three-electrode testing system with a 3 mm diameter GC as the working electrode, a platinum wire as the counter electrode and an Ag/AgCl as the reference electrode (Fisher Scientific) in 20 mM KCl (Sigma-Aldrich) electrolyte solution that was thoroughly degassed with $O_2$ gas. The $Co_3O_4$/ECNFs were cut as 3 mm diameter wafers and then tapped onto the GC as modified electrodes for the electrochemical analysis of electro-reduction of oxygen. Cyclic voltammetry was then carried out after the modified GC electrode being immersed in a $N_2$ saturated 20 mM KCl solution for 15 min. Cyclic voltammetry was carried out at different scan rates with a potential window between -1.0 V and 0.9 V. The magnetic field setup was conducted by the Helmholtz arrangement of the pair of coils (see details in SI)

## References


1. Shao, M., Chang, Q., Dodelet, J. P., & Chenitz, R. (2016). Chem. Rev., 116, 3594-3657.
2. Zhu, C., Li, H., Fu, S., Du, D., & Lin, Y. (2016). Chem. Soc. Rev., 45, 517-531.
3. Higgins, D., Zamani, P., Yu, A., & Chen, Z. (2016). Energy Environ. Sci., 9, 357-390.
4. Zhang, J., & Dai, L. (2016). ACS Catal., 5, 7244-7253.
5. Choi, C. H., Chung, M. W., Kwon, H. C., Chung, J. H., & Woo, S. I. (2014). Appl. Catal., B, 144, 760-766.
6. Li, M., Zhang, L., Xu, Q., Niu, J., & Xia, Z. (2014). J. Catal., 314, 66-72.
7. Wan, K., Yu, Z. P., Li, X. H., Liu, M. Y., Yang, G., Piao, J. H., & Liang, Z. X. (2015). ACS Catal., 5, 4325-4332.
8. Deng, Y. J., Wiberg, G. K. H., Zana, A., Sun, S. G., & Arenz, M. (2017). ACS Catal., 7, 1-6.
9. Moniri, S., Van Cleve, T., & Linic, S. (2017). J. Catal., 345, 1-10.
10. Xin, H., Holewinski, A., & Linic, S. (2011). ACS Catal., 2, 12-16.
11. Guo, D., Shibuya, R., Akiba, C., Saji, S., Kondo, T., & Nakamura, J. (2016). Science, 351, 361-365.
12. Zeng, M., Liu, Y., Zhao, F., Nie, K., Han, N., Wang, X., & Li, Y. (2016). Adv. Funct. Mater., 26, 4397-4404.

13. He, D. S., He, D., Wang, J., Lin, Y., Yin, P., Hong, X., & Li, Y. (2016). J. Am. Chem. Soc., 138, 1494-1497.
14. Zagal, J. H., & Koper, M. (2016). Angew. Chem. Int. Ed., 55, 14510-14521.
15. Chen, G., Sunarso, J., Zhu, Y., Yu, J., Zhong, Y., Zhou, W., & Shao, Z. (2016). ChemElectroChem, 3, 1760-1767.
16. Alia, S. M., Pylypenko, S., Neyerlin, K. C., Cullen, D. A., Kocha, S. S., & Pivovar, B. S. (2014). ACS Catal., 4, 2680-2686.
17. Shin, H., Kim, H. I., Chung, D. Y., Yoo, J. M., Weon, S., Choi, W., & Sung, Y. E. (2016). ACS Catal., 6, 3914-3920.
18. Sun, T., Wu, Q., Che, R., Bu, Y., Jiang, Y., Li, Y., ... & Hu, Z. (2015). ACS Catal., 5, 1857-1862.
19. Ghassemzadeh, L., Kreuer, K. D., Maier, J., & Müller, K. (2010). J. Phys. Chem. C, 114, 14635-14645.
20. Holewinski, A., Idrobo, J. C., & Linic, S. (2014). Nat. Chem., 6, 828-834.
21. Sun, M., Dong, Y., Zhang, G., Qu, J., & Li, J. (2014). J. Mater. Chem. A, 2, 13635-13640.
22. Shimizu, K., Sepunaru, L., & Compton, R. G. (2016). Chem. Sci., 7, 3364-3369.
23. Zhu, J., Chen, M., Qu, H., Luo, Z., Wu, S., Colorado, H. A., & Guo, Z. (2013). Energy Environ. Sci., 6, 194-204.
24. Zeng, Z., Liu, Y., Zhang, W., Chevva, H., & Wei, J. (2017). J. Power Sources, 358, 22-28.

25. Liang, Y., Li, Y., Wang, H., Zhou, J., Wang, J., Regier, T., & Dai, H. (2011). Nat. Mater., 10, 780-786.
26. Ma, T. Y., Dai, S., Jaroniec, M., & Qiao, S. Z. (2014). J. Am. Chem. Soc., 136, 13925-13931.
27. Xu, L., Jiang, Q., Xiao, Z., Li, X., Huo, J., Wang, S., & Dai, L. (2016). Angew. Chem. Int. Ed., 128, 5363-5367.
28. Liang, Y., Wang, H., Zhou, J., Li, Y., Wang, J., Regier, T., & Dai, H. (2012). J. Am. Chem. Soc., 134, 3517-3523.
29. Dutta, P., Seehra, M. S., Thota, S., & Kumar, J. (2007). J. Phys. Condens. Matter., 20, 015218.
30. Meher, S. K., & Rao, G. R. (2011). J. Phys. Chem. C, 115, 25543-25556.
31. Shin, D., Jeong, B., Mun, B. S., Jeon, H., Shin, H. J., Baik, J., & Lee, J. (2013). J. Phys. Chem. C, 117, 11619-11624.
32. Mao, X., Rutledge, G. C., & Hatton, T. A. (2014). Nano Today, 9, 405-432.
33. Patel, V. K., Saurav, J. R., Gangopadhyay, K., Gangopadhyay, S., & Bhattacharya, S. (2015). RSC Adv., 5, 21471-21479.
34. Zhang, J., Gao, W., Dou, M., Wang, F., Liu, J., Li, Z., & Ji, J. (2015). Analyst, 140, 1686-1692.
35. Edla, R., Gupta, S., Patel, N., Bazzanella, N., Fernandes, R., Kothari, D. C., & Miotello, A. (2016). Appl. Catal. A, 515, 1-9.
36. Vetter, K. J. (2016). Electrochemical kinetics: theoretical aspects. Elsevier.
37. Wang, J. (2006). Analytical electrochemistry. John Wiley & Sons.

38. Muhammad, H., Tahiri, I. A., Muhammad, M., Masood, Z., Versiani, M. A., Khaliq, O., & Hanif, M. (2016). J. Electroanal. Chem., 775, 157-162.
39. Zhang, W., Zeng, Z., & Wei, J. J. (2017). Phys. Chem. C., 121, 18635-18642.
40. Toupin, M., Brousse, T., & Bélanger, D. (2004). Chem. Mater., 16, 3184-3190.
41. Lioubashevski, O., Katz, E., & Willner, I. (2004). J. Phys. Chem. B, 108, 5778-5784.
42. Wang, L., Yang, H., Yang, J., Yang, Y., Wang, R., Li, S., & Ji, S. (2016). Ionics, 22, 2195-2202.
43. Wei, J., Liu, H., Dick, A. R., Yamamoto, H., He, Y., & Waldeck, D. H. (2002). J. Am. Chem. Soc., 124, 9591-9599.
44. Wei, J., Liu, H., Khoshtariya, D. E., Yamamoto, H., Dick, A., & Waldeck, D. H. (2002). Angew. Chem. Int. Ed., 41, 4700-4703.
45. Klingler, R. J., & Kochi, J. K. (1981). J. Phys. Chem., 85, 1731-1741.
46. Lviron, E., (1979). J. Electroanal. Chem. Interf. Electrochem., 101, 19-28.
47. Takami, T. Functional Cobalt Oxides: Fundamentals, Properties and Applications. CRC Press (2014).
48. Chapyshev, S. V. (2009). J. Org. Chem., 74, 7238-7244.

# CHAPTER VII

# MAGNETIC RESPONSE OF CRYPTOCHROME 1

This chapter has been submitted as: Zeng, Z., Wei, J.*, Liu, Y., Zhang W., & Mabe, T. Magnetic Response of Cryptochrome 1 in Photoinduced Heterogeneous Electron Transfer.

## An Overview

Cryptochromes are flavoproteins whose light-induced photocycle and magnetoreception are implicated to underpin crucial biological functions and potential biomimetic magneto-opto-electronics. In this communication, for the first time, we observed a magnetic response of cryptochrome 1 (CRY1) immobilized as a monolayer at a gold electrode, which was illuminated with blue light using an opto-magnetic electrochemical system. These new results present the magnetic field enhanced photo-induced electron transfer of CRY1 to the electrode by voltammetry, exhibiting a magnetic responsive electron transfer rate constant and electrical current changes. The magnetic field effect on electron transfer kinetics of CRY1 was further analyzed based on transition state theory. This was accomplished by considering the contribution to the activation energy due to magnetic field induced degeneracy of the unpaired electron spins in the light-excited CRY1s. A mechanism of spin-correlated heterogeneous electron transfer, which involves the light activated radical pairs ([$FAD^{\bullet -}$ + $Trp(H)^{\bullet +}$]) in CRY1, is proposed to explain the magnetic response

## Introduction

Cryptochromes, a class of flavoproteins, can result in photo-induced electron transfer by absorbing blue light (300-500 nm), whose photochemistry is implicated to underpin crucial biological function associated with phototropism, circadian clocks and bird navigation.[1-6] Many researchers have further reported that plants[7] and animals[8,9] (sea turtles, spotted newts, lobsters, honeybees, and European robins, etc.) have the ability to perceive magnetic fields from the earth to direct their circadian rhythms and orientation behaviors due to the magnetoreception role of cryptochromes. Magnetoreception has been explained by a radical-pair based mechanism. The magnetic sensitivity arises from chemical intermediates formed by photoexcitation of cryptochrome proteins.[5,6] Although the light-induced photocycle in cryptochromes and magnetic field effects in active states of cryptochromes have been examined through transient absorption and electron-spin-resonance observations together with the concept and methods of quantum physics and molecular dynamics,[10-13] the magnetic field associated electron transfer is less explored.[14,15] More recently, theoretical and spectroscopic studies[16-19] suggest that electron transfer between light activated FAD and tryptophan (Trp) residues leads to the formation of a spin-correlated radical pair, whose subsequent relaxation is sensitive to external magnetic fields. To date, the heterogeneous electron transfer of cryptochromes has not been reported. This is especially true for the magnetic sensitivity at a solid interface, which would be of interest for a biomimetic opto-magnetic compass. Here, we propose to study the magnetic response by an electrochemical analysis of the magnetic field effect in light-induced electron transfer of immobilized CRY1 (molecular weight of 67 kDa, Fig. S7-1)

on a gold slide that is coated with a self-assembled monolayer (SAM) of mixed -S-$(CH_2)_{10}$-COOH and -S-$(CH_2)_8$-OH (Figure 7-1).[20] The covalent bonds anchoring the protein should eliminate a gating mechanism for electron transfer of the protein at the surface resulting from large-conformational motion.[21]

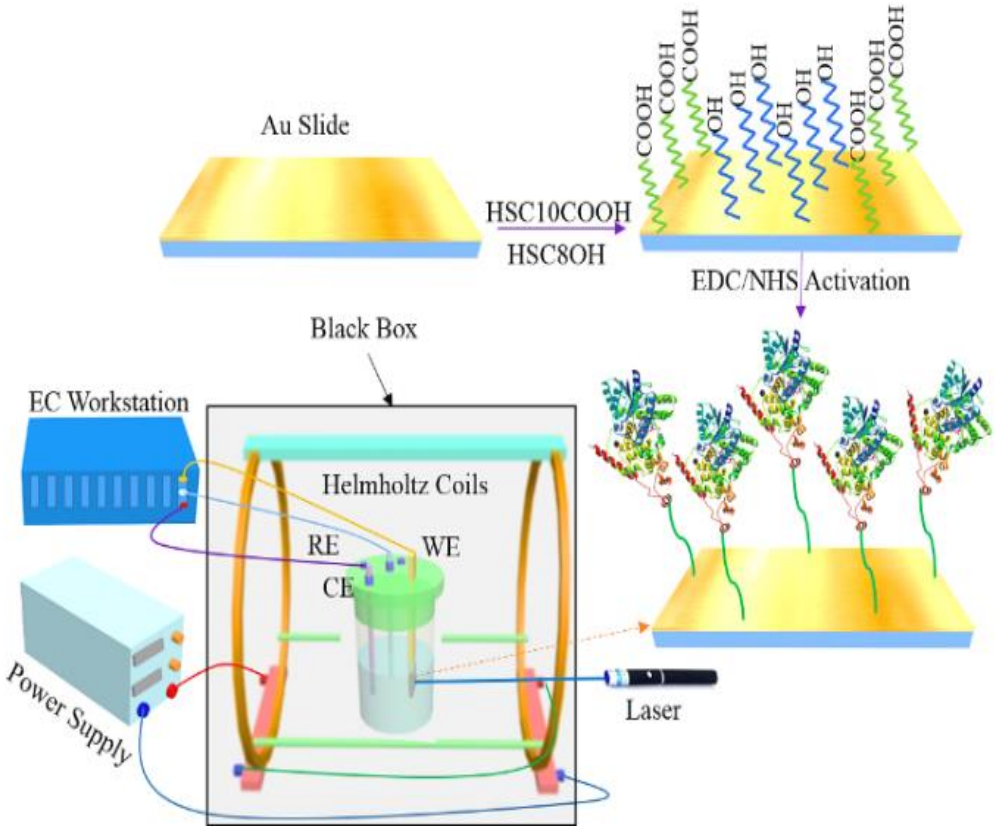


Figure 7.1. SAM Illustration. Illustration of the protocol for the self-assembled monolayer (SAM) formation and CRY1s immobilization on the gold slide electrode and a schematic of the home-setup, opto-magnetic electrochemical system used for the electrochemical electron transfer study of the immobilized CRY1.

**Results and Discussion**

Figure 7.2A shows oxidation voltammograms (baseline subtracted from original data in Fig. S7.2) of adsorbed CRY1 films with and without blue light excitation at a scan rate of 4 V $s^{-1}$. Light excitation of CRY1 is necessary to observe the Faradaic current signal because there was no such signal observed in the absence of blue light. In a comparison experiment, the enzymatic flavoprotein, glucose oxidase, was immobilized on the SAM

modified gold slide. Voltammograms were performed with and without blue light illumination at the same scan rate of 4 V $s^{-1}$ (Fig. S7.3B). There was no Faradaic response at blue light illumination both with and without a 1.32 mT magnetic field. This suggests that electrons could not be directly transferred from FAD of glucose oxidase to the electrode linked with a SAM, which shows a good agreement with a previous study on direct electron transfer of immobilized glucose oxidase on a gold electrode.[22] In contrast, an oxidation peak was observed from CRY1 which was excited by light while immobilized on the electrode. The peak current increased monotonically with increasing magnetic field strength. CRY1 can absorb blue light with an apparent peak absorbance at approximately 350 nm (Fig. S7.4). This corresponds to an optical band gap of 1.98 ± 0.16 eV (Fig. S7.5). Fluorescence spectra of CRY1 show an emission peak at approximately 450 nm under an excitation wavelength of 375 nm (Fig. S7.6).

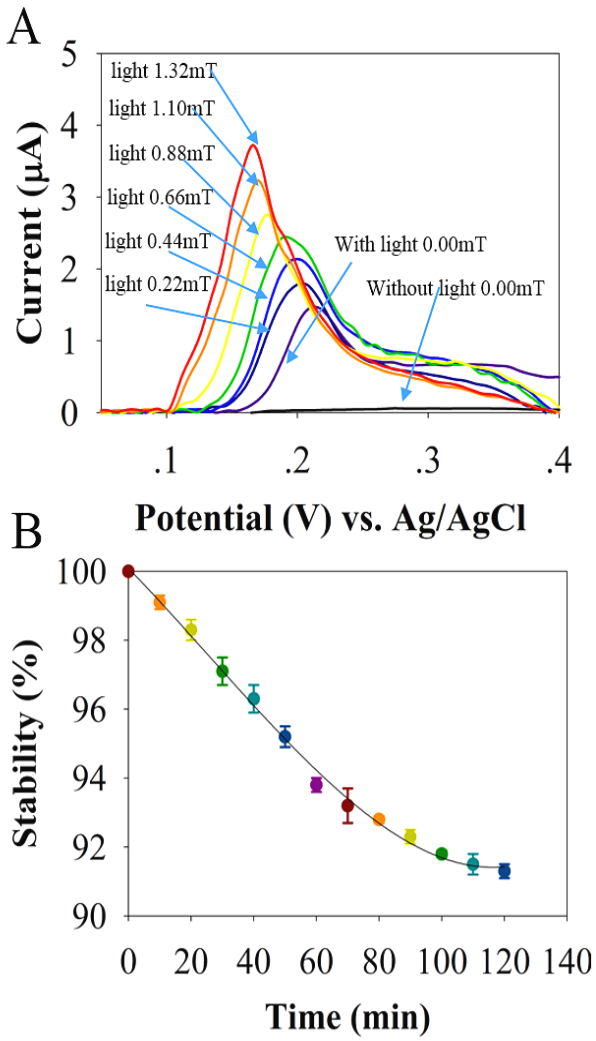


Figure 7.2. Cyclic Voltammograms. The gold slide surface (A) immobilized with CRY1 with and without blue light excitation in the absence of magnetic field and with blue light excitation under different magnetic fields at the scan rate of 4 V $s^{-1}$. (B) Time profiles for the surface concentration of immobilized CRY1 with blue light excitation at the scan rate of 4 V $s^{-1}$ in the absence of magnetic field.

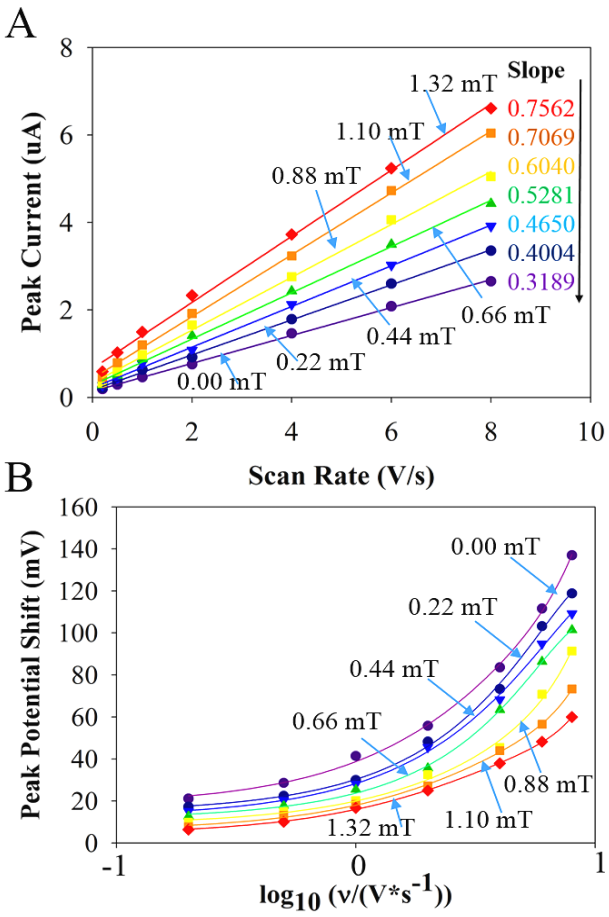


Figure 7.3. Electron Transfer Model. (A) The linear dependence of the peak current on the voltage scan rate under different magnetic fields. (B) The dependence of the peak potential on log(scan rate) under different magnetic fields and fits of the data to the extended Marcus electron transfer model. Note that the scan rates (v) are 0.2 V $s^{-1}$, 0.5 V $s^{-1}$, 1 V $s^{-1}$, 2 V $s^{-1}$, 4 V $s^{-1}$, 6 V $s^{-1}$, and 8 V $s^{-1}$.

The anodic peak of photo-excited CRY1 has a full width at half height (FWHH) of 43 mV, suggesting a two-electron transfer reaction of the CRY1s-SAM-gold electrode in this electrochemical study according to FWHH=62.5/nα (n is the number of transfer electron and α is the transfer coefficient) for an irreversible redox reaction.[23,24] Note that

photoexcitation of the fully oxidized form in CRY1 produces an excited singlet state, which may be rapidly reduced by the electron transfer along a chain of three tryptophan residues within the CRY1 to form the radical pair [$FAD^{\bullet -}$ + $Trp(H)^{\bullet +}$].[16-19] This may be the reason that there is no obvious reversible process due to the absence of electrochemical reduction of the excited CRY1 within the voltammetry scan range.

Association strength and stability of the adsorbed CRY1 films were assessed by voltammograms. This was performed using the same CRY1s-SAM-electrode at subsequent times. In this procedure, the electrode was placed in the supporting electrolyte solution, and after 20 seconds, a voltammogram was initiated with a scan rate of 4 V $s^{-1}$. Voltammograms were performed at subsequent time points (each measurement with light excitation but in the absence of magnetic field) until the peak current was found to stabilize. The peak current is proportional to the amount of CRY1 adsorbed on the surface. Thus, Figure 7.2B shows a profile of the adsorbed species concentration as a function of time. The peak current is found to stabilize after 110 minutes. 91.3 ± 0.2% of the initial amount of CRY1 adsorbed on the surface is maintained after 120 minutes, indicating the good stability of immobilized CRY1 at the gold slide surface. The slope of the peak current versus scan rate plot (Figure 7.3A line with slope of 0.3189), with n=2, gives a surface coverage of 8.02 ± 0.09 × $10^{-14}$ mol $cm^{-2}$ of active CRY1s and an estimated average area on the gold slide occupied per CRY1 molecule of $2.26\times10^{3}$ $nm^{2}$.

The peak current, $i_p$, displays as a function of the voltage scan rate for the electrodes coated with CRY1 at a magnetic field. The magnitude of peak current was found to exhibit a linear dependence on the scan rate, which is consistent with the redox reaction of

immobilized species at electrode surfaces.[25] There is no measurable Faradaic current from CRY1s-SAM-gold slide electrode without light illumination (Fig. S7.7) or SAM only gold slide electrode without CRY1s immobilized (Fig. S7.8,9) at different magnetic fields. This is evident that the changes of oxidation peak current from the CRY1s-SAM-gold slide at different magnetic fields (Fig. S7.10,11) are resulted from concurrence of the blue light excitation and the magnetic field effect on CRY1s. Figure 7.2A shows the oxidation peak potential left-shifts and Figure 7.3A displays the slope increase of the peak current vs. scan rate plot (Table S7.1) with magnetic field increases, suggesting that the electron transfer rate increases with the increase of magnetic field strength.[25]

The dependence of the oxidation peak's position on the voltage scan rate can be used to characterize the electron transfer rate constant.[26-28] Briefly, the electron transfer between an electroactive reporter, such as CRY1, and an electrode can be written as follows, by assuming the direct electron superexchange tunneling is the dominant pathway:

$$CRY1^* \xrightarrow{k_{ox}} Electrode \tag{7-1}$$

where the excited CRY1* is the electron donor and the electrode is the electron acceptor during the oxidation reaction (Figure 7.1A). The rate constant, $k_{ox}$, is subject to the overpotential, $\eta$. Based on the extended Marcus theory for heterogeneous electron transfer,[26-28] the standard heterogeneous rate constant ($k^0$) can be expressed as (see details in SI):

$$k^0 = \frac{2\pi}{\hbar}\left|H_{DA}\right|^2 \frac{1}{\sqrt{4\pi\lambda k_B T}} \int_{-\infty}^{\infty} \rho(\varepsilon) f(\varepsilon) \exp\left(-\frac{\left(\lambda + (\varepsilon_F - \varepsilon)\right)^2}{4\lambda k_B T}\right) d\varepsilon \tag{7-2}$$

in which, h is the Planck constant, $H_{DA}$ is the effective electronic coupling between the electrode and the CRY1 states, $\lambda$ is the reorganization energy, $k_B$ is the Boltzmann's constant, T is temperature in Kelvin, $\rho(\varepsilon)$ is the electron density of states of the electrode, $f(\varepsilon)$ is Fermi function, $\varepsilon_F$ is the Fermi energy, $\varepsilon$ is the energy of an electronic state in the electrode.

Table 7.1. Electron Transfer

| Magnetic Field (mT) | $k^o$ ($s^{-1}$) | Magnetic Response |
|---|---|---|
| **0.00** | 13±1 | 0.0 |
| **0.22** | 15±3 | 0.1 |
| **0.44** | 18±3 | 0.2 |
| **0.66** | 23±2 | 0.3 |
| **0.88** | 30±4 | 0.4 |
| **1.10** | 39±3 | 0.5 |
| **1.32** | 49±5 | 0.6 |

Fitting of the Faradaic peak potential shift from formal potential vs. log(ν) was used to obtain $k^0$ values for electron transfer rate constant of the CRY1 immobilized on the gold slide (see details in SI). Figure 7.3B shows a plot of the peak shift vs. the voltage scan rate under different magnetic fields (Table S7.2), along with the best fit for the electron transfer rate constant with a representative reorganization energy of 0.8 eV for FAD proteins.[24] In the absence of an external magnetic field, the standard heterogeneous rate constant for light-excited CRY1s-SAM-gold slide system is calculated to be 13 $s^{-1}$. In the presence of an external magnetic field, the standard rate constant increased by approximately 15%, 38%, 77%, 131%, 200%, 277% at 0.22, 0.44, 0.66, 0.88, 1.10, 1.32 mT magnetic field, respectively, compared to the $k^0$ without magnetic field (Table 7.1).

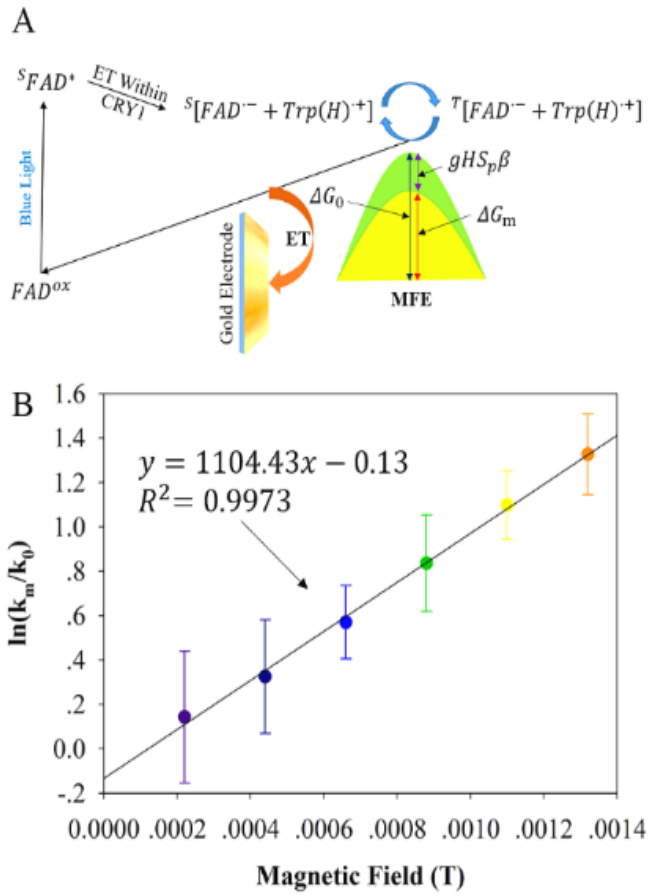


Figure 7.4. Mechanism. (A) A proposed mechanism of the magnetic field effect (MFE) in the spin-correlated heterogeneous electron transfer (ET) for immobilized CRY1. (B) Plot of $\ln(k_m/k_0)$ versus magnetic field for the gold slide surface immobilized with CRY1 under blue light excitation with the linear fit.

Figure 7.4A displays a proposed mechanism for the heterogeneous electron transfer of CRY1 with blue light illumination. At ground level, the resting state of flavin in CRY1 appears to be in the fully oxidized form $FAD^{ox}$.[29] Considering that photo-induced electron transfer of glucose oxidase does not appear in our system (Fig. S7.3B), we believe that the oxidation peak of CRY1 arises from the photo-activated, spin-correlated radical pairs

([FAD•$^-$ + Trp(H)•$^+$]) which exist either in singlet (S) or triplet (T) state, and then back to the ground state in the fully oxidized form ($FAD^{ox}$). The magnetic field effects in the electron transfer kinetics of CRY1-SAM-gold electrodes were analyzed according to the transition state theory by considering the contribution of the enhanced electron energy states to the activation energy due to magnetic field induced degeneracy (Figure 7.4A). Due to the unpaired electron spins in CRY1 radical pairs and light excitation,[30] the rise of Zeeman energy, $g\beta HS_p$, caused by an external magnetic field,[31] contributes to the activation energy by reducing the net enthalpy of activation barrier and thus the reaction rate is facilitated. The electron transfer rate of light-excited CRY1s at the electrode can be expressed in an Arrhenius form as (see details in SI):

$$\frac{k_m}{k_0} = \exp\left(\frac{gS_p\beta}{k_BT}\cdot H + \frac{\Delta S_m^*}{k_B}\right) \qquad (7\text{-}3)$$

where $k_m$, $k_0$ is the electron transfer rate constant with or without magnetic fields, g is the experimental determined response to an applied magnetic field, $S_p$ is electron spin, β is the Bohr magneton, H is the magnetic field, $k_B$ is Boltzmann's constant, T is temperature, $\Delta S_m^*$ is the magnetically dependent entropy term. Qualitatively, according to equ. 7-3, the magnetic enhanced photo-induced electron transfer of CRY1 results from the magnetoreception role of radical pair [FAD•$^-$ + Trp(H)•$^+$], and the initial energy is shifted by the Zeeman energy ($g\beta HS_p$) under sufficient magnetic field with minimal entropy ($\Delta S_m^*/k_B \rightarrow 0$). Quantitatively, a best fit to the experimentally obtained $\ln(k_m/k_0)$ vs. magnetic field H gives the following equation (Figure 7.4B):

$$\frac{k_m}{k_0} = \exp\left(1104.4316 \cdot H - 0.1336\right) \quad (7\text{-}4)$$

This analysis is hard to determine a particular g for a single CRY1 protein. However, the pre-factor value (1104) of H offers a sense how sensitive the CRY1 modified electrode responds to an external magnetic field from a perspective of the transition state theory. To this end, one can conclude that the magnetic field polarization on unpaired electron spins of radical pair [$FAD^{\bullet -}$ + $Trp(H)^{\bullet +}$] and the induced energy degeneracy would be most likely responsible for the enhanced heterogeneous electron transfer of light-excited CRY1. However, there are open questions for further studies, such as how the direction of the magnetic field and the orientation of the immobilized CRY1 correlate to the photo-induced "magnetic sensing" capability during the electron transfer, and what is the role of the radical pair spin interexchange in the electron transfer kinetics.

**Conclusion**

This work demonstrates new findings on how magnetic fields influence blue light-induced heterogeneous electron transfer of CRY1. This ensued by immobilizing CRY1 on a gold slide surface that functioned as an electrode. Coupling magnetic fields with photoelectrochemistry of CRY1, we obtained a function of electron transfer rate constant with magnetic field strength, and the correlation of oxidation current with the magnetic field strength, which, for the first time, verifies its magnetic response (magnetoreception role) at a solid electrode interface. It should be of great significance and potential for successful convergence of the "nature aware" paradigm aiming at the application of

biomimetic magnetoreception functions, which may open an avenue to new types of bioinspired opto-magneto-electronics.

**Experimental**

CRY1 characterization: Ultraviolet-visible spectroscopy (UV-Vis spectroscopy, Varian Cary 6000i) and fluorescence spectroscopy (Horiba FluoroMax-4) were used to investigate the absorbance and fluorescence properties of Homo sapiens CRY1 (Novus Biologicals), respectively.

Preparation of immobilized CRY1 onto the gold slide electrode surface: The gold coated slides contained 20 nm of Au deposited on a 11.5 mm × 11.5 mm glass slide (surface area of 1.32 $cm^2$) by electron beam evaporation (Kurt Lesker PVD75). Gold slides were cleaned with $O_2$ plasma (South Bay Technologies PC2000 Plasma Cleaner) for 3 minutes. The slides were then incubated in a mixture of 11-mercaptoundecanoic acid ($HS(CH_2)_{10}COOH$, Sigma Aldrich) and 8-mercapto-octanol ($HS(CH_2)_8OH$, Sigma Aldrich) in an absolute ethanol solution (ACROS Organics) with 1:2 mole ratio overnight to form a self-assembled monolayer (SAM). After SAM formation, the gold slides were incubated in a 10 mM PBS solution with 0.5 mM 1-(3-dimethylaminopropyl)-3-ethylcarbodiimide hydrochloride (EDC, TCI)/ N-hydroxysuccinimide (NHS, Sigma Aldrich) for 2 hours to activate the carboxylic acid groups.[32] Next, the gold slide was rinsed with 10 mM PBS solution and immediately moved to a freshly prepared 10 mM PBS solution containing 1 mg/mL of CRY1 for 2 hours in a black box. The gold slides were rinsed with 10 mM PBS solution and dried before experiments.

Electrochemical measurement: cyclic voltammetry on immobilized CRY1 was carried out using a Bio-logic VMP3 electrochemical workstation with a three-electrode testing system. A platinum wire counter electrode (Fisher Scientific), a Ag/AgCl (saturated KCl) reference electrode (Fisher Scientific), and a gold slide that functioned as the working electrode made up the system. Note that the gold slide was in full contact with the electrolyte and was electrically connected through a piece of copper tape. Cyclic voltammetry measurements were performed in 10 mM PBS under a nitrogen environment at room temperature. The photo-induced measurement was carried out using a hand held blue laser (447 nm, BigLasers Co.). For the surface coverage calculation with CRY1 proteins immobilized on the electrode surface, the peak current ($i_p$) is given by:

$$\mathrm{i}_p = \frac{n^2 F^2}{4RT} \nu N \tag{7-5}$$

where n is the number of electrons transferred, R is gas constant, F is the Faraday's constant, T is the temperature, ν is the voltage scan rate, and N is the number of active sites on the surface.

Magnetic field setup: Since the magnetic field of each individual coil is non-uniform, two narrow coils with a large radius r is built parallel to one another and on the same axis with a distance as same as the radius r. The arrangement of the two parallel coils makes the magnetic field uniform in a typical region based on the superimposition of the two fields. Given the Helmholtz arrangement of the pair of coils, the following equation is used to calculate the magnetic field:

$$H = 0.72\mu I\frac{n}{r} \quad (7\text{-}6)$$

where H is the magnetic flux density, μ is the magnetic field constant, I is the coil current (in A), n is the number of turns in each coil, and r is the coil radius. After simplifying, using the equation of H=0.7433×I in mT, we can get the magnetic field of 0.22 mT, 0.44 mT, 0.66 mT, 0.88 mT, 1.10 mT, and 1.32 mT by setting the power supply and adjusting the current for the Helmholtz coils.

## References


1. Giovani, B., Byrdin, M., Ahmad, M., & Brettel, K. (2003). Nature Structural & Molecular Biology, 10(6), 489.
2. Sancar, A. (2003). Chemical reviews, 103(6), 2203-2238.
3. Maeda, K., Henbest, K. B., Cintolesi, F., Kuprov, I., Rodgers, C. T., Liddell, P. A., ... & Hore, P. J. (2008). Nature, 453(7193), 387-390.
4. Wang, J., Du, X., Pan, W., Wang, X., & Wu, W. (2015). Journal of Photochemistry and Photobiology C: Photochemistry Reviews, 22, 84-102.
5. Dodson, C. A., Hore, P. J., & Wallace, M. I. (2013). Trends in biochemical sciences, 38(9), 435-446.
6. Hore, P. J., & Mouritsen, H. (2016). Annual review of biophysics, 45, 299-344.
7. Galland, P., & Pazur, A. (2005). Journal of plant research, 118(6), 371-389.
8. Ritz, T., Adem, S., & Schulten, K. (2000). Biophysical journal, 78(2), 707-718.
9. Rodgers, C. T., & Hore, P. J. (2009). Proceedings of the National Academy of Sciences, 106(2), 353-360.
10. Harris, S. R., Henbest, K. B., Maeda, K., Pannell, J. R., Timmel, C. R., Hore, P. J., & Okamoto, H. (2009). Journal of The Royal Society Interface, rsif-2008.
11. Solov'yov, I. A., Domratcheva, T., Moughal Shahi, A. R., & Schulten, K. (2012). Journal of the American Chemical Society, 134(43), 18046-18052.

12. Solov'yov, I. A., & Schulten, K. (2012). The Journal of Physical Chemistry B, 116(3), 1089-1099.
13. Nießner, C., Denzau, S., Stapput, K., Ahmad, M., Peichl, L., Wiltschko, W., & Wiltschko, R. (2013). Journal of The Royal Society Interface, 10(88), 20130638.
14. Kao, Y. T., Saxena, C., He, T. F., Guo, L., Wang, L., Sancar, A., & Zhong, D. (2008). Journal of the American Chemical Society, 130(39), 13132-13139.
15. Henbest, K. B., Maeda, K., Hore, P. J., Joshi, M., Bacher, A., Bittl, R., ... & Schleicher, E. (2008). Proceedings of the National Academy of Sciences, 105(38), 14395-14399.
16. Kattnig, D. R., Solov'yov, I. A., & Hore, P. J. (2016). Physical Chemistry Chemical Physics, 18(18), 12443-12456.
17. Bialas, C., Jarocha, L. E., Henbest, K. B., Zollitsch, T. M., Kodali, G., Timmel, C. R., ... & Hore, P. J. (2016). J. Am. Chem. Soc, 138(51), 16584-16587.
18. Sheppard, D. M., Li, J., Henbest, K. B., Neil, S. R., Maeda, K., Storey, J., ... & Hore, P. J. (2017). Scientific Reports, 7.
19. Cailliez, F., Müller, P., Firmino, T., Pernot, P., & de la Lande, A. (2016). Journal of the American Chemical Society, 138(6), 1904-1915.
20. Sanders, M., Lin, Y., Wei, J., Bono, T., & Lindquist, R. G. (2014). Biosensors and Bioelectronics, 61, 95-101.
21. Wei, J., Liu, H., Khoshtariya, D. E., Yamamoto, H., Dick, A., & Waldeck, D. H. (2002). Angewandte Chemie International Edition, 41(24), 4700-4703.
22. Holland, J. T., Lau, C., Brozik, S., Atanassov, P., & Banta, S. (2011). Journal of the American Chemical Society, 133(48), 19262-19265.

23. Phillips, J. B., Jorge, P. E., & Muheim, R. (2010). Journal of the Royal Society Interface, 7(Suppl 2), S241-S256.
24. Liu, Y., Dolidze, T. D., Singhal, S., Khoshtariya, D. E., & Wei, J. (2015). The Journal of Physical Chemistry C, 119(27), 14900-14910.
25. Wei, J., Liu, H., Dick, A. R., Yamamoto, H., He, Y., & Waldeck, D. H. (2002). Journal of the American Chemical Society, 124(32), 9591-9599.
26. Weber, K., & Creager, S. E. (1994). Analytical Chemistry, 66(19), 3164-3172.
27. Khoshtariya, D. E., Wei, J., Liu, H., Yue, H., & Waldeck, D. H. (2003). Journal of the American Chemical Society, 125(25), 7704-7714.
28. Yin, X., Wierzbinski, E., Lu, H., Bezer, S., de Leon, A. R., Davis, K. L., ... & Waldeck, D. H. (2014). The Journal of Physical Chemistry A, 118(35), 7579-7589.
29. Kottke, T., Batschauer, A., Ahmad, M., & Heberle, J. (2006). Biochemistry, 45(8), 2472-2479.
30. Ritz, T., Thalau, P., Phillips, J. B., Wiltschko, R., & Wiltschko, W. (2004). Nature, 429(6988), 177-180.
31. Chapyshev, S. V., Misochko, E. Y., Akimov, A. V., Dorokhov, V. G., Neuhaus, P., Grote, D., & Sander, W. (2009). The Journal of organic chemistry, 74(19), 7238-7244.
32. Zeng, Z., Shi, X., Mabe, T., Christie, S., Gilmore, G., Smith, A. W., & Wei, J. (2017). Analytical Chemistry, 89(10), 5221-5229.

# CHAPTER VIII

# CONCLUDING

Chapter 2 and 3 presented a new $SiO_2$ topped nanoledge aperture structure for nanometric-sized protein trapping and sensing. For the nanoledge structure, we applied the decomposition and quantitative analysis of SP generation by a semi-analytical model, and numerical simulation of optical transmission spectra and RI sensitivity by a FDTD method, which certificated that nanoledge structure with on-top $SiO_2$ layer had the potential to be effectively applied in T-SPR for protein detection. Experimentally, TIRF imaging showed that proteins can diffuse into the nanoledge structure (with 280 nm open gap) by using similar size straight nanoslits (100 nm and 300 nm) to investigate the protein migration behavior. The diffusion of the labeled BSA into the nano-structure was measured by FCS with the results indicating that BSA molecules in the nanostructure undergo Brownian motion and have a diffusion coefficient of around 70 $\mu m^2/s$, which helped to estimate its hydrodynamic radius of 3 nm. Further studies of the protein trapping and potential sensing applications were provided by fabricating the subwavelength nanoledge device and testing the SPR optical transmission shift and RI sensitivity for determining the binding events between the mAb and a cancer biomarker f-PSA in the nanoledge cavity.

In chapter 4, after applying 1.34 mT magnetic field, $MnO_2$/ECNFs showed enhanced magneto-capacitance of 141.7 F $g^{-1}$ at the cyclic voltage sweeping rates of 5 mV $s^{-1}$. The capacitance of $MnO_2$/ECNFs was increased by 58.1% at the current density of 0.5

A $g^{-1}$ during the galvanostatic charge/discharge test. Meanwhile, in the presence of 1.34 mT magnetic field, the magneto-supercapacitor presented “low resistance shift” for bulk electrolyte and the $MnO_2$/ECNFs electrode. Longer charge/discharge time of the electrode is observed under magnetic field than that without magnetic field, while did not sacrifice its life cycle stability. The insightful discussion of the potential mechanism suggests that the magneto-supercapacitance enhancement can be primarily attributed to the magnetic susceptibility of $MnO_2$ induced electron spin energy degeneracy for facilitated electron transfer reaction, the magnetohydrodynamic impact on electrolyte transportation and improved cation intercalation/de-intercalation under the mT magnetic field, thus resulting in higher charge density at the electrode/electrolyte interfaces, thicker double layer, and lower internal resistance. This study may pave a way to the development of sustainable metal oxide-based supercapacitors with magneto-capacitance enhancement by applying a low magnetic field.

Chapter 5 demonstrates a new strategy for uniformly electrodepositing α-$MnO_2$ film on aligned ECNFs and the α-$MnO_2$ film was well characterized. In contrast to earlier studies with an inhomogeneous surface coverage, the reported α-$MnO_2$ film with a 4 h-45 μA electrodeposition was homogenous with a thickness of 1710 nm. From the electrocatalytic performance studies, the bifunctional catalyst system of α-$MnO_2$/ECNFs-GC displayed a 3.84-electron pathway through the rapid decomposition of hydrogen peroxide at the α-$MnO_2$ surfaces. The analysis of electron transfer kinetics suggested a faster hydrogen peroxide decomposition than its generation from reduction of oxygen, and a two-step four-electron pathway cycling mechanism was proposed to give an insightful

understanding of the electrocatalytic ORR at the bifunctional catalyst system. These findings represent significant improvement in stable metal oxide/carbonaceous nanomaterial-based oxygen reduction catalysts.

Chapter 6 demonstrates a new strategy for uniformly electrodepositing $Co_3O_4$ on well-aligned ECNFs with a constant low-current of 50 μA and the change in the mechanism of $Co_3O_4$ growth with the electrodeposition time was explored, which provides the three-stage kinetics of the $Co_3O_4$ growth process with a halfway growth at about 3.59 h. From the $Co_3O_4$ thickness dependent ORR performance, the GC electrode modified with $Co_3O_4$ /ECNFs (5 h electrodeposition) shows a high exchanged electron number of 3.48, which is ascribed to an effective confinement of hydrogen peroxide. Furthermore, a significant improvement in exchanged electron number can be achieved by applying an external magnetic field at a mT level due to the magnetic field polarization on unpaired electron spin of $Co_3O_4$ and the electron energy degeneracy which facilitates a faster rate of oxygen reduction by the $Co_3O_4$/ECNFs to fulfill a 4-electron pathway during the oxygen reduction reaction process.

In chapter 7, we used a home-setup opto-magnetic electrochemical system and, for the first time, observed the magnetic response of cryptochrome 1 which was immobilized as a monolayer at a solid (gold) electrode surface when the electrode was illuminated with a blue light. The oxidation current of the immobilized cryptochrome 1 increases monotonically with increasing magnetic field strength at a specific voltammetric scan rate. The electrochemical electron transfer kinetic study of the cryptochrome electrode by changing voltammetric scan rates demonstrates that the heterogenous electron transfer rate

constant increases with the increasing magnetic field strength as well. We attempted to shed some light to the magnetic field effect on this system by considering the contribution of the enhanced electron energy states to the activation energy due to magnetic field induced degeneracy of the unpaired electron spin in the light-excited cryptochromes. A semi-quantitative relationship of the electron transfer rate constant with the magnetic field strength was established which may direct future studies of novel cryptochrome-inspired magneto-opto-electronics. This study is a breakthrough of the magnetic response of cryptochromes which presents great significance and potential for successful convergence of the "nature aware" paradigm aiming at their biomimetic magnetoreception functions and may open an avenue to new types of bioinspired opto-magneto-electronic.

## APPENDIX A

## SURFACE PLASMON GENERATION

Semi-analytical analysis: for the plane-wave basis, the magnetic field below the slit H(y,z) can be written as[1-2]

$$H_{below-slit}(y,z) = (N_p)^{-1/2} \exp(-ikn_1 z) + \int_{-\infty}^{\infty} dur_u \exp(ikn_1 uy) \exp(ikn_1 vz) \qquad \text{(S1)}$$

where $r_u$ is the plane-wave reflection coefficients, and u and v are applied for numerical integration with $u^2+v^2=1$.

Meanwhile, the magnetic field inside the slit H(y,z) could also be obtained:

$$H_{inside-slit}(y,z) = t_0 f_0(y,z) \qquad \text{(S2)}$$

with the fundamental mode:

$$f_0(y,z) = (N_0)^{-1/2} \exp(-ikn_1 z)(|y| < w/2) or 0(|y| \geq w/2) \qquad \text{(S3)}$$

and the transmission mode:

$$t_0 = \frac{2(N_0 / N_p)^{1/2}}{(n_1 / n_2) w' I_0 + 1} \qquad \text{(S4)}$$

by matching the perfectly-conducting (PC) boundary conditions at z=0 due to the assumption of continuity of $E_y$ and $H_x$,[3] and the reflection mode

$$r_u = \delta(0) - t_0 \left( N_0 / N_p \right)^{1/2} w' \frac{n_1}{n_2 \left(1-u^2\right)^{1/2}} \quad \text{(S5)}$$

where $\delta$ represents the Dirac distribution,[4] w' represents the normalized width, and the normalization constants $N_0$ and $N_p$ for the power flow on the slit aperture being unitary are given by $N_0=w/(2\varepsilon n_2)$ and $N_p= w/(2\varepsilon n_1)$, respectively.[1]

Python Numerical Calculations were used for solving the semi-analytical model.[5]

```
import numpy as N
from scipy import special
def I0_integrand(u, w):
    return N.sinc(N.outer(u, w)) ** 2
def I1_integrand(u, w, gamma):
    v = N.sqrt(N.asarray(1 - u ** 2, dtype=complex))
    wu = N.outer(u, w)
    return N.sinc(wu) * N.exp(-1j * N.pi * wu) / (v + gamma)[:, N.newaxis]
def lalanne_integral(func, order=20, *args):
    points, weights = special.orthogonal.p_roots(order)
    x1, w1 = (N. pi / 4) * (points + 1), (N.pi / 4) * weights
    x2, w2 = (points + 1) / 2, weights / 2
    gauss1 = func(N.cos(x1), *args) + func(-N.cos(x1), *args)
    uuu = 1 / x2 - 1
    uu = N.sqrt(uuu ** 2 + 1)
    gauss2 = (func(uu, *args) + func(-uu, *args)) \
        * (((uuu + 1) ** 2) / uu)[:, N.newaxis]
    return (w1[:, N.newaxis] * gauss1).sum(axis=0) \
        - 1j * (w2[:, N.newaxis] * gauss2).sum(axis=0)
def calc_I0(w_norm):
    return lalanne_integral(I0_integrand, 20, w_norm)
def calc_I1(w_norm, epsilon, n):
    gamma_SP = -N.sqrt(n ** 2 / (n ** 2 + epsilon))
    return lalanne_integral(I1_integrand, 120, w_norm, gamma_SP)
def interface_calculation(w, wl, epsilon, n1, n2, theta):
    w_norm = w * n1 / wl
    temp = (n1 / n2) * w_norm * calc_I0(w_norm)
    r0 = (temp - 1) / (temp + 1)
    alpha = (-1j * (1 - r0) * calc_I1(w_norm, epsilon, n1)
        * N.sqrt((w_norm * n1 ** 2 / (n2 * N.pi))
        * (N.sqrt(N.abs(epsilon)) / (-epsilon - n1 ** 2))))
    t0 = ((1 - r0) * N.sinc(w_norm * N.sin(theta))
        ) * N.sqrt(n1 / (n2 * N.cos(theta)))
    beta = -alpha * t0 / (1 - r0)
    return r0, t0, alpha, beta
def calculation():
    w = N.array([0.1,0.2,0.3,0.4,0.5,0.6,0.7,0.8,0.9,1.0])
    epsilon = -10.21 + 1.43j
```

```
        I0 = calc_I0(w)
        I1 = calc_I1(w, epsilon, 1.0)
        print                                                   "                                                   w'
{0[0]:10.2}{0[1]:10.2}{0[2]:10.2}{0[3]:10.2}{0[4]:10.2}{0[5]:10.2}{0[6]:10.2}{0[7]:10.2}{0[8]:10.2}{0[9]:10.2}".f
ormat(w)
        print                                                   '                                                   I0
{0[0]:10.2f}{0[1]:10.2f}{0[2]:10.2f}{0[3]:10.2f}{0[4]:10.2f}{0[5]:10.2f}{0[6]:10.2f}{0[7]:10.2f}{0[8]:10.2f}{0[9]:1
0.2f}'.format(I0)
        print                                                   '                                                   I1
{0[0]:10.2f}{0[1]:10.2f}{0[2]:10.2f}{0[3]:10.2f}{0[4]:10.2f}{0[5]:10.2f}{0[6]:10.2f}{0[7]:10.2f}{0[8]:10.2f}{0[9]:1
0.2f}'.format(I1)
        w = N.array([0.1,0.2,0.3,0.4,0.5,0.6,0.7,0.8,0.9,1.0])
        epsilon = -17.94 + 1.61j
        I0 = calc_I0(w)
        I1 = calc_I1(w, epsilon, 1.0)
        print                                                   "                                                   w'
{0[0]:10.2}{0[1]:10.2}{0[2]:10.2}{0[3]:10.2}{0[4]:10.2}{0[5]:10.2}{0[6]:10.2}{0[7]:10.2}{0[8]:10.2}{0[9]:10.2}".f
ormat(w)
        print                                                   '                                                   I0
{0[0]:10.2f}{0[1]:10.2f}{0[2]:10.2f}{0[3]:10.2f}{0[4]:10.2f}{0[5]:10.2f}{0[6]:10.2f}{0[7]:10.2f}{0[8]:10.2f}{0[9]:1
0.2f}'.format(I0)
        print                                                   '                                                   I1
{0[0]:10.2f}{0[1]:10.2f}{0[2]:10.2f}{0[3]:10.2f}{0[4]:10.2f}{0[5]:10.2f}{0[6]:10.2f}{0[7]:10.2f}{0[8]:10.2f}{0[9]:1
0.2f}'.format(I1)
        w = N.array([0.1,0.2,0.3,0.4,0.5,0.6,0.7,0.8,0.9,1.0])
        epsilon = -26.27 + 1.85j
        I0 = calc_I0(w)
        I1 = calc_I1(w, epsilon, 1.0)
        print                                                   "                                                   w'
{0[0]:10.2}{0[1]:10.2}{0[2]:10.2}{0[3]:10.2}{0[4]:10.2}{0[5]:10.2}{0[6]:10.2}{0[7]:10.2}{0[8]:10.2}{0[9]:10.2}".f
ormat(w)
        print                                                   '                                                   I0
{0[0]:10.2f}{0[1]:10.2f}{0[2]:10.2f}{0[3]:10.2f}{0[4]:10.2f}{0[5]:10.2f}{0[6]:10.2f}{0[7]:10.2f}{0[8]:10.2f}{0[9]:1
0.2f}'.format(I0)
        print                                                   '                                                   I1
{0[0]:10.2f}{0[1]:10.2f}{0[2]:10.2f}{0[3]:10.2f}{0[4]:10.2f}{0[5]:10.2f}{0[6]:10.2f}{0[7]:10.2f}{0[8]:10.2f}{0[9]:1
0.2f}'.format(I1)
        w = N.array([0.1,0.2,0.3,0.4,0.5,0.6,0.7,0.8,0.9,1.0])
        epsilon = -35.80 + 2.43j
        I0 = calc_I0(w)
        I1 = calc_I1(w, epsilon, 1.0)
        print                                                   "                                                   w'
{0[0]:10.2}{0[1]:10.2}{0[2]:10.2}{0[3]:10.2}{0[4]:10.2}{0[5]:10.2}{0[6]:10.2}{0[7]:10.2}{0[8]:10.2}{0[9]:10.2}".f
ormat(w)
        print                                                   '                                                   I0
{0[0]:10.2f}{0[1]:10.2f}{0[2]:10.2f}{0[3]:10.2f}{0[4]:10.2f}{0[5]:10.2f}{0[6]:10.2f}{0[7]:10.2f}{0[8]:10.2f}{0[9]:1
0.2f}'.format(I0)
        print                                                   '                                                   I1
{0[0]:10.2f}{0[1]:10.2f}{0[2]:10.2f}{0[3]:10.2f}{0[4]:10.2f}{0[5]:10.2f}{0[6]:10.2f}{0[7]:10.2f}{0[8]:10.2f}{0[9]:1
0.2f}'.format(I1)
        w = N.array([0.1,0.2,0.3,0.4,0.5,0.6,0.7,0.8,0.9,1.0])
        epsilon = -46.05 + 3.11j
        I0 = calc_I0(w)
        I1 = calc_I1(w, epsilon, 1.0)
        print                                                   "                                                   w'
```

```
{0[0]:10.2}{0[1]:10.2}{0[2]:10.2}{0[3]:10.2}{0[4]:10.2}{0[5]:10.2}{0[6]:10.2}{0[7]:10.2}{0[8]:10.2}{0[9]:10.2}".f
ormat(w)
        print                                                                                                   '                                                                                                   I0
{0[0]:10.2f}{0[1]:10.2f}{0[2]:10.2f}{0[3]:10.2f}{0[4]:10.2f}{0[5]:10.2f}{0[6]:10.2f}{0[7]:10.2f}{0[8]:10.2f}{0[9]:1
0.2f}'.format(I0)
        print                                                                                                   '                                                                                                   I1
{0[0]:10.2f}{0[1]:10.2f}{0[2]:10.2f}{0[3]:10.2f}{0[4]:10.2f}{0[5]:10.2f}{0[6]:10.2f}{0[7]:10.2f}{0[8]:10.2f}{0[9]:1
0.2f}'.format(I1)
        w = N.array([0.1,0.2,0.3,0.4,0.5,0.6,0.7,0.8,0.9,1.0])
        epsilon = -57.32 + 3.87j
        I0 = calc_I0(w)
        I1 = calc_I1(w, epsilon, 1.0)
        print                                                                                                   "                                                                                                   w'
{0[0]:10.2}{0[1]:10.2}{0[2]:10.2}{0[3]:10.2}{0[4]:10.2}{0[5]:10.2}{0[6]:10.2}{0[7]:10.2}{0[8]:10.2}{0[9]:10.2}".f
ormat(w)
        print                                                                                                   '                                                                                                   I0
{0[0]:10.2f}{0[1]:10.2f}{0[2]:10.2f}{0[3]:10.2f}{0[4]:10.2f}{0[5]:10.2f}{0[6]:10.2f}{0[7]:10.2f}{0[8]:10.2f}{0[9]:1
0.2f}'.format(I0)
        print                                                                                                   '                                                                                                   I1
{0[0]:10.2f}{0[1]:10.2f}{0[2]:10.2f}{0[3]:10.2f}{0[4]:10.2f}{0[5]:10.2f}{0[6]:10.2f}{0[7]:10.2f}{0[8]:10.2f}{0[9]:1
0.2f}'.format(I1)
        w = N.array([0.1,0.2,0.3,0.4,0.5,0.6,0.7,0.8,0.9,1.0])
        epsilon = -68.98 + 4.68j
        I0 = calc_I0(w)
        I1 = calc_I1(w, epsilon, 1.0)
        print                                                                                                   "                                                                                                   w'
{0[0]:10.2}{0[1]:10.2}{0[2]:10.2}{0[3]:10.2}{0[4]:10.2}{0[5]:10.2}{0[6]:10.2}{0[7]:10.2}{0[8]:10.2}{0[9]:10.2}".f
ormat(w)
        print                                                                                                   '                                                                                                   I0
{0[0]:10.2f}{0[1]:10.2f}{0[2]:10.2f}{0[3]:10.2f}{0[4]:10.2f}{0[5]:10.2f}{0[6]:10.2f}{0[7]:10.2f}{0[8]:10.2f}{0[9]:1
0.2f}'.format(I0)
        print                                                                                                   '                                                                                                   I1
{0[0]:10.2f}{0[1]:10.2f}{0[2]:10.2f}{0[3]:10.2f}{0[4]:10.2f}{0[5]:10.2f}{0[6]:10.2f}{0[7]:10.2f}{0[8]:10.2f}{0[9]:1
0.2f}'.format(I1)
    if __name__ == '__main__':
        calculation()
```

Table S2.1. $I_0$ and $I_1$ for gold at different wavelengths when the refractive index $n_1$ is 1.45 ($I_0$ equals to each other for different $\lambda$)

| W' | $I_0$ | 600nm ε=-10.21+1.43i $I_1$ | 700nm ε=-17.94+1.61i $I_1$ | 800nm ε=-26.27+1.85i $I_1$ | 900nm ε=-35.80+2.43i $I_1$ | 1000nm ε=-46.05+3.11i $I_1$ | 1100nm ε=-57.32+3.87i $I_1$ | 1200nm ε= -68.98+4.68i $I_1$ |
|---|---|---|---|---|---|---|---|---|
| 0.1 | 3.09-4.09i | -0.05-2.74i | 0.20-2.84i | 0.34-2.88i | 0.43-2.91i | 0.49-2.92i | 0.54-2.93i | 0.57-2.94i |
| 0.2 | 2.94-2.61i | 0.64-2.40i | 0.92-2.45i | 1.06-2.46i | 1.16-2.47i | 1.23-2.47i | 1.28-2.47i | 1.32-2.46i |
| 0.3 | 2.72-1.69i | 1.12-1.90i | 1.40-1.87i | 1.54-1.85i | 1.64-1.83i | 1.71-1.81i | 1.76-1.80i | 1.80-1.78i |
| 0.4 | 2.43-1.05i | 1.36-1.32i | 1.61-1.23i | 1.74-1.17i | 1.82-1.12i | 1.88-1.09i | 1.92-1.06i | 1.96-1.04i |
| 0.5 | 2.13-0.64i | 1.37-0.77i | 1.57-0.62i | 1.66-0.54i | 1.72-0.48i | 1.77-0.43i | 1.80-0.39i | 1.82-0.36i |
| 0.6 | 1.82-0.34i | 1.20-0.32i | 1.32-0.16i | 1.38-0.06i | 1.42+0.01i | 1.44+0.06i | 1.45+0.10i | 1.47+0.13i |
| 0.7 | 1.54-0.18i | 0.91-0.04i | 0.97+0.12i | 0.99+0.21i | 1.00+0.27i | 1.01+0.32i | 1.01+0.36i | 1.01+0.38i |
| 0.8 | 1.30-0.10i | 0.61+0.07i | 0.62+0.20i | 0.61+0.28i | 0.60+0.32i | 0.59+0.36i | 0.58+0.38i | 0.57+0.40i |
| 0.9 | 1.11-0.06i | 0.35+0.05i | 0.33+0.13i | 0.31+0.18i | 0.29+0.21i | 0.28+0.23i | 0.27+0.24i | 0.26+0.25i |
| 1.0 | 0.97-0.07i | 0.19-0.06i | 0.17-0.02i | 0.15-0.01i | 0.13+0.00i | 0.12+0.01i | 0.11+0.01i | 0.10+0.02i |

Table S2.2. $I_0$ and $I_1$ for gold at different wavelengths when the refractive index $n_1$ is 1.0 ($I_0$ equals to each other for different $\lambda$)

| w' | $I_0$ | 600nm ε=-10.21+1.43i $I_1$ | 700nm ε=-17.94+1.61i $I_1$ | 800nm ε=-26.27+1.85i $I_1$ | 900nm ε=-35.80+2.43i $I_1$ | 1000nm ε=-46.05+3.11i $I_1$ | 1100nm ε=-57.32+3.87i $I_1$ | 1200nm ε= -68.98+4.68i $I_1$ |
|---|---|---|---|---|---|---|---|---|
| 0.1 | 3.09-4.09i | 0.27-2.89i | 0.44-2.92i | 0.53-2.93i | 0.59-2.94i | 0.63-2.94i | 0.67-2.95i | 0.69-2.95i |
| 0.2 | 2.94-2.61i | 0.99-2.48i | 1.18-2.47i | 1.27-2.47i | 1.34-2.46i | 1.39-2.46i | 1.42-2.45i | 1.45-2.45i |
| 0.3 | 2.72-1.69i | 1.48-1.89i | 1.66-1.83i | 1.75-1.80i | 1.82-1.78i | 1.86-1.76i | 1.90-1.75i | 1.92-1.74i |
| 0.4 | 2.43-1.05i | 1.69-1.22i | 1.84-1.12i | 1.92-1.06i | 1.97-1.03i | 2.01-1.00i | 2.04-0.97i | 2.06-0.96i |
| 0.5 | 2.13-0.64i | 1.63-0.60i | 1.74-0.47i | 1.79-0.40i | 1.83-0.35i | 1.85-0.31i | 1.87-0.28i | 1.89-0.26i |
| 0.6 | 1.82-0.34i | 1.37-0.12i | 1.43+0.02i | 1.45+0.09i | 1.47+0.15i | 1.48+0.18i | 1.49+0.21i | 1.49+0.24i |
| 0.7 | 1.54-0.18i | 1.00+0.16i | 1.01+0.28i | 1.01+0.35i | 1.01+0.40i | 1.00+0.43i | 1.00+0.46i | 1.00+0.48i |
| 0.8 | 1.30-0.10i | 0.62+0.24i | 0.60+0.33i | 0.58+0.38i | 0.57+0.41i | 0.56+0.44i | 0.55+0.45i | 0.54+0.47i |
| 0.9 | 1.11-0.06i | 0.33+0.16i | 0.29+0.21i | 0.27+0.24i | 0.25+0.26i | 0.24+0.27i | 0.23+0.28i | 0.22+0.28i |
| 1.0 | 0.97-0.07i | 0.16-0.01i | 0.13+0.01i | 0.11+0.01i | 0.10+0.02i | 0.09+0.02i | 0.08+0.02i | 0.07+0.02i |

Table S2.3. $I_0$ and $I_1$ for gold at different wavelengths when the refractive index $n_1$ is 1.45 ($I_0$ equals to each other for different λ) with more detailed w' range

| w' | $I_0$ | 600nm ε=-10.21+1.43i $I_1$ | 700nm ε=-17.94+1.61i $I_1$ | 800nm ε=-26.27+1.85i $I_1$ | 900nm ε=-35.80+2.43i $I_1$ | 1000nm ε=-46.05+3.11i $I_1$ | 1100nm ε=-57.32+3.87i $I_1$ | 1200nm ε= -68.98+4.68i $I_1$ |
|---|---|---|---|---|---|---|---|---|
| 0.02 | 3.14-7.35i | -0.73-2.86i | -0.49-2.98i | -0.37-3.03i | -0.29-3.06i | -0.23-3.08i | -0.19-3.09i | -0.16-3.10i |
| 0.04 | 3.13-5.93i | -0.55-2.84i | -0.31-2.96i | -0.19-3.01i | -0.10-3.04i | -0.05-3.06i | -0.00-3.07i | 0.03-3.08i |
| 0.06 | 3.12-5.19i | -0.37-2.82i | -0.13-2.93i | -0.01-2.98i | 0.08-3.01i | 0.14-3.02i | 0.18-3.04i | 0.22-3.04i |
| 0.08 | 3.11-4.54i | -0.21-2.79i | 0.04-2.89i | 0.17-2.94i | 0.25-2.96i | 0.32-2.98i | 0.36-2.99i | 0.40-3.00i |
| 0.12 | 3.07-3.73i | 0.10-2.69i | 0.36-2.78i | 0.50-2.82i | 0.59-2.84i | 0.65-2.85i | 0.70-2.86i | 0.74-2.86i |
| 0.14 | 3.04-3.37i | 0.25-2.63i | 0.52-2.71i | 0.65-2.74i | 0.75-2.76i | 0.81-2.77i | 0.86-2.78i | 0.90-2.78i |
| 0.16 | 3.01-3.07i | 0.39-2.56i | 0.66-2.63i | 0.80-2.66i | 0.89-2.67i | 0.96-2.68i | 1.01-2.68i | 1.05-2.68i |
| 0.18 | 2.98-2.81i | 0.52-2.49i | 0.79-2.54i | 0.94-2.56i | 1.03-2.57i | 1.10-2.58i | 1.15-2.58i | 1.19-2.58i |
| 0.22 | 2.90-2.39i | 0.76-2.31i | 1.04-2.34i | 1.18-2.35i | 1.28-2.35i | 1.35-2.35i | 1.40-2.34i | 1.44-2.34i |
| 0.24 | 2.86-2.18i | 0.86-2.22i | 1.14-2.23i | 1.29-2.23i | 1.39-2.23i | 1.46-2.22i | 1.51-2.22i | 1.55-2.21i |

Table S2.4. $I_0$ and $I_1$ for gold at different wavelengths when the refractive index $n_1$ is 1.0 ($I_0$ equals to each other for different λ) with more detailed w' range

| w' | $I_0$ | 600nm ε=-10.21+1.43i $I_1$ | 700nm ε=-17.94+1.61i $I_1$ | 800nm ε=-26.27+1.85i $I_1$ | 900nm ε=-35.80+2.43i $I_1$ | 1000nm ε=-46.05+3.11i $I_1$ | 1100nm ε=-57.32+3.87i $I_1$ | 1200nm ε= -68.98+4.68i $I_1$ |
|---|---|---|---|---|---|---|---|---|
| 0.02 | 3.14-7.35i | -0.44-3.02i | -0.28-3.07i | -0.20-3.09i | -0.14-3.10i | -0.10-3.11i | -0.07-3.12i | -0.05-3.12i |
| 0.04 | 3.13-5.93i | -0.26-3.01i | -0.09-3.05i | -0.01-3.07i | 0.05-3.08i | 0.09-3.09i | 0.12-3.09i | 0.15-3.10i |
| 0.06 | 3.12-5.19i | -0.08-2.98i | 0.09-3.02i | 0.18-3.03i | 0.24-3.05i | 0.28-3.05i | 0.31-3.06i | 0.33-3.06i |
| 0.08 | 3.11-4.54i | 0.10-2.94i | 0.27-2.97i | 0.36-2.99i | 0.42-3.00i | 0.46-3.01i | 0.49-3.01i | 0.52-3.01i |
| 0.12 | 3.07-3.73i | 0.43-2.82i | 0.60-2.85i | 0.69-2.86i | 0.76-2.87i | 0.80-2.87i | 0.84-2.87i | 0.86-2.87i |
| 0.14 | 3.04-3.37i | 0.58-2.75i | 0.76-2.77i | 0.85-2.78i | 0.92-2.78i | 0.96-2.78i | 1.00-2.78i | 1.02-2.78i |
| 0.16 | 3.01-3.07i | 0.73-2.67i | 0.91-2.68i | 1.00-2.68i | 1.07-2.68i | 1.11-2.68i | 1.15-2.68i | 1.18-2.68i |
| 0.18 | 2.98-2.81i | 0.86-2.58i | 1.05-2.58i | 1.14-2.58i | 1.21-2.58i | 1.26-2.58i | 1.29-2.57i | 1.32-2.57i |
| 0.22 | 2.90-2.39i | 1.11-2.37i | 1.30-2.36i | 1.39-2.35i | 1.46-2.34i | 1.51-2.33i | 1.54-2.32i | 1.57-2.32i |
| 0.24 | 2.86-2.18i | 1.22-2.26i | 1.40-2.23i | 1.50-2.22i | 1.57-2.21i | 1.61-2.20i | 1.65-2.19i | 1.68-2.18i |

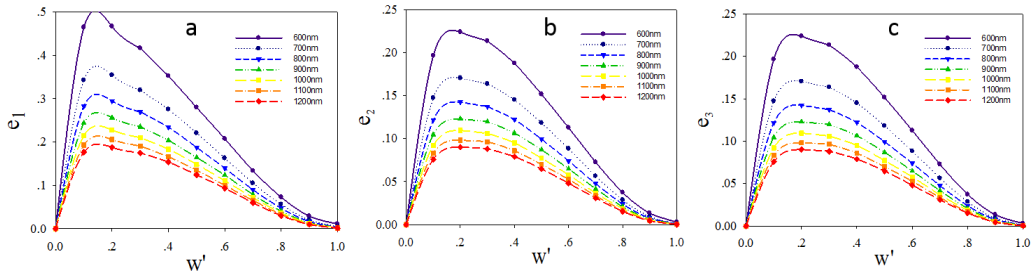


Figure S.2.1. SPP Generation.

$$b_j = a_1 a_1 ... a_p \qquad \text{(S6)}$$

$$c_k = b_1 b_2 ... b_q \qquad \text{(S7)}$$

$$\mu\left(a_i / b_j\right) = \frac{No.ofa_i}{\sum_{i=1}^{n=p} No.ofa_i} \qquad \text{(S8)}$$

$$\mu\left(b_j / c_k\right) = \frac{No.ofb_j}{\sum_{j=1}^{n=q} No.ofb_j} \qquad \text{(S9)}$$

$$\mu\left(a_i / c_k\right) = \sum_{j=1}^{n=q} \mu\left(a_i / b_j\right) \mu\left(b_j / c_k\right) \qquad \text{(S10)}$$

where p and q represents the number of observable random variables (here are $w_1$ or $w_2$, λ, $n_1$, $n_2/n_3/n_4$); μ(m/n) represents the influence factor coefficient of m on the calculation of n. With some acceptable algorithm approximation assumptions,[7] such as (sin(q))~(q), (\)~(*), and (t+1)~t.

Based on the factor analysis, below is the scheme of the relationship between independent variables (factors) (w, λ, $n_2/n_3/n_4$, $n_1$) and resulted parameters (w', $I_0$, $I_1$, e, v, and ϵ).

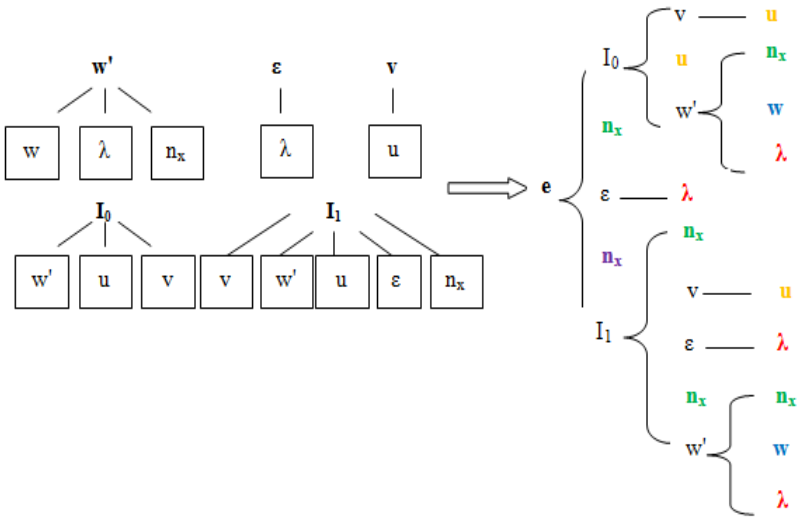


Figure S2.2. The relationships between the factors of w, λ, $n_2/n_3/n_4$, $n_1$ and u on w', $I_0$, $I_1$, e, v, and ϵ, respectively.[6]

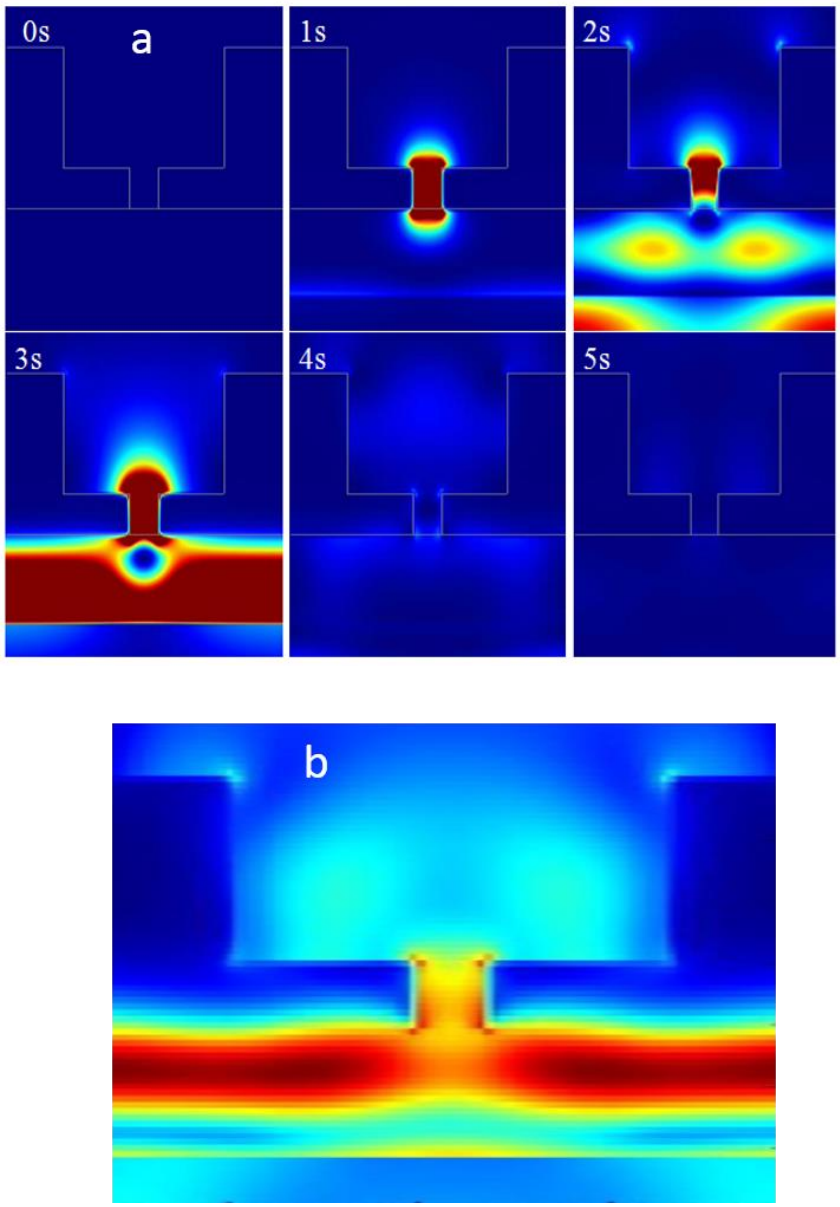


Figure S.2.3. FDTD simulation.

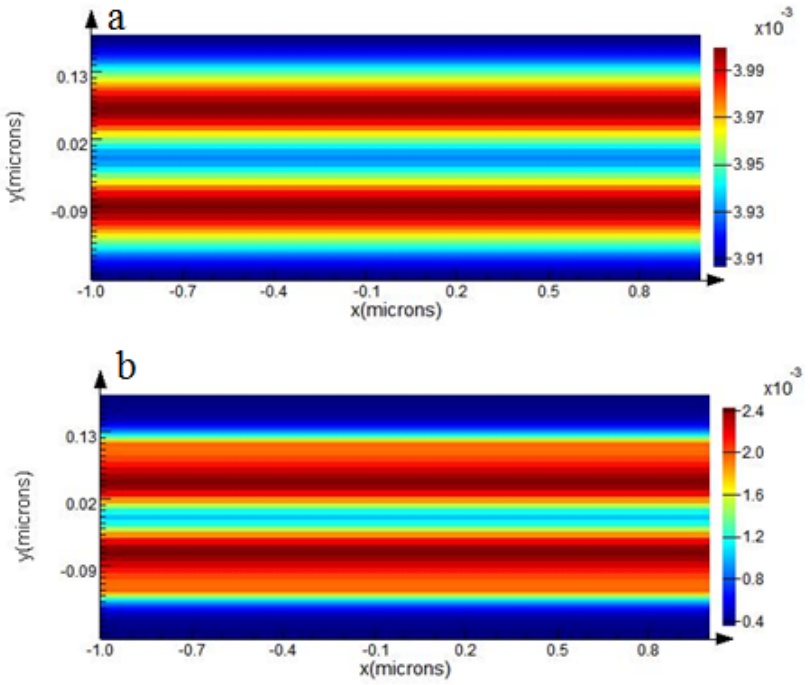


Figure S.2.4. FDTD simulation for EM field.

Table S2.5 Maximum Transmission of $w_2$-$w_1$ nanoslit systems with different $w_1$ and $w_2$.

| $w_1$ (nm) | $w_2$ (nm) | | | | | |
|---|---|---|---|---|---|---|
| | 300 | 280 | 260 | 240 | 220 | 200 |
| 100 | 0.220 | 0.208 | 0.190 | 0.171 | 0.151 | 0.132 |
| 90 | 0.228 | 0.215 | 0.199 | 0.180 | 0.161 | 0.142 |
| 80 | 2.231 | 0.221 | 0.207 | 0.191 | 0.172 | 0.154 |
| 70 | 0.229 | 0.223 | 0.213 | 0.200 | 0.185 | 0.168 |
| 60 | 0.256 | 0.238 | 0.217 | 0.203 | 0.193 | 0.181 |
| 50 | **0.283** | 0.270 | 0.251 | 0.231 | 0.208 | 0.185 |
| 40 | 0.279 | 0.274 | 0.266 | 0.255 | 0.241 | 0.225 |
| 30 | 0.194 | 0.199 | 0.202 | 0.203 | 0.204 | 0.204 |
| 20 | 0.121 | 0.118 | 0.114 | 0.110 | 0.106 | 0.103 |
| 10 | 0.023 | 0.020 | 0.018 | 0.016 | 0.014 | 0.013 |

Table S2.6. The SPP generation efficiency $e_1$, $e_2$, $e_3$ for the nanoledge geometry $w_2/w_1$ of 280nm-50nm.

| $n_2=n_3=n_4$ | $e_1$ | $e_2$ | $e_3$ | $\Delta e$ |
|---|---|---|---|---|
| 1 | 0.4791 | 0.1806 | 0.1613 | 0 |
| 1.1 | 0.4223 | 0.2123 | 0.1589 | -0.0275 |
| 1.2 | 0.3821 | 0.2508 | 0.1542 | -0.0339 |
| 1.3 | 0.3407 | 0.2823 | 0.1498 | -0.0482 |
| 1.4 | 0.3107 | 0.3158 | 0.1426 | -0.0519 |
| 1.5 | 0.2803 | 0.3483 | 0.1306 | -0.0618 |

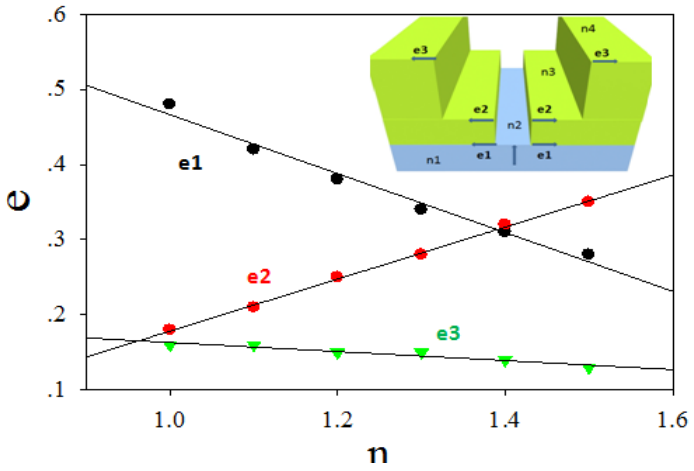


Figure S2.5. Individual SPP generation efficiency of the three interfaces of nanoledge with $w_2/w_1$ 280nm-50 nm as a function of refractive index $n_2=n_3=n_4$, $n_1$ is 1.45 for quartz.

Focused Ion Beam Fabrication of Nanoledge Structures: quartz slides (25×25 $mm^2$) were used as the substrate for sample preparation. These were rinsed first with acetone in an ultrasonic bath for 10 min, and then rinsed with deionized water and dried under a nitrogen stream. Then the slides were placed on a hot plate with the temperature set at 180 $^0C$ to remove any traces of water remaining. These slides were exposed to an oxygen plasma for 300 s at a pressure of 200 mTorr to remove organic contaminants on the surface. A 250 nm thin layer of gold (99.95%, Alfa Aesar, USA) was evaporated onto the cleaned quartz slides at around $2.0\times10^{-6}$ Torr, at a deposition rate of 0.2 nm $s^{-1}$ in an electron beam evaporator. A 2.5 nm layer of titanium was first coated before the gold to promote adhesion to the substrate. These gold films were stored under nitrogen in sealed vials prior to FIB milling. The fabrication of the nanoledge structure was done using a dual-beam focused ion beam system (Seiko Instruments SMI3050SE). The focused ion beam column was equipped with a $Ga^+$ source and operated at 30 keV under a 5 pA beam current. The

nanoledge structure measured ~50 nm wide in the Au-quartz interface and ~250 nm wide in the Au-air interface, with a slit length of 30 μm. A vector scan with different line densities were used to introduce different etching depths into the Au film to obtain different widths in the two interfaces. The total area of the array was maintained to be $30\times30\ \mu m^2$.

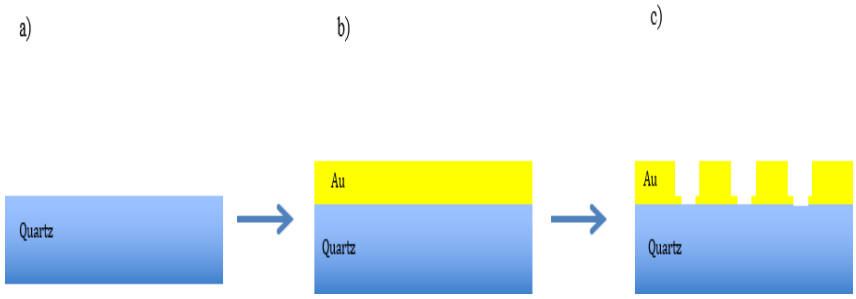


Figure S2.6. Schematic of FIB milling routine employed for fabricating the nanoledge structure. a) Cleaning the substrates b) Thin metal film deposition c) FIB milling of the targeted nanoledge structure.

Electron Beam Lithography Fabrication of Nanoledge Structures: electron beam lithography (EBL, Raith e-Line) was used for the fabrication of Au nanoledge structures in arrays (30×30 $\mu m^2$). Three consecutive EBL steps were followed to achieve the final structure as described as follow. The fabrication scheme is illustrated in Fig S7.

Conductive indium tin oxide coated glass slides (ITO) (Delta's Technologies) were used as the substrates to minimize charging during the fabrication. ITO substrates were rinsed using three solvents: acetone, methanol and iso-propanol; ultrasonication was done in each solvent for 5 min. The ITO substrates were rinsed with DI water and dried with a nitrogen stream. These substrates were baked at 180 $^oC$ for 2 min to remove any moisture from the surface. In step one, as illustrated Fig S7 (a), poly-methyl-methacrylate (950 A4 PMMA, Microchem) was spun on the substrate at a speed of 1500 rpm for 40 s using a spin processor (Laurell *WS-400-6NPP-LITE*) and baked on a hot plate at 180 $^0C$ for 5 min. EBL was performed at an acceleration voltage of 20 keV and with an exposure dose of 300 $\mu C/cm^3$ using a 7.5 μm aperture to write the markers on PMMA in order to define the

coordinate system on the substrate which will act as the reference on the subsequent steps. The sample was then developed for 90 s in a developing solvent consisting of methyl isobutyl ketone and isopropanol in a 3:1 ratio to dissolve the exposed PMMA. Then gold was evaporated on to this sample to a thickness of 50 nm, with a 5 nm of Titanium to help the Au to better adhere to the substrate. The rate of evaporation was maintained at 0.3 Å $s^{-1}$ to allow smooth deposition of the metal. After the metal deposition, the samples were kept overnight in acetone to remove the remaining PMMA resist.

In step 2 (Fig S7 (b)), the substrate with the coordinates obtained from step one was taken and rinsed with acetone, methanol, iso-propanol: 3 minutes in each solvent, in order to remove any dirt particles on the substrate. The substrates were then dried with a nitrogen stream and baked at 90 $^0$C for 4 min to remove any moisture from the surface. Negative e-beam resist (maN 2403, Micro Resist Technologies) was spun on the substrates at a speed of 3000 rpm for 30 s using the spin processor to obtain a final film thickness of 300 nm. The resist-coated substrates were baked for 60 s on a hot plate at 90 $^o$C. Then the resist–coated substrates were placed under the EBL system to make the 80 nm width nano-slits. Electron beam exposure was performed at an acceleration voltage of 20 keV using the 7.5 μm with an exposure dose of 100 μC/$cm^3$. The samples were developed using an alkaline developing solution (CD-26, MicroChem) for 90 s to dissolve the unexposed resist. Gold (Au) was evaporated on to the sample at a thickness of 50 nm, with a 5 nm Ti layer to promote adhesion. After the metal deposition, the remaining resist was removed by soaking in Remover PG 1165 under 90 $^o$C for about 60 min followed by 5 min sonication.

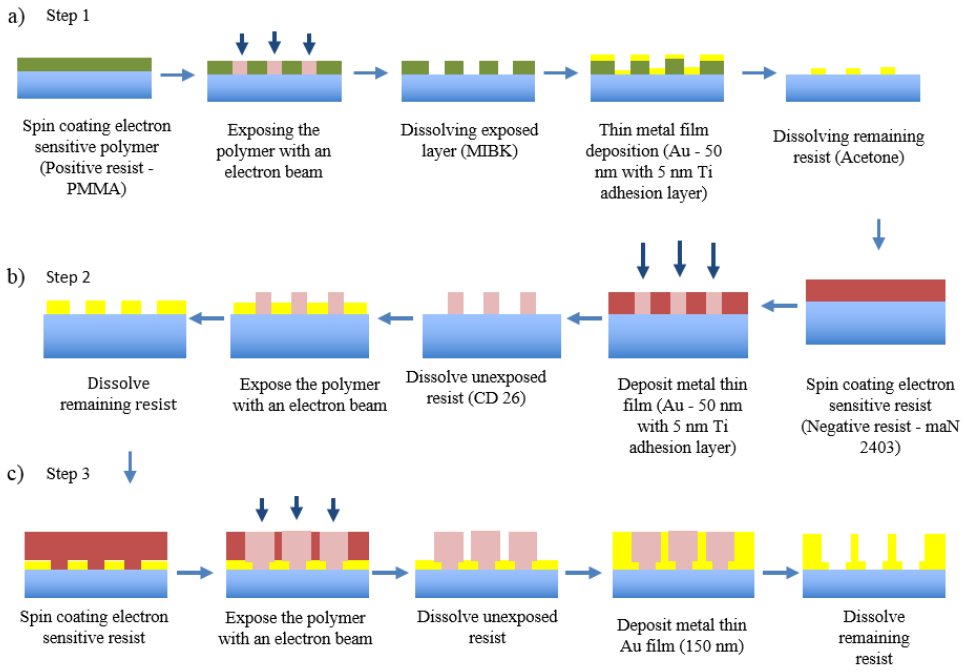


Figure S2.7. Schematic of steps followed in fabricating the Nanoledge structures using Electron Beam Lithography. a) Step 1 - Fabrication of alignment markers on the substrate b) Step 2 - Fabrication of 50 nm width slits using negative e-beam resist c) Step 3 – Alignment and fabrication of the 250 nm width slit on top of the bottom 50 nm slit to obtain the intended nanoledge structure.

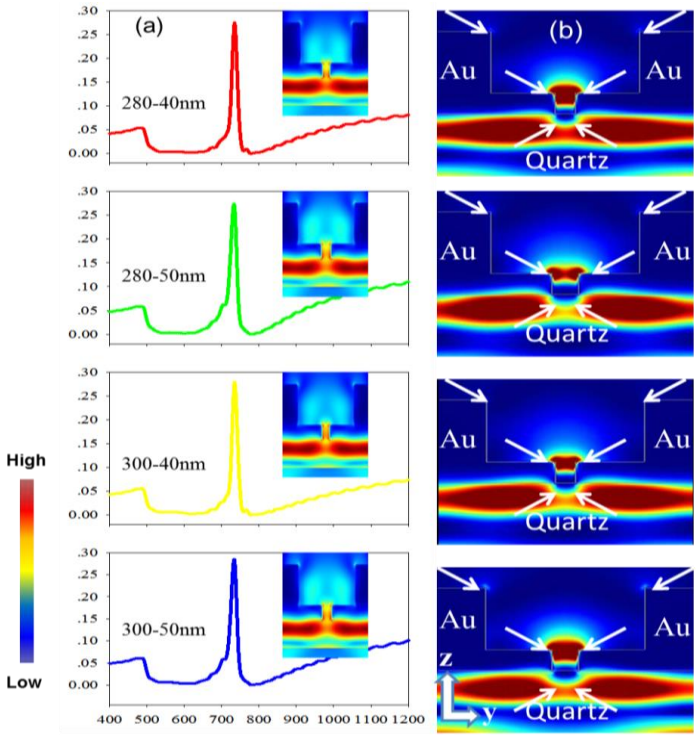


Figure S2.8. Panel (a) shows the calculated transmission spectra of the four $w_2$-$w_1$ nanoledge systems with the TM field profiles illustrated in the insets. Panel (b) the corresponding TE field dynamics at 3 seconds calculated for the four nanoledge systems.

In step three (Fig S7 (c)), the sample prepared in step 2 was taken and cleaned as previously described. The negative e-beam resist was spun coated as before with the same conditions and baked for 1 min in a hot plate at 90 $^{o}$C. The samples were again placed under the EBL system and the same exposure parameters were used as similar to step two. With the help of the pre-defined coordinates the second nanoslit array was overlaid right on the 80 nm nanoslit array. After the exposure, the sample was developed using the CD 26. Gold was deposited to a thickness of 150 nm. Lift-off of the remaining resist was performed as similar to step 2 in order to obtain the final nanoledge structure.

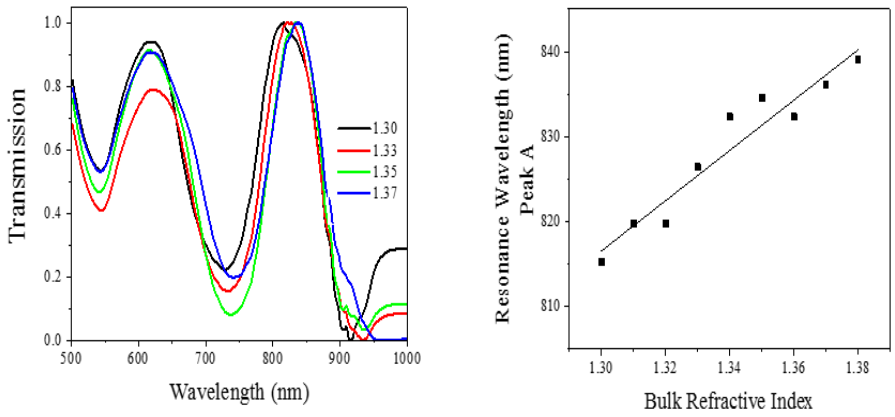


Figure. S2.9. Refractive index sensitivity measurements of EBL Fabricated nanoledge (see main Fig. 6a) were obtained by recording the transmission spectra of the nanoledges while changing the refractive index of the outside medium by using refractive index standards as illustrated in (a). Resonance wavelength of the peak A is plotted versus the refractive index in (b). Three lines depict the refractive index response of three different arrays of nanoledges. The slope of the lines gives the refractive index sensitivity which was calculated to be 311 $nmRIU^{-1}$ and standard deviation of the refractive index sensitivity between the three arrays is given as the error of this measurement.

References


1. Lalanne, P., Hugonin, J. P., & Rodier, J. C. (2006). JOSA A, 23(7), 1608-1615.
2. Wei, P. K., Chou, H. L., Cheng, Y. R., Wei, C. H., Fann, W., & Tegenfeldt, J. O. (2005). Optics communications, 253(1), 198-204.
3. Lalanne, P., Hugonin, J. P., & Rodier, J. C. (2005). Physical review letters, 95(26), 263902.
4. Chimento, P. (2013). Two-dimensional optics: diffraction and dispersion of surface plasmons. Quantumoptica Group, Leiden Institute of Physics (LION), Faculty of Science, Leiden University.
5. DuBridge, L. A. (1933). Physical Review, 43(9), 727.
6. Kline, P. (2014). An easy guide to factor analysis. Routledge.
7. Vazirani, V. V. (2013). Approximation algorithms. Springer Science & Business Media.

## APPENDIX B

## PROTEIN TRAPPING

Semi-analytical analysis and FDTD simulations: with the semi-analytical model, the SP excitation efficiency *e* for one side of the aperture is readily calculated with the following equations:

$$e_1 = \left|\alpha_1^+\left(w_1/2\right)\right|^2 = \left|\alpha_1^-\left(w_1/2\right)\right|^2 = \frac{4w_1^{'}n_1^3}{\pi n_2^2}\left|\frac{\varepsilon^{1/2}}{\varepsilon+n_1^2}\right|\left|\frac{I_1}{1+\left(n_1/n_2\right)w_1^{'}I_0}\right|^2 \qquad \text{(S1)}$$

in which

$$I_0 = \int_{-\infty}^{\infty} du\left[\sin\left(\pi w_1^{'}u\right)/\left(\pi w_1^{'}u\right)\right]^2/v \qquad \text{(S2)}$$

$$I_1 = \int_{-\infty}^{\infty} du\frac{\exp\left(-i\pi w_1^{'}u\right)\sin\left(\pi w_1^{'}u\right)/\left(\pi w_1^{'}u\right)}{v\left\{v+\left[n_1^2/\left(\varepsilon+n_1^2\right)\right]^{1/2}\right\}} \qquad \text{(S3)}$$

$$w_1^{'} = n_1 w_1/\lambda \qquad \text{(S4)}$$

$$e_2 = \left|\alpha_2^+\left(w_1/2\right)\right|^2 = \left|\alpha_2^-\left(w_1/2\right)\right|^2 = \frac{4w_2^{'}n_3^2}{\pi n_2}\left|\frac{\varepsilon^{1/2}}{\varepsilon+n_3^2}\right|\left|\frac{I_1^{'}}{1+\left(n_3/n_2\right)w_2^{'}I_0^{'}}\right|^2 \qquad \text{(S5)}$$

$$I_0^{'} = \int_{-\infty}^{\infty} du\left[\sin\left(\pi w_2^{'}u\right)/\left(\pi w_2^{'}u\right)\right]^2/v \qquad \text{(S6)}$$

$$I_1^{'} = \int_{-\infty}^{\infty} du \frac{\exp\left(-i\pi w_2^{'} u\right)\sin\left(\pi w_2^{'} u\right)/\left(\pi w_2^{'} u\right)}{v\left\{v + \left[n_3^2/\left(\varepsilon + n_3^2\right)\right]^{1/2}\right\}} \qquad \text{(S7)}$$

$$w_2^{'} = n_2 w_1 / \lambda \qquad \text{(S8)}$$

Similarly, for the Au/medium interface at the top of the nanoledge aperture (blue), *e* is given by

$$e_3 = \left|\alpha_3^{+}\left(w_2/2\right)\right|^2 = \left|\alpha_3^{-}\left(w_2/2\right)\right|^2 = \frac{4 w_3^{'} n_4^2}{\pi n_3}\left|\frac{\varepsilon^{1/2}}{\varepsilon + n_4^2}\right|\left|\frac{I_1^{"}}{1 + \left(n_4/n_3\right) w_3^{'} I_0^{"}}\right|^2 \qquad \text{(S9)}$$

with

$$I_0^{"} = \int_{-\infty}^{\infty} du\left[\sin\left(\pi w_3^{'} u\right)/\left(\pi w_3^{'} u\right)\right]^2 / v \qquad \text{(S10)}$$

$$I_1^{"} = \int_{-\infty}^{\infty} du \frac{\exp\left(-i\pi w_3^{'} u\right)\sin\left(\pi w_3^{'} u\right)/\left(\pi w_3^{'} u\right)}{v\left\{v + \left[n_4^2/\left(\varepsilon + n_4^2\right)\right]^{1/2}\right\}} \qquad \text{(S11)}$$

$$w_3^{'} = n_3 w_2 / \lambda \qquad \text{(S12)}$$

where e is the SP generation efficiency, α is the SP generation coefficient, w is the width of the nanoledge structure, ε is the dielectric constant, n is the refractive index, I is the integration calculation, w' represents the scaled width and u and v are applied for numerical integration with $u^2+v^2=1$.

Moreover, FDTD simulations reiterate the previous study by adding additional 10 nm $SiO_2$ film at the top of Au layer. Refractive index of the $SiO_2$ film used in calculations was equal to 1.41.[1]

Table S3.1. The SP generation efficiency $e_1$, $e_2$, $e_3$ for the nanoledge geometry $w_2/w_1$ of 280 -50nm with different n.

| $n_1$, $n_2$, $n_3$, $n_4$ | $e_1$ | $e_2$ | $e_3$ | $\Delta e$ |
|---|---|---|---|---|
| $n_1$=1.45, $n_2$=$n_3$=1, $n_4$=1.41 | 0.48 | 0.18 | 0.25 | |
| $n_1$=1.45, $n_2$=$n_3$=1.2, $n_4$=1.41 | 0.38 | 0.25 | 0.20 | -0.08 |
| $n_1$, $n_2$, $n_3$, $n_4$ | $e_1$ | $e_2$ | $e_3$ | $\Delta e$ |
| $n_1$=1.45, $n_2$=$n_3$=$n_4$=1 | 0.48 | 0.18 | 0.16 | |
| $n_1$=1.45, $n_2$=$n_3$=1, $n_4$=1.2 | 0.48 | 0.18 | 0.20 | 0.04 |
| $n_1$=1.45, $n_2$=$n_3$=$n_4$=1.2 | 0.38 | 0.25 | 0.15 | -0.04 |
| $n_1$=1.45, $n_2$=$n_3$=1.2, $n_4$=1 | 0.38 | 0.25 | 0.13 | -0.06 |

Table S3.2. The SP generation efficiency $e_1$, $e_2$, $e_3$ for the nanoledge geometry $w_2/w_1$ of 280 -50 nm with different bulk refractive index ($n_1$=1.45, $n_4$=1.41, and $n_2$=$n_3$=1.0-1.5).

| $n_2$=$n_3$ | $e_1$ | $e_2$ | | $e_3$ | $\Delta e$ |
|---|---|---|---|---|---|
| 1.0 | 0.48 | 0.18 | | 0.25 | 0 |
| 1.1 | 0.42 | 0.21 | | 0.23 | -0.05 |
| 1.2 | 0.38 | 0.25 | | 0.20 | -0.08 |
| 1.3 | 0.34 | 0.28 | | 0.18 | -0.11 |
| 1.4 | 0.31 | 0.32 | | 0.15 | -0.14 |
| 1.5 | 0.28 | 0.35 | | 0.12 | -0.16 |

Table S3.3. The SP generation efficiency $e_1$, $e_2$, $e_3$ for the nanoledge geometry $w_2/w_1$ of 280nm-50nm with different bulk refractive index ($n_1$=1.45, $n_4$=1, and $n_2$=$n_3$=1.0-1.5).

| $n_2$=$n_3$ | $e_1$ | $e_2$ | $e_3$ | $\Delta e$ |
|---|---|---|---|---|
| 1.0 | 0.48 | 0.18 | 0.16 | 0 |
| 1.1 | 0.42 | 0.21 | 0.16 | -0.03 |
| 1.2 | 0.38 | 0.25 | 0.15 | -0.04 |
| 1.3 | 0.34 | 0.28 | 0.15 | -0.05 |
| 1.4 | 0.31 | 0.32 | 0.14 | -0.05 |
| 1.5 | 0.28 | 0.35 | 0.13 | -0.06 |

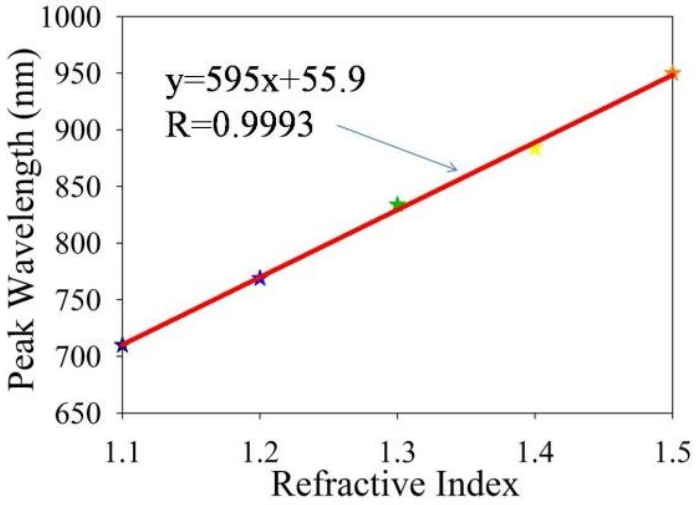


Figure S3.1. FDTD calculation of the peak wavelength of 280-50 nm nanoslit system vs refractive indices of bulk solutions.

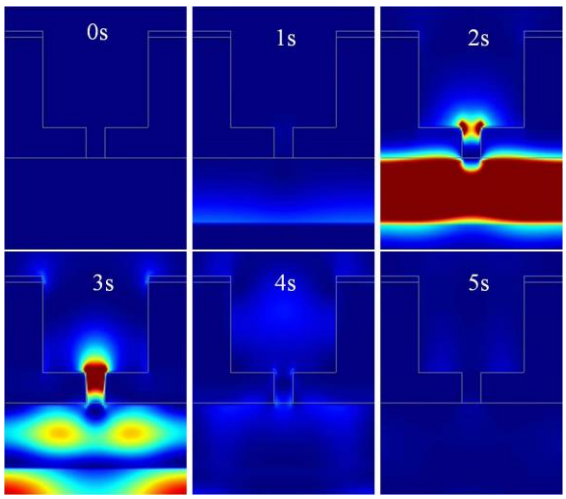


Figure S3.2. Movie screenshots of the TE field propagation through the simulation volume of 280-50 nm nanoledge system with $SiO_2$. The time of each screenshot shows the elapse of the movie.

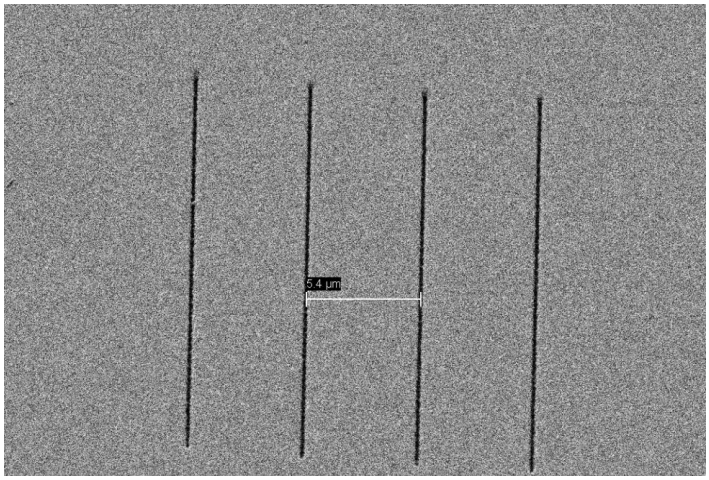


Figure S3.3. SEM image of nanoslits (100 nm width) with period of 5.4 µm.

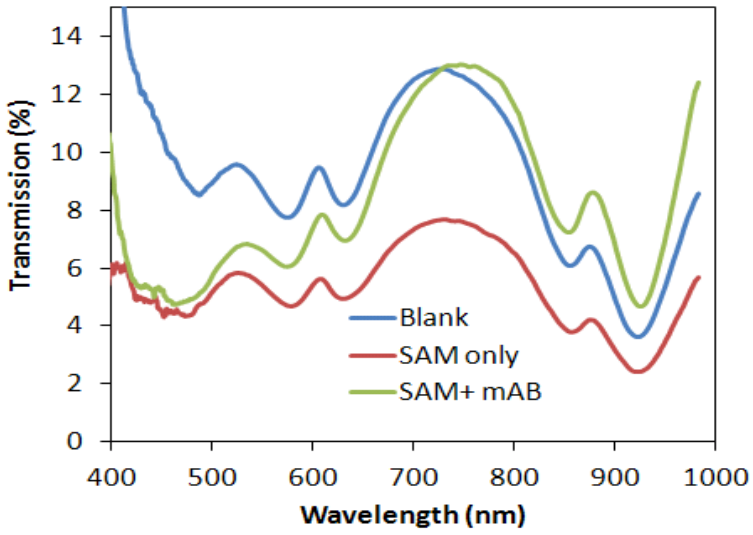


Figure S3.4. Optical transmission through a nanoledge device.

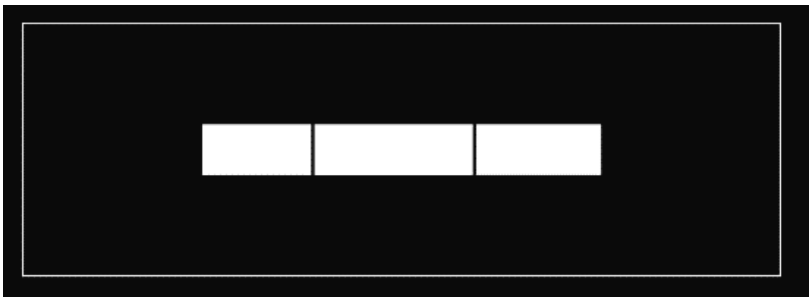

Figure S3.5. Design of dark field photomask for optical lithography. Not shown to scale.

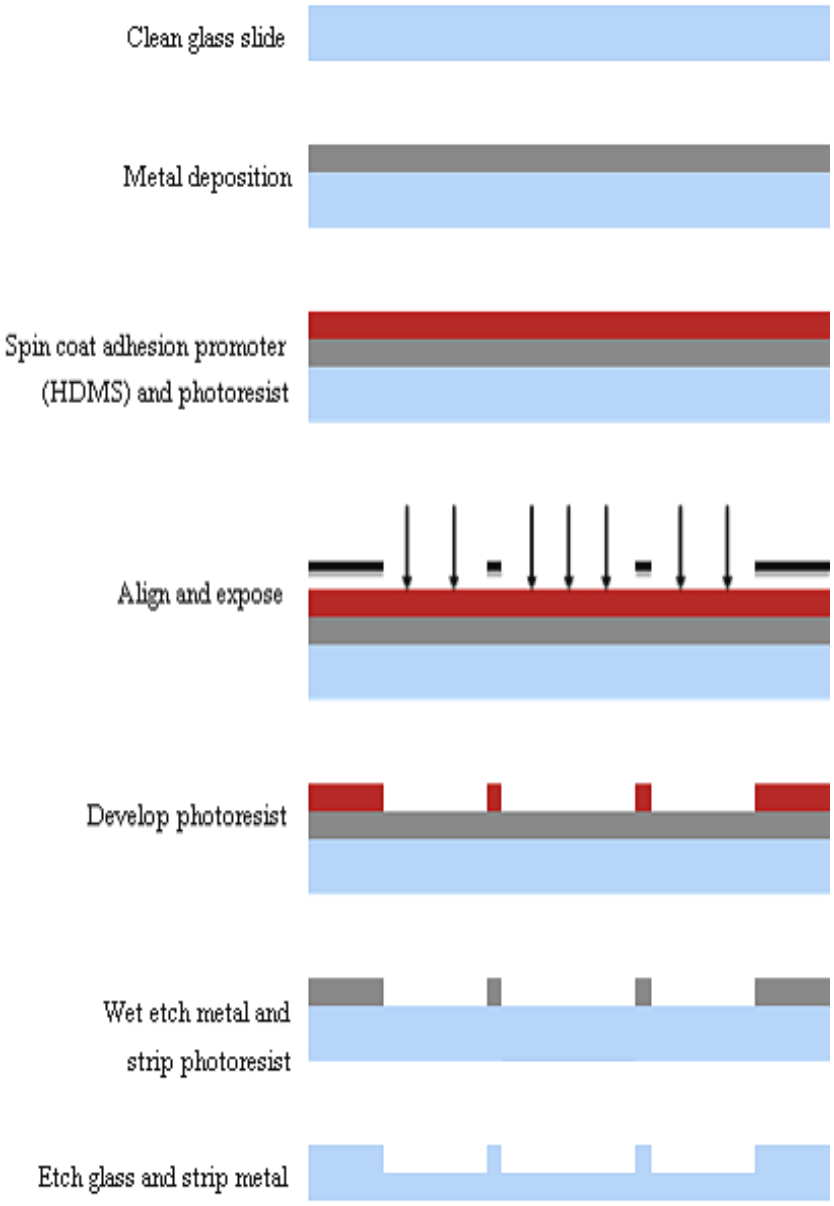


Figure S3.6. Lithography process for fabrication of the flow channel with dam structures.

## APPENDIX C

## IMPROVED SUPERCAPACITOR PERFORMANCE

Synthesis of $MnO_2$/ECNFs nanocomposites: electrospinning was used to produce carbon nanofibers. 10 wt.% Polyacrylonitrile (PAN, Mw = 150,000, Aldrich) solution in dimethylformamide was electrospun onto a collector to form a fiber fabric film. The applied positive voltage was 18 kV and the distance between the needle tip and the collector was 15 cm. The dense fiber fabric was collected from the steel collector covered with aluminum foil and pressed by two heated metal plates into a compact sheet at 100 °C under 5 MPa pressure for 5 min. The obtained sheet was then put into a furnace for stabilization. The heating rate was 3 °C/min from room temperature to 280 °C and kept for 2 h. The as-stabilized nanofibers were carbonized at 1000 °C for 2 h at a heating rate of 5 °C/min under $N_2$ atmosphere. After the ECNFs were prepared, $MnO_2$ was electrodeposited onto 1 $cm^2$ ECNFs by the galvanostatic method with a three-electrode setup using the charging current of 40 μA, and the charge time of 3 h, where Au electrode taped with ECNFs, platinum wire and Ag/AgCl were used as working electrode, counter electrode and reference electrode, respectively. To assure that the deposition of $MnO_2$ took place uniformly and firmly at the ECNFs' surfaces, the ECNFs electrode was treated with 5% $HNO_3$ solution for 2 h to introduce –OH and –COOH groups to facilitate the deposition. An aqueous precursor solution with 10 mM $MnSO_4$ and 100 mM $Na_2SO_4$ was used as the supporting electrolyte.

After the deposition, the working electrodes were washed with distilled water and then dried at 80 °C for 5 h.

Electrochemical measurements: electrochemical performance of the as-prepared electrodes was performed on a bio-logic VMP3 electrochemical workstation using a three-electrode testing system with a platinum wire as counter-electrode and Ag/AgCl as reference electrode in 6 M KOH electrolyte solution. The ECNFs film was cut 1 $cm^2$ for cyclic voltammetry (CV), electrochemical impedance spectroscopy (EIS), and galvanostatic charge/discharge tests. CV was carried out at different scan rates with a potential window of 0.8 V vs Ag/AgCl. CV tests were performed at scan rates range from 5 mV $s^{-1}$ to 100 mV $s^{-1}$, electrochemical impedance spectroscopy (EIS) was performed between 0.01 Hz -10 kHz, and charge/discharge tests were performed at current density from 0.5 A $g^{-1}$ to 20 A $g^{-1}$.

Magnetic field setup: since the magnetic field of each individual coil is non-uniform, the arrangement of the two narrow coils with a large radius r is built parallel to one another and on the same axis with a distance of the same radius size r, so that the magnetic field is uniform in a typical region based on the superimposition of the two fields. Given the Helmholtz arrangement of the pair of coils, the following equation is used to calculate the magnetic field: $B = 0.72\mu I\frac{n}{r}$, where B is the magnetic flux density, μ is the magnetic field constant, I is the coil current, n is the number of turns in each coil, and r is the coil radius. In this way, we can get the magnetic field of 0.45 mT, 0.89 mT, and 1.34 mT by setting the power supply current for the Helmholtz coils as shown in Figure 1a.

Materials characterization: Field emission scanning electron microscope (FESEM) (Carl Zeiss Auriga-BU FIB FESEM Microscope) was performed to study the morphological properties of ECNFs/$MnO_2$. Raman spectroscopy (Horiba XploRA One Raman Confocal Microscope System), x-ray powder diffraction (XRD) (Agilent Technologies Oxford Germini X-Ray Diffractometer), and Fourier transform infrared spectroscopy (FTIR) (Varian 670) were employed to study the elements components of ECNFs/$MnO_2$. Thermogravimetric analysis (TGA) (SDT Q600) and energy-dispersive X-ray spectroscopy (EDX) (Hitachi S-4800-I FESEM w/Backscattered Detector & EDX) were performed to study the weight ratio of $MnO_2$ on $MnO_2$/ECNFs. Superconducting quantum interference device vibrating sample magnetometer (SQUID VSM, Quantum Design, Inc.) was used to measure the magnetic properties of the $MnO_2$/ECNFs electrodes.

From the CV curves, the specific capacitance could be calculated on the basis of the following equation:

$$C = \int_{E1}^{E2} i\, dE / 2mS(E2 - E1) \quad \text{(S1)}$$

From the charge/discharge curves, the specific capacitance could be calculated as the following equation:

$$C = It/m(E2 - E1) \quad \text{(S2)}$$

where C is the specific capacitance (F/g), $\int_{E1}^{E2} i\,dE$ is the integrated area in cyclic voltammograms, m is the mass of the active sample (g), S is the scan rate (V/s), and (E2-E1) is the potential window (V), I is the discharge current (A), t is the discharge time in the potential window (s).[1-3]

For an electron transfer at electrode:

$$A + e \longrightarrow D \quad \text{(S3)}$$

Based on molecular basis, transition state theory expresses the electron transfer rate at the equilibrium state as:

$$k = A\exp\left[-\frac{\Delta G_0^*}{k_B T}\right] \quad \text{(S4)}$$

where $k$ ($s^{-1}$) is rate constant, $k_B$ is Boltzmann's constant ($1.3806568 \times 10^{-23}$ J $K^{-1}$), and $T$ is temperature in Kelvin. For an activated redox group,

$$\Delta G_0^* = \Delta H_0^* - T\Delta S_0^* \quad \text{(S5)}$$

$$k_0 = A\exp\left[\frac{\Delta S_0^*}{k_b}\right]\exp\left[-\frac{\Delta H_0^*}{k_b T}\right] \quad \text{(S6)}$$

When a magnetic field applied to the $MnO_2$ electrode, the entropy $\Delta S_0^{\ *}$ —> $\Delta S_0^{\ *} + \Delta S_m^{\ *}$, and enthalpy $\Delta H_0^{\ *}$ —> $\Delta H_0^{\ *} + \Delta H_m^{\ *}$, the rate constant then is expressed as:

$$k_m = A\exp\left[\frac{\Delta S_0^{\ *}}{k_b}\right]\exp\left[\frac{\Delta S_m^{\ *}}{k_b}\right]\exp\left[-\frac{\Delta H_0^{\ *}}{k_b T}\right]\exp\left[-\frac{\Delta H_m^{\ *}}{k_b T}\right] \qquad \text{(S7)}$$

$$\text{with } \Delta H_m^{\ *} = -gHS\beta$$

In Equ S7, the effects of magnetic field are expressed in enthalpy and entropy, and separated from non-magnetic entropy and enthalpy.

To simplify the process, only one of the unpaired electrons in Mn(IV/III) with spin ½ is considered for this derivative regarding the rate constant, scheme 4-1S below illustrates the simplified model for the energetics of the electron transfer/exchange reaction between Mn(IV/III).

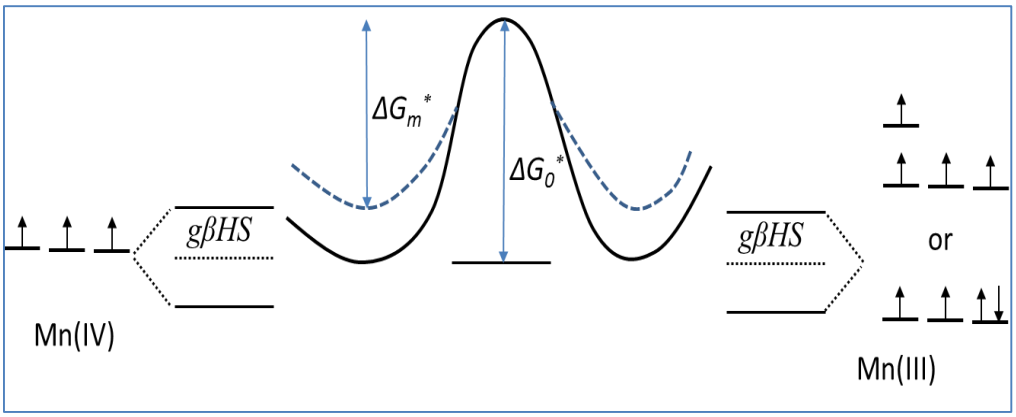


Scheme S4.1. Schematic illustration of a case at magnetic field effects on the electron transfer/exchange between Mn(IV/III). The gβHS represents the energetic degeneracy of the electron spin S under magnetic field. Two electron configurations (high spin and low spin) of the Mn(III) are illustrated.

The ratio of the rate constant change of magnetic field to non-magnetic field is:

$$\frac{k_m}{k_0} = \exp\left[\frac{\Delta S_m^*}{k_b}\right]\exp\left[-\frac{\Delta H_m^*}{k_b T}\right] = \exp\left[\frac{\Delta S_m^*}{k_b}\right]\exp\left[\frac{gHS\beta}{k_b T}\right] \quad \text{(S8)}$$

If $gHS\beta << k_b T$, and $\lim_{x\to 0}\exp[x] \to 1+x$, the Equation 10 becomes:

$$\frac{k_m}{k_0} = \left[1+\frac{gHS\beta}{k_b T}\right]\exp\left[\frac{\Delta S_m^*}{k_b}\right] \quad \text{(S9)}$$

The entropy of spin state can be expressed as:

$$\frac{S^*}{k_b} = -\sum_i n_i p_i \ln p_i \quad \text{(S10)}$$

Where the n is the number of species (electrons) and each electron has several assessable states and the probability of the species being in a state *i* is $p_i$. With sufficient magnetic field for spin polarization, one unpaired spin only has one state then the entropy term is one; while no magnetic field, the unpaired electron may be present in one of the two states, spin up and spin down. Thus the equation S9 can be derived as:

$$\frac{k_m}{k_0} = 2\left[1 + \frac{gHS\beta}{k_b T}\right] \tag{S11}$$

This equation gives us how the magnetic field induced degeneracy effects on the electron transfer reaction rate constant between Mn(IV/III) at the electrode. The actual case is more complicated because the number of unpaired electrons and spin states involved while also changes with the redox status. However, one can conclude that the magnetic field polarization on unpaired electron spin and the energy degeneracy would facilitate the redox reaction.

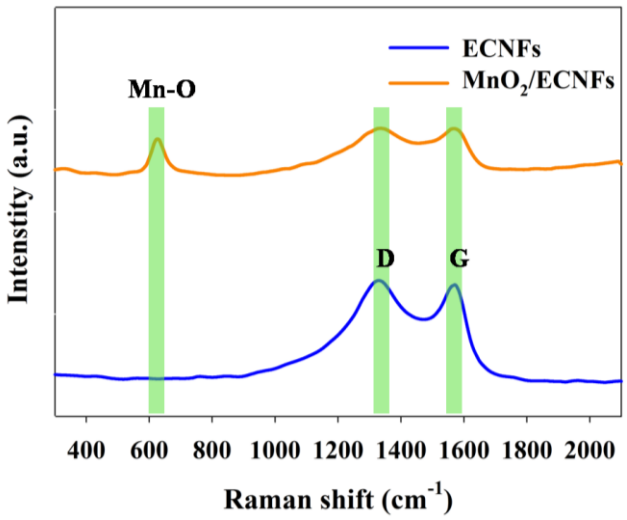


Figure S4.1 Raman spectra of ECNFs and $MnO_2$/ECNFs. At Raman shift of 1328 $cm^{-1}$ and 1572 $cm^{-1}$. ECNFs shows D-band and G-band, respectively. While, for $MnO_2$/ECNFs, Mn-O presents at the Raman shift of 627 $cm^{-1}$.[4]

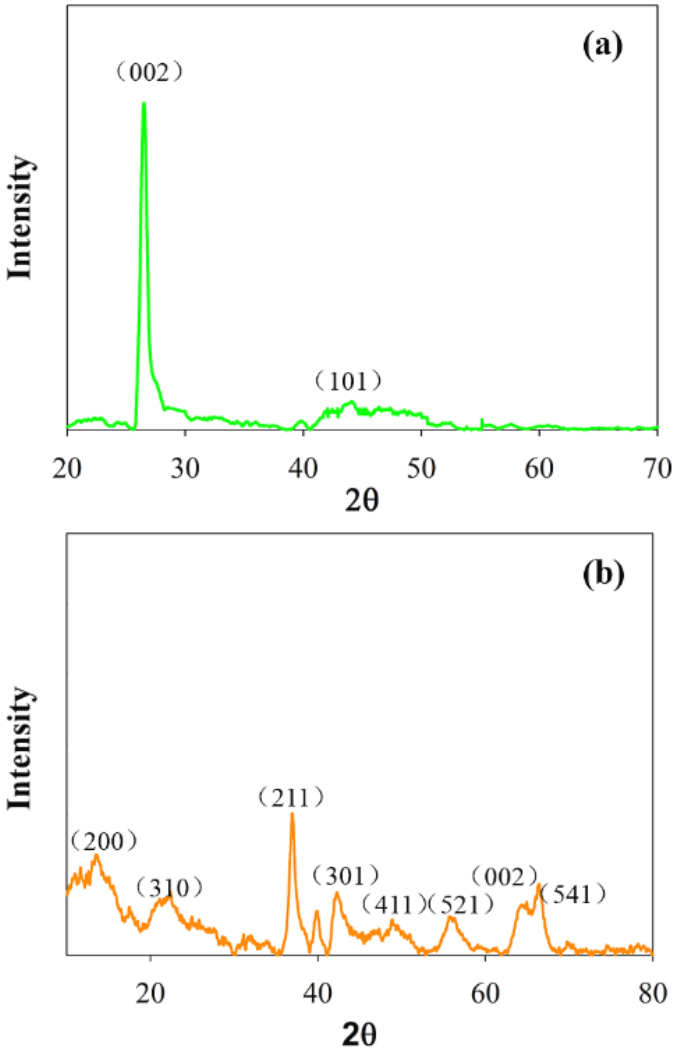


Figure S4.2 XRD spectra of ECNFs (a) and $MnO_2$ (b). The well-resolved peak at 37.1° in the XRD pattern is attributed to $MnO_2$.[5]

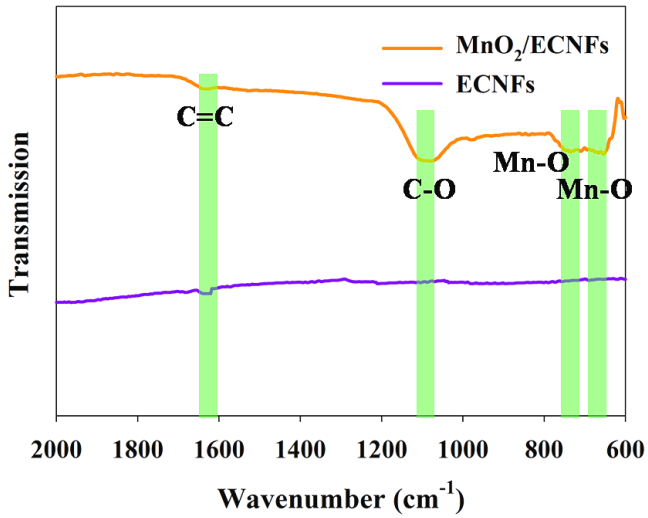


Figure S4.3 FTIR spectra of ECNFs and $MnO_2$/ECNFs. At wavenumber of 1623 $cm^{-1}$, ECNFs shows C=C. While, for $MnO_2$/ECNFs, Mn-O present at the wavenumber of 648 $cm^{-1}$ and 731 $cm^{-1}$. C-O presents at the Raman shift of 1104 $cm^{-1}$.[6]

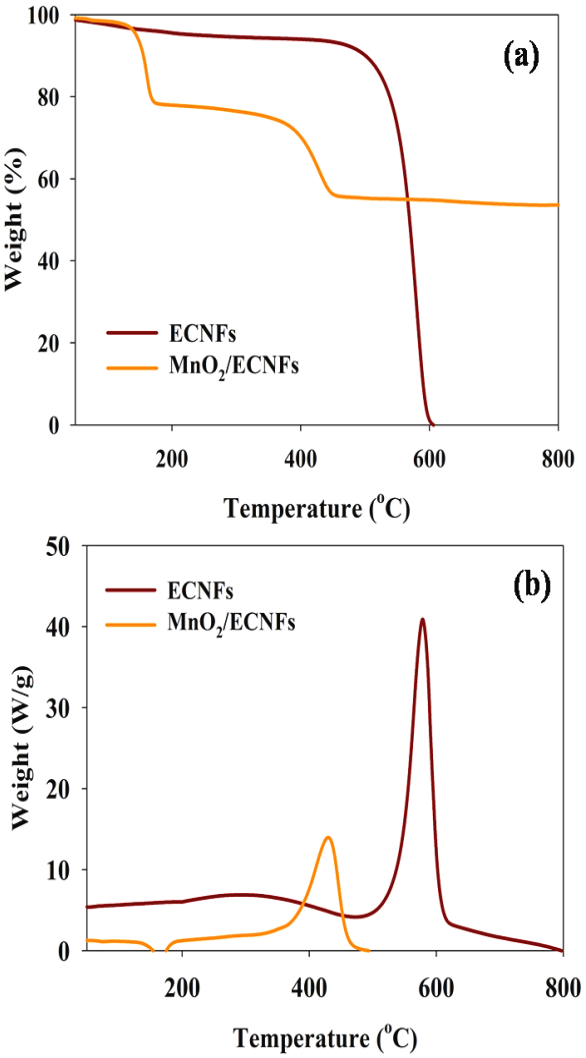


Figure S4.4 TGA and DSC of ECNFs and $MnO_2$/ECNFs to 800 °C in air. Due to the residue solvent evaporation, the ECNFs shows a weight loss before 431 °C. And then ECNFs decomposes until 605 °C. Unlike ECNFs, the $MNO_2$/ECNFs still achieve about 53% after 605 °C. So the $MnO_2$/ECNFs comprise 53% $MnO_2$ and 47% ECNFs.

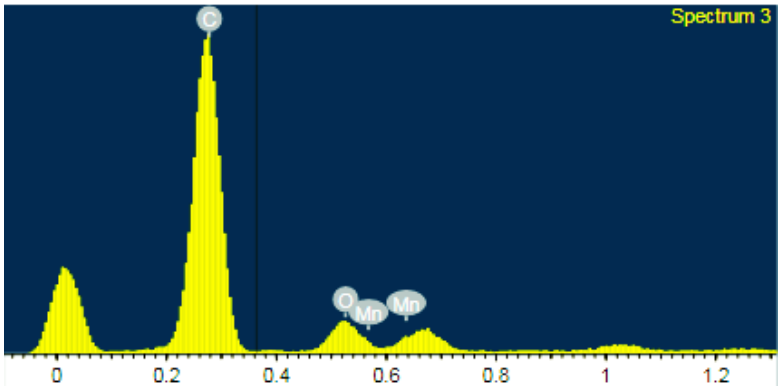


Figure S4.5. EDX of $MnO_2$/ECNFs. The weight% of C, O and Mn is 56.84%, 15.19%, 27.97% respectively. And the weight ratio of Mn: O is about 2:1. By averaging the EDX results of different spectrum zones, the average weight% of C, O and Mn is about 51.18%, 17.14%, and 31.68% respectively.

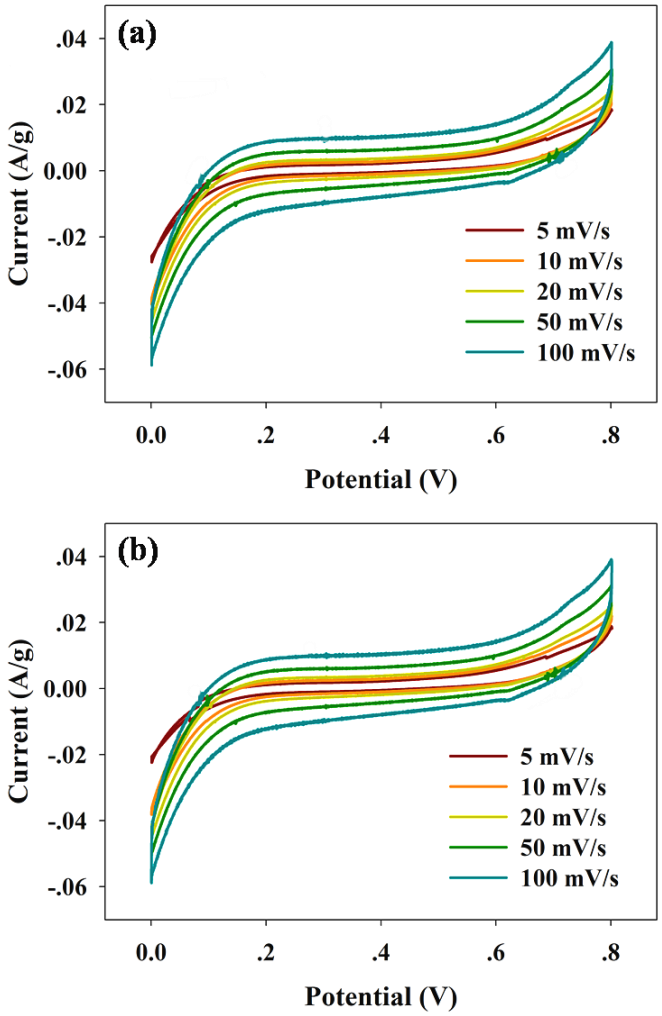


Figure S4.6. (a) Cyclic voltammetry loops of the ECNFs electrodes tested in the absence of magnetic field (0 mT) at different scan rates. (b) Cyclic voltammetry loops of the ECNFs electrodes tested in the presence of magnetic field (1.34 mT) at different scan rates.

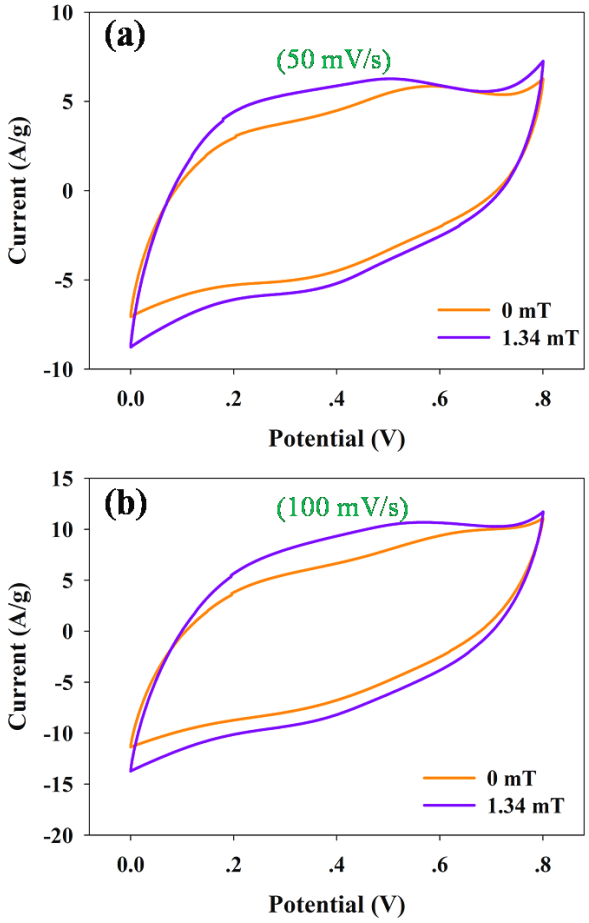


Figure S4.7 Cyclic voltammetry loops of the $MnO_2$/ECNFs electrodes tested in the presence (1.34 mT)/ absence (0 mT) of magnetic field at different scan rates of 50 mV $s^{-1}$ (a) and 100 mV $s^{-1}$ (b).

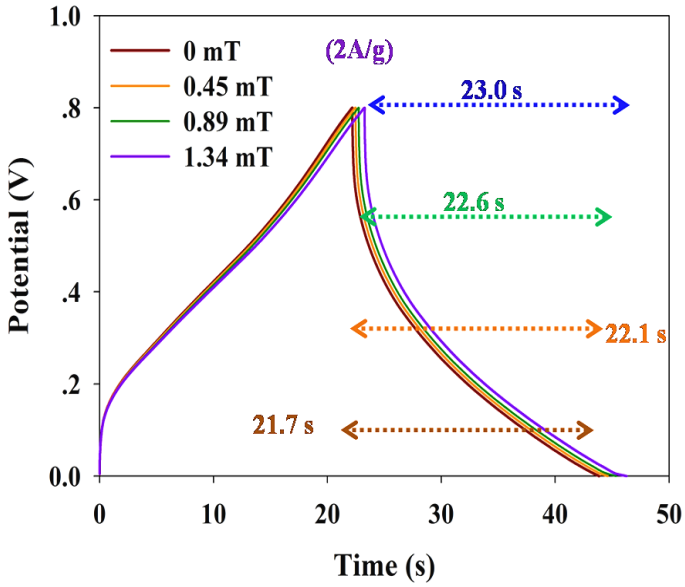


Figure S4.8 Galvanostatic charge/discharge curves of the $MnO_2$/ECNFs tested in the presence of different magnetic fields under the current density of 2 A $g^{-1}$.

References


1. Yu, G., Hu, L., Liu, N., Wang, H., Vosgueritchian, M., Yang, Y., ... & Bao, Z. (2011). *Nano letters*, *11*(10), 4438-4442.
2. Zhang, L. L., & Zhao, X. S. (2009). *Chemical Society Reviews*, *38*(9), 2520-2531.
3. Liu, Y., Zeng, Z., & Wei, J. (2016). *Front. Nanosci. Nanotech*, *2* (2), 78-85.
4. Wang, T., Song, D., Zhao, H., Chen, J., Zhao, C., Chen, L., & Xie, E. (2015). *Journal of Power Sources*, *274*, 709-717.
5. Li, X., Liu, J., Zhao, Y., Zhang, H., Du, F., Lin, C., & Sun, Y. (2015). *ChemCatChem*, *7*(12), 1848-1856.
6. Dubal, D. P., Dhawale, D. S., Salunkhe, R. R., & Lokhande, C. D. (2010). *Journal of the Electrochemical Society*, *157*(7), A812-A817.

# APPENDIX D

## OXYGEN REDUCTION REACTION

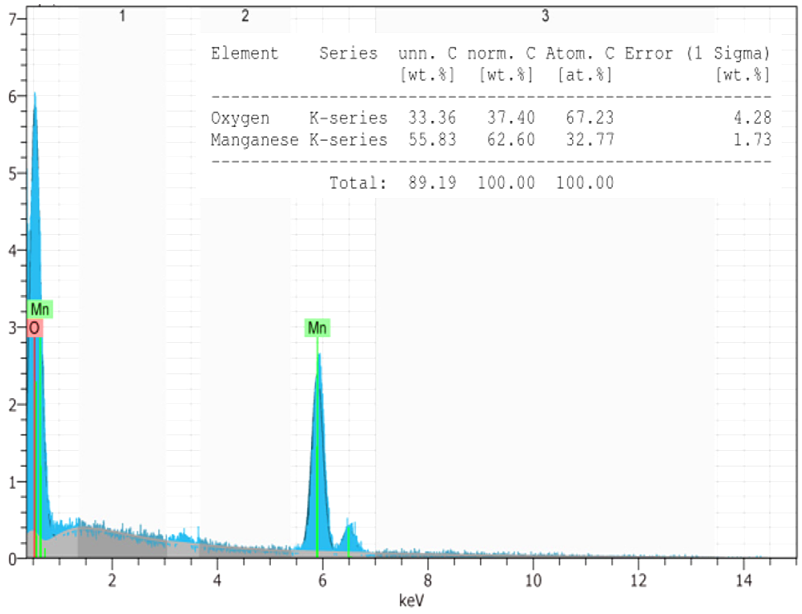


Figure S5.1. EDX of $MnO_2$/ECNFs after electrodeposition for 4 hours.

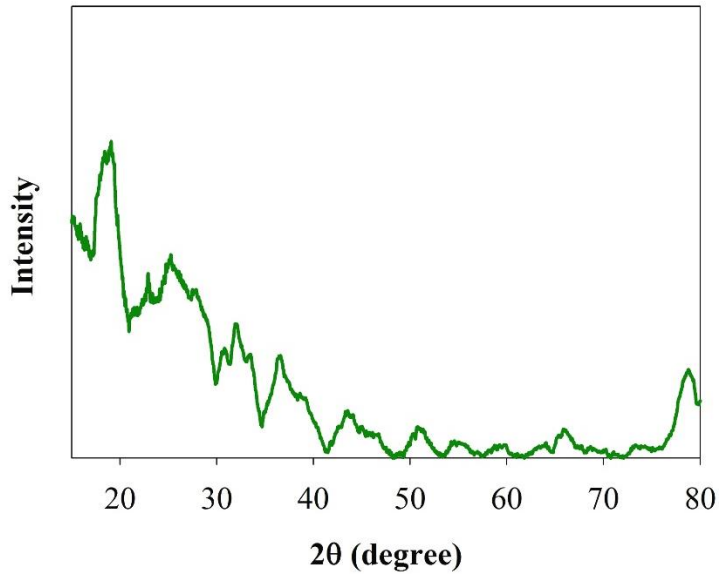


Figure S5.2. XRD of $MnO_2$/ECNFs after electrodeposition for 2 hours.

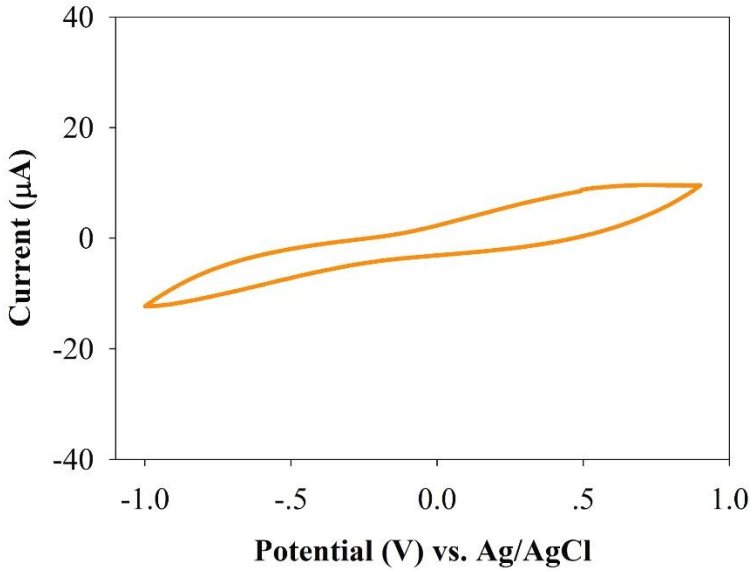


Figure S5.3. Cyclic voltammogram of the $H_2O_2$ reduction reaction at a electrode modified with ECNFs in $N_2$ saturated 20 mM KCl electrolyte solution with 1 mM $H_2O_2$ at the scan rate of 200 mV/s.

## APPENDIX E

## 4-ELECTRON PATHWAY

Since the magnetic field of each individual coil is non-uniform, the arrangement of the two narrow coils with a large radius r is built parallel to one another and on the same axis with a distance of the same radius size *r*, so that the magnetic field is uniform in a typical region based on the superimposition of the two fields. Given the Helmholtz arrangement of the pair of coils, the following equation is used to calculate the magnetic field:

$$H = 0.72\mu I\frac{n}{r} \tag{S1}$$

where $H$ is the magnetic flux density, $\mu$ is the magnetic field constant, $I$ is the coil current (in A), $n$ is the number of turns in each coil, and $r$ is the coil radius.

After simplifying, using the equation of $H$=0.7433×$I$ in millitesla (mT), we can get the magnetic field of 0.22 mT, 0.44 mT, 0.66 mT, 0.88 mT, 1.10 mT, and 1.32 mT by setting the power supply current for the Helmholtz coils.

Based on the molecular basis, transition state theory expresses the electron transfer rate at the equilibrium state as:[1,2]

$$k_0 = A\exp\left(-\frac{\Delta G_0}{k_B T}\right) \tag{S2}$$

where $k_0$ (cm $s^{-1}$) is rate constant without an external magnetic field, $k_B$ is Boltzmann's constant ($1.3806568 \times 10^{-23}$ J $K^{-1}$), and $T$ is temperature in Kelvin. Furthermore,

$$\Delta G_0 = \Delta H_0 - T\Delta S_0 \quad \text{(S3)}$$

then,

$$k_0 = A\exp\left(\frac{\Delta S_0}{k_B}\right)\exp\left(-\frac{\Delta H_0}{k_B T}\right) \quad \text{(S4)}$$

When a magnetic field applied to the $Co_3O_4$/ECNFs (5 h electrodeposition) modified electrode, the entropy $\Delta S_0 \to \Delta S_0 + \Delta S_m$, and enthalpy $\Delta H_0 \to \Delta H_0 + \Delta H_m$. In the presence of an external magnetic field, the rate constant then is expressed as:

$$k_m = A\exp\left(\frac{\Delta S_0}{k_B}\right)\exp\left(-\frac{\Delta H_0}{k_B T}\right)\exp\left(\frac{\Delta S_m}{k_B}\right)\exp\left(-\frac{\Delta H_m}{k_B T}\right) \quad \text{(S5)}$$

with $\Delta H_m = -gHS_p\beta$ (S6)

$A$ is the pre-factor depending on the convolution of a suitable weighted frequency ($v_n$) for crossing the activation barrier and the transmission coefficient or averaged transition probability for electron transfer per passage of the system through the intersection region from reactant to product, and in classical transition theory, $A$ is taken as $k_BT/h$ where $k_B$ is Boltzmann's constant, $T$ is absolute temperature, and $h$ is Planck constant.

The ratio of the rate constant with magnetic field to the ratio of the rate constant without magnetic field is:

$$\frac{k_m}{k_0} = \exp\left(\frac{\Delta S_m}{k_B}\right)\exp\left(-\frac{\Delta H_m}{k_B T}\right) = \exp\left(\frac{\Delta S_m}{k_B}\right)\exp\left(\frac{gHS_p\beta}{k_B T}\right) = \exp\left(\frac{gS_p\beta}{k_B T}\cdot H + \frac{\Delta S_m}{k_B}\right) \quad \text{(S7)}$$

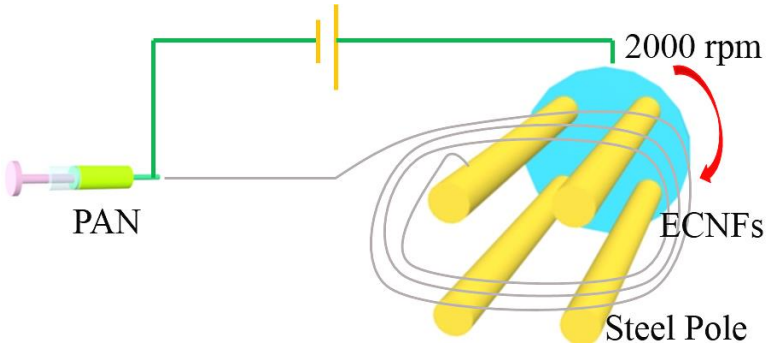


Figure S6.1. Illustrations of the aligned electrospinning technique.

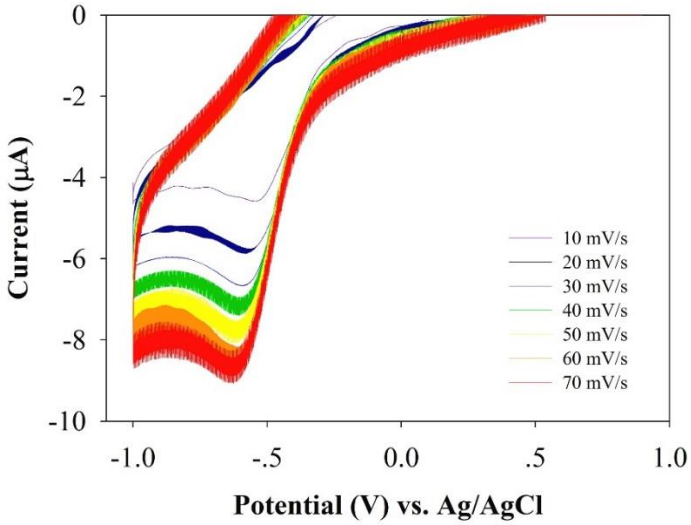


Figure S6.2. Cyclic voltammograms of the ORR at a bare glassy carbon electrode in $O_2$ saturated 20 mM KCl electrolyte solution at scan rates of 10-70 mV $s^{-1}$.

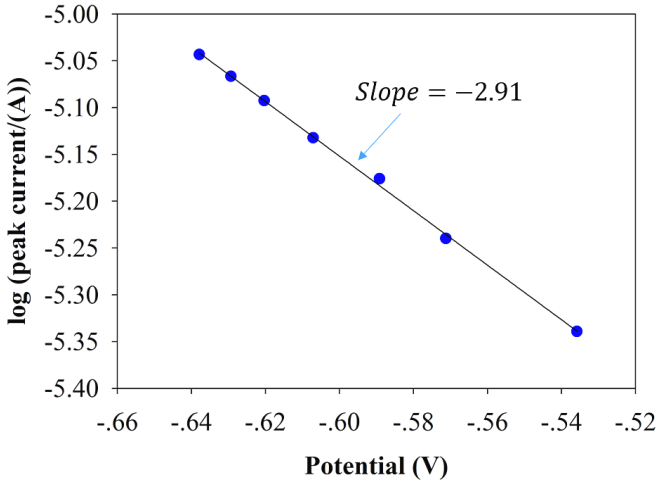


Figure S6.3. The linear dependence of the log of the peak current on the potential for the transfer coefficient calculation.

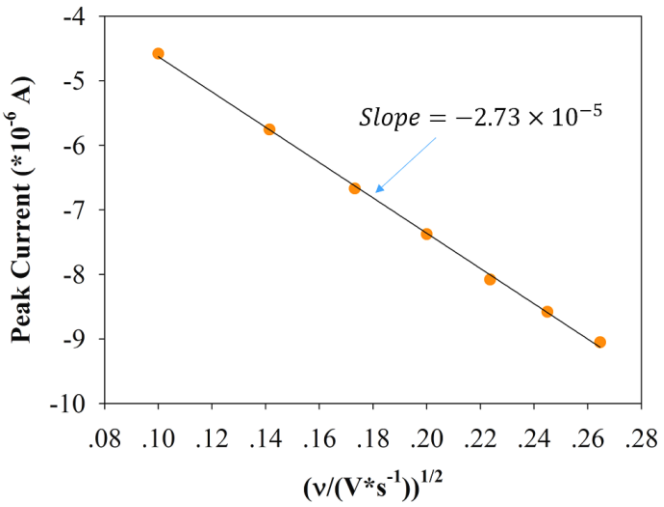


Figure S6.4. The linear dependence of the peak current on the square root of the scan rate for the number of electrons exchanged calculation.

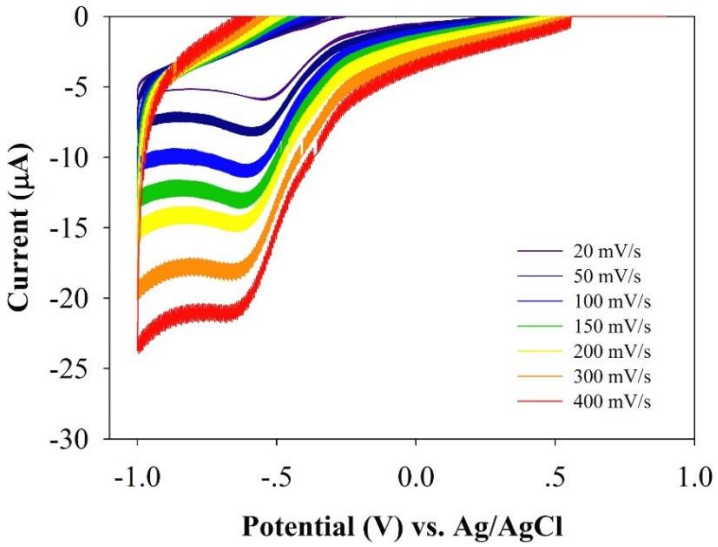


Figure S6.5. Cyclic voltammograms of the ORR at a bare glassy carbon electrode in $O_2$ saturated 20 mM KCl electrolyte solution at scan rates of 20-400 mV $s^{-1}$.

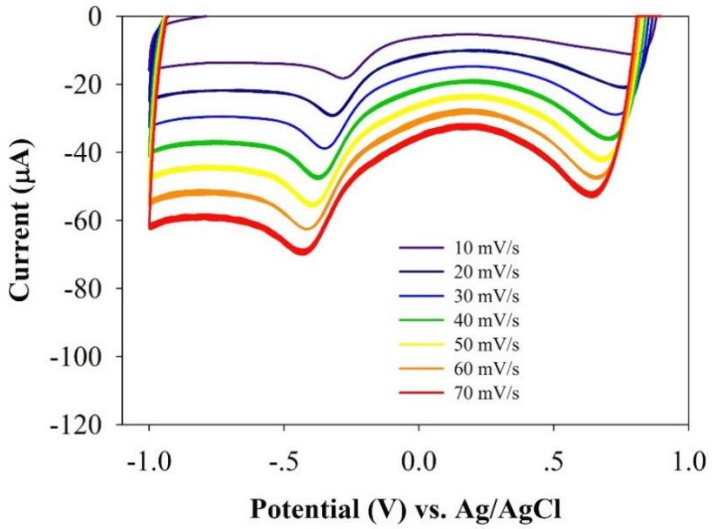


Figure S6.6. Cyclic voltammograms of the ORR at a $Co_3O_4$/ECNFs (5 h electrodeposition) modified electrode in $O_2$ saturated 20 mM KCl electrolyte solution at scan rates of 10-70 mV $s^{-1}$.

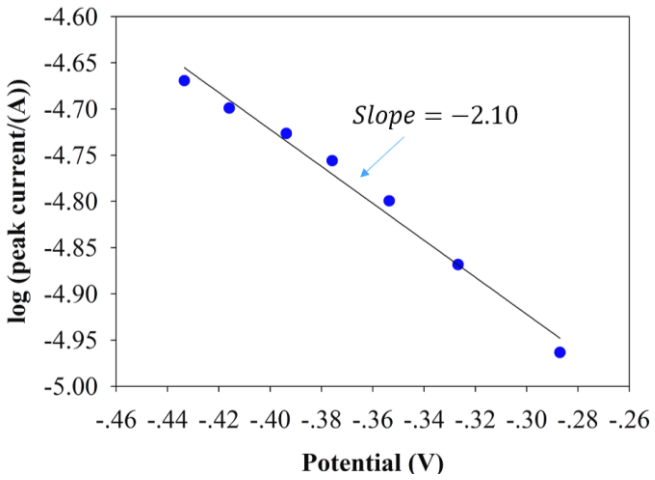


Figure S6,7. The linear dependence of the log of the peak current on the potential for the transfer coefficient calculation.

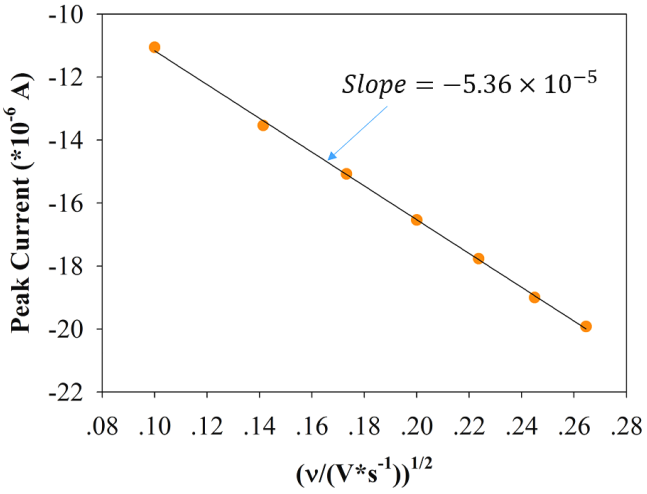


Figure S6.8. The linear dependence of the peak current on the square root of the scan rate for the number of electrons exchanged calculation.

Table S6.1. Time-dependent number of electrons exchanged of the ORR at the electrode modified with $Co_3O_4$/ECNFs in $O_2$ saturated 20 mM KCl electrolyte solution.

| Time | Slope 1 | Slope 2 | n |
|---|---|---|---|
| 1 h | -1.32±0.11 | $(-3.56\pm0.07)\times10^{-5}$ | 3.09±0.14 |
| 2 h | -1.43±0.02 | $(-4.03\pm0.12)\times10^{-5}$ | 3.27±0.09 |
| 3 h | -1.61±0.05 | $(-4.46\pm0.10)\times10^{-5}$ | 3.36±0.12 |
| 4 h | -1.77±0.04 | $(-4.81\pm0.05)\times10^{-5}$ | 3.43±0.07 |
| 5 h | -2.10±0.08 | $(-5.36\pm0.04)\times10^{-5}$ | 3.48±0.06 |
| 6 h | -1.96±0.06 | $(-5.13\pm0.02)\times10^{-5}$ | 3.46±0.03 |
| 8 h | -1.94±0.06 | $(-5.02\pm0.07)\times10^{-5}$ | 3.42±0.08 |

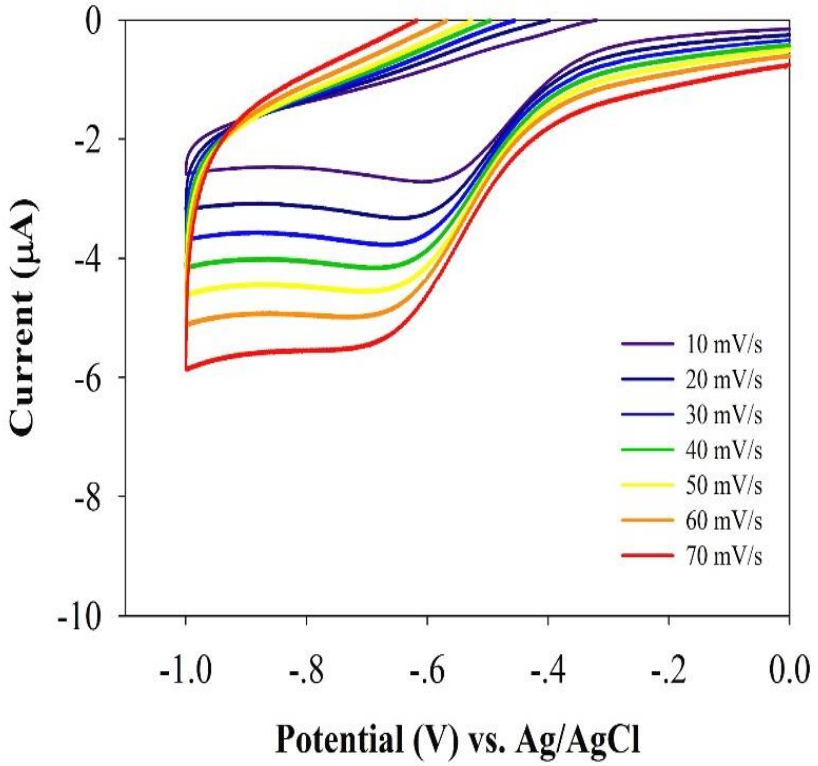


Figure S6.9. Cyclic voltammogram of the $H_2O_2$ reduction reaction at a $Co_3O_4$/ECNFs (5 h electrodeposition) modified electrode in $N_2$ saturated 20 mM KCl electrolyte solution with 1 mM $H_2O_2$ at the scan rate of 10-70 mV $s^{-1}$.

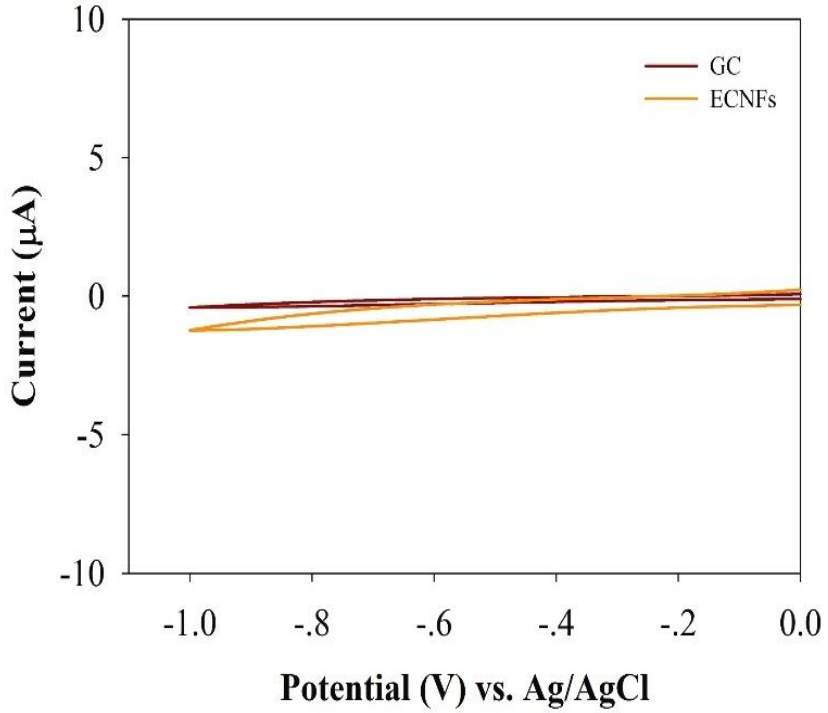


Figure S6.10. Cyclic voltammogram of the $H_2O_2$ reduction reaction at a bare glassy carbon electrode and an ECNFs modified GC electrode in $N_2$ saturated 20 mM KCl electrolyte solution with 1 mM $H_2O_2$ at the scan rate of 70 mV $s^{-1}$.

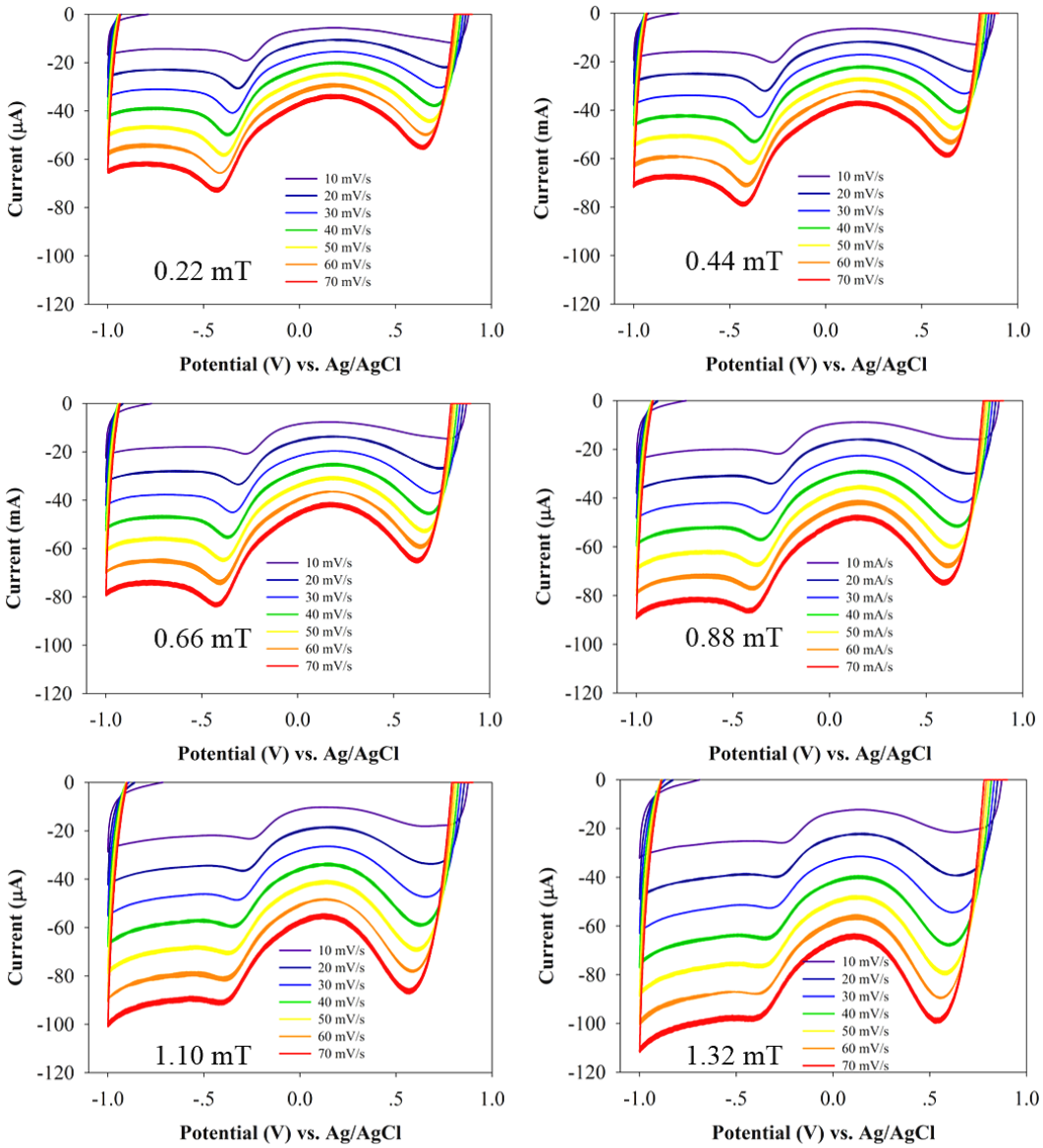


Figure S6.11. Cyclic voltammograms of the ORR at a $Co_3O_4$/ECNFs (5 h electrodeposition) modified electrode in $O_2$ saturated 20 mM KCl electrolyte solution at scan rates of 10-70 mV $s^{-1}$ under different magnetic fields.

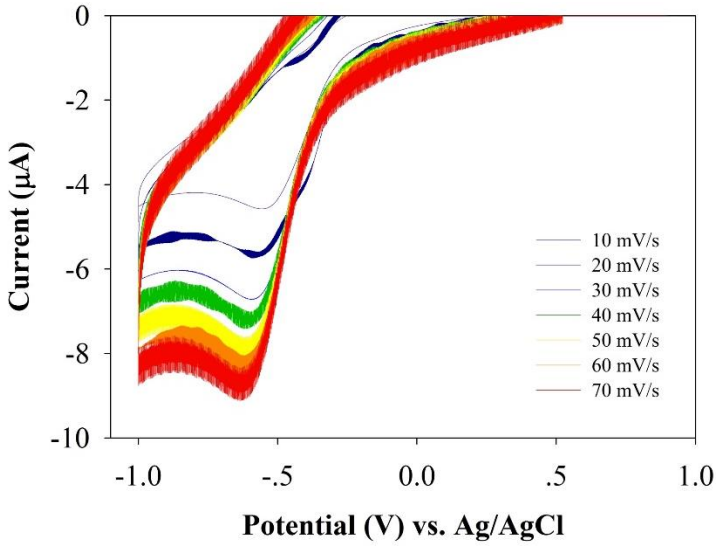


Figure S6.12. Cyclic voltammograms of the ORR at a bare glassy carbon electrode in $O_2$ saturated 20 mM KCl electrolyte solution at scan rates of 10-70 mV $s^{-1}$ under 1.32 mT magnetic field.

Table S6-2. Values for the estimation of $k^0$ at the scan rate of 20 mV $s^{-1}$.

| Magnetic field (mT) | $E_0$ (V) | $E_p$ (V) | $2(E_0-E_p)$ (V) | ET rate constant (cm $s^{-1}$) |
|---|---|---|---|---|
| 0.00 | -0.2755 | -0.3267 | 0.1025 | 0.004509 |
| 0.22 | -0.2692 | -0.3187 | 0.0991 | 0.004606 |
| 0.44 | -0.2621 | -0.3114 | 0.0987 | 0.004651 |
| 0.66 | -0.2612 | -0.3058 | 0.0892 | 0.004786 |
| 0.88 | -0.2524 | -0.2975 | 0.0901 | 0.004792 |
| 1.10 | -0.2443 | -0.2881 | 0.0876 | 0.004834 |
| 1.32 | -0.2360 | -0.2781 | 0.0842 | 0.004890 |

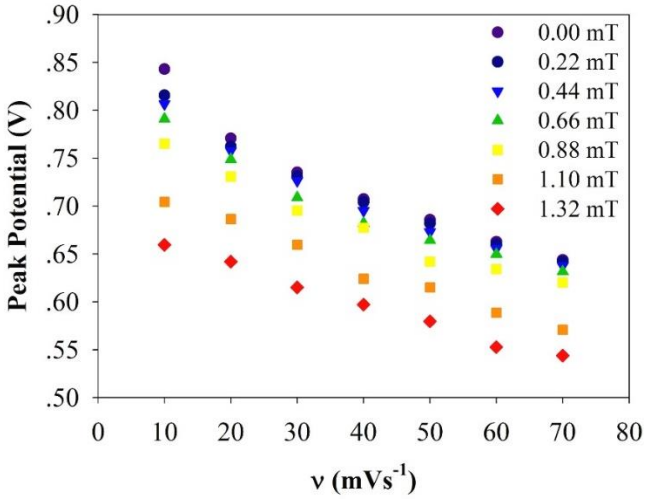


Figure S6.13. The dependence of the peak potential on the scan rate under different magnetic fields.

Table S6.3. Rate constant data for Co(III)/Co(II) redox reaction in the $Co_3O_4$ film on the electrode.

| Magnetic Field (mT) | $k_{Co}^{0}$ ($s^{-1}$) |
|---|---|
| 0.00 | 0.049±0.011 |
| 0.22 | 0.063±0.005 |
| 0.44 | 0.071±0.008 |
| 0.66 | 0.079±0.004 |
| 0.88 | 0.086±0.007 |
| 1.10 | 0.095±0.003 |
| 1.32 | 0.102±0.004 |

References

1. Zeng, Z., Liu, Y., Zhang, W., Chevva, H., & Wei, J. (2017). *Journal of Power Sources*, *358*, 22-28.
2. Lee, H. C. (2010). Doctoral dissertation, University of Iowa.

## APPENDIX F

## CRYPTOCHROME 1

The electron transfer between an electroactive reporter such as CRY1 and an electrode can be written as follows by assuming the direct superexchange pathway is the dominant pathway.[1]

$$CRY1^{*} \xrightarrow{k_{ox}} Electrode \tag{S1}$$

Note that here the electron acceptor is actually the electrode. A very important feature of electrochemistry is that the rate constant $k_{ox}$ is subject to the overpotential $\eta$. Therefore, in cyclic voltammetry, the crucial step is to get the expression of $k_{ox}$ in terms of $\eta$ by using a density of states (DOS) treatment and assuming a Marcus (Gaussian) density of states.

We assume that the DOS of the oxidized form is a normalized Gaussian distribution with $\sqrt{2\lambda k_B T}$ as the standard deviation, then

$$\rho(\varepsilon) = \frac{1}{\sqrt{4\pi\lambda k_B T}} \exp\left( -\frac{\left(\lambda + (\varepsilon_F - \varepsilon) + e\eta\right)^2}{4\lambda k_B T} \right) \tag{S2}$$

where $\rho(\varepsilon)$ is the DOS of the electrode, $\lambda$ is the reorganization energy, $k_B$ is the Boltzmann's constant, $T$ is temperature in Kelvin, $\varepsilon_F$ is the Fermi energy, $\varepsilon$ is the energy of an electronic state in the electrode, $e$ is the elementary charge, and $\eta$ is the overpotential.

And the overall oxidation rate constant can be obtained by using the established Fermi's golden rule:

$$k_{ox} = \frac{2\pi}{\hbar}\left|H_{DA}\right|^2 \int_{-\infty}^{\infty} \rho(\varepsilon) f(\varepsilon) \cdot \rho(\varepsilon,\lambda)\, d\varepsilon = \frac{2\pi}{\hbar}\left|H_{DA}\right|^2 \frac{1}{\sqrt{4\pi\lambda k_B T}} \int_{-\infty}^{\infty} \rho(\varepsilon) f(\varepsilon) \exp\left(-\frac{\left(\lambda + (\varepsilon_F - \varepsilon) + e\eta\right)^2}{4\lambda k_B T}\right) d\varepsilon \qquad \text{(S3)}$$

where $h$ is the Planck constant, $H_{DA}$ is the effective electronic coupling between the electrode and the probe states, $f(\varepsilon)$ is Fermi function. Since $\eta$ is a function of time $t$ and scan rate $v$, the rate constants for oxidation $k_{ox}$ depend on the time and scan rate.

To compare the intrinsic charge transfer properties of different systems, the standard heterogeneous rate constant $k^0$ is used

$$k^0 = k_{ox}(\eta = 0) \qquad \text{(S4)}$$

Hence the standard heterogeneous rate constant $k^0$ is given by

$$k^0 = \frac{2\pi}{\hbar}\left|H_{DA}\right|^2 \frac{1}{\sqrt{4\pi\lambda k_B T}} \int_{-\infty}^{\infty} \rho(\varepsilon) f(\varepsilon) \exp\left(-\frac{\left(\lambda + (\varepsilon_F - \varepsilon)\right)^2}{4\lambda k_B T}\right) d\varepsilon \qquad \text{(S5)}$$

These calculations allow us to make plots of the Faradaic peak potential shift from formal potential versus $log(v)$ for different $k^0$ values. Note that formal potential is the y-intercept at the scan rate of 0 V $s^{-1}$ by plotting peak potential vs. scan rate. These calculated curves can then be compared to plots of the experimental Faradaic peak potential shift versus $log(v)$ to extract the $k^0$ values for different systems.

Based on molecular basis, transition state theory expresses the electron transfer rate at the equilibrium state as:[2]

$$k_0 = A\exp\left(-\frac{\Delta G_0^{*}}{k_B T}\right) \tag{S6}$$

where $k_0$ ($s^{-1}$) is rate constant, $k_B$ is Boltzmann's constant ($1.3806568 \times 10^{-23}$ J $K^{-1}$), and $T$ is temperature in Kelvin. For an activated oxidation group,

$$\Delta G_0^{*} = \Delta H_0^{*} - T\Delta S_0^{*} \tag{S7}$$

then,

$$k_0 = A\exp\left(\frac{\Delta S_0^{*}}{k_B}\right)\exp\left(-\frac{\Delta H_0^{*}}{k_B T}\right) \tag{S8}$$

When a magnetic field applied to the gold slide electrode immobilized with CRY1, the entropy $\Delta S_0^{*} \rightarrow \Delta S_0^{*} + \Delta S_m^{*}$, and enthalpy $\Delta H_0^{*} \rightarrow \Delta H_0^{*} + \Delta H_m^{*}$, in the presence of an external magnetic field, the rate constant then is expressed as:

$$k_m = A\exp\left(\frac{\Delta S_0^{*}}{k_B}\right)\exp\left(-\frac{\Delta H_0^{*}}{k_B T}\right)\exp\left(\frac{\Delta S_m^{*}}{k_B}\right)\exp\left(-\frac{\Delta H_m^{*}}{k_B T}\right) \tag{S9}$$

$$\Delta H_m^{*} = -gHS_{\mathrm{p}}\beta \tag{S10}$$

where $A$ is the pre-factor depending on the convolution of a suitable weighted frequency ($v_n$) for crossing the activation barrier and the transmission coefficient or averaged

transition probability for electron transfer per passage of the system through the intersection region from reactant to product, and in classical transition theory, $A$ is taken as $k_BT/h$ where $k_B$ is Boltzmann's constant, $T$ is absolute temperature, and $h$ is Planck constant.

The ratio of the rate constant with magnetic field to that without magnetic field is:

$$\frac{k_m}{k_0} = \exp\left(\frac{\Delta S_m^*}{k_B}\right)\exp\left(-\frac{\Delta H_m^*}{k_B T}\right) = \exp\left(\frac{\Delta S_m^*}{k_B}\right)\exp\left(\frac{gHS_p\beta}{k_B T}\right) = \exp\left(\frac{gS_p\beta}{k_B T}\cdot H + \frac{\Delta S_m^*}{k_B}\right) \quad \text{(S11)}$$

Since coulomb and resonance integral values should be taken into account in the CRY1 system, the indirect band gap formula in the semiconductor system was used:[3,4]

$$\alpha h\nu = C\left(h\nu - E_0\right)^2 \quad \text{(S12)}$$

where $\alpha$ is the absorption coefficient, $h$ is the Plank constant, $\nu$ is the frequency, $C$ is the coefficient, and $E_o$ is the optical band gap, $(\alpha h\nu)^{1/2}$ has a linear relationship with $h\nu$, which could be used to estimate $E_o$. The Beer-Lambert law states that

$$A = \alpha bc \quad \text{(S13)}$$

where $A$ is the measured absorbance, $b$ is the path length, and $c$ is the analyte concentration. Among them, $b$ and $c$ are fixed values, so the $E_o$ could be calculated as the following equation:

$$\left(Ah\nu / bc\right)^{1/2} = D\left(h\nu - E_0\right) \quad \text{(S14)}$$

where $(Ahv/bc)^{1/2}$ has a linear relationship with hν with a slope of $D$ and $E_o$ is the x-intercept. Note that $hv$ is equal to $1240/\lambda$ in units of eV. In addition, changing the path length and concentration did not affect the result of x-intercept ($E_o$). With the UV-Vis absorption spectrum results, the relationship $(Ahv)^{1/2}$ vs. $hv$ could be used to estimate $E_o$.

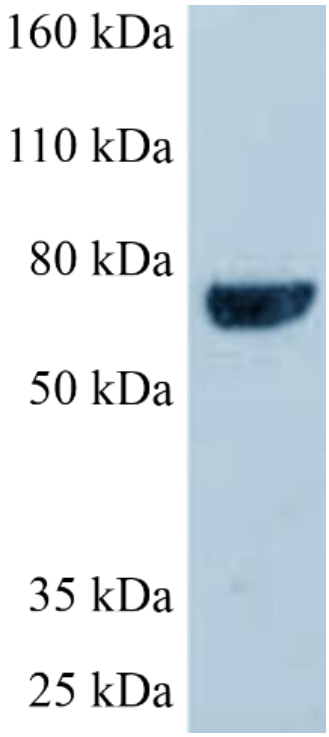


Figure S7.1. Polyacrylamide gel electrophoresis analysis of purified CRY1 with a molecular weight of 67 kDa.

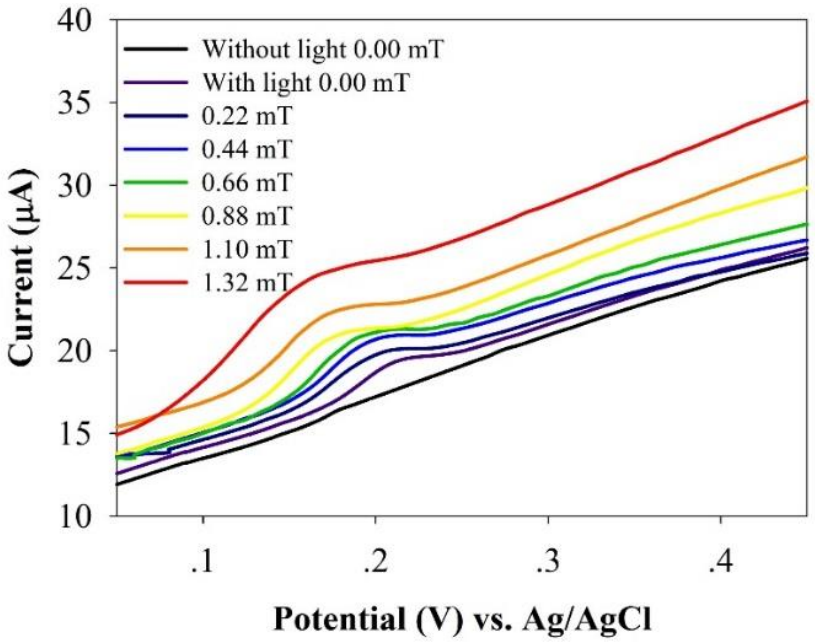


Figure S7.2. Cyclic voltammograms for the gold slide surface immobilized with CRY1 with/without blue light excitation in the absence of magnetic field and with blue light excitation under different magnetic fields at the scan rate of 4 V $s^{-1}$.

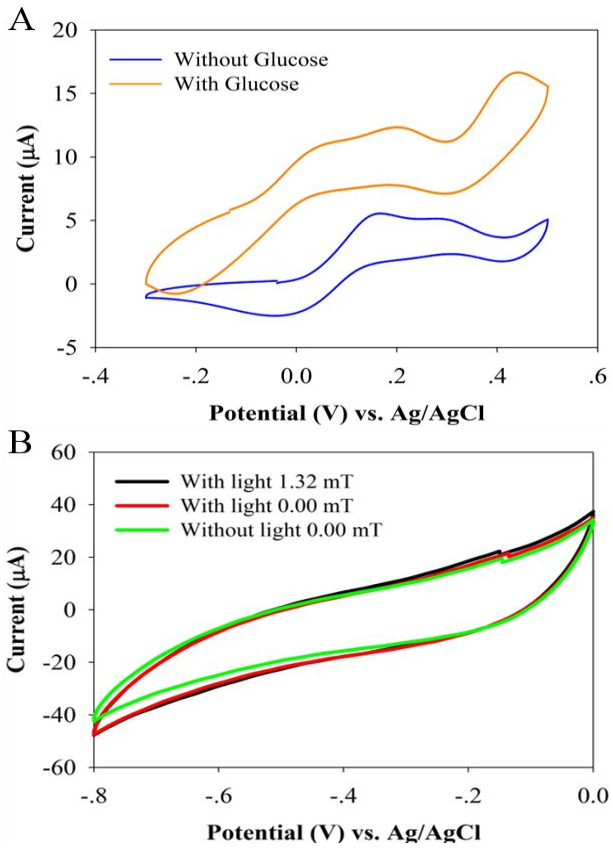


Figure S7.3. A. Cyclic voltammograms for the gold slide surface immobilized with glucose oxidase in the presence/absence of glucose with addition of 5 mM hydroquinone as a mediator in 10 mM PBS under a nitrogen environment at the scan rate of 5 mV $s^{-1}$ for the verification of gluocose oxidase immobilization (the reaction between glucose and glucose oxidase affects the redox of hydroquinone[5]). B. Cyclic voltammograms for the gold slide surface immobilized with glucose oxidase with/without blue light excitation in the presence /absence of 1.32 mT magnetic field in 10 mM PBS under a nitrogen environment at the scan rate of 4 V $s^{-1}$ for the study of photo-excitation and magnetic field effects on glucose oxidase.

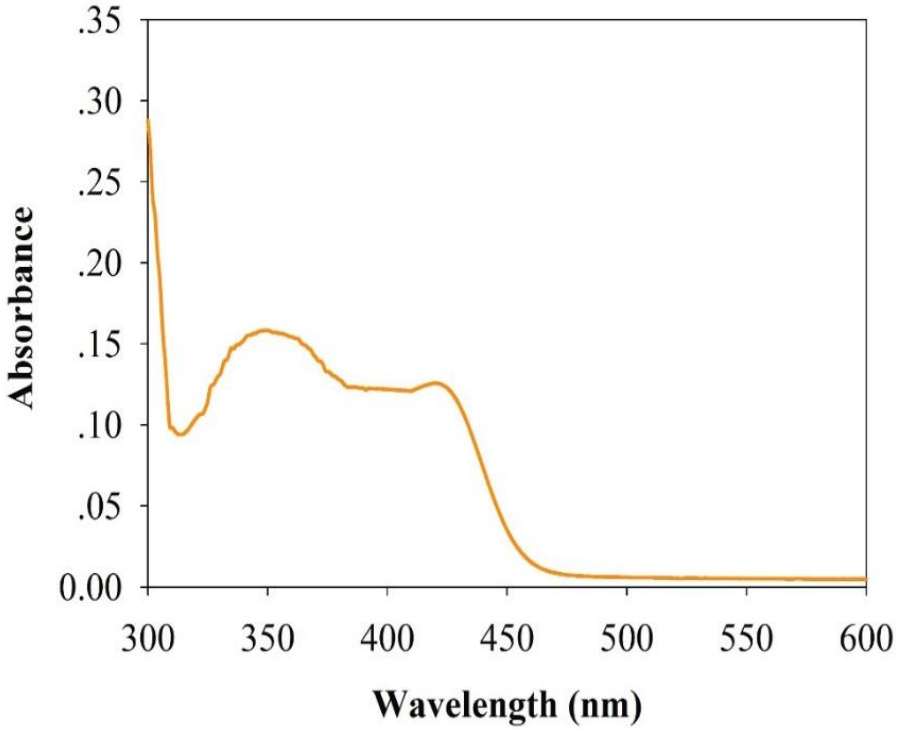


Figure S7.4. UV-Vis absorption spectrum of CRY1, indicating its blue-light receptor role.

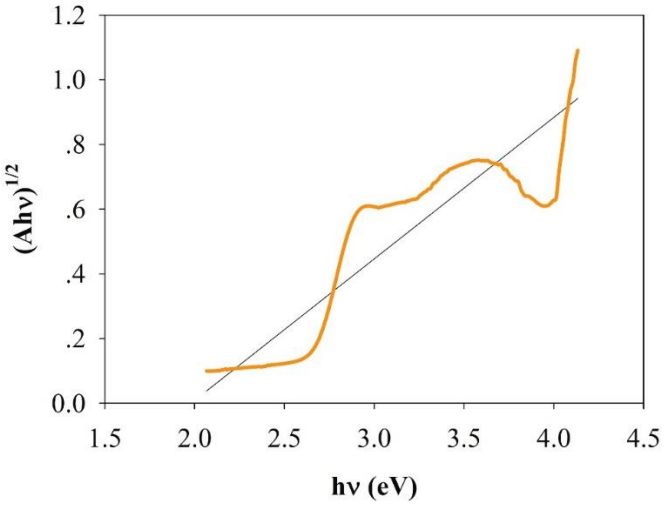


Figure S7.5 UV-Vis absorption spectrum of the CRY1 used to estimate the optical band gap $E_o$ (1.98±0.16 eV).

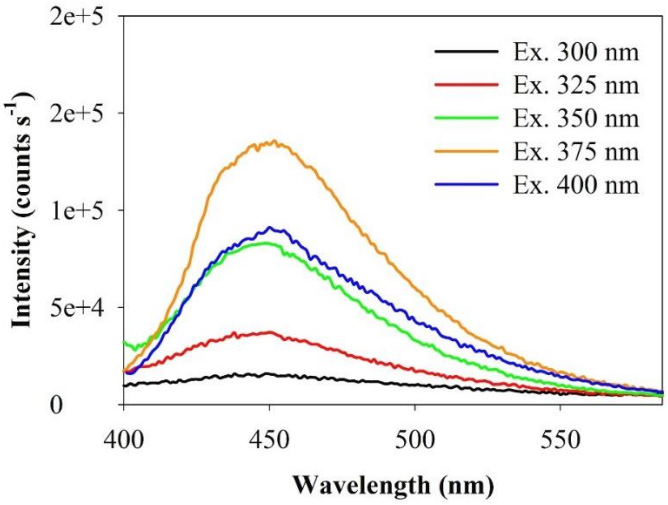


Figure S7.6. Fluorescence emission spectra of CRY1.

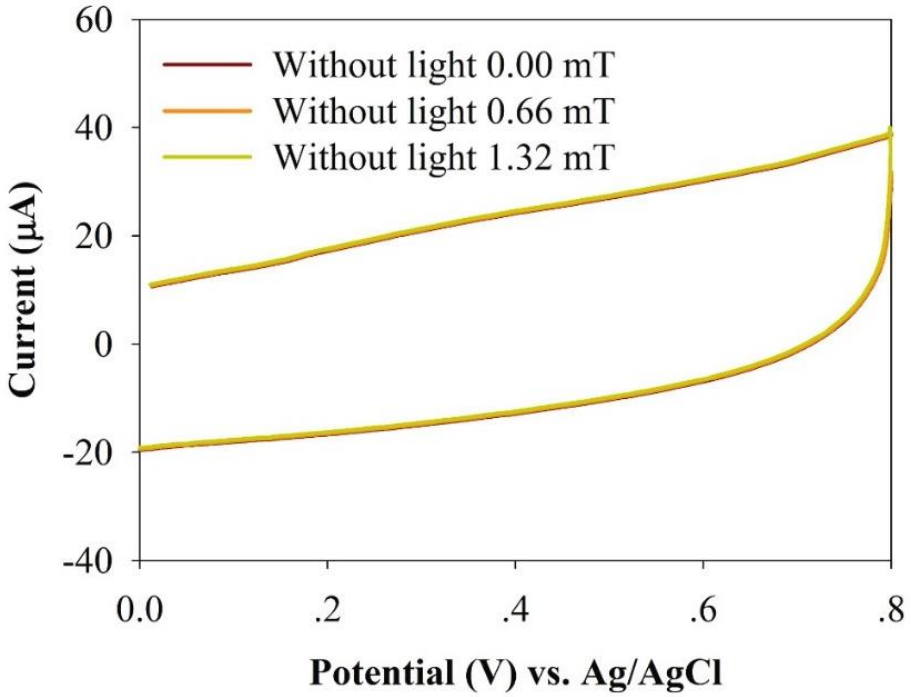


Figure S7.7. Cyclic voltammograms for the gold slide surface immobilized with CRY1 without blue light excitation under different magnetic fields at the scan rate of 4 V $s^{-1}$.

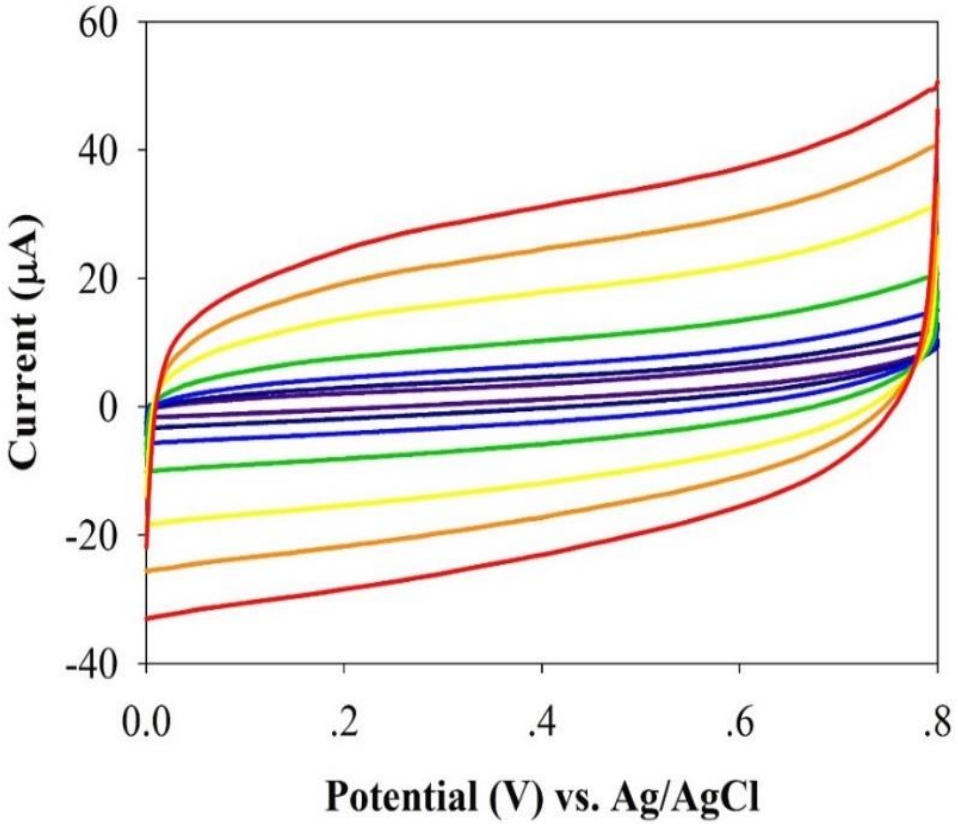


Figure S7.8. Cyclic voltammograms for the SAM/gold slide surface in which has not been immobilized with CRY1 with blue light excitation in the absence of an external magnetic field at the scan rate of 0.2 V $s^{-1}$, 0.5 V $s^{-1}$, 1 V $s^{-1}$, 2 V $s^{-1}$, 4 V $s^{-1}$, 6 V $s^{-1}$, and 8 V $s^{-1}$.

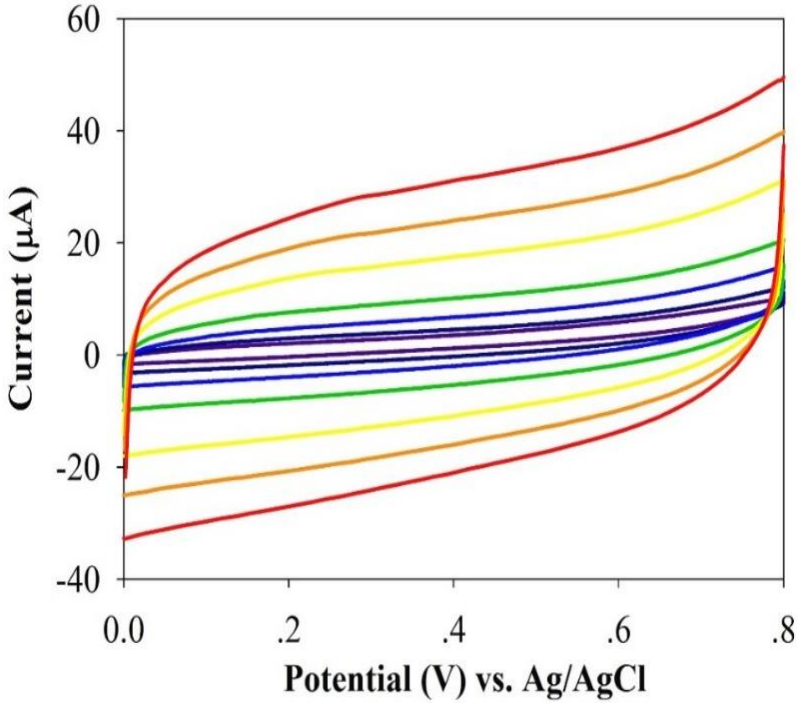


Figure S7.9. Cyclic voltammograms for the SAM/gold slide surface in which has not been immobilized with CRY1 with blue light excitation under 1.32 mT of magnetic field at the scan rate of 0.2 V $s^{-1}$, 0.5 V $s^{-1}$, 1 V $s^{-1}$, 2 V $s^{-1}$, 4 V $s^{-1}$, 6 V $s^{-1}$, and 8 V $s^{-1}$.

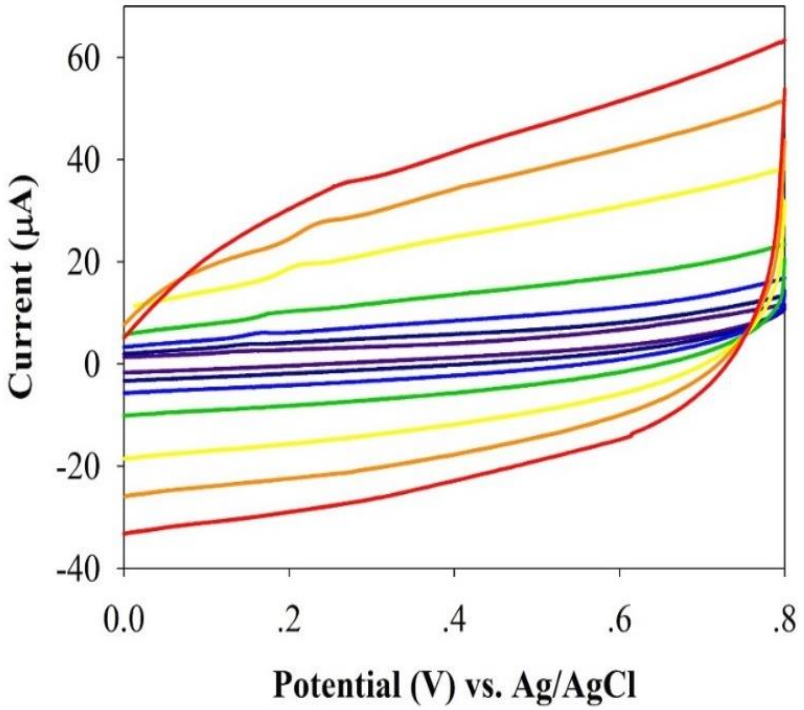


Figure S7.10. Cyclic voltammograms for the gold slide surface immobilized with CRY1 with blue light excitation in the absence of an external magnetic field at the scan rate of 0.2 V $s^{-1}$, 0.5 V $s^{-1}$, 1 V $s^{-1}$, 2 V $s^{-1}$, 4 V $s^{-1}$, 6 V $s^{-1}$, and 8 V $s^{-1}$.

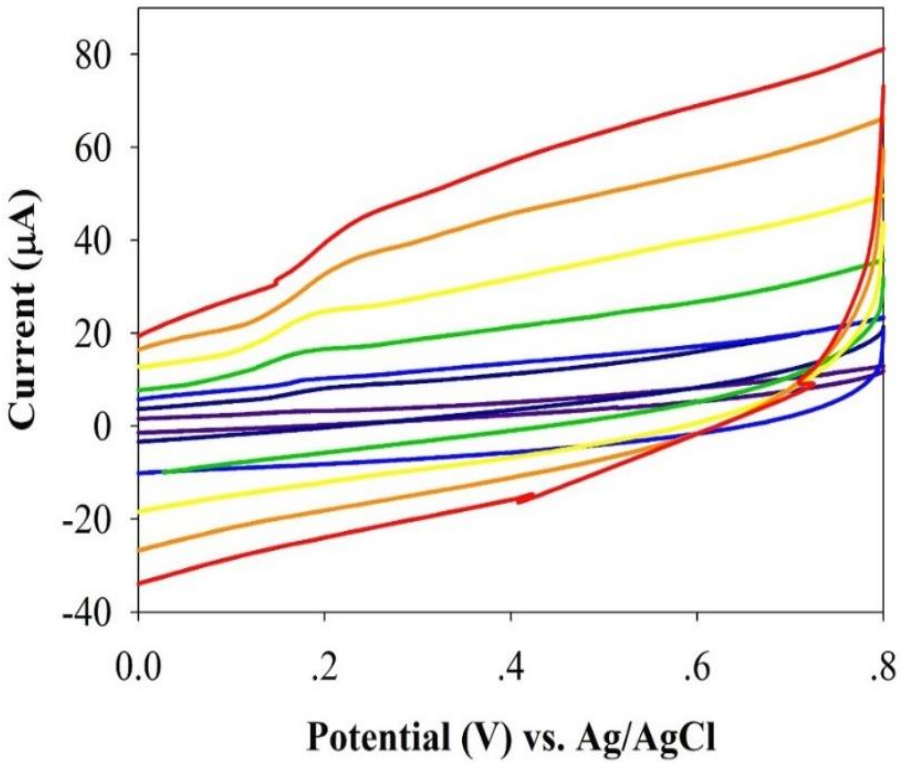


Figure S7.11. Cyclic voltammograms for the gold slide surface immobilized with CRY1 with blue light excitation under 1.32 mT of magnetic field at the scan rate of 0.2 V $s^{-1}$, 0.5 V $s^{-1}$, 1 V $s^{-1}$, 2 V $s^{-1}$, 4 V $s^{-1}$, 6 V $s^{-1}$, and 8 V $s^{-1}$.

Table S7.1 The dependence of the peak current on the voltage scan rate under different magnetic fields.

| | Peak Current (μA) | | | | | | |
|---|---|---|---|---|---|---|---|
| Scan Rate (V/s) | 0.00 mT | 0.22 mT | 0.44 mT | 0.66 mT | 0.88 mT | 1.10 mT | 1.32 mT |
| 0.2 | 0.1929 | 0.2195 | 0.2755 | 0.2812 | 0.3297 | 0.4611 | 0.5912 |
| 0.5 | 0.2946 | 0.3738 | 0.4304 | 0.5004 | 0.5956 | 0.7923 | 1.0261 |
| 1 | 0.4615 | 0.6332 | 0.7752 | 0.8749 | 0.9747 | 1.1971 | 1.4968 |
| 2 | 0.7551 | 0.9176 | 1.0802 | 1.4067 | 1.6537 | 1.9178 | 2.3322 |
| 4 | 1.4628 | 1.7877 | 2.1226 | 2.4283 | 2.7576 | 3.2334 | 3.7239 |
| 6 | 2.0840 | 2.6007 | 3.0236 | 3.4965 | 4.0614 | 4.7258 | 5.2398 |
| 8 | 2.6518 | 3.3525 | 3.9135 | 4.4291 | 5.0483 | 6.0389 | 6.6106 |

Table S7.2. The dependence of the peak potential on the scan rate under different magnetic fields.

| | Peak Potential Shift (V) | | | | | | |
|---|---|---|---|---|---|---|---|
| Scan Rate V/s | 0.00 mT | 0.22 mT | 0.44 mT | 0.66 mT | 0.88 mT | 1.10 mT | 1.32 mT |
| 0.2 | 0.0211 | 0.0172 | 0.0151 | 0.0127 | 0.0098 | 0.0077 | 0.0064 |
| 0.5 | 0.0286 | 0.0224 | 0.0203 | 0.0178 | 0.0150 | 0.0131 | 0.0101 |
| 1 | 0.0414 | 0.0299 | 0.0280 | 0.0254 | 0.0201 | 0.0183 | 0.0167 |
| 2 | 0.0558 | 0.0482 | 0.0456 | 0.0356 | 0.0325 | 0.0271 | 0.0250 |
| 4 | 0.0836 | 0.0733 | 0.0682 | 0.0634 | 0.0454 | 0.0439 | 0.0379 |
| 6 | 0.1116 | 0.1032 | 0.0948 | 0.0863 | 0.0708 | 0.0565 | 0.0482 |
| 8 | 0.1370 | 0.1188 | 0.1092 | 0.1014 | 0.0914 | 0.0733 | 0.0601 |

References

1. Yin, X., Wierzbinski, E., Lu, H., Bezer, S., de Leon, A. R., Davis, K. L., ... & Waldeck, D. H. (2014). The Journal of Physical Chemistry A, 118(35), 7579-7589.
2. Lee, H. C. (2010). Magnetic field effects on electron transfer reactions: heterogeneous photoelectrochemical hydrogen evolution and homogeneous self exchange reaction.
3. Yu, D., Yang, Y., Durstock, M., Baek, J. B., & Dai, L. (2010). ACS nano, 4(10), 5633-5640.
4. Zeng, Z., Zhang, W., Arvapalli, D. M., Bloom, B., Sheardy, A., Mabe, T., ... & Wei, J. (2017). Physical Chemistry Chemical Physics, 19(30), 20101-20109.
5. Liu, Y., Dolidze, T. D., Singhal, S., Khoshtariya, D. E., & Wei, J. (2015). The Journal of Physical Chemistry C, 119(27), 14900-14910.